Characterisation of a microwave-pumped slab-cooled carbon-dioxide laser

A thesis
submitted in partial fulfilment
of the requirements for the Degree
of
Doctor of Philosophy in Physics
in the
University of Canterbury

by

Andrew J Richards

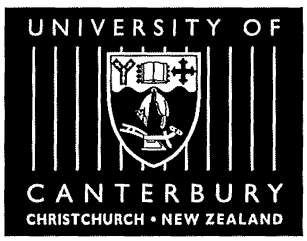

University of Canterbury
1999

Abstract

Microwave excitation of slab-cooled carbon-dioxide lasers is investigated. Incentives such as reduced cost, compact structure and higher power densities make microwave excitation of CO_2 lasers an attractive prospect.

Design parameters for such lasers are developed in contrast to direct-current and radio-frequency excited devices. The manner in which power is coupled into the discharge cavity is found to be critical to the performance of the laser.

This thesis adapts the standard theoretical models used to analyse radio frequency to microwave-excited discharges. The microwave frequency used here, 2.45 GHz, is close to the plasma frequency and several of the discharge characteristics differ as a result. The plasma sheath region is shown to be very small at this frequency and the addition of a quartz dielectric plate is required to give current stability to the discharge. Comparison of the electron density and its spatial distribution are made between RF and microwave regimes.

Several power supplies were used in the experimental part of the project. A 6 kV, 1 A switch-mode supply was modified and a high voltage DC switch with adjustable mark/space ratios was built so as to provide a range of microwave excitation characteristics.

An optical spectrometer was adapted and software developed to enable sidelight spectra to be recorded and analysed. These spectra can be used to examine gas dynamics and find estimates of the characteristic temperature of the discharge.

Three prototype microwave-excited carbon-dioxide laser cavities have been built and characterised experimentally. Laser output of 3 W has been observed with an efficiency of 5%.

Acknowledgements

I would like to thank my supervisor Phil Butler who got this project off the ground and guided me though this endeavour. Thanks also to my co-supervisor Tom Seed for his No. 8 wire solutions and for reminding me that there is more than one way to skin a cat. Stephen Hemmingson and Rob Thirkettle who built V1 through V3, and along with Grahame Kershaw and Wayne Smith attended to all those alterations and additions which every project seems to require. Clive Rowe, who was always able to provide a wealth of wisdom on a vast range of topics. Phil Butler, Mike Reid and Bryan Lawrence who allowed me to develop some extracurricular skills which kept me from bankruptcy. Glynn Jones, for the lamp. The office staff, especially Paul and Gill, and Ross and Graeme in the electronics workshop.

I would also like to thank my friends without whom my life would have been a lot grayer. Thanks to: Tom King for a second pair of hands on the odd occasion and for sharing my appreciation of things well-made. John Pritchard, for many enjoyable hours hanging from my fingertips. Jason Harris, romantic symbolic manipulator extraordinaire. Siva Naguleswaran, terrorist in residence. Duncan McLeod, the physics departments own DJ. Steve Cooper, self confessed magpie and designer of wooden engines. Dave Frame, who, along with Tom and John participated in the odd pint. Ata and Andy at the Foundry Bar who I'll be blaming for my fuzzy memory if I miss anyone off this list. My parents, for teaching me how to think. And finally, Caroline, who I owe more than anyone.

Contents

Chapter 1

Introduction

The objective of this research was to examine and characterise a microwave-pumped slab-cooled CO_2 laser. Most high power CO_2 lasers in use today use radio frequency (RF) fields as the method of excitation. While the basics of RF excitation of these lasers are well understood there has been relatively little investigation of pumping such lasers with microwave radiation.

1.1 Historical background and overview

Lasing in carbon dioxide (CO_2) was first discovered by Patel *et al.* [75, 77, 76] in 1964. These experiments determined the vibrational energy levels involved in the lasing transition. However, due to the low output power ($\sim 1\,\mathrm{mW}$), no great importance was attached to this discovery until later that year when the benefits of adding nitrogen (N_2) and helium (He) became apparent [78]. The first vibrationally excited state of nitrogen $\nu = 1$, a meta-stable state, is near-resonant with the upper lasing level of the CO_2 molecule (also a vibrational state). The combination of direct excitation and indirect excitation via nitrogen is considerably more efficient. Consequently, the following year saw output power levels jump to the order of 100 W [79, 64]. The reason that helium had a marked effect on the output power was not clear initially, however, it is now generally accepted that helium plays a significant role in the depopulation of the lower lasing level. Unaided, this de-excitation process can be a severe bottleneck in the lasing process. Helium helps to maintain discharge conditions, specifically the electron energy distribution, so that conditions are suitable for the efficient transfer of energy to the CO_2 molecule. In addition, the high thermal conductivity of helium increases the rate at which excess heat can be extracted from the discharge. Researchers and industry immediately saw the potential of such high power lasers and an intense interest in the subject developed.

It soon became apparent that the output power of the laser was strongly limited by its ability to cool the laser gas. Many variations on forced cooling systems using air and water were successful. However the simplest way to cool the gas was to remove it from the system and replace it with cool gas. This led to fast axial flow and transversely excited atmospheric lasers [19, 93, 21, 38], of which

the latter was capable of producing output powers in the 1-15 kW range. In this project, an efficient cooling system is used which can operate in flowing or sealed-off modes.

The addition of small quantities of xenon to the laser gas [15, 81, 73, 16] was found to have a significant effect on the output power, although in a less spectacular fashion than with the addition of N_2 and He. In RF lasers, increases in output power of 24% have been reported [33]. Xenon is a low ionisation potential gas, 2-3 eV less than the other gas components, and has a large cross-section for high energy electrons. In general, this means discharges containing xenon can be sustained at lower voltages with a more favourable electron energy distribution.

For compactness, convenience and a variety of other reasons, it is desirable to have a laser which can operate sealed-off from an external gas supply for a long period of time. Witteman [99] reported average output powers of $\sim$ 64 W with sealed-off lifetimes of the order of 1000 hours. The lasers examined in this project are all capable of sealed-off operation, however, no special techniques have been employed to ensure long sealed-off lifetimes. The addition of xenon, in addition to increasing output power, has been shown to increase the lifetime of such lasers due to its ability to discourage dissociation. Small amounts of water (H_2O) or hydrogen (H_2) added to the gas mixture can also increase tube lifetimes by promoting the catalytic recombination of dissociated CO_2. Performance enhancing gases were not added to the mixtures used in this project.

The use of hollow, narrow bore waveguides as part of the optical resonator was first proposed by Marcatili and Schmeltzer [56] in 1964 and first successfully demonstrated by Smith [87] in 1971. It was found that by confining the discharge within a hollow dielectric waveguide it was possible to use very narrow discharge tubes without suffering huge diffraction losses. For the CO_2, as well as many other lasers, the narrow bore of the discharge tube leads to increased gain, line-width, power generated per unit volume and saturation intensity. These performance improvements result from an increased de-excitation rate (due to the small distance to the walls), a reduction in gas temperature (for the same reason) and the ability to operate at higher pressures.

All the early CO_2 lasers excited their gas by direct current (DC) discharge. This method has the advantage of simplicity but is ultimately limiting with respect to output power because of gas cooling and voltage requirements. The only way to increase the output power of a DC (tube) laser is to increase its length. Increasing the diameter of the tube will increase the available gain volume, however, this is balanced by a reduction in gas cooling due the increased average distance to the walls. Increasing the length of discharge tube beyond one metre requires a high voltage to create and sustain the discharge. Power supplies for such devices become cumbersome and dangerous. The eventual step to radio frequency excitation was pioneered by Laakmann and others [49, 50, 90, 27] and the first report of successful operation of an RF-excited CO_2 waveguide laser was by Lachambre [51]. As well as RF excitation, this laser also employed the

technique of optical waveguiding described above.

RF-excited devices have a number of advantages over their DC counterparts. RF-excited discharges generally lead to more favourable excitation conditions, can be operated at higher pressures and do not require a resistive ballast. In addition, the power supplies are compact and relatively safe. Such lasers are also well suited to run in pulse mode via power supply modulation which leads to the precise power control essential in industrial applications. Microwave-excited lasers also have these advantages over DC lasers. However, the discharges in microwave-excited lasers behave differently to RF-excited discharges in some respects.

The last decade has seen a dramatic increase in the variety and applications of the CO_2 laser. Thin rectangular, diffusion-cooled devices [51, 14, 31] have dramatically increased gas cooling rates and have opened up the possibility of area scaling of laser power [3, 44]. Lasers using this geometry do not suffer from overheating when their width is increased. Thus an increase in the width or length increases the output power. This means very high output powers can be achieved in relatively compact regions. Lasers of this type, first demonstrated by Yatsiv [101], are often called slab lasers due to the thin rectangular nature of the discharge cavity and optical waveguide. Compact, sealed-off design at the kilowatt level is now a possibility [69, 18].

1.2 Applications of CO_2 lasers

Industry was quick to grasp the possibilities CO_2 lasers and their applications presented to materials processing. They provided a tool which could accurately cut, drill and score material with none of the problems associated with tool pressure, tool wear and non-localised heating. High power CO_2 lasers now routinely cut steel several centimetres thick. Lower power lasers also perform a variety of tasks including micro-machining, micro-soldering, ablation and vaporisation. Medicine has found the laser to be an effective surgical tool, resulting in less bleeding, faster recovery, reduced pain and fewer post-operative complications. Military systems often use CO_2 lasers for tactical systems like target sensing, precision guidance and coded communication. High energy short pulse CO_2 lasers have played a big part in the development of laser fusion where a high energy (100 kJ) laser pulse is directed onto a small mixture containing hydrogen and deuterium. With such a wealth of possible applications, there has been intense interest in understanding the many physical mechanisms so that more compact, efficient and versatile devices can be constructed.

1.3 Microwave pumping

Microwave excitation may have some advantages over RF excitation. For example, higher power densities at smaller electrode separation should be pos-

sible due to the reduction in thickness of plasma sheaths. The first reported case of microwave excitation was by Handy *et al.*[29] in 1978 where a DC tube geometry was excited by inserting it into a microwave waveguide. Since then there have been several attempts to create simple microwave-excited systems at 2.45 GHz [25, 74, 68, 53, 42, 59, 40, 41, 60], a frequency chosen because of the widespread availability of microwave magnetrons which work at this frequency.

The research reported in this thesis involved the construction and optimisation of a CO_2 laser designed to operate at microwave frequencies. The conventional microwave oven magnetron was chosen as the source of microwave power as it provides a robust source of 2.45 GHz radiation which can be incorporated into a compact laser leading to a cheap and reliable device. Coupling microwave radiation from the magnetron to a laserhead is not a common microwave application so coupling techniques had to be developed to transfer the energy from the magnetron to the laser gas without unwanted side effects. This method of gas pumping changes the design constraints on standard laser components such as the optics, vacuum system and diagnostic procedures. For example, in a microwave excited laser there is no requirement for the discharge electrodes to be electrically separated. This means that the side walls of the discharge cavity can be omitted if desired. The opportunities which result from the use of 2.45 GHz microwaves have been examined.

Three microwave pumped devices were constructed and examined in order to understand the processes involved when a laser discharge is excited at 2.45 GHz. Conclusions are drawn about the effectiveness and suitability of microwave pumping of CO_2 lasers. While the idea of exciting CO_2 lasers with microwaves has been around for many years the concept is still relatively novel, especially for lasers using the slab geometry.

One approach to microwave excitation is to use the simple glass tube design of the DC laser. In this system the gas filled tube is inserted into a waveguide in such a way that an electric field capable of causing a discharge is present in the gas. Lasers using this design were constructed by Handy [29], Wester [98] and Freisinger [25]. In slow-flow lasers of this design the output power is still limited by discharge length, as it is in conventional DC lasers. Cooling the gas is also a problem. As the discharge tube is placed inside a microwave cavity, a cooling-water jacket would absorb all the microwave energy. This means that a special cooling liquid or gas must be used. Alternatively, a fast axial flow system can be used. The approach due to Handy required a DC current to maintain the discharge and produced 1 W of output power. Wester's design could not cool the laser gas sufficiently and no lasing was observed. The design of Freisinger sacrificed size and portability for power and produced 700 W using a fast axial flow system.

More recently designs due to Nishimae and Yoshizawa [68] and März and Oestreicher [59] which use the slab configuration have achieved output powers of 100 and 20 W respectively. The design of März and Oestreicher appears to be similar

to the designs presented in this work except that the power is coupled into the laserhead from a secondary guide. The specific method of excitation of the laser developed by Nishimae and Yoshizawa is not well described in their paper.

1.4 Thesis outline

Chapter 2 introduces the basic concepts which underlie the operation of the CO_2 laser. Unlike many other lasers, the lasing transition in CO_2 occurs between rotational-vibrational states of the molecule rather than between electronic levels. This leads to an interesting inverse dependence of population inversion on gas temperature. Although lasing occurs on transitions of the CO_2 molecule, CO_2 is often the smallest fraction of the laser gas. This is because of the highly efficient excitation mechanism that can be utilised by the addition of nitrogen and helium to the gas mix. Electrons excited by the electric field can excite the upper lasing level directly or via the first vibrational state of N_2. The presence of other gas species, such as xenon and water, and the possibility of significant dissociation complicate matters. However, some general parameters have been established which help quantify the ability of a discharge to produce efficient laser output. The excitation method and related processes are described.

In chapter 3, the reasoning, design and constructional details of three lasers are discussed and illustrated. A key design issue was the decision to use the slab geometry as the primary gas cooling mechanism. Heat transfer plays an important role in the performance of a CO_2 laser because of the dependence of output power on gas temperature. Heat transfer in the laserhead is modelled in order to estimate the performance limits of these devices. The vacuum design for the three lasers is presented and analysed.

The excitation of a CO_2 laser requires the creation of a plasma, via some mechanism, inside a suitably designed optical resonator. In order to create a discharge, the gas must be subjected to an electric potential capable of causing ionisation. The unavailability of a power supply which could adequately drive a magnetron in a fashion suitable for experimental purposes meant that one had to be designed and constructed. Design details are presented in chapter 4. The task of exciting the laser gas is challenging as the microwaves must be launched from the magnetron into a waveguide which is capable of coupling the high-frequency field into the small discharge area. The necessity of a vacuum seal around the discharge cavity complicates the design, as does the need to eliminate discharges which may occur in undesirable regions of the evacuated section. Matters are further complicated by the fact that a different impedance is presented to the magnetron/waveguide section when the discharge is lit than when it is not. Even when lit, the discharge must be carefully controlled so that it is uniform, stable and of a suitable nature to induce a population inversion in the gas. Several excitation methods are investigated to address these issues.

Once a population inversion has been established, the optics are responsible for

extracting a suitable output beam. The optics in narrow bore and thin slab lasers differ considerably from those in more conventional lasers. When laser radiation is confined to propagate in region so small that part of the beam is occluded by the surrounding structure, waveguiding occurs. Such lasers often include free space sections in addition to the waveguide. The geometry of these sections is critical to the performance of the resonator as a whole. A judicious choice of mirror curvature, size and spacing can result in low coupling losses and good mode discrimination. A short review of waveguide laser theory is presented in chapter 5 followed by an analysis of the optical requirements of the lasers studied in this work. The optics used here are adequate for the purpose but not optimal.

Microwave discharges differ from RF and DC discharges in a number of ways. Chapter 6 examines how these differences affect the behaviour of a microwave pumped laser. A circuit model is used to describe how the addition of a quartz dielectric helps to improve discharge uniformity and stability.

Output power, efficiency and other performance-related measurements are presented in chapter 7. Significant differences between the lasers are investigated. Most notably, the choice of gas mixture is found to be more critical at microwave frequencies than was expected.

Some standard discharge parameters are difficult to measure for a microwave pumped CO_2 laser. Chapter 8 develops some methods for determining discharge parameters using sidelight spectroscopy. It is relatively easy to sample the optical emissions of the discharge using a fibre-optic. The spectrum obtained in this way can be analysed to produce estimates of such parameters as the vibrational and rotational temperature of the gas. A reliable method of measuring the ground state vibrational temperature of nitrogen is described. Discharge uniformity is important for optimum power extraction. Intensity profiles from the three lasers designed and built during this thesis are examined in relation to well tuned radio-frequency discharges.

Chapter 2

The CO_2 laser

2.1 Vibrational-rotational structure of CO_2

In order to understand the CO_2 laser it is necessary to be familiar with the energy level structure of the CO_2 molecule, its internal interactions and its interactions with nitrogen (N_2).

The lasing transition in CO_2 lasers occurs between two vibrational-rotational states of the molecule. Carbon-dioxide is a linear triatomic molecule which means that it can undergo rotational and vibrational motion in addition to translation. In general, the solution of the quantum mechanical equation of motion of a molecule is quite a complex problem. However, in the case of CO_2, the translational, vibrational and rotational motions can be treated separately making the task of modelling much simpler. The molecule can be described by several simple-harmonic oscillators which have small anharmonic contributions. The anharmonicity constants for these oscillators can be found experimentally via spectroscopy.

2.2 Vibrational modes

As CO_2 is a linear symmetric molecule with an axis of symmetry along its major axis, its vibrational motion can be separated into three normal modes. These are symmetric stretching (ν_1), bending (ν_2) and asymmetric stretching (ν_1), as shown in figure 2.1,

2.3 Wave equation

We can approximate the wave equation of CO_2 by,

$$(H_r + H_v)\psi_{mol} = E_{rv}\psi_{mol} \tag{2.1}$$

where E_{rv} is the sum of the vibrational and rotational energies and ψ_{mol} is the wave function describing the rotation and vibration of the molecule.

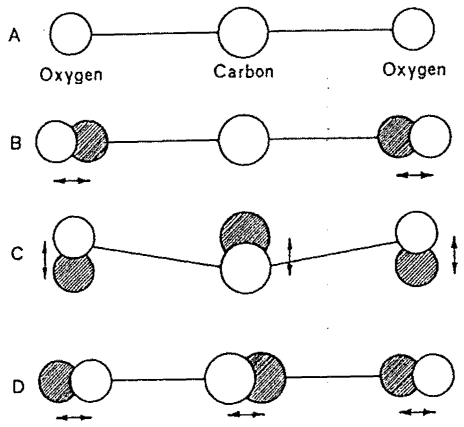

Figure 2.1: Vibrational normal modes of the CO_2 molecule. (A) Molecular structure, (B) Symmetric stretching, (C) Bending, (D) Asymmetric stretching.

Neglecting any perturbation of the vibrational state by the rotation state,

$$\psi_{mol} = \psi_r \psi_v \tag{2.2}$$

which, by substitution, gives $E_{rv} = E_r + E_v$.

The equation for ψ_r can be solved in terms of the spherical harmonics and associated Legendre function leading to a discrete set of energies given by,

$$E_r = Bj(j+1) \tag{2.3}$$

where B is the rotational constant. Note that for each rotational quantum number j there are $2j+1$ degenerate energy levels (described by m).

It can be seen by examining the vibrational part of the wave function that the bending vibration is a degenerate mode (figure 2.1c) as the vibration can take place in two orthogonal planes perpendicular to the axis of the molecule. This state is most conveniently described in terms of the total number of quanta excited and the number of angular momentum quanta. Thus the vibrational state of the molecule can be described by $(n_1 n_2^l n_3)$, where n_i is the number of quanta in the state ν_i and l is the number of angular momentum quanta excited in the ν_2 state.

Solving the harmonic part of the Hamiltonian in terms of the Hermite polynomials, the energy eigenvalues may be written,

$$E_v^0 = \hbar[\omega_1(n_1 + \frac{1}{2}) + \omega_2(n_2+1) + \omega_3(n_3 + \frac{1}{2})] \tag{2.4}$$

2.4 Rotational line distribution

The thermal distribution of rotational levels is according to Boltzmann statistics,

$$n_{vj} = N_v C g(j) \exp\left[-F(j)\frac{hc}{kT}\right] \tag{2.5}$$

where n_{vj} is the number of molecules with rotational number j per unit volume, N_v is the total number of molecules per unit volume having a particular vibrational state, C is a normalisation constant and $g(j)$ is the degeneracy $2j+1$. $F(j)$ is given by,

$$F(j) = B_v j(j+1) - D_v j^2(j+1)^2 \tag{2.6}$$

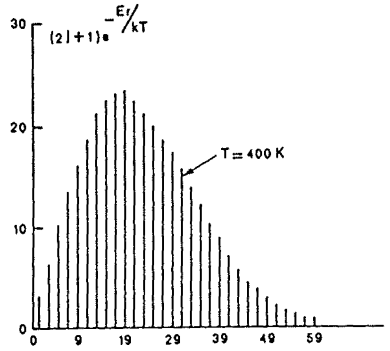

Figure 2.2: Rotational level distribution as a function of j.

The rotational distribution can be expressed,

$$n_{vj} \simeq N_v \left(\frac{2hcB}{kT}\right)(2j+1)\exp\left[-F(j)\frac{hc}{kT}\right] \tag{2.7}$$

As can be seen in figure 2.2, the population goes through a maximum for increasing j. The maximum is found at,

$$j_{max} \simeq \sqrt{\frac{kT}{2Bhc}} - \frac{1}{2} \tag{2.8}$$

The above expression for n_{vj} (equation 2.7) holds as long as the bending vibration has angular momentum $l = 0$. This is the case for the levels involving the laser transitions $(00^01)-(10^00)$ and $(00^01)-(02^00)$.

2.5 Energy levels

Figure 2.3 shows the low lying vibrational levels of CO_2. There are three bands in which lasing can be induced. These are the sequence band, the hot band and the regular band. Transitions in the sequence and hot bands are not used for high power work because they have low quantum efficiencies compared to those of the regular band and do not benefit from the indirect excitation provided by nitrogen in the same way. Furthermore, intra-cavity and selective optics are required to make these transitions lase in preference to the higher gain transitions in the regular band.

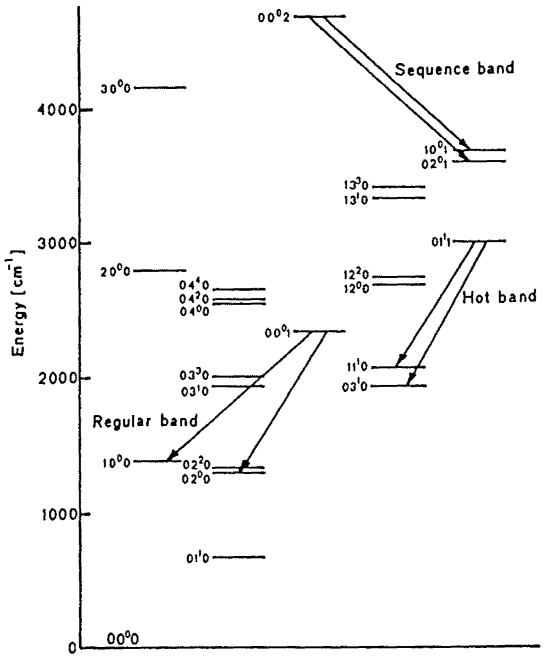

Figure 2.3: Some of the low lying vibrational levels of the CO_2 molecule.

2.5.1 Transitions of the regular bands

The infrared spectrum of CO_2 results from transitions between vibrational-rotational levels and is subject to certain selection rules. Symmetric vibrations only have even j numbers and antisymmetric vibrations only odd j numbers. In addition, the electric dipole selection rule for transitions between the lasing levels (00^01)-$(10^00)_{\mathrm{I}}$ and (00^01)-$(02^00)_{\mathrm{II}}$ is $\Delta j = \pm 1$. The standard spectroscopic convention of labelling transitions by the j number of the lowest state is followed. Transitions with $\Delta j = -1$ are called *P-branch* transitions and those with $\Delta j = +1$ are called *R-branch* transitions. Figure 2.4 shows both *P*- and R-branch absorption spectra of the CO_2 molecule in the (00^01)-$(10^00)_{\mathrm{I}}$ and (00^01)-$(02^00)_{\mathrm{II}}$ bands, which correspond to band centres of the lasing transitions at 9.4 and 10.4 μm.

2.6 Temperature model of the laser processes

Lasing in CO_2 involves transitions between different vibrational modes of the molecule. Thermalisation within each mode is much faster than between different modes as there is no excess energy to be exchanged with translation. Vibrational interaction with translation is improbable as the translational energies are usually about a factor of three smaller than those required to induce vibrational transitions. Each vibrational mode can therefore be described by a temperature.

Excitation by electrical discharge is different for each vibrational mode and is

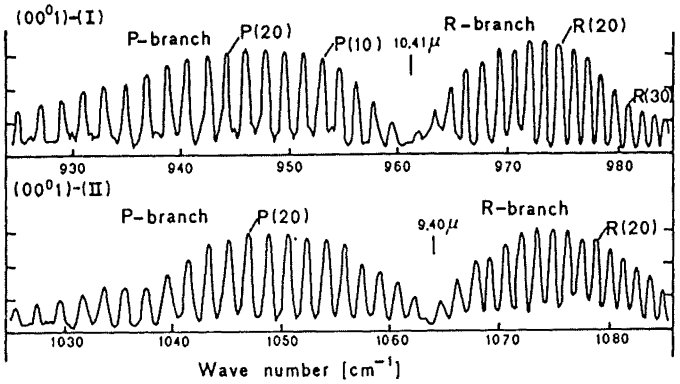

Figure 2.4: Absorption spectra of CO_2 in the 9.4 and 10.4 μm bands.

much less effective for the ν_1 and ν_2 modes than for N_2 and the ν_3 mode. As each vibrational mode is pumped at a different rate by the electrical discharge, three vibrational temperatures are required to describe the vibrational state of the CO_2 in the laser gas.

Relaxation between translation and rotation is very fast [91] ($\sim 10^{-8}$ s) and comparable to the thermalisation within a vibrational mode. Translation and rotation can therefore be described by the same temperature.

In the "five-temperature" model, three vibrational temperatures are assigned for CO_2, one for N_2 and one for translation and rotation. Under certain conditions the temperatures of the ν_1 and ν_2 vibrations are equal and a four-temperature model may be used. This model provides a useful starting point for understanding the lasing process of the CO_2 laser.

2.7 Excitation of the upper laser level

Under most circumstances an electrical discharge is used to excite the 00^01 vibrational level of CO_2 and create a population inversion. The electric field - be it DC, RF or microwave - accelerates electrons which collide with the neutral gas atoms. The power transferred to these neutral atoms can be split into,

- Vibrational excitation: excitation of the vibrational levels of CO_2 and N_2
- Gas heating: caused by elastic collisions
- Electronic excitation and ionisation (the fraction of power involved in gas ionisation is very low)

Excitation of the upper lasing level 00^01 level occurs via one of two routes,

- Direct excitation of (00^01):

$$e + CO_2(00^00) \longrightarrow CO_2(00^01) + (e - E_{kinetic}) \tag{2.9}$$

or,

- Indirect excitation of 00^01 via the low vibrational levels of N_2:

$$e + N_2(\nu = 0) \longrightarrow N_2(\nu = n \leq 8) + (e - E_{kinetic}) \tag{2.10}$$

followed by,

$$N_2(\nu = n) + CO_2(00^00) \longrightarrow N_2(\nu = n - 1) + CO_2(00^01) \tag{2.11}$$

Direct excitation: (equation 2.9) of the 00^01 level is very efficient. The cross section for this process is appreciably larger than those for the excitation of the 10^00 and 02^00 levels, see figure 2.5.

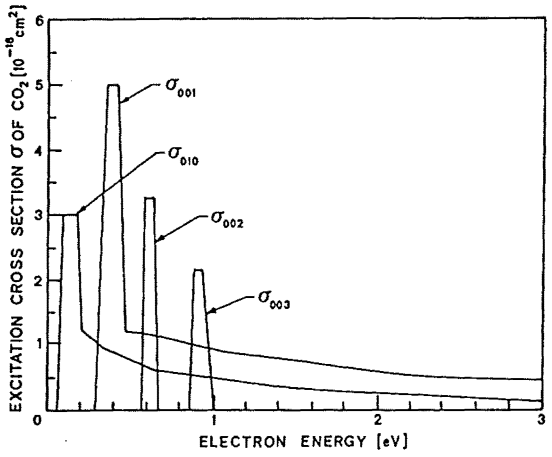

Figure 2.5: Cross section for vibrational excitation of CO_2 by electron impact [28].

Direct electron excitation can also lead to excitation of the 00^0n levels with appreciable cross sections (figure 2.5). These excited states quickly decay to the 00^01 level via collisions of the form,

$$CO_2(00^0n) + CO_2(00^00) \longrightarrow CO_2(00^0(n-1)) + CO_2(00^01) \tag{2.12}$$

Indirect excitation: As stated in section 1.1, the addition of N_2 to the gas mixture greatly enhances the output of the laser. Examining the energy level diagram for N_2 and CO_2 (figure 2.7), it can be seen that the first excited state of N_2 is closely resonant with the $CO_2(00^01)$ level ($\Delta E \simeq 18\,\mathrm{cm}^{-1}$). Note also that the N_2 molecule is symmetric and therefore has no dipole moment. This means that radiative transitions between the vibrational levels of N_2 are forbidden and that the levels are metastable. In this state, N_2 can decay only via collisions with other gas molecules or the vessel walls. Thus the most probable form of

de-excitation for N_2 is by excitation of the 00^01 state of CO_2 (equation 2.11). This leads to very efficient pumping of the CO_2 molecule. Higher vibrational levels of N_2 ($\nu = 2 - 8$) also play a significant role in the excitation of the upper lasing level. This is because the anharmonicity of N_2 does not lead to energy differences (from 00^01) which are larger than the average kinetic energy kT up to values of $\nu = 8$. Figure 2.6 shows the cross section for vibrational excitation of N_2 by electron impact as a function of electron energy.

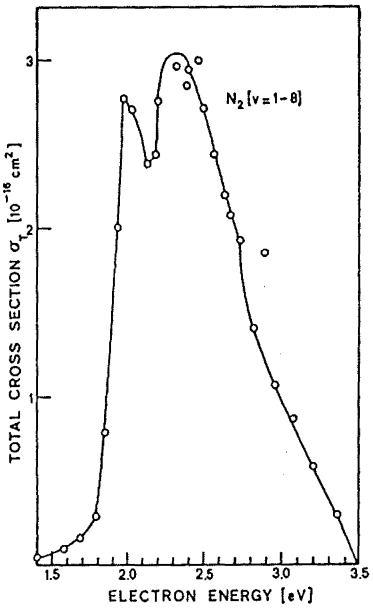

Figure 2.6: Total effective cross section for the vibrational excitation of $N_2(\nu = 1-8)$ by electron impact [83, 84].

There is also a similar effect between carbon-monoxide (CO) and CO_2. In a discharge containing no H_2O or H_2 a significant amount of the CO_2 can dissociate, sometimes as much as 50% (the dissociation energy of CO_2 is only 2.8 eV). The resulting CO molecules can transfer a significant amount of energy to the ν_3 vibration as the cross section for vibrational excitation of CO is quite large (compared to N_2). The difference in energy between the vibrational level of CO and the (00^01) level is $170\,cm^{-1}$ which is smaller than the average kinetic energy ($170\,cm^{-1} = 245\,K$). However, CO is not as effective as N_2 because of this larger energy difference and also because CO has a dipole moment and can spontaneously decay. The cross section for vibrational excitation of CO is shown in figure 2.8.

Figures 2.5 and 2.6 indicate that electron energies in the range 1-3.5 eV are required for optimum excitation of the upper lasing level. The kinetic energy range of the electrons can be controlled experimentally by varying parameters; such as: gas composition, gas pressure, tube diameter (DC) and electrode spacing (RF). Note that at excessively high electron energies (> 4 eV) any lasing action is likely to be suppressed as the cross section for 00^01 excitation is greatly reduced whereas the cross section for the lower lasing level is enhanced (figure 2.9).

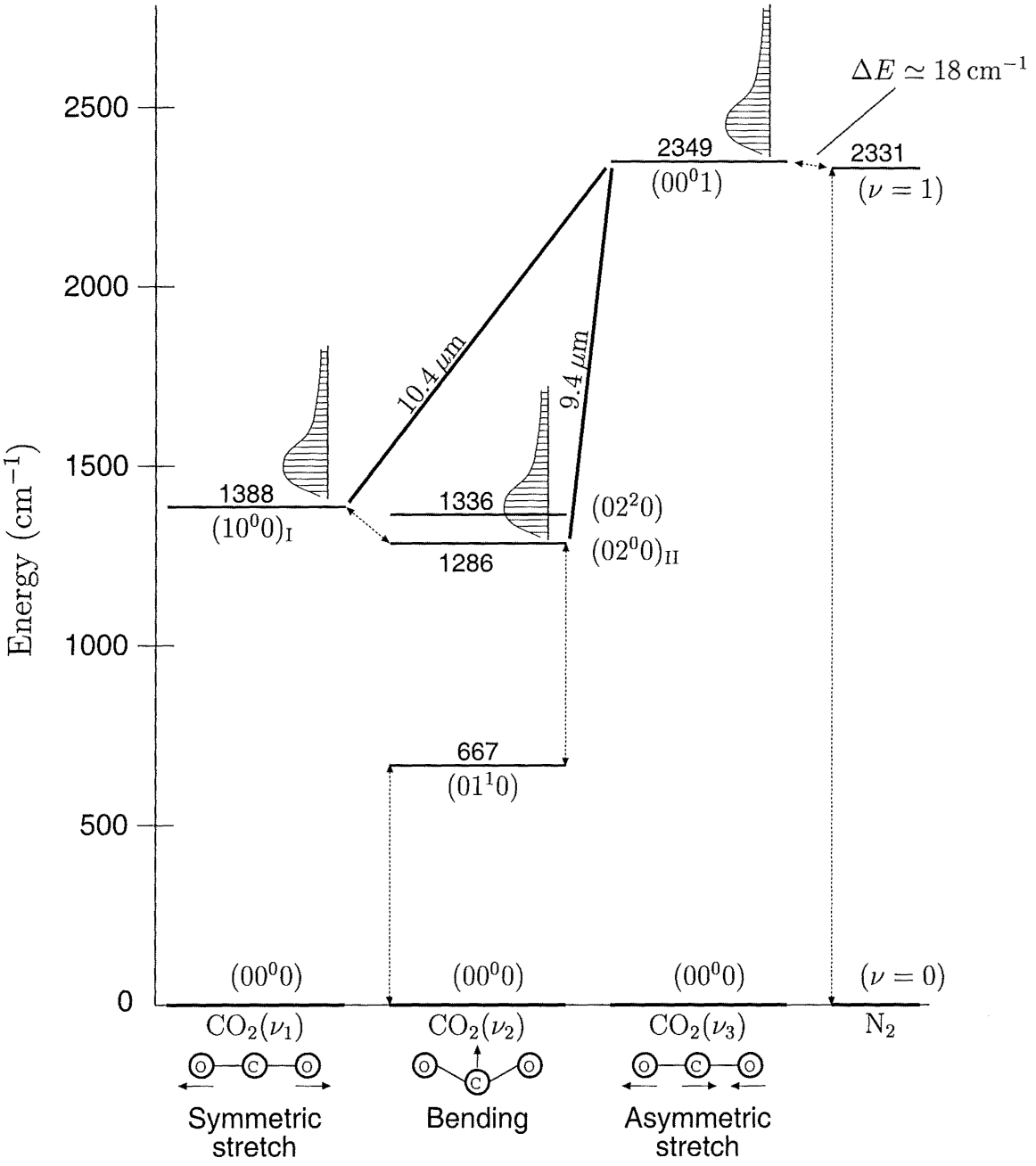

Figure 2.7: Relevant vibrational levels of the CO_2 molecule and the first vibrational state of N_2.

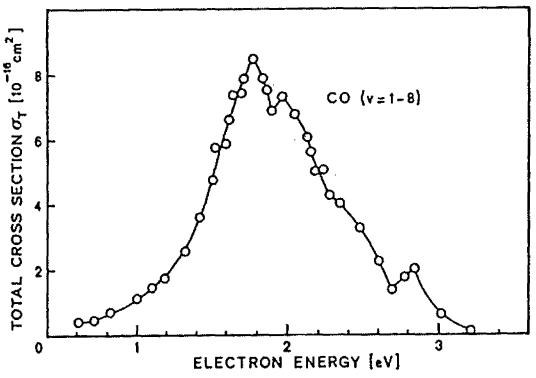

Figure 2.8: Total effective cross section for the vibrational excitation of CO ($\nu = 1-8$) by electron impact [83, 84].

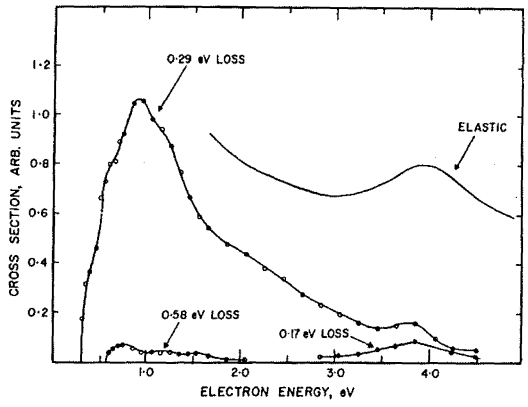

Figure 2.9: Energy dependence of inelastic and elastic cross sections in CO_2. The 0.17, 0.29 and 0.58 eV energy losses correspond to the 10^00, 00^01 and 00^02 modes respectively.

One standard tool that is used to measure the efficiency with which the 00^01 is pumped is the ratio E/N. That is, the ratio of electric field to neutral particle density. An equivalent ratio, by a factor, is the ratio of electric field to pressure, E/p. Figure 2.10 shows how the input power is distributed in two gas mixtures for a range of E/N. For the gas ratios shown, E/N values of 2×10^{-16} V cm^2 result in optimum excitation of the upper lasing level.

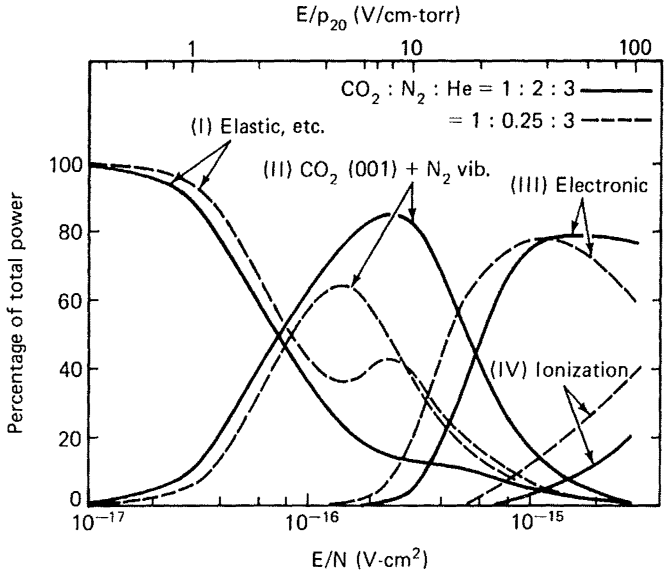

Figure 2.10: Percentage of power transferred to (I) elastic collisions, rotational excitation of N_2 and excitation of bend and stretch modes of CO_2; (II) CO_2 (00^01) level and the first eight vibrational levels of N_2; (III) electronic excitation. Increasing the ratio of N_2 to CO_2 increases the predicted efficiency given by (II). (from [55])

2.8 The role of He, H_2O and Xe

Helium present in the gas mixture plays no part in the excitation of the upper lasing level. Its first excited state occurs at 159850 cm^{-1} compared with 2349 cm^{-1} for the 00^01 state making any interaction extremely unlikely. The primary reason for its addition to the laser mixture is to provide cooling. As all its energy levels are above 20 eV, it remains fairly undisturbed in a plasma in which typical electron energies are between 1 and 3 eV. Its effect on the plasma properties are limited to small energy transfers by inelastic collisions with translational energies. Having approximately six times the thermal conductivity of CO_2 and N_2, its addition to the laser gas means that the thermal conductivity of the gas is effectively determined by helium alone. A CO_2 discharge containing He can generally sustain a higher current or heat input without overheating the plasma than one without He.

A small amount (0.2 torr) of H_2O is often added to the laser mixture to prevent the

dissociation of CO_2 into CO and O_2. In such systems the percentage dissociation can drop from around 50% to near 0%.

Xenon (Xe) is another additive which usually leads to higher power laser output. Xe has an ionisation potential of 12.1 eV, which is 2-3 eV less than the other gas components. This means that the electric field of the discharge establishes itself at a lower level to maintain the discharge than it would without Xe. The low ionisation potential of Xe also facilitates the production of new electrons for maintaining the discharge. If the current remains the same, the electric field is reduced, which in turn decreases the mean energy of the electrons in the discharge.

2.9 The lasing process

The lasing transition in CO_2 lasers can occur on one of two bands; from the asymmetric stretch (00^01) mode to either the symmetric stretch (10^00) mode (10.4 μm band) or the bending (02^00) mode (9.4 μm band). The actual transition occurs on one of the rotational sublevels of the vibrational mode (see figure 2.7). Note that the 9.4 μm and 10.4 μm bands have quantum efficiencies of 45 and 40% respectively, second only to CO lasers in the gas laser field. If 60% of the input energy reaches the upper lasing level, a wall-plug efficiency of $\sim$ 27% is expected. Whilst an ideal laser might achieve an efficiency of 27%, in practice it is very difficult to obtain. However, efficiencies greater than 20% have been reported.

	$00^01 \rightarrow 10^00$ (10.4 μm band)	$00^01 \rightarrow 02^00$ (9.4 μm band)
P-branch	0.34 s^{-1}	0.20
R-branch	0.33 s^{-1}	0.19

Table 2.1: Transition data (Einstein A coefficients) for the lasing transitions.

In practice it is the P-branch of the 10.4 μm which lases unless some special line selection device is used. This is because 10.4 μm band has a larger wavelength, higher A coefficients (table 2.9) and thus higher gain. The P-branch is always favoured over the R-branch.

2.9.1 Gas temperature

Maintaining the laser gas at a low temperature in a CO_2 laser is essential [23]. When the gas temperature rises above 200°C the lower lasing level starts to be excited thermally, having a significant impact on the population involved and thus output power. At temperatures above 450°C, all laser output is quenched. This means that a number of measures must be taken to ensure that the gas temperature remains low. In practice this involves either use of an efficient cooling mechanism or the fast flow of the gas so that it does not overheat during its journey through the laser cavity.

2.9.2 Discharge processes

Table 2.2 lists some of the common interactions which take place inside the CO_2 laser discharge. T-V processes involve an exchange of energy between translation and vibration whereas V-V processes transfer energy from one vibration state to another.

T-V processes,

$$CO_2(01^10) + M \Longleftrightarrow CO_2(00^00) + M + 667\,cm^{-1} \quad (2.13)$$
$$N_2(v=1) + M \Longleftrightarrow N_2(v=0) + M + 2331\,cm^{-1} \quad (2.14)$$
$$O_2(v=1) + M \Longleftrightarrow O_2(v=0) + M + 1556\,cm^{-1} \quad (2.15)$$
$$H_22(010) + M \Longleftrightarrow H_2O(000) + M + 1595\,cm^{-1} \quad (2.16)$$

V-V Processes (intermolecular),

$$CO_2(00^01) + N_2 \Longleftrightarrow CO_2(00^00) + N_2(v=1) + 18\,cm^{-1} \quad (2.17)$$
$$H_2O(010) + CO_2(00^00) \Longleftrightarrow H_2O(000) + CO_2(01^10) + 928\,cm^{-1} \quad (2.18)$$
$$CO_2(00^01) + H_2O(000) \Longleftrightarrow CO_2(00^00) + H_2O(010) + 754\,cm^{-1} \quad (2.19)$$
$$N_2(v=1) + H_2O(000) \Longleftrightarrow N_2(v=0) + H_2O(010) + 736\,cm^{-1} \quad (2.20)$$
$$H_2O(010) + O_2(v=0) \Longleftrightarrow H_2O(000) + O_2(v=1) + 39\,cm^{-1} \quad (2.21)$$
$$O_2(v=1) + CO_2(00^00) \Longleftrightarrow O_2(v=0) + CO_2(01^10) + 889\,cm^{-1} \quad (2.22)$$
$$CO_2(00^01) + O_2(v=0) \Longleftrightarrow CO_2(00^00) + O_2(v=1) + 793\,cm^{-1} \quad (2.23)$$
$$N_2(v=1) + O_2(v=0) \Longleftrightarrow N_2(v=0) + O_2(v=1) + 775\,cm^{-1} \quad (2.24)$$

V-V processes (intramolecular),

$$CO_2(00^01) + M \Longleftrightarrow CO_2(03^10) + M + 416\,cm^{-1} \quad (2.25)$$
$$CO_2(10^00) + M \Longleftrightarrow CO_2(02^00) + M + 102\,cm^{-1} \quad (2.26)$$

Table 2.2: Transitions associated with a CO_2 laser gas mix. M represents a neutral gas molecule which may gain or impart translational energy during the interaction.

Chapter 3

Laser design

3.1 Introduction

This chapter deals with the design of the three laserheads used in these experiments. For convenience the three lasers have been labelled V1, V2 and V3 for version 1, 2 and 3. The numbering system follows the experimental development of the laser. The V1 design was a relatively simple design which demonstrated lasing and other basic characteristics. V2 was designed to produce a more uniform, stable discharge while being relatively simple and easy to manufacture. Lasing was not a high priority. The V3 design incorporated the useful features of the first two designs while adding a number of new features to improve the experimental versatility of the device.

The following list presents some of the important design criteria for a generic microwave-pumped diffusion-cooled CO_2 laser.

- High thermal conductivity in the laserhead - Rapid heat removal from the laser gas is essential to sustain a population inversion (see section 2.9.1).
- Efficient and robust microwave coupling.
- Uniform electric field (or E/N, see section 2.7) along the length of the discharge - An even E/N value over the discharge will mean the lasing characteristics in any small volume would be uniform throughout.
- Efficient vacuum system - The vacuum system must be flexible and capable of high flow rates at operational pressures.
- Efficient optics - As well as being a discharge chamber the cavity must be an efficient optical resonator.
- Durability - The laser must be made of materials which are durable and will not change the characteristics over time due to outgassing or oxidisation.

In the next three sections the laserhead designs are detailed. Following this the heat transfer and vacuum characteristics of these devices are examined.

3.2 The V1 cavity

The V1 cavity was the first laser design for this project and is based on the microwave cavity work of Jamison [72] in an earlier part of this project. The design is simple from a constructional point of view. The photograph in figure 3.1 shows the device which is constructed from brass. The unit was fabricated from two blocks which were milled to the appropriate shape and then joined. Although brass has a slightly better reflectance in the infrared than aluminium, the angle of incidence at which the laser beam hits the waveguide walls makes this small difference largely irrelevant. Brass was chosen more for its ability to be welded than for its optical properties.

Figure 3.2 shows an exploded view of the laser detailing the vacuum seal and optics. The unit is sealed by four O-rings, two on the ends and two on the sides, and four windows of various descriptions. Positioned along the sides are two quartz windows which are transparent to microwave radiation and allow the laserhead to become some part of a microwave cavity. Quartz was used for its ability to withstand high thermal gradients. In addition, its optical transparency in the ultraviolet wavelengths makes it a suitable window through which the nitrogen spectra of the discharge may be viewed. On the edges of the quartz the temperature is held fixed by the cooling water at $\sim$10°C whilst in the centre the temperature can reach well over 100°C as a result of heating via the plasma. Ordinary glass (BK7) fractured under such gradients. The other part of the vacuum seal is created by the optics at each end of the cavity. These optics consist of a one-inch gold plated 99% reflector and a zinc selenide (ZnSe) output coupler with a transmission of 10%.

The mirrors can be aligned by adjusting four screws which apply pressure to a small holder in which the mirror sits. Although this type of mount is not properly kinematic, it does give more than enough control to align the optics well. The alignment is accomplished by sending a helium-neon laser beam through the cavity and using the reflections from first the gold mirror and then the ZnSe window to adjust the mirror positions. One of the problems that arises when the mirrors act as part of the vacuum seal is that the change in pressure from atmosphere to a few torr can alter the alignment. As alignment is most easily accomplished at atmosphere, it can be disturbed when the laser is pumped down to working pressures. Although it is relatively easily to correct, this problem is a time-consuming feature of an experimental laser. The optical setup is discussed in more detail in chapter 5.

Water cooling channels run along each electrode facilitating rapid heat transfer (see section 3.5). Gas enters the discharge chamber through a hole near the electrode on one end of the laser and flows, if desired, along the length of the chamber and is extracted at the other end via a similar hole. The basic dimensions of the laserhead are $465 \times 50.8 \times 47.5$ mm with the discharge length being 375 mm. Drawings of the laser, including other relevant dimensions, are given in figures 3.3 and 3.4.

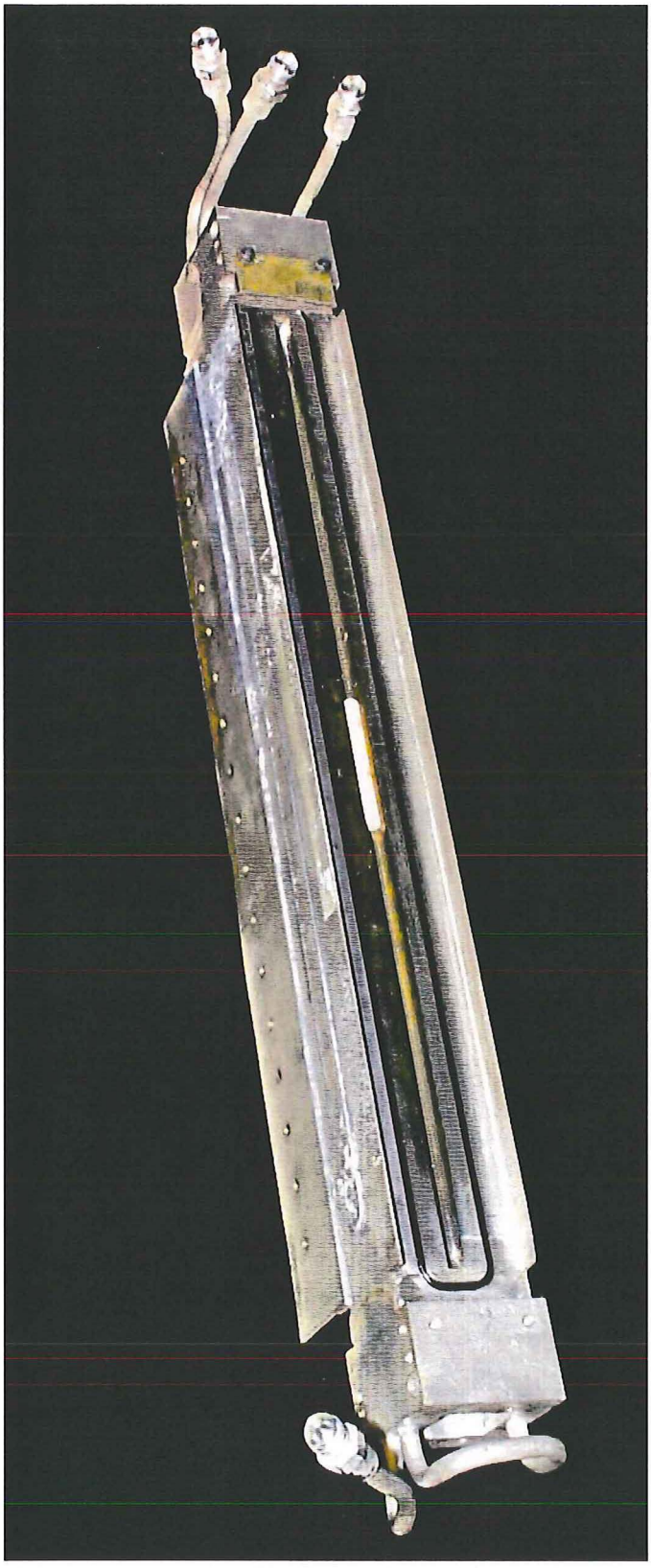

Figure 3.1: Photograph of the V1 laser.

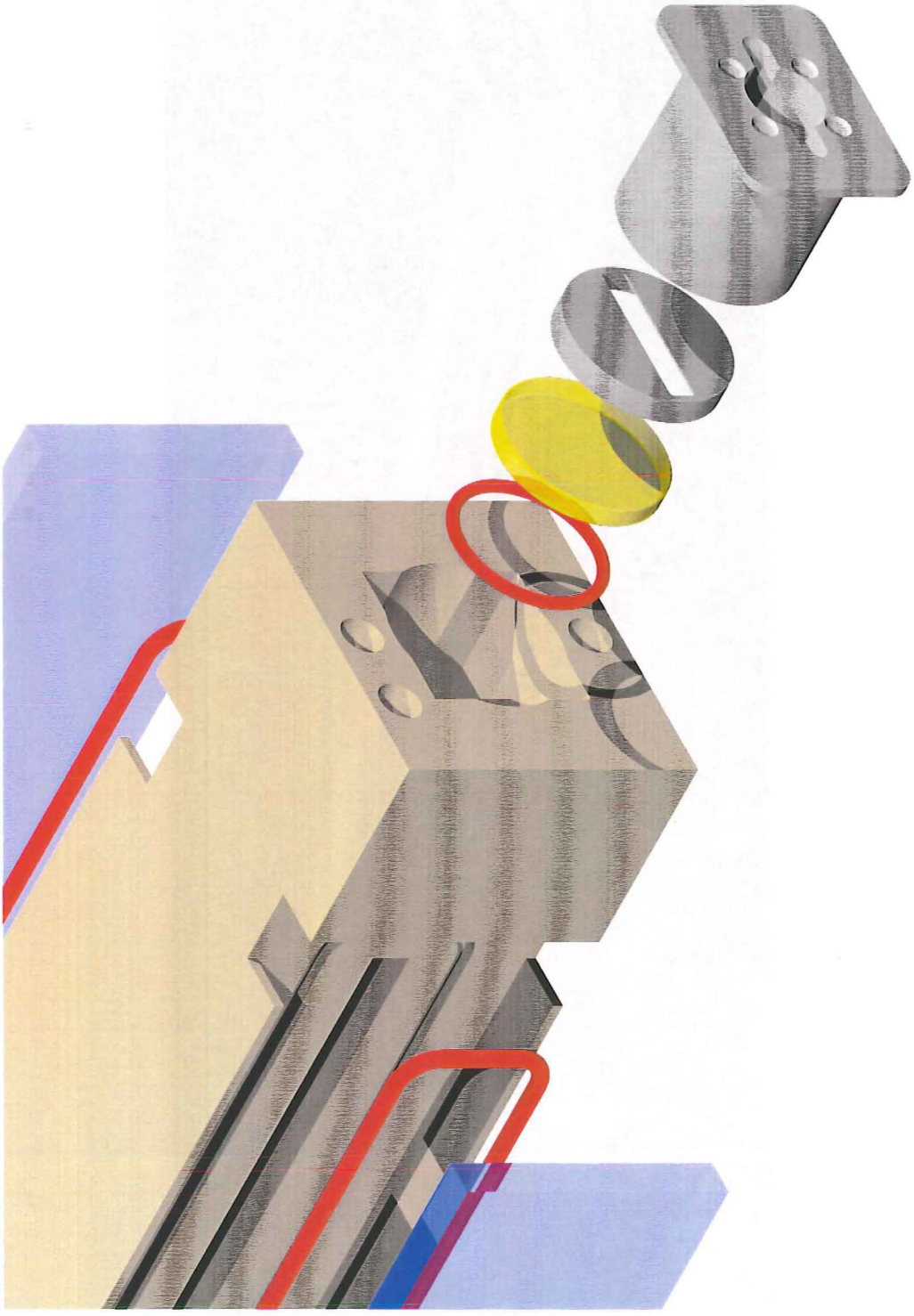

Figure 3.2: Exploded view of the V1 laser.

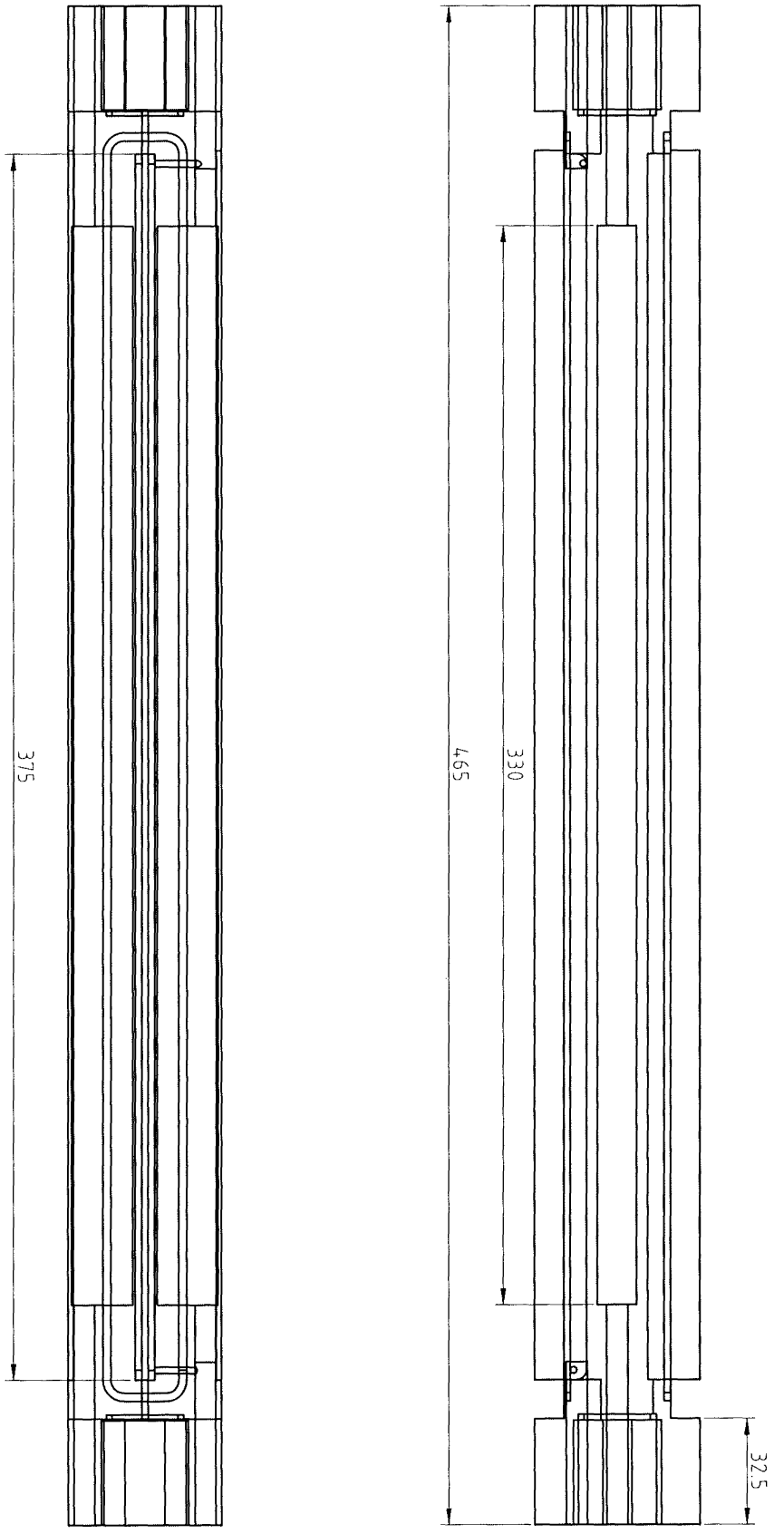

Figure 3.3: Drawings of the V1 laser.

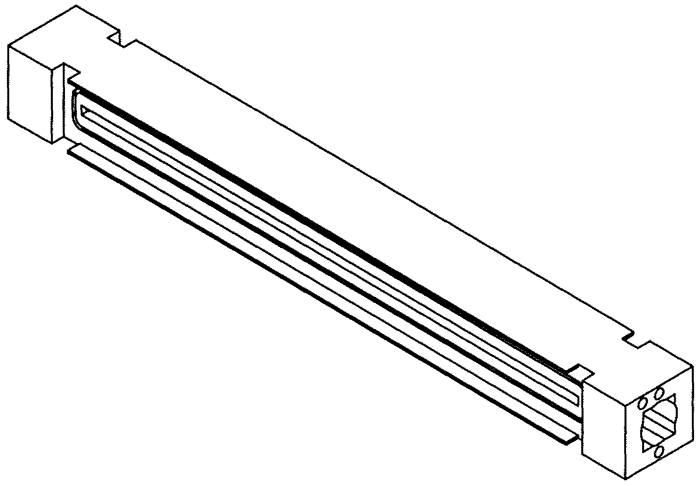

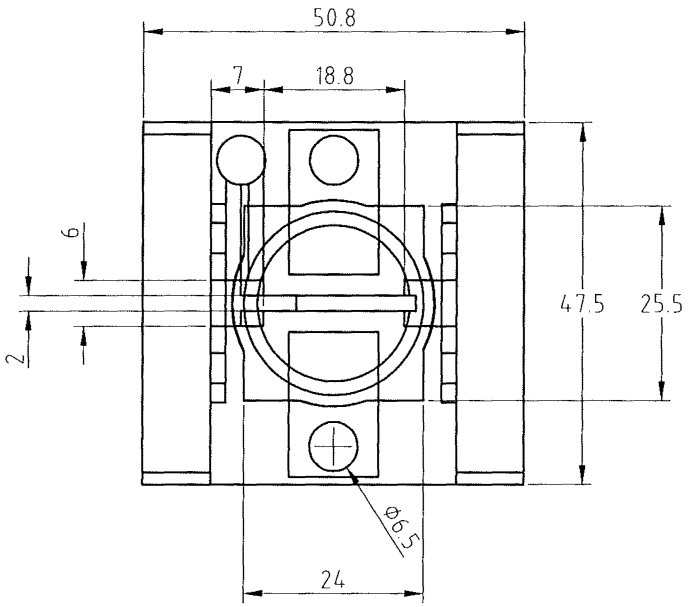

Figure 3.4: Drawings of the V1 laser.

As a prototype this laser performed well. It demonstrated a microwave-induced discharge in a cavity also designed as an optical resonator. It was capable of cooling the gas quickly and evenly, and it lased producing an output power of approximately 3 W. Conversely, the discharge, although reasonably easy to excite at low pressures, became difficult to excite and was unstable at pressures over 30 torr. The optics, while being simple and effective, incorporated the vacuum as part of their adjustment making alignment tedious. The design also lacked a certain amount of versatility as an experimental device. These issues have been addressed to varying degrees in the following two designs.

3.3 The V2 cavity

The V2 cavity was built to test the effectiveness of adding a dielectric slab in series with the discharge, to help create a more uniform plasma which could be operated at higher pressures. The motivation for adding this dielectric element is discussed in section 6.9. The photograph in figure 3.6 shows the assembled device. This design differs in a number of ways from the V1 design. The changes can be more easily observed by examining the exploded view shown in figure 3.7. Most obviously, there is only one main O-ring (in addition to the two which seal the mirror holes). This O-ring is now in the discharge plane which eliminates the need to seal the two halves of the device together with a weld. In addition, fabrication of the individual components is simplified. The discharge and optical cavity has four walls, three aluminium and one quartz.

Microwaves enter the discharge chamber through the quartz slab. The T-shape of the top aluminium plate (figure 3.7) creates a high local field in the evacuated section which causes breakdown in the gas.

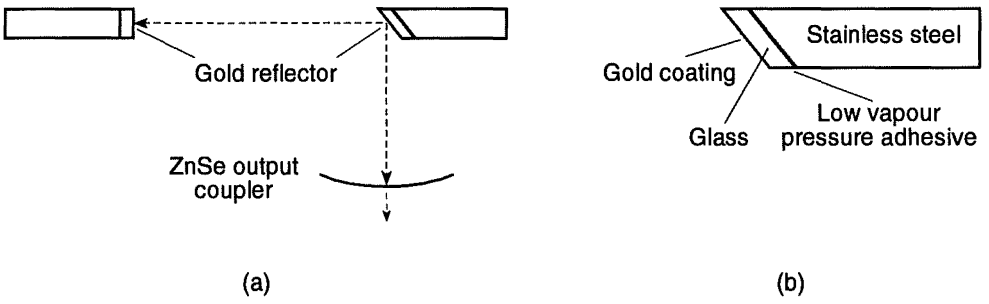

Figure 3.5: L-shaped optics of the V2 laser. (a) Optical path. (b) Mirror design.

The position of the main O-ring means that the optics cannot be situated on the ends of the laser and that the infrared beam must be extracted perpendicularly from the optical axis. By making the optical cavity into a carefully designed L-shape it is possible to extract the IR radiation without significant loss. Figure 3.5a shows the optical cavity shape. The mirrors for the discharge cavity optics must fit into a small gap (2-3 mm) which means that they must be custom made.

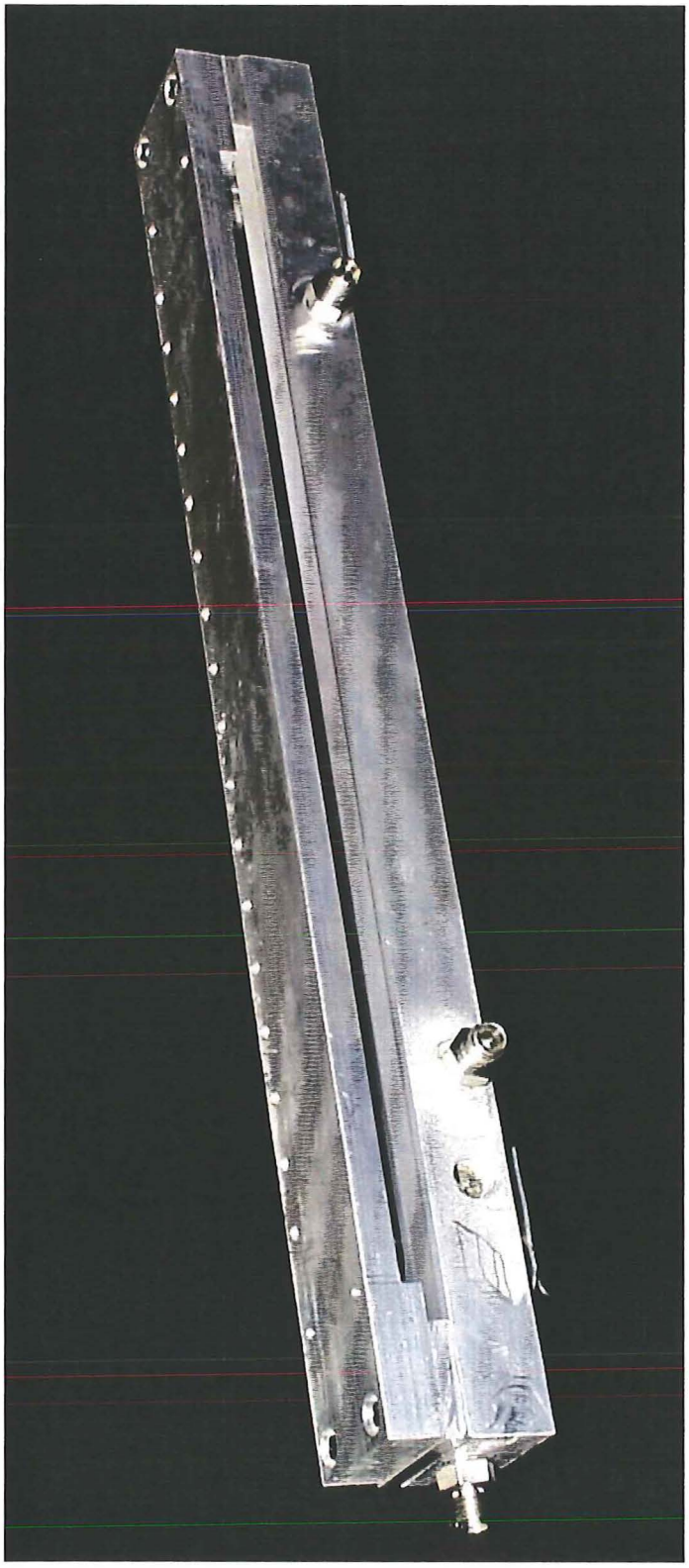

Figure 3.6: Photograph of the V2 laser.

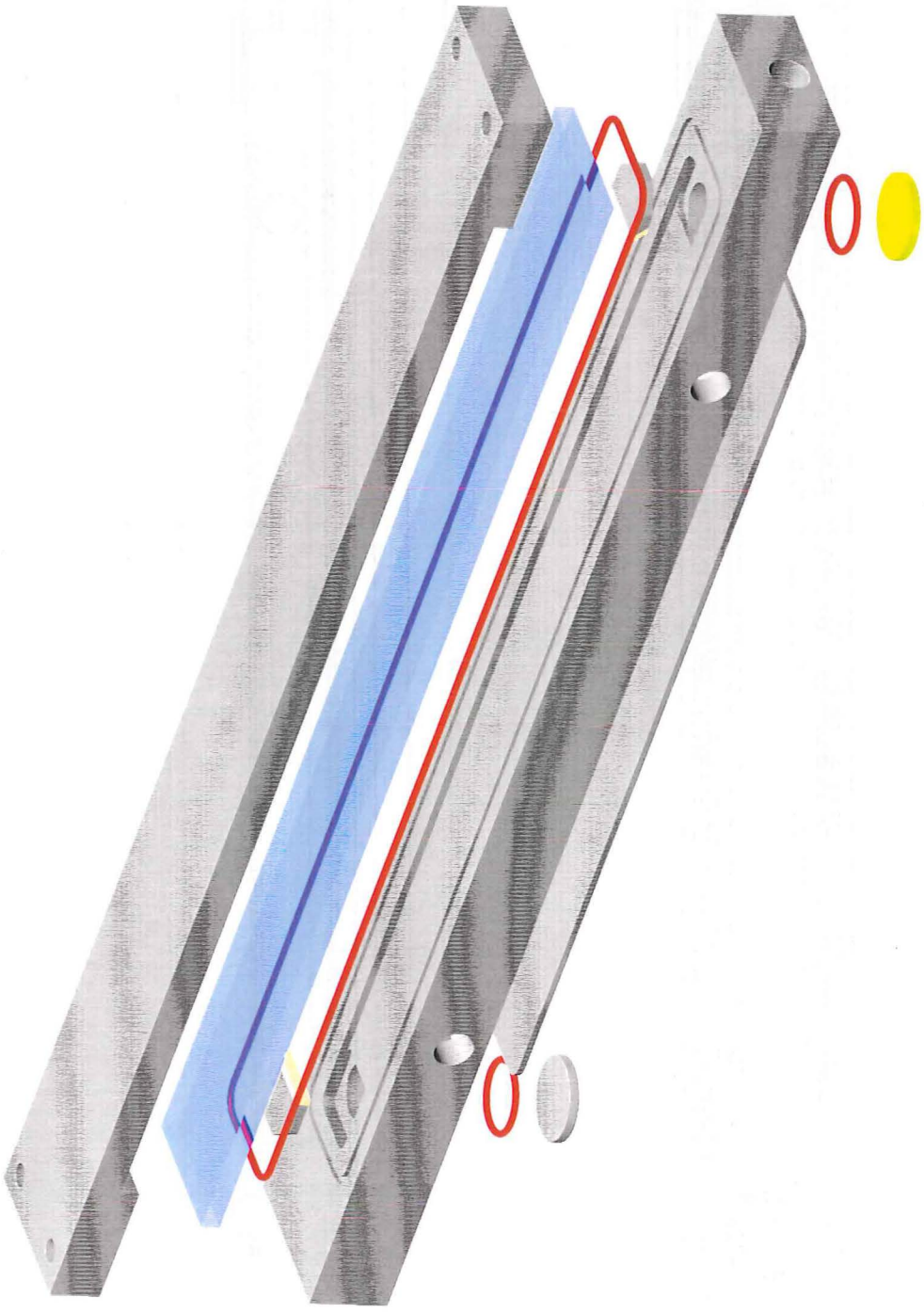

Figure 3.7: Exploded view of the V2 laser.

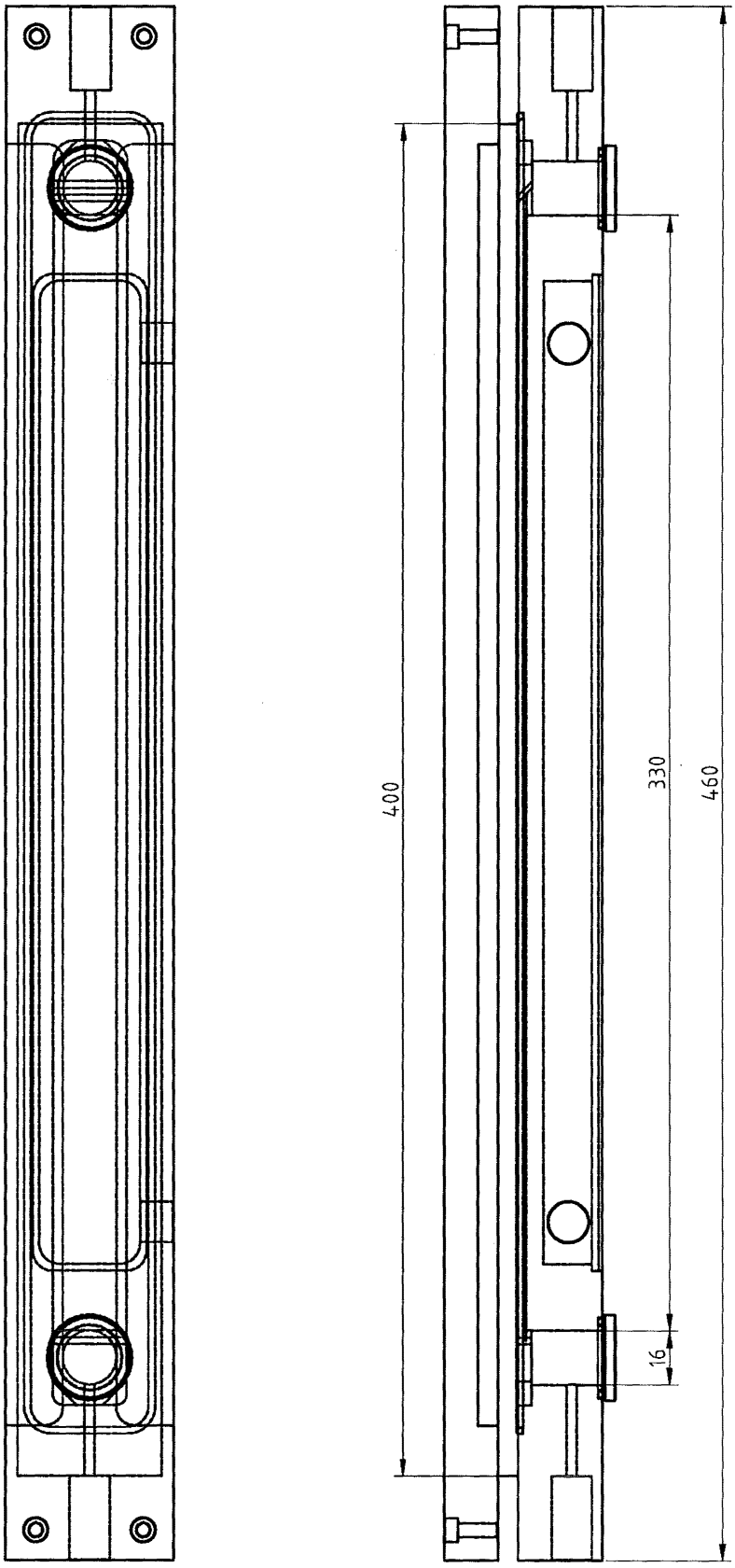

Figure 3.8: Drawings of the V2 laser.

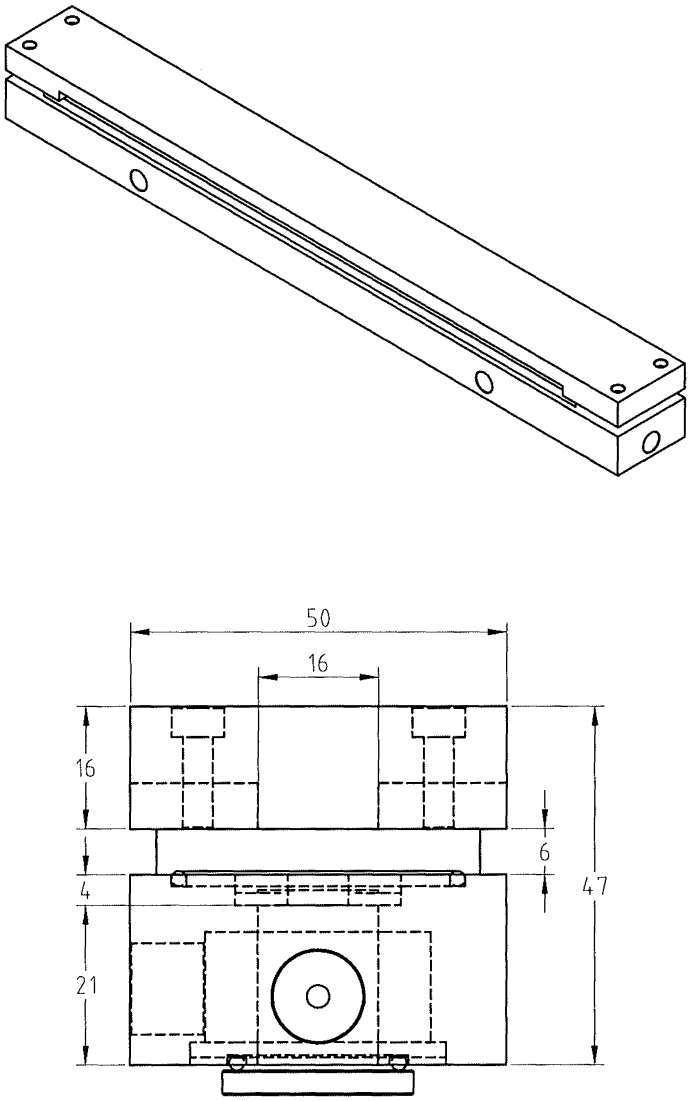

Figure 3.9: Drawings of the V2 laser.

Figure 3.5b shows the basic mirror design for the in-cavity optics. The optics for this laser are discussed in more detail in section 5.2.2.

CAD drawings of the V2 laser are shown in figures 3.8 and 3.9.

3.4 The V3 cavity

While the V2 laser is a good production type laser, in that it is compact and easy to manufacture, it lacks versatility. For this reason the V3 laser was designed to be more versatile while incorporating the advantages of the previous models. Specifically it includes: a quartz dielectric, variable discharge gap, completely internal optical resonator and increased gas volume. A photograph of the device is shown in figure 3.10, followed by an exploded view in figure 3.11.

By moving the optics inside the laser they are no longer susceptible to changes in the gas pressure. This means that the optics can be aligned at atmospheric pressure, once, and will stay aligned under vacuum. Small changes to the cavity can also be made without disturbing the optics. The mirror mounts are also proper kinematic mounts (see figures 3.14 and 3.18).

The vacuum system has been designed to accommodate much increased gas throughput, details are presented in section 3.6. In addition to increased throughput, the evacuated volume has been enlarged to help keep the gas cool and lower the concentration of dissociation products. As only a small fraction of the total gas volume is actually participating in the discharge, there is a large reservoir of gas which can be continually exchanged with the discharge gas. Pulsing the discharge helps to facilitate mixing.

In general, the performance of this device was good. It was an effective microwave applicator capable of creating a population inversion in the gas. The maximum average laser power extracted was around 3 W. Definite advantages of the V3 laser included the ease of alignment and the ability to alter the gap or to make other small changes to the geometry. The only real problem with the device was that small discharges would sometimes light in undesirable areas of the evacuated section. While this is not strictly detrimental to the laser performance (unless it heats the gas sufficiently) these discharges do alter the shape of the main discharge leading to unpredictable output. Most of these unwanted discharges occurred near the mirror holders because they were not sufficiently microwave-shielded. Several design modifications to the laser should eliminate this problem.

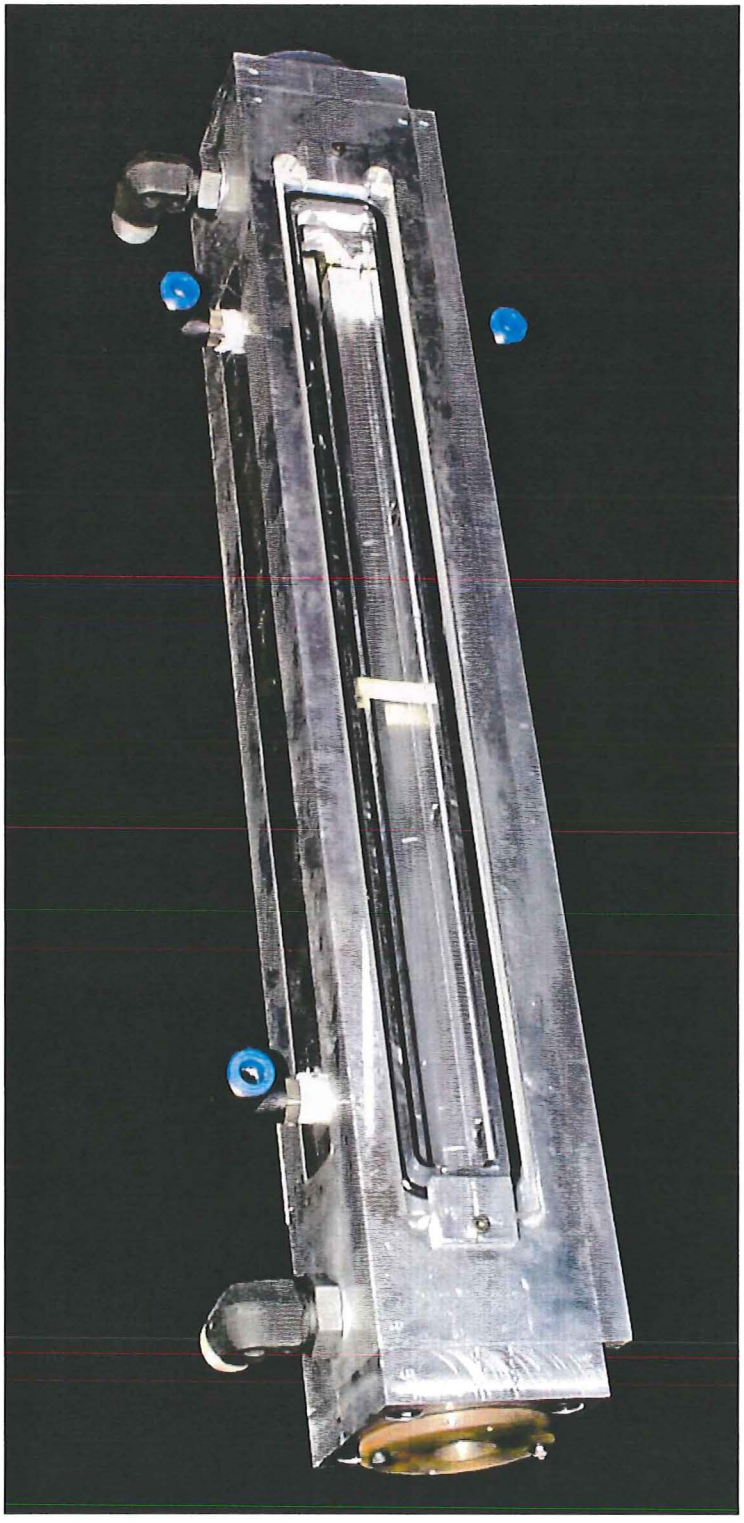

Figure 3.10: Photograph of the V3 laser.

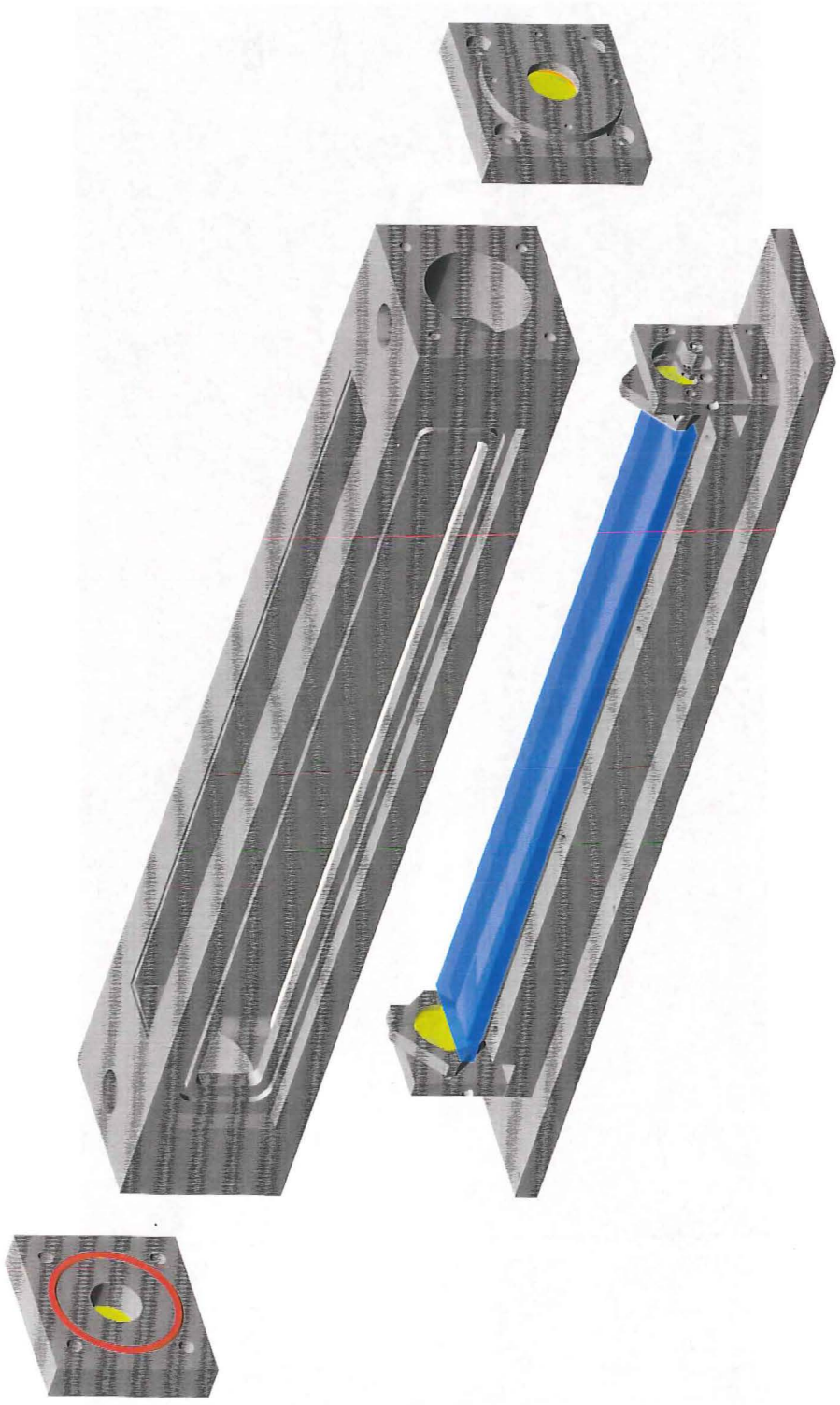

Figure 3.11: Exploded view of the V3 laser.

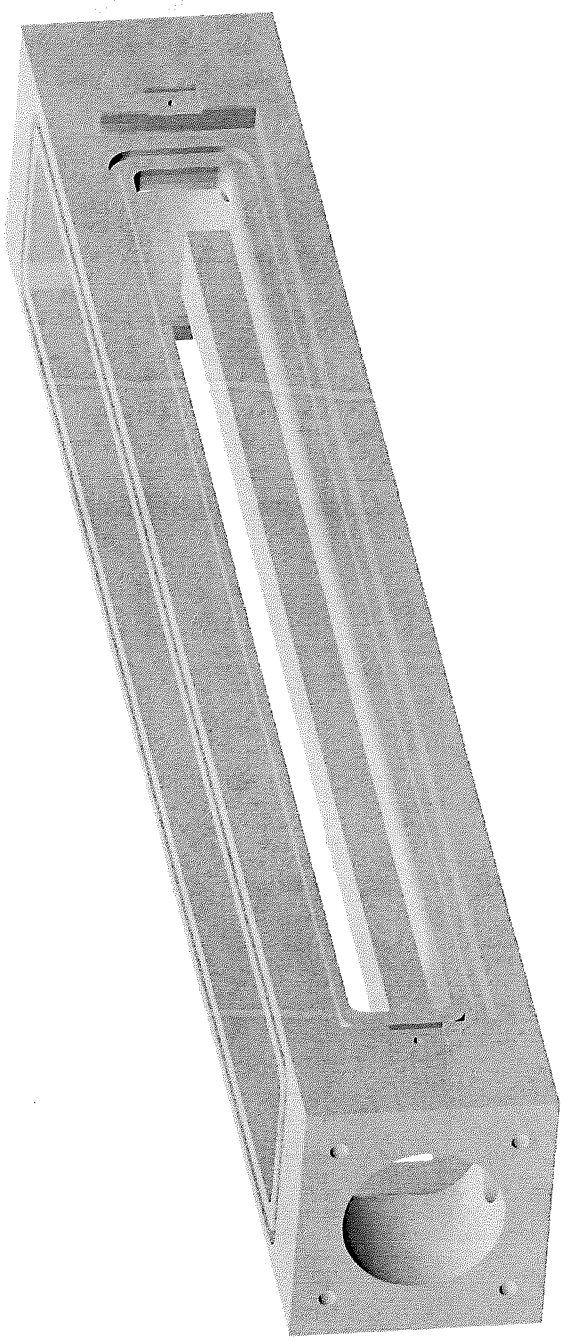

Figure 3.12: Body of the V3 laser.

Figure 3.13: Exploded view of the V3 end assembly.

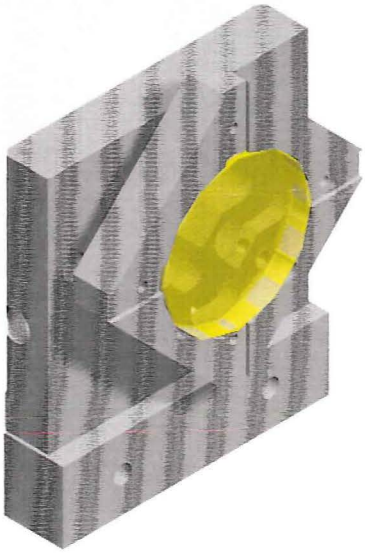

Figure 3.14: Exploded view of the V3 mirror holder.

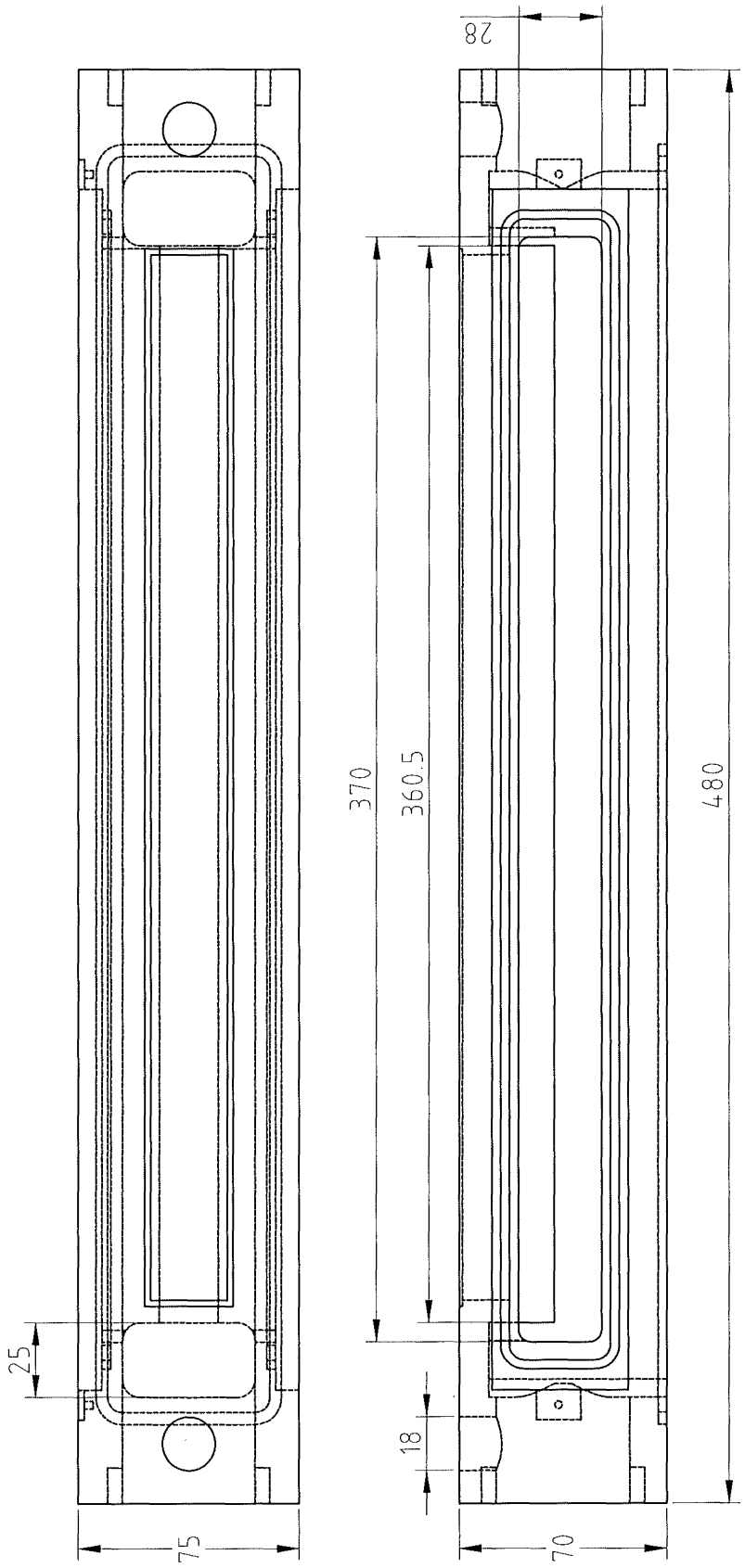

Figure 3.15: Drawings of the V3 laser.

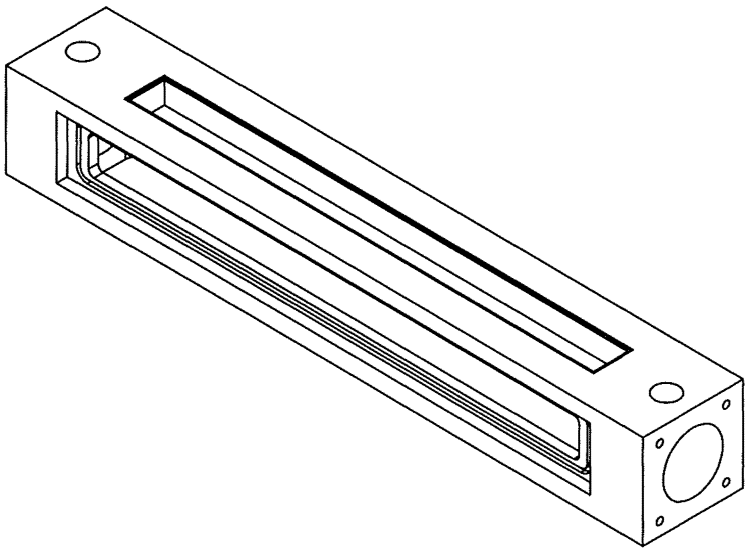

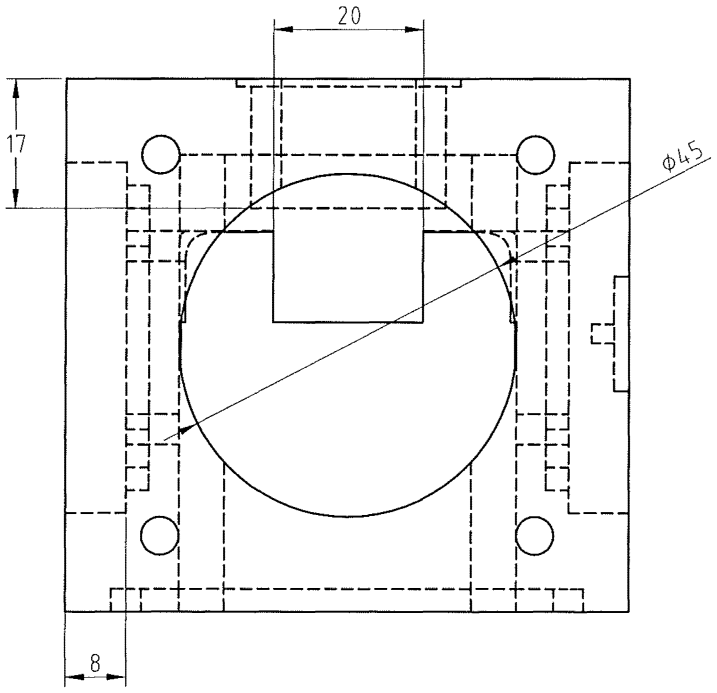

Figure 3.16: Drawings of the V3 laser.

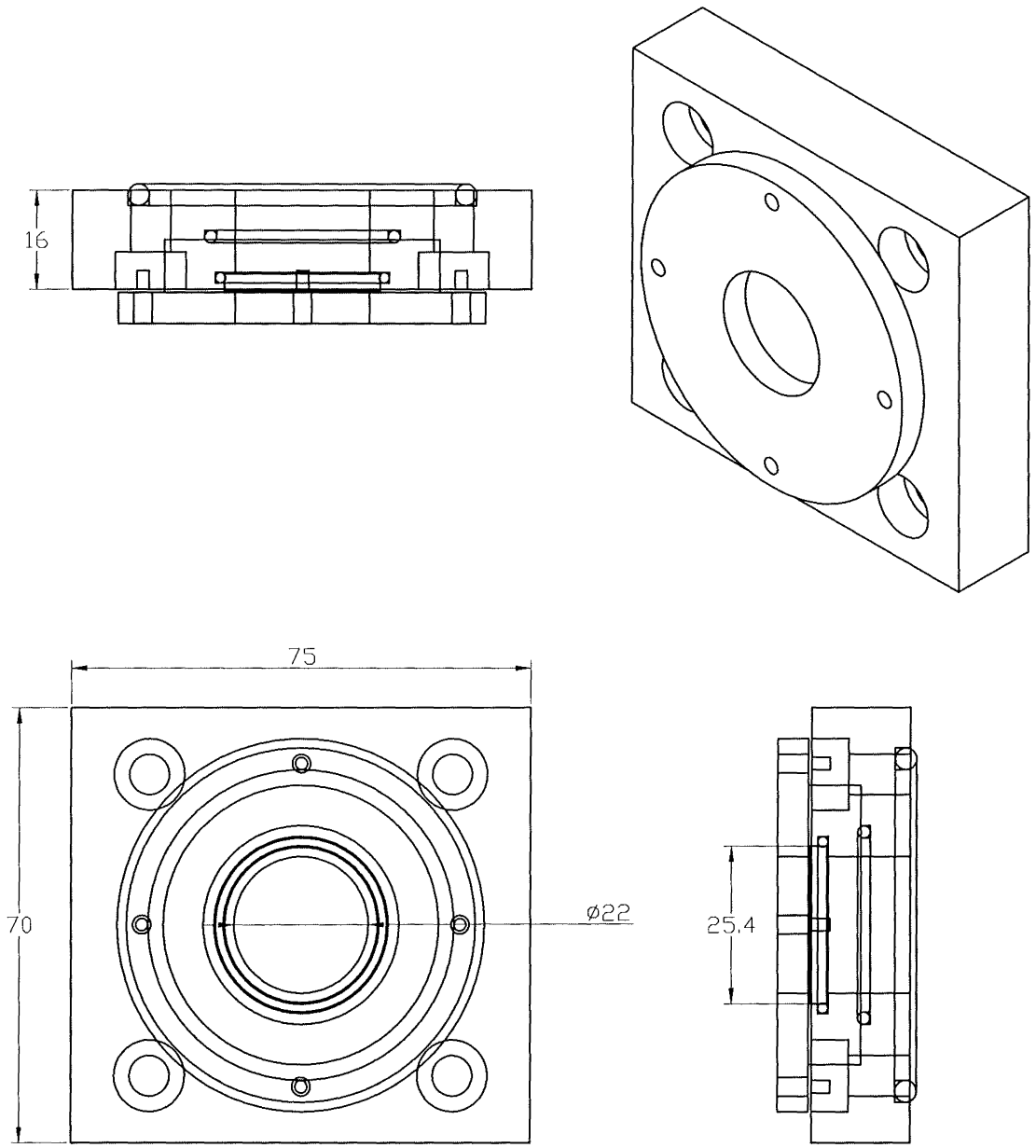

Figure 3.17: Drawings of the V3 end assembly.

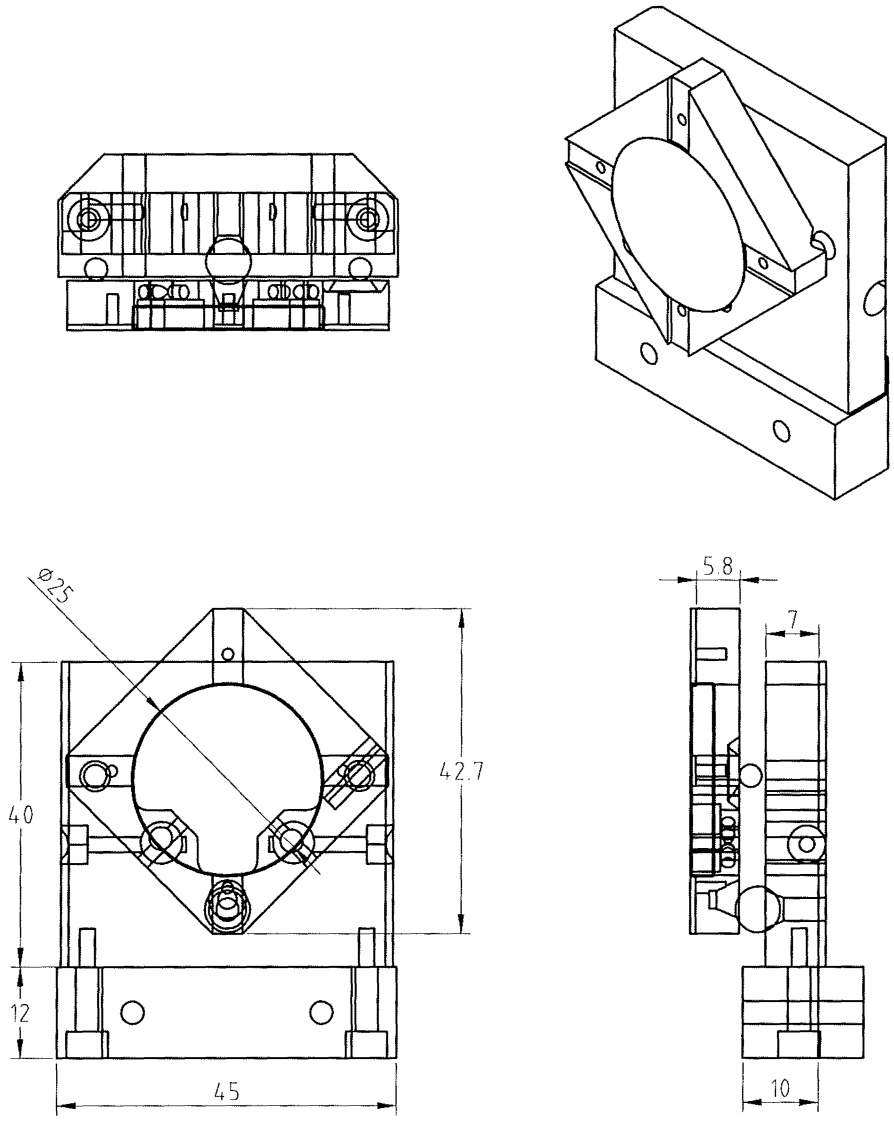

Figure 3.18: Drawings of the V3 mirror holder.

3.5 Heat conduction

The thermal gas temperature plays a significant role in the ability of the gas to sustain a population inversion (see section 2.9.1). For the diffusion cooling and area scaling to be effective it was necessary to ensure that the geometry of the laser was such that it could remove excess heat from the laser swiftly.

3.5.1 Heat transfer basics

Heat transfer in a solid is proportional to the temperature gradient along any chosen axis,

$$\frac{q}{A} \sim \frac{\partial T}{\partial x} \tag{3.1}$$

or

$$q = -kA\frac{\partial T}{\partial x} \tag{3.2}$$

where q is the heat transfer rate [W], A [m^3] is the area across which heat is being transfered, $\partial T/\partial x$ is the temperature gradient in the direction of heat flow and k [W/m/°C] is the thermal conductivity. Equation (3.2) is Fourier's law of heat conduction.

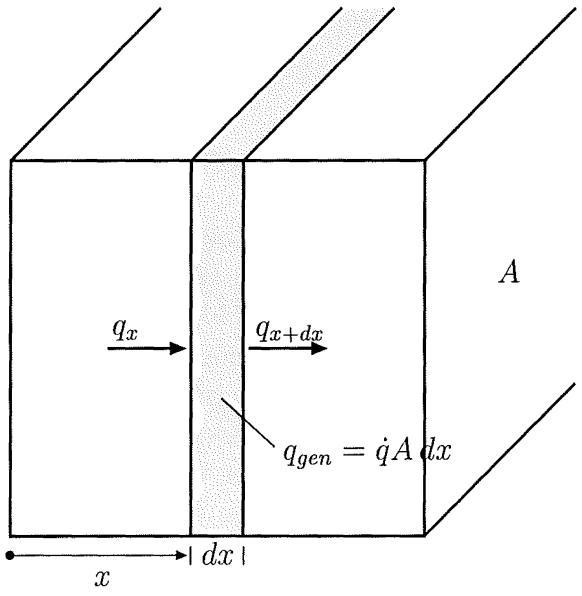

Figure 3.19: Heat flow in a one-dimensional solid.

The basic equation governing heat transfer, in a one dimensional solid, for an element of width dx is,

$$\begin{aligned}\text{Energy conducted in left face} + \text{heat generated within element} = \\ \text{change in internal energy} + \text{energy conducted out right face}\end{aligned} \tag{3.3}$$

as depicted in figure 3.19.

These quantities are given as follows,

$$\text{Energy in left face} = q_x = -kA\frac{\partial T}{\partial x} \tag{3.4}$$

$$\text{Energy generated within element} = \dot{q}Adx \tag{3.5}$$

$$\text{Change in interval energy} = \rho cA\frac{\partial T}{\partial \tau}dx \tag{3.6}$$

$$\text{Energy out right face} = q_{x+dx} = -kA\left.\frac{\partial T}{\partial x}\right|_{x+dx} \tag{3.7}$$

where $\dot{q}$ is the energy generated per unit volume [W/m^3], c is the specific heat of the material [J/kg°C], ρ is the density [kg/m^3] and τ is time.

Combining the above gives,

$$\frac{\partial}{\partial x}\left(k\frac{\partial T}{\partial x}\right) + \dot{q} = \rho c\frac{\partial T}{\partial \tau} \tag{3.8}$$

or,

$$\frac{\partial^2 T}{\partial x^2} + \frac{\partial^2 T}{\partial y^2} + \frac{\partial^2 T}{\partial z^2} + \frac{\dot{q}}{k} = \frac{1}{\alpha}\frac{\partial T}{\partial \tau} \tag{3.9}$$

where $\alpha = k/\rho c$ is called the *thermal diffusivity* of the material and is measured in units of m^2/s.

3.5.2 Laser model

The laser geometries presented in previous sections of this chapter will be modelled to give an estimate of the heat flow in the laserhead. A transient analysis of this problem, where the temperature T is a function of both x and t, was avoided due to the numerical instabilities which result from discontinuities in the parameters $c(x), \rho(x)$ and $k(x)$. No readily available numerical technique would allow the solution of coupled boundary value problems such as this. Therefore the analysis presented here is a steady state one. While this type of approach will not predict the time it takes the system to reach equilibrium, it does have the advantage that the model can be solved exactly.

A system reaches thermal equilibrium when all points in the system do not change temperature with time, $\partial T/\partial x = 0$. The steady state version of equation (3.9) can be written,

$$\frac{\partial}{\partial x}\left(k(x)\frac{\partial T(x,t)}{\partial x}\right) + \dot{q}(x) = 0 \tag{3.10}$$

Furthermore, if the thermal conductivity k is constant with respect to x then,

$$k\frac{\partial^2 T(x)}{\partial x^2} + \dot{q}(x) = 0 \tag{3.11}$$

Material	W/m/K
Metals	
Silver (pure)	410
Copper (pure)	385
Aluminium (pure)	202
Brass	111
Nickel (pure)	93
Iron (pure)	73
Carbon steel, 1% C	43
Lead (pure)	35
Chrome-nickel steel (18% Cr, 8% Ni)	16.3
Nonmetallic solids	
Quartz, parallel to C-axis	11
Magnesite	4.15
Marble	2.08-2.94
Sandstone	1.83
Glass, window	0.78
Glass wool	0.038
Liquids	
Mercury	8.21
Water	0.556
Ammonia	0.540
Lubricating oil, SAE 50	0.147
Freon 12, CC12F2	0.073
Gases	
Hydrogen	0.175
Helium	0.141
Air	0.024
Water vapour (saturated)	0.0206
Carbon dioxide	0.0146

Table 3.1: Thermal conductivity k of various materials.

The thermal conductivity of a gas is not dependent on the gas pressure over a wide range of pressures. This means that the thermal conductivity of the laser gas can been approximated by the constituent with the highest thermal conductivity. In our case this gas is helium which also happens to be the most abundant gas in the mixture. The assumption is therefore reasonable. The thermal conductivity data used is shown in table 3.1. Tables 3.2 and 3.3 list density and heat capacity data.

Material	kg/m^3
Aluminium	2700
Brass	8500
Quartz	2600
Water	1000

Table 3.2: Density ρ of laserhead materials.

Material	J/kg·K
Aluminium	900
Brass	390
Helium	5200
Quartz	700
Water	4200

Table 3.3: Heat capacity c of laserhead materials.

3.5.3 Heat transfer in the V1 laser

The model of the physical situation (figure 3.20a) is set up as shown in figure 3.20b. One dimensional 'slabs' of material with relevant thermal characteristics form an axis along which heat may propagate.

The flowing water at the top and bottom of the laser provide fixed boundary conditions ($T = 0°C$). One of these boundaries is assigned to be at $x = 0\,mm$, the other is therefore at $x = 8\,mm$. Although the tap water temperature varies between 10 and 20°C, the model only deals with temperature differences. This means that the initial temperature can be assigned arbitrarily. Thus, for simplicity in what follows, $T = 0$ implies the temperature of the cooling water unless otherwise stated. Furthermore, although more convenient units have chosen for the annotation of position (x), the following differential equations and solutions have been formulated in SI units.

Using equation (3.11) the V1 laserhead may be modelled by three coupled differential equations of the form,

$$\frac{d^2T_{Br1}}{dx^2} = 0 \qquad (0 < x \leq 3\,mm) \tag{3.12}$$

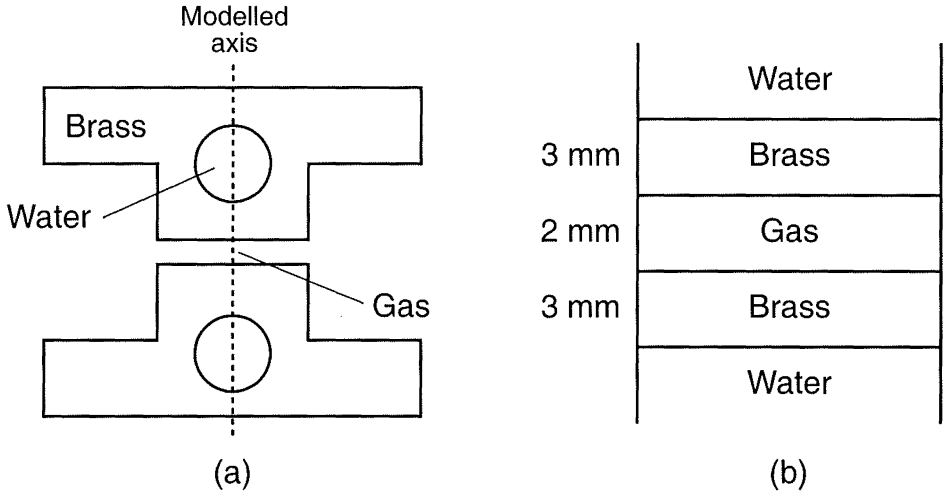

Figure 3.20: Heat transfer model for the V1 laser. (a) Physical setup, (b) One-dimensional model.

$$k_{\mathrm{He}}\frac{d^2T_{Gas}}{dx^2}+\dot{q} = 0 \qquad (3 < x \leq 5\,\mathrm{mm}) \tag{3.13}$$

$$\frac{d^2T_{Br1}}{dx^2} = 0 \qquad (5 < x \leq 8\,\mathrm{mm}) \tag{3.14}$$

where $T_i(x)$ is the temperature in the element i and is valid over the range shown. The heat input to the gas section is governed by $\dot{q}$ which has been set to a constant to keep the problem tractable. Although this is a simplification, numerical solutions for $T(x,t)$ on an even more simplified problem have shown that the shape of the heat input curve makes very little difference to the resulting thermal distribution. The value of $\dot{q}$ was set at 7.8×10^7 W/m^3 which is the power density appropriate for 1000 W into a cavity measuring 2 mm × 16 mm × 400 mm.

The above equations are subject to the boundary conditions,

$$T_{Br1}(0) = 0 \qquad \text{(Water at 0°C at } x = 0\,\mathrm{mm}) \tag{3.15}$$

$$T_{B11}(0.003) = T_{Gas}(0.003) \qquad \text{(Temps. match at the boundaries)} \tag{3.16}$$

$$T_{Gas}(0.005) = T_{Br2}(0.005) \tag{3.17}$$

$$T_{Br2}(0.008) = 0 \tag{3.18}$$

In addition, the heat flow out of one face must equal the heat flow into the next,

$$k_{Br1}\frac{\partial T_{Br1}(x)}{\partial x} = k_{Gas}\frac{\partial T_{Gas}(x)}{\partial x} \qquad (\text{at } x = 3\,\mathrm{mm}) \tag{3.19}$$

$$k_{Gas}\frac{\partial T_{Gas}(x)}{\partial x} = k_{Br2}\frac{\partial T_{Br2}(x)}{\partial x} \qquad (\text{at } x = 5\,\mathrm{mm}) \tag{3.20}$$

The solution to these equations is,

$$T(x) = \begin{cases} T_{Br1} = 704x & (0 < x \leq 3\,\mathrm{mm}) \\ T_{Gas} = -3.46\times10^3 + 1.85\times10^6 x - 2.31\times10^8 x^2 & (3 < x \leq 5\,\mathrm{mm}) \\ T_{Br2} = -5.63 - 704x & (5 < x \leq 8\,\mathrm{mm}) \end{cases} \tag{3.21}$$

The function $T(x)$ is plotted in figure 3.21. The maximum temperature in the gas is approximately (230+water temp)°C.

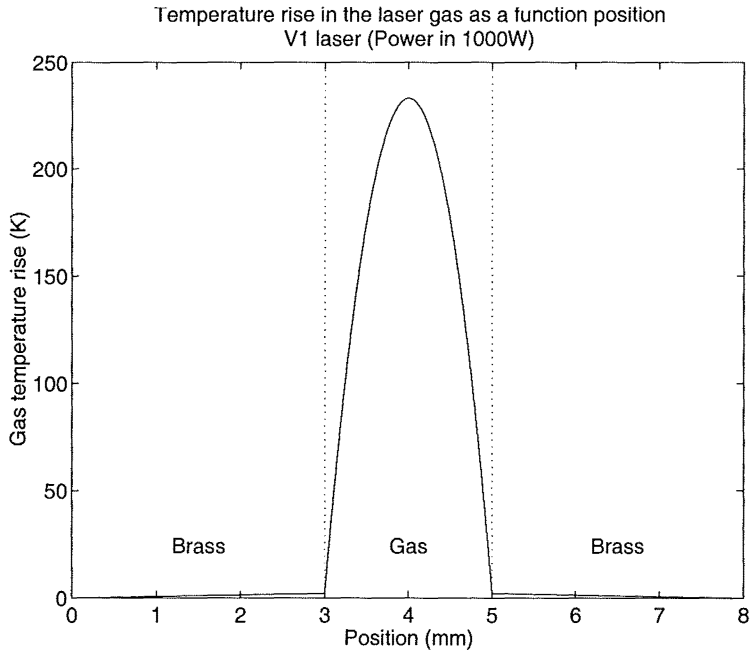

Figure 3.21: Temperature rise vs position for 1000 W heat input to the V1 laserhead.

3.5.4 Heat transfer in the V2 laser

The V2 laserhead has been modelled as shown in figures 3.22a and 3.22b. The quartz slab adds another equation to the set, however the solution is still of the same form. The solution for $T(x)$ is given by,

$$T(x) = \begin{cases} T_{Al1} = 371x & (0 < x \leq 4) \\ T_{Qu} = -25.8 + 6.28 \times 10^3 x & (4 < x \leq 9.5) \\ T_{Gas} = -2.5 \times 10^4 + 4.83 \times 10^6 x - 2.31 \times 10^8 x^2 & (9.5 < x \leq 11.5) \\ T_{Al2} = 6.24 - 402x & (11.5 < x \leq 15.5) \end{cases} \tag{3.22}$$

and is plotted in figure 3.23. Note that the addition of the quartz slab has a very minor influence on the maximum temperature rise in the gas.

3.5.5 Heat transfer in the V3 laser

The solution for the V3 laser is almost identical to that of the V2 laser. The physical situation is modelled as shown in figures 3.24a and 3.24b. The solution for $T(x)$ is given by,

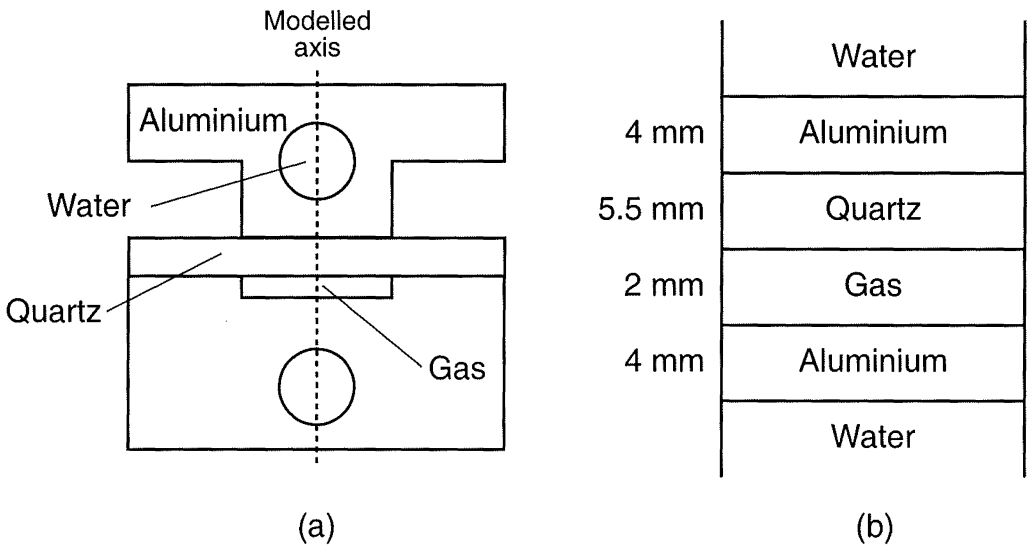

Figure 3.22: Heat transfer model for the V2 laser. (a) Physical setup, (b) One-dimensional model.

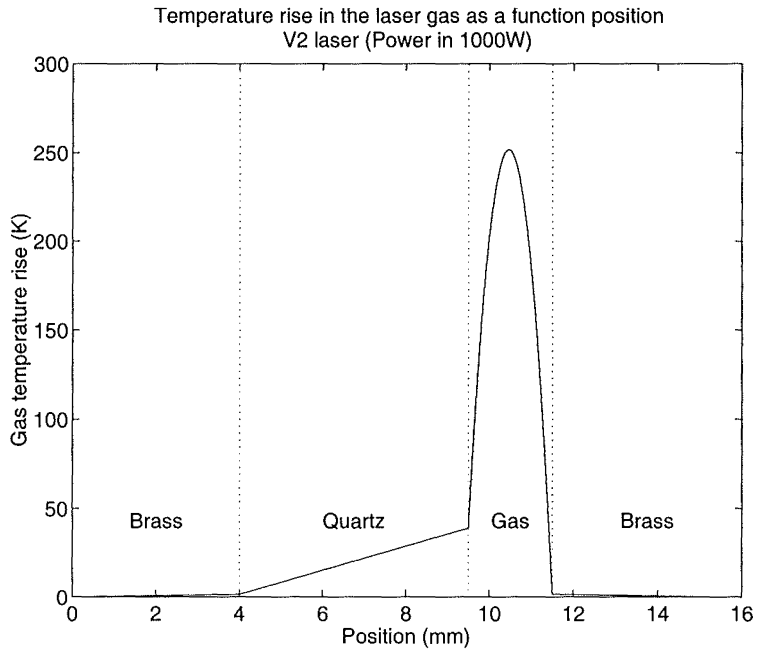

Figure 3.23: Temperature rise vs position for 1000 W heat input to the V2 laserhead.

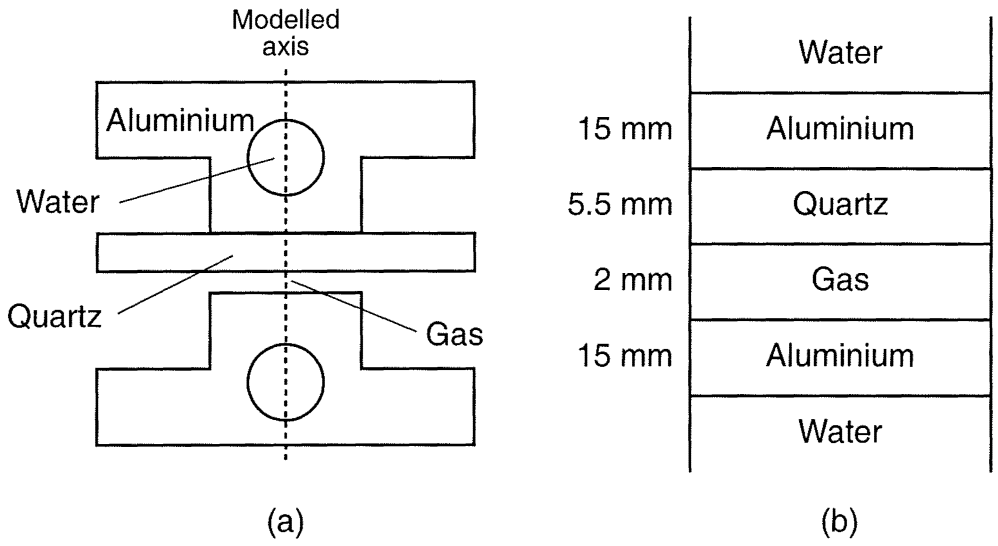

Figure 3.24: Heat transfer model for the V3 laser. (a) Physical setup. (b) One-dimensional model.

$$T(x) = \begin{cases} T_{Al1} = 371x & (0 < x \leq 15) \\ T_{Qu} = -96.7 + 6.82 \times 10^3 x & (15 < x \leq 20.5) \\ T_{Gas} = -1.06 \times 10^5 + 9.91 \times 10^6 x - 2.31 \times 10^8 x^2 & (20.5 < x \leq 22.5) \\ T_{Al2} = 15.1 - 402x & (22.5 < x \leq 37.5) \end{cases} \tag{3.23}$$

and is plotted in figure 3.25.

3.5.6 Gap spacing

Analysis of the three laserheads has shown that as long as the materials used have a high thermal conductivity compared with that of helium, the results look similar. One parameter which does affect the steady state temperature profile and which was not varied is the gap space in which the discharge resides. To examine the effect that alteration of this spacing has on the temperature profile, the model used for the V1 laser is altered to incorporate a variable gap spacing g.

The solution $T(x, g)$ is given by

$$T(x,g) = \begin{cases} T_{Br1}(x) = 70.4x & (0 < x \leq 3\,\text{mm}) \\ T_{Gas}(x) = -138 - 4.16 \times 10^{-1} g^{-1} + \\ \qquad 4.62 \times 10^4 x + 277 x g^{-1} - \\ \qquad 4.62 \times 10^4 x^2 g^{-1} & (3 < x \leq g + 3\,\text{mm}) \\ T_{Br2}(x) = 4.22 \times 10^{-1} + 70.4g - 70.4x & (g + 3 < x \leq g + 6\,\text{mm}) \end{cases} \tag{3.24}$$

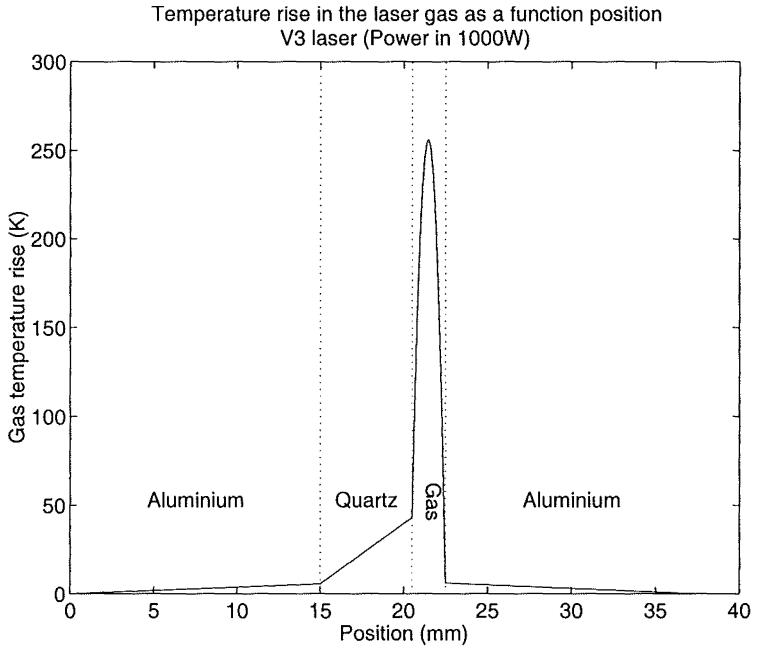

Figure 3.25: Temperature rise vs position for 1000 W heat input to the V3 laserhead.

We can now find the maximum temperature rise in the gas by finding the maximum of $T_{Gas}(x, g)$. The function $\text{Max}(T_{Gas}(x, g))$ is plotted versus gap spacing in figure 3.26. $\text{Max}(T_{Gas}(x, g))$ is the highest temperature reached by the gas in the model with gap spacing g. The figure shows that correct gap spacing is critical for the laser to produce high output power. The maximum temperature rises with respect to gap spacing even though the power density decreases due to the increased volume created by the larger gap.

3.5.7 Time evolution

In this section the time evolution of the temperature profile in the laser gas will be studied under the simple conditions of zero heat input and fixed temperature walls. This is almost the situation which occurs in the V1 laser after the microwave pulse has ended and the plasma is left to cool diffusively until the next microwave pulse. From this analysis it is possible to get a reasonable idea of the time taken for the plasma to cool after being heated by the magnetron.

The differential equation governing this situation is a simplified version of equation (3.8) in which only a single axis is used and $\dot{q}$ has been set to zero. The equation is,

$$\frac{\partial^2 T(x,t)}{\partial x^2} = \frac{1}{\alpha}\frac{\partial^2 T(x,t)}{\partial t^2} \tag{3.25}$$

subject to the boundary conditions,

$$T(0,t) = 0 \quad \text{and} \quad T(0.002,t) = 0 \tag{3.26}$$

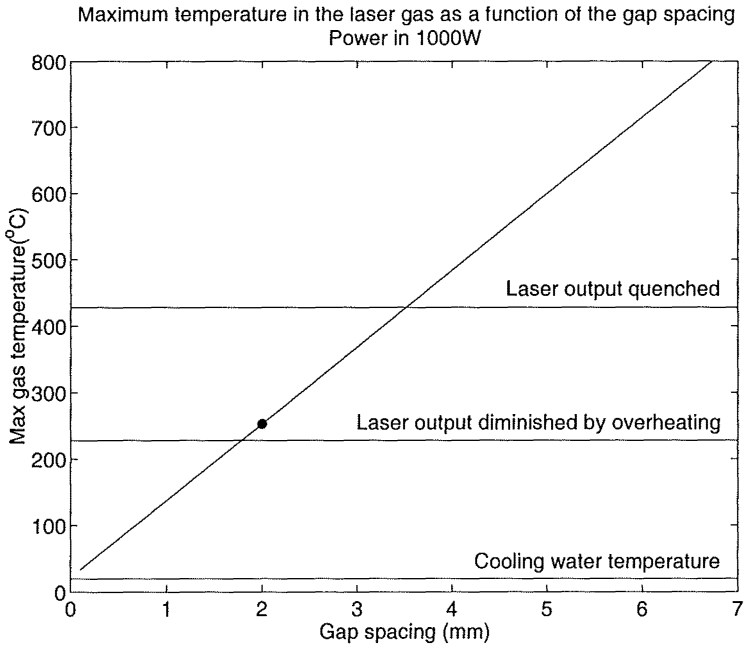

Figure 3.26: Maximum temperature in the laser gas according to the V1 temperature model as a function of the gap spacing. The power input is 1000 W. The gap spacing used in these experiments is indicated (•).

and the initial condition,

$$T(x,0) = 40\left(1+\sin\left(\frac{(x-0.0005)\pi}{0.001}\right)\right) \tag{3.27}$$

The initial condition, plotted in figure 3.27, was chosen because it matches the boundary conditions at $t = 0$ and because smooth functions cause fewer problems with numerical techniques. The actual shape of the initial temperature profile makes very little difference to the final result. An initial temperature of 100 K above the walls was assumed.

The numerical solution to these equations is graphed in figure 3.28. A cross section through this graph at $x = 1\,\text{mm}$ is shown in figure 3.29. The point at which the temperature reaches $1/e$ of its initial value may be taken to be a characteristic time for cooling. For this geometry it occurs at $t \simeq 60\,\mu\text{s}$. This $1/e$ value would occur at $60\,\mu\text{s}$ regardless of the the initial temperature. This is because the decay curve is exponential if transients are ignored.

3.5.8 Other factors

While the above equations represent a reasonable model of the physical situation, a number of assumptions have been made either implicitly or explicitly which will affect the results.

In real systems, unless specific measures are taken to prevent it, thermal contact

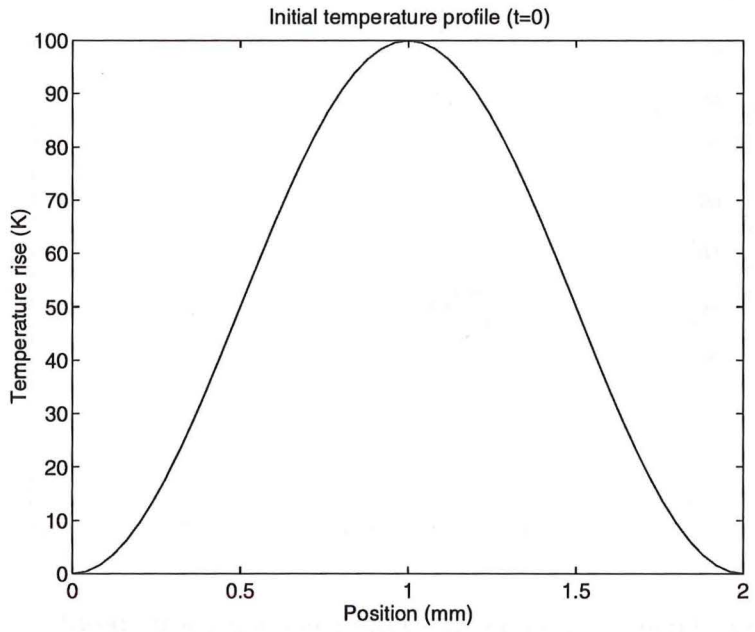

Figure 3.27: Initial conditions for the time evolution model (sine wave).

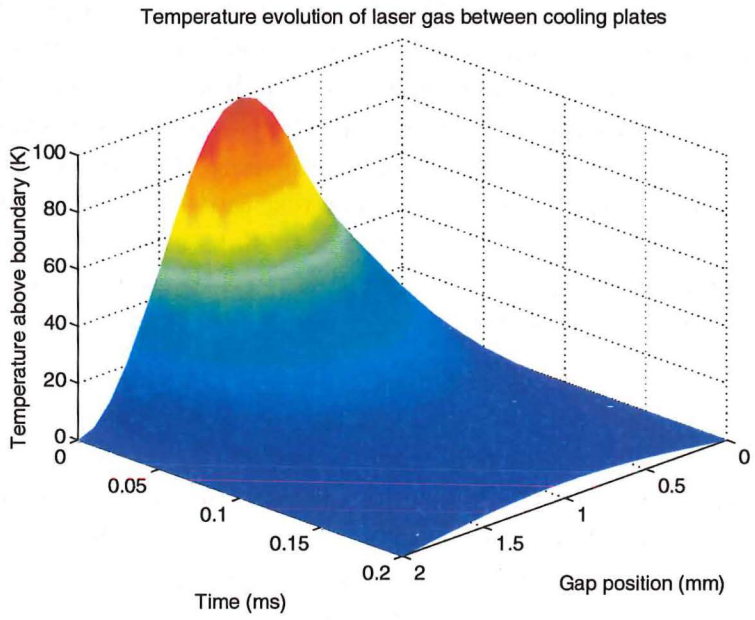

Figure 3.28: Time evolution of a gas temperature profile between two parallel plates at temperature T=0.

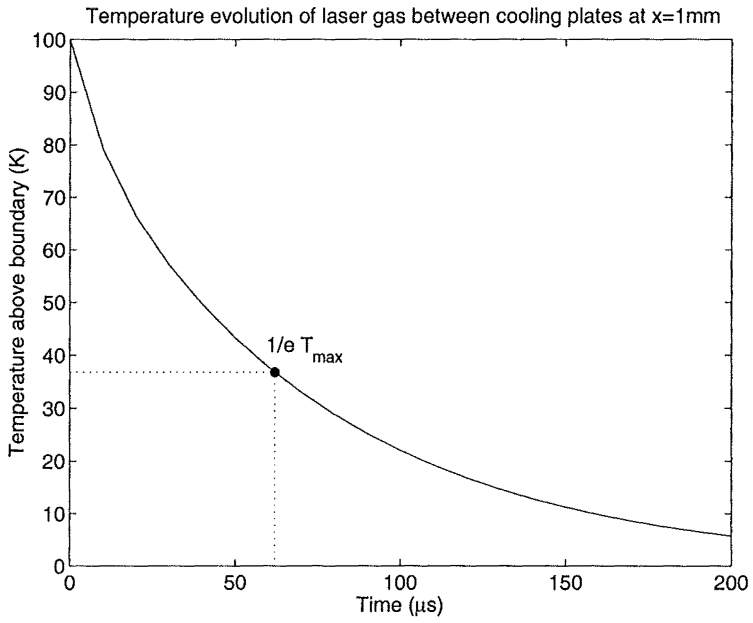

Figure 3.29: Time evolution of the above gas temperature profile at $x = 1\,\text{mm}$.

resistance changes the manner in which heat flows between two objects. Thermal contact resistance occurs because there is usually a layer of air or some other substance which separates the objects which are in physical contact. This resistance can be reduced by placing the objects in firm contact and by applying a soft solid or liquid with high thermal conductivity to the interface. In practice the effect of thermal contact resistance is a discrete temperate drop across the boundary. The resistances associated with these temperature drops are nearly always determined empirically. In the case of the lasers presented here, the interface between the gas and metal (or quartz) suffers no contact resistance because of the molecular nature of the gas. However, between the quartz slabs and metal there may be a significant temperature drop. The net result would be to increase the temperature maximum of the gas by a constant.

The input power of 1000 W has been assumed to be distributed evenly throughout the gas volume. This is unlikely to be the case in any real laser. Electric field variations along the length of the cavity cause the power to be distributed unevenly inside the plasma. This means that some sections of the plasma may see many times the power input than other sections if the field variation is significant. In this model the differential equations governing the temperature profile are linear. This means a linear increase in the input power results in a linear increase in the temperature profile. Therefore linear scaling of the axes in figures 3.21, 3.23 and 3.25 does not result in a change in shape of the temperature profile. These figures can then be used to estimate, for example, the effect of doubling the input power to a section of the cavity.

In conclusion, the laserhead designs V1, V2 and V3 are quite capable of removing

any amount of heat that the 1.2 kW magnetron being used is capable of delivering, as long as the power input to the discharge is not concentrated in small areas.

3.6 The vacuum system

A vacuum system capable of fast gas flow at low pressures is very desirable in an experimental CO_2 laser. Such systems can be cooled by gas replacement when operating at large gap spacings and the contaminants resulting from outgassing and discharge processes can be swiftly removed, at operating pressure. The design of the vacuum system connected to the V3 laser is presented and analysed in this section.

3.6.1 Pumping rate and conductance

In order to describe the vacuum system, a few basic terms must be defined.

The pumping rate S (or volume flow rate) at any point can be described by,

$$S = \frac{Q}{P} \qquad [\text{L s}^{-1}] \tag{3.28}$$

where Q is the throughput in [mbar L s^{-1}] and P is the pressure in [mbar] at the point at which the pumping speed is defined. The throughput Q gives a measure of the actual quantity of gas flowing through the system. Note that one litre of gas at one atmosphere does not contain the same number of molecules as one litre of the same gas at 10 mbar. Throughput is given by,

$$Q = \frac{PV}{t} = PS \qquad [\text{mbar L s}^{-1}] \tag{3.29}$$

which measures a given quantity of gas (PV) passing a plane in a time t. In order to describe how flow rates vary with different pumping speeds and geometries a conductance C, which is the inverse of the resistance to gas flow, is defined at a certain pressure. Conductance is usually more convenient to work with than resistance. It can be described as the quantity flow rate of gas flowing through a device divided by the resulting pressure drop,

$$C = \frac{Q}{P_1 - P_2} \qquad [\text{L s}^{-1}] \tag{3.30}$$

Note that pumping rates and conductances have the same units.

Conductances in series and parallel can be combined to give a composite conductances according to the following,

$$\begin{array}{lcll} C & = & C_1 + C_2 & \text{Series} \\ \dfrac{1}{C} & = & \dfrac{1}{C_1} + \dfrac{1}{C_2} & \text{Parallel} \end{array} \tag{3.31}$$

3.6.2 Gas flow regions

Flow in a device can be placed in one of three categories. *Viscous flow*, (1 to 1000 mbar ($\sim$ 1 atmosphere)) describes a situation where collisions between molecules occur frequently and the mean free path is much smaller than the containing vessel. *Molecular flow* ($< 10^{-3}$ mbar) is when the particle flow density is so low that collisions with other molecules are very uncommon and any pumping which takes place does so by random migration. In this case, the mean free path of the constituents is much greater than the size of the containing vessel. Falling between viscous and molecular flow is *intermediate flow* (10^{-3} to 1 mbar) in which the mean free path of molecules is of the same size as the containing vessel. Note that the pressures quoted here are only general approximations. A better way of categorising the gas nature and flow is via Reynolds and Knudsen numbers (see later).

3.6.3 Conductance of vacuum components

Expressions for the conductance of various vacuum elements vary depending on the flow regime in which the system is operating. Here only viscous flow is considered as all operational pressures for this apparatus fall within this regime.

The viscous conductance of a straight circular pipeline for air at 20°C is given [30] by,

$$C_v = \frac{136.5 D^4 P}{L} \tag{3.32}$$

where D is the pipe bore in cm, P is the average pressure in the pipe in mbar, ie. $P = (P_1 + P_2)/2$ and L is the length of the pipe in cm. Figure 3.5 lists the typical internal diameters of pipe used in this experiment versus the conductance per metre per torr.

When gas flows through an orifice or constriction, one must consider the conductance of the orifice. The conductance of an orifice for air at 20°C is given by,

$$C = 20A \qquad \text{(Viscous)} \tag{3.33}$$

where A is the area of the orifice in cm^2.

When other gases are used a conversion factor must be applied. Table 3.4 lists these conversion factors for various gases.

The particle velocity distribution in a gas is given by the Maxwell Boltzmann statistics,

$$\frac{dn}{dv} = \frac{2N}{\sqrt{\pi}} \left(\frac{m}{2kT}\right)^{3/2} v^2 e^{-mv^2/(2kT)} \tag{3.34}$$

where dn/dv is the number of particles with velocity between v and $v + dv$ in a gas at temperature T and whose particles have mass m. The average, peak and

Gas	Viscous flow coefficient
Air	1.00
Helium	0.93
Oxygen	0.91
Nitrogen	1.05
Hydrogen	2.07
Carbon dioxide	1.26
Water vapour	1.73

Table 3.4: Conductance conversion factors at 20°C.

Pipe	O.D. (mm)	Wall thickness	$\Longrightarrow$ ID (mm)	C_v/P (1 metre) (L s^{-1} $mbar^{-1}$)
$\frac{1}{4}''$	6.35 ± 0.051	0.762± 0.064	4.826 ± 0.115	$(7.4 \pm 0.7) \times 10^{-2}$
$\frac{3}{8}''$	9.52 ± 0.051	0.813± 0.064	7.984 ± 0.115	0.55 ± 0.03
$\frac{1}{2}''$	12.7 ± 0.051	0.813± 0.064	11.887 ± 0.115	2.7 ± 0.1

Table 3.5: Specified dimensions, implied ID and conductances for NZ standard refrigeration copper tube (coil lengths).

RMS velocities v, v_p and v_{RMS} are useful quantities and are given by,

$$v = \left(\frac{8kT}{\pi m}\right)^{1/2} \qquad v_p = \left(\frac{2kT}{m}\right)^{\frac{1}{2}} \qquad v_{RMS} = \left(\frac{3kT}{m}\right) \tag{3.35}$$

The average or mean free path of a molecule λ in a gas is,

$$\lambda = \frac{1}{\sqrt{2}\pi n d_0^2} \quad \text{or} \quad \lambda = \frac{kT}{\sqrt{2}\pi d_0^2 P} \tag{3.36}$$

where d_0 is the molecular diameter [m] and n is the gas density $[m^{-3}]$. The mean free path and molecular diameters for relevant gases are shown in table 3.6.

Gas	d_0 (cm)	λ (cm)
Helium	2.6×10^{-8}	1.03×10^{-3}
Nitrogen	3.14×10^{-8}	7.09×10^{-4}
Carbon dioxide	3.22×10^{-8}	6.74×10^{-4}

Table 3.6: Mean free paths and atomic diameters for CO_2 laser gases at 10 torr and 300 K.

The coefficient of viscosity η which gives some measure of the internal friction or drag in a gas is defined as *the tangential force per unit area for unit rate of*

decrease of velocity with distance. It is given [82] by,

$$\eta = \frac{0.998}{\pi d_0^2}\left(\frac{mkT}{\pi}\right)^{\frac{1}{2}} \qquad [\text{kg m}^{-1}\text{ s}^{-1}] \text{ or } [\text{Pa s}] \tag{3.37}$$

Note that η is not dependent on pressure when the mean free path of the gas is less than the characteristic size of the containing vessel and while it is not so small that the interaction between molecules is reduced.

The Reynolds Number, defined,

$$R_e = \frac{\rho v D}{\eta} \tag{3.38}$$

describes how the gas flows through a system. Here v is the stream velocity of the gas, ρ is its density and D is the diameter of the tube. If $R_e > 2200$ turbulent flow occurs. For $R_e < 1200$ laminar flow occurs. In the intermediate region between 1200 and 2200 the flow can be either laminar or turbulent depending on the geometry of the system.

The Knudsen number describes the flow regime under which the gas will operate. It is defined,

$$K_n = \frac{\lambda}{d} \tag{3.39}$$

where d is a characteristic dimension of the vacuum system and λ is the mean free path. Values of $K_n < 0.01$ reflect viscous flow. For $K_n > 1$ the flow is molecular and intermediate flow occurs for the region $0.01 < K_n < 1$.

3.7 Vacuum setup

Figure 3.30 is a schematic of the vacuum setup of the V3 laser. The design aim was to provide for the possibility of high gas flow at low pressures. In order to achieve this, a relatively large tube diameter ($\frac{1}{2}''$) was used in the smallest practical lengths.

3.7.1 Analysis

As was mentioned previously, the Knudsen number describes the regime under which the gas will operate. Figure 3.31 shows the Knudsen number over typical pressures used in this experiment (10-50 torr). The figure indicates that a viscous flow is expected in all situations likely to arise in this experiment.

The Reynolds number for this setup may be calculated from equations (3.38) and (3.37). Using a minimum diameter of 2 mm, $\rho = nm = Pm/kT$ and $v = Q/AP$, it is found that,

$$R_e = \frac{4m}{\pi kT\eta}\frac{Q}{D} = 77Q \tag{3.40}$$

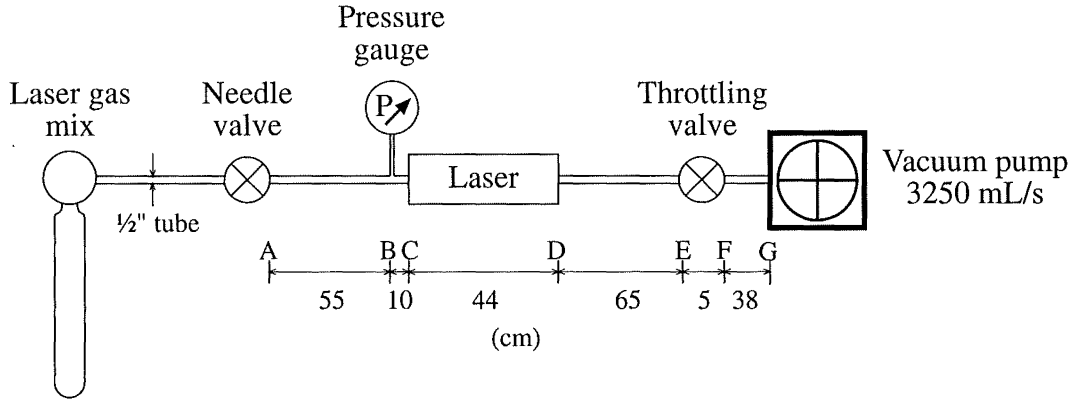

Figure 3.30: Vacuum setup of the V3 laser.

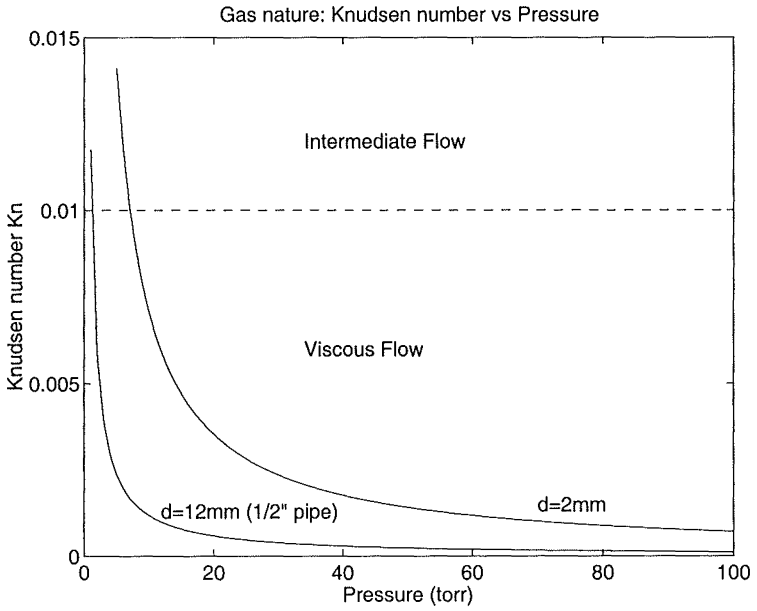

Figure 3.31: Knudsen number K_n for typical pressures and characteristic lengths.

Assuming a maximum flow rate of 100 mL/s at atmosphere, then $Q = 10$ Pa m^3/s which gives $R_e \simeq 780$. This value is clearly less than 1100 and so the flow in all parts of the laser vacuum system will be laminar.

3.7.2 Conductance

As the laser was to be studied under a variety of pressure and flow conditions, it was designed to produce the best practical flow rates our equipment could achieve. In order to estimate the maximum possible flow rate it was necessary to determine the conductance of the laser and vacuum lines.

Figure 3.30 shows the lengths of $\frac{1}{2}''$ pipe used in vacuum lines. Note that the laser cavity (section CD) is of irregular shape. The section between points A and B can be ignored in terms of conductances as the pressure is not of interest there. Opening the valve at A will compensate for any restricting conductance in this region. The total conductance of the system can be calculated from equations (3.31) and (3.32). So,

$$\frac{1}{C_{\text{Total}}} = \frac{1}{C_{BC}} + \frac{1}{C_{CD}} + \frac{1}{C_{DE}} + \frac{1}{C_{EF}} + \frac{1}{C_{FG}} + \frac{1}{S_{\text{pump}}} \tag{3.41}$$

where C_{xy} is given by equation (3.32) and the length and diameter are shown in the figure, except C_{CD} which has been approximated as a 44 cm pipe with a diameter of 2 cm. S_{pump} has a value of 3.25 L/s. The gas was assumed to consist entirely of helium and the conversion factor of 0.93 from table 3.4 was used. Figure 3.32 shows the calculated conductance of the system over the working pressure range.

From this conductance the maximum throughput of the system may be estimated. Figure 3.33 shows the predicted flow rate at the exhaust of the vacuum pump (ie at 760 torr) with some experimentally measured points. Experimentally measured flow rates would be expected to be somewhat less than the predicted values as the effect of obstacles (eg mirrors) and bends in the vacuum line have not been considered in the calculation of the overall conductance. Note that these flow rates are the maximum achievable flow rates at the given pressure for this system. Slower flow at the same pressure is possible by closing the valve at E-F.

Finally the pressure drop is considered across the laser system as a whole and more importantly across the laser itself. A large pressure drop across the laser could make optimisation of the laser output difficult. Using equation (3.30) the pressure drop across the vacuum system excluding the pump is,

$$P_G - P_A = \frac{PC_{\text{Total}}}{C_{BG}} \tag{3.42}$$

The pressure drop resulting from maximum possible flow through the vacuum line is shown in figure 3.34. Experimental measurements support these predicted values. A drop of half a torr should not result in any significant differences in behaviour of the laser at either end of the cavity.

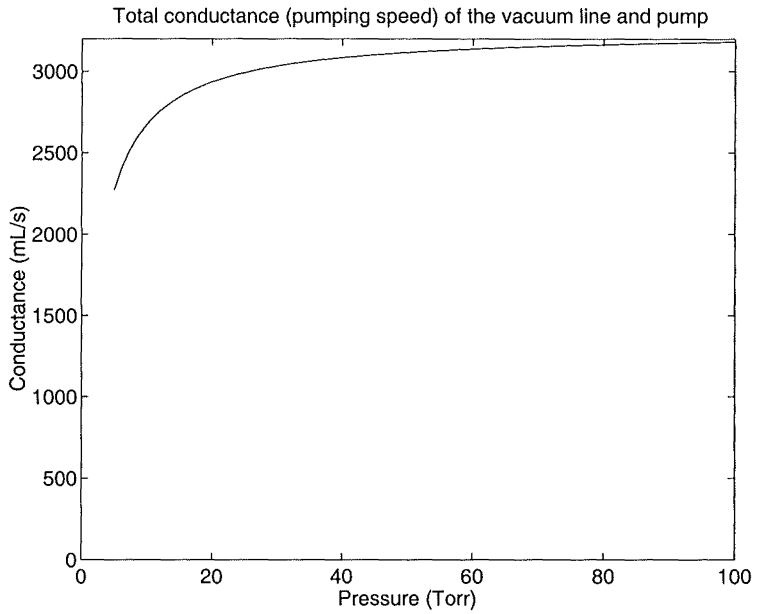

Figure 3.32: The overall pumping speed of the pump, laser and associated vacuum lines at point B of figure 3.30.

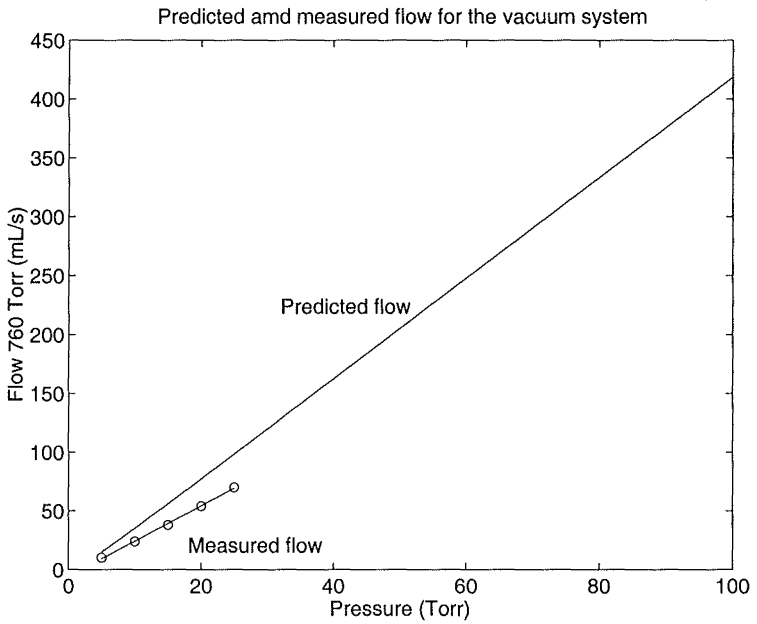

Figure 3.33: Predicted and measured flow through the laser vacuum system. (Measured at 760 torr from the exhaust of the pump)

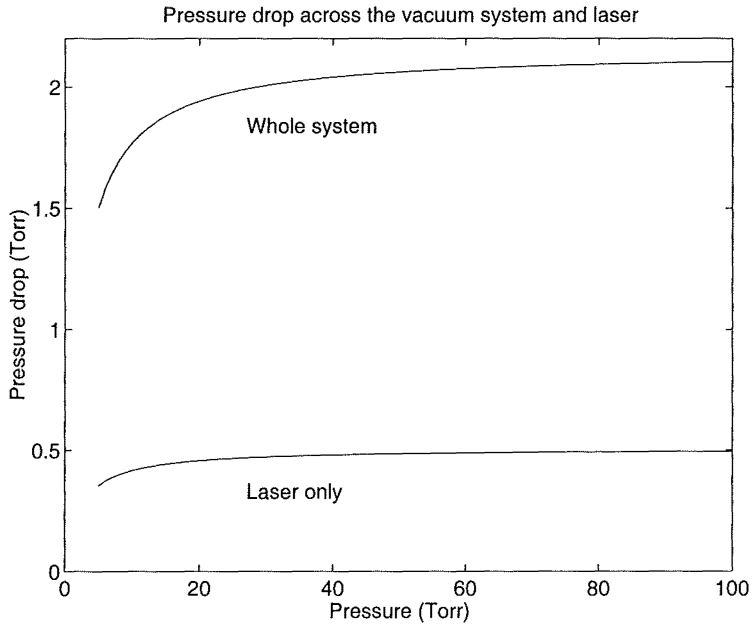

Figure 3.34: Pressure drop resulting from flow through the vacuum system.

Chapter 4

Microwave excitation

4.1 Introduction

The focus of this chapter is on the coupling of microwaves from a magnetron into a thin discharge cavity so as to produce a population inversion in the laser gas. The following section is a short introduction to waveguides and explains the basic concepts along with notational definitions and conventions.

4.2 Waveguides

A waveguide is a hollow conducting tube of arbitrary cross section [43]. Wave propagation in waveguides occurs according to Maxwell's equations, subject to boundary conditions on the surface of the conductor. Maxwell's equations are,

$$\begin{aligned} \nabla \times \mathbf{E} &= -\mu \frac{\partial \mathbf{H}}{\partial t} \\ \nabla \times \mathbf{H} &= \epsilon \frac{\partial \mathbf{E}}{\partial t} \\ \nabla \cdot \mathbf{H} &= 0 \\ \nabla \cdot \mathbf{D} &= 0 \end{aligned} \tag{4.1}$$

subject to the boundary conditions,

$$\begin{aligned} \mathbf{E}_{\parallel} &= 0 \\ \mathbf{H}_{\perp} &= 0 \end{aligned} \tag{4.2}$$

where inside the waveguide the charge and current densities are zero, ($\rho = 0$ and $\mathbf{J} = 0$) and the conductivity is assumed to be very large inside the guide walls ($\sigma \to \infty$).

Equations (4.1) and (4.2) for propagation in a guiding structure, that is uniform along the z axis, have two sets of solutions. The first solution is when the axial or z component of the electric field is always zero and the second when the z component of the magnetic field is always zero.

To solve equations (4.1) subject to the constraints (4.2) the solution is separated into a function of the transverse variables (x, y) and a function of the axial and time variables (z, t). It is found that,

$$\mathbf{H}_t = \frac{1}{k_t^2}[ik_l \nabla_t H_z - i\omega\epsilon(\nabla_t \times \mathbf{E}_z)] \tag{4.3}$$

$$\mathbf{E}_t = \frac{1}{k_t^2}[ik_l \nabla_t E_z + i\omega\mu(\nabla_t \times \mathbf{H}_z)] \tag{4.4}$$

where $\mathbf{E}_t$ and $\mathbf{H}_t$ are functions of the transverse variables (x, y) and $\mathbf{E}_z$ and $\mathbf{H}_z$ are functions of (z, t).

Both boundary conditions cannot be applied simultaneously unless either E_z or H_z is zero. This means that the solutions come in two forms: one called *transverse magnetic* and the other *transverse electric.*

Transverse magnetic (TM) waves (also called E waves) are a solution in which,

$$H_z = 0 \quad \text{(everywhere)} \tag{4.5}$$

Likewise transverse electric (TE) waves (also H called waves) are a solution in which,

$$E_z = 0 \quad \text{(everywhere)} \tag{4.6}$$

These modes occur regardless of the cross section of the waveguide.

Both the TM and TE waves have an infinite set of modes. In rectangular guides these are usually labelled TM_{mn} and TE_{mn}, which may or may not be able to propagate in a waveguide according to a cutoff frequency ω_{mn} above which certain TM_{mn} or TE_{mn} modes cannot propagate.

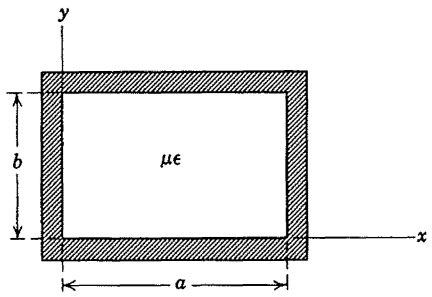

Figure 4.1: A rectangular waveguide of width a and height b.

For a rectangular waveguide shown in figure 4.1, the TE or H wave cutoff frequency is given by,

$$\omega_{mn} = \frac{\pi}{\sqrt{\mu\epsilon}} \left(\frac{m^2}{a^2} + \frac{n^2}{b^2} \right)^{\frac{1}{2}} \tag{4.7}$$

where m and n are the mode numbers of the wave. It is readily shown that the fields are given by,

$$H_z = H_0 \cos\left(\frac{m\pi x}{a}\right) \cos\left(\frac{n\pi y}{b}\right) e^{i(k_{l,mn} z - \omega t)} \tag{4.8}$$

$$\begin{pmatrix} H_x \\ H_y \end{pmatrix} = \mathbf{H}_0 \frac{ik_{l,mn}}{k^2} \begin{pmatrix} \frac{m\pi}{a} \sin\left(\frac{m\pi x}{a}\right) \cos\left(\frac{n\pi y}{b}\right) \\ \frac{n\pi}{b} \cos\left(\frac{m\pi x}{a}\right) \sin\left(\frac{n\pi y}{b}\right) \end{pmatrix} e^{i(k_{l,mn} z - \omega t)} \tag{4.9}$$

$$E_z = 0 \tag{4.10}$$

$$\begin{pmatrix} E_x \\ E_y \end{pmatrix} = H_0 \frac{i\omega\epsilon}{k^2} \begin{pmatrix} \frac{n\pi}{b} \cos\left(\frac{m\pi x}{a}\right) \sin\left(\frac{n\pi y}{b}\right) \\ \frac{m\pi}{a} \sin\left(\frac{m\pi x}{a}\right) \cos\left(\frac{n\pi y}{b}\right) \end{pmatrix} e^{i(k_{l,mn} z - \omega t)} \tag{4.11}$$

For transverse magnetic waves (the TM or E waves) the fields are given by,

$$E_z = E_0 \sin\left(\frac{m\pi x}{a}\right) \sin\left(\frac{n\pi y}{b}\right) e^{i(k_{l,mn} z - \omega t)} \tag{4.12}$$

$$\begin{pmatrix} E_x \\ E_y \end{pmatrix} = \mathbf{E}_0 \frac{ik_{l,mn}}{k^2} \begin{pmatrix} \frac{m\pi}{a} \cos\left(\frac{m\pi x}{a}\right) \sin\left(\frac{n\pi y}{b}\right) \\ \frac{n\pi}{b} \sin\left(\frac{m\pi x}{a}\right) \cos\left(\frac{n\pi y}{b}\right) \end{pmatrix} e^{i(k_{l,mn} z - \omega t)} \tag{4.13}$$

$$H_z = 0 \tag{4.14}$$

$$\begin{pmatrix} H_x \\ H_y \end{pmatrix} = E_0 \frac{i\omega\epsilon}{k^2} \begin{pmatrix} \frac{n\pi}{b} \sin\left(\frac{m\pi x}{a}\right) \cos\left(\frac{n\pi y}{b}\right) \\ \frac{m\pi}{a} \cos\left(\frac{m\pi x}{a}\right) \sin\left(\frac{n\pi y}{b}\right) \end{pmatrix} e^{i(k_{l,mn} z - \omega t)} \tag{4.15}$$

with the cutoff frequencies again given by equation (4.7).

4.3 Simple magnetron power supplies

The microwave magnetrons used in these experiments are direct current devices which have similar VI characteristics to Zener diodes. This means that they are non-conducting below a threshold voltage. Above this voltage they will start to draw current. For the magnetrons used here, the turn-on point is around -3400 V. When operated well above this voltage (~ 4000 V), these magnetrons produce higher output powers but the efficiency drops significantly. Operating voltages used in this investigation were between -3400 V and -3900 V.

Under normal operation in a microwave oven, microwave magnetrons are pulsed at 50 Hz with a 50% duty cycle. The standard electrical setup is shown below in figure 4.2. The mains voltage of 230 V (rms) at 50 Hz is transformed to around 1.8 kV using a saturable core transformer. The output of the transformer is then voltage doubled via a half wave voltage doubler, which is made from a single diode and a capacitor. The unloaded output from this configuration looks like a conventional unfiltered half-wave rectified signal which has been offset by 1.8 kV. The capacitor charges through the diode to 1.8kV during the positive part of the cycle and discharges through the load (magnetron) during the negative part with an additional 1.8kV provided by the transformer. The ingenious design of the saturable core transformers used in these circuits means that the output microwave pulse is almost a 50 Hz square wave. This was the only power supply design used by Jamison [72] in an earlier work on this project.

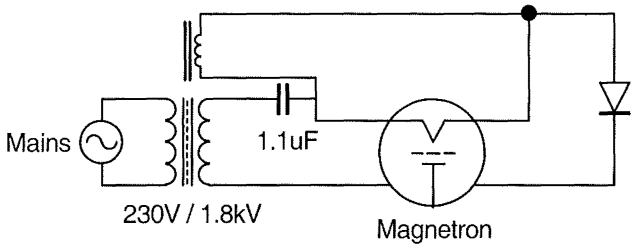

Figure 4.2: Schematic of a standard magnetron power supply.

While a 50 Hz, 50% duty cycle is useful for cooking chicken it does not offer much flexibility in a research situation. A more useful power supply configuration is shown in figure 4.3. This design can produce a fullwave rectified signal and can drive the magnetron in true CW mode. As the transformers used in this design were the same as those used in the circuits of figure 4.2, it was necessary run two in parallel so that the current limits on the secondaries were not exceeded.

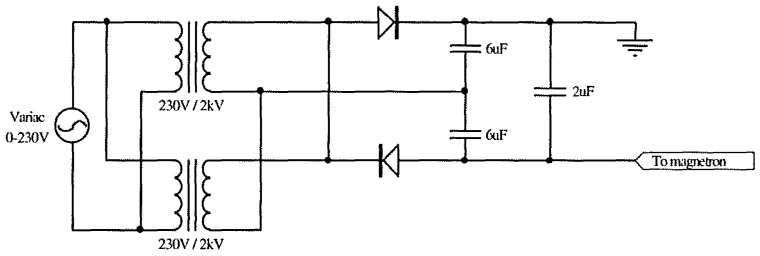

Figure 4.3: Schematic of the fullwave magnetron power supply.

By attaching a variac to the primaries of the transformer, the input and thus output voltage could be easily varied. By reducing the voltage sufficiently, the output power of the magnetron can be varied. This is because the capacitors cannot sufficiently sustain the current required to keep the magnetron oscillating during the low voltage intervals of the cycle. Therefore, this allows crude control over the output power and pulse width. The fullwave power supply was useful for exciting and testing various microwave and plasma cavity configurations.

4.4 A more controllable power supply

Ultimately modifications of power supplies designed to cook food did not have the characteristics required to study the population inversion in a gas. A more sophisticated design was required. In an experimental situation it is desirable to have the maximum possible flexibility in microwave output. Optimal design specifications include: pulse widths from 1 μs to continuous, pulse repetition rate from 0 Hz (DC) to $\sim$ 40 kHz and adjustable magnetron input voltage for some

control over output power. Due to the lack of any commercial devices which could meet these specifications it was decided that one should be built. The resulting supply consisted of a 6 kV, 1 A DC power supply from a defunct copper vapour laser and a fast high voltage switch. The DC supply was converted for negative voltage operation and modulated by a microcontroller-driven vacuum-tube switch designed and built by the author.

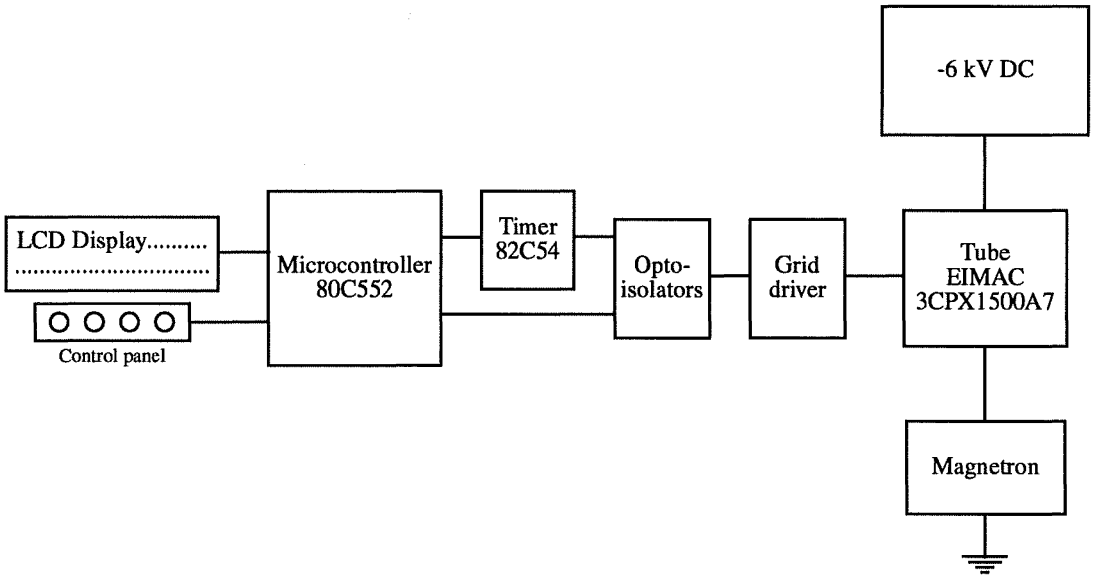

Figure 4.4: Schematic of the magnetron power supply/modulator's basic components.

A block diagram of the supply is shown in figure 4.4. A DC power supply capable of supplying 0 to -6 kV at 0 to 1 A was modulated (switched) by an EIMAC 3CPX1500A7 vacuum tube. The tube was controlled by a microcontroller and a specialist timer chip. The pulse output and control signals from the microcontroller and timer are opto-isolated (6 kV) and sent to a grid driver circuit which switches the tube. In this way the operator can have precise control over the pulse repetition frequency and duty cycle. A photograph of the supply is shown in figure 4.5.

4.4.1 The DC supply

The DC power supply used was a Quentron 7000A switch-mode supply based on the Siemens TDA4718 switch-mode controller. The supply was capable of producing from 0 to 6 kV at 0 to 1 A. As magnetrons must be driven by negative voltages and this power supply was originally a positive supply, it was necessary to reverse the polarity. This was accomplished by transposing the outputs of the floating rectified signal so that the positive lead was grounded and then modifying the final output and safety circuits so that they functioned correctly with negative voltages. The polarity reversal involved the insertion of an inversion module between the voltage and current sensing circuitry and feedback control

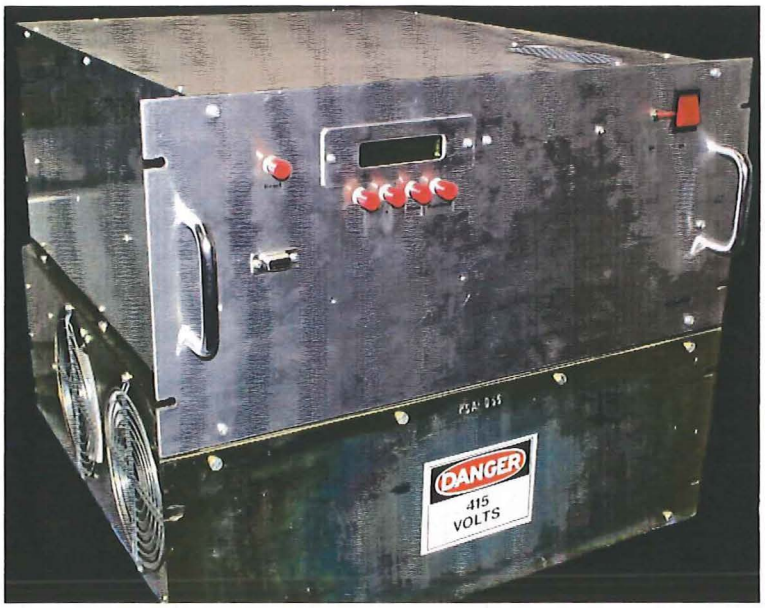

Figure 4.5: Photograph of the power supply switch sitting atop the DC switchmode supply.

circuitry. The supply still functions as if it were a positive supply.

The maximum DC output current and voltage can be controlled by current loops fed to the supply from a controller box. This box also displays the actual and set voltages and currents, giving the operator a good indication of how much power is being sent to the tube/magnetron.

4.4.2 The electron tube

The electron tube used to switch the high voltage was an EIMAC 3CPX1500A7 ceramic/metal high-μ power triode. In air it is capable of pulsing up to 10 kV at 50 A. For the heater and plate voltages in use, the grid requires a -30 V bias (relative to the cathode) in order to turn the tube off. A positive bias of 90 V will then turn the tube on (10 A max plate current).

4.4.3 The magnetron

Many magnetrons have been used during the course of these experiments and all share very similar characteristics. A typical example is the AWI BL750J which delivers 1200 W of microwave power at full duty cycle.

4.4.4 Opto-isolation

As all the grid driver circuitry floats at -5 kV it was necessary to electrically isolate it from the microcontroller circuitry which operates near earth. This could be achieved simply by the use of high voltage capacitors, however, this makes it difficult to send control signals (eg. RUN/STOP). The solution was to use opto-isolators as shown in figure 4.6.

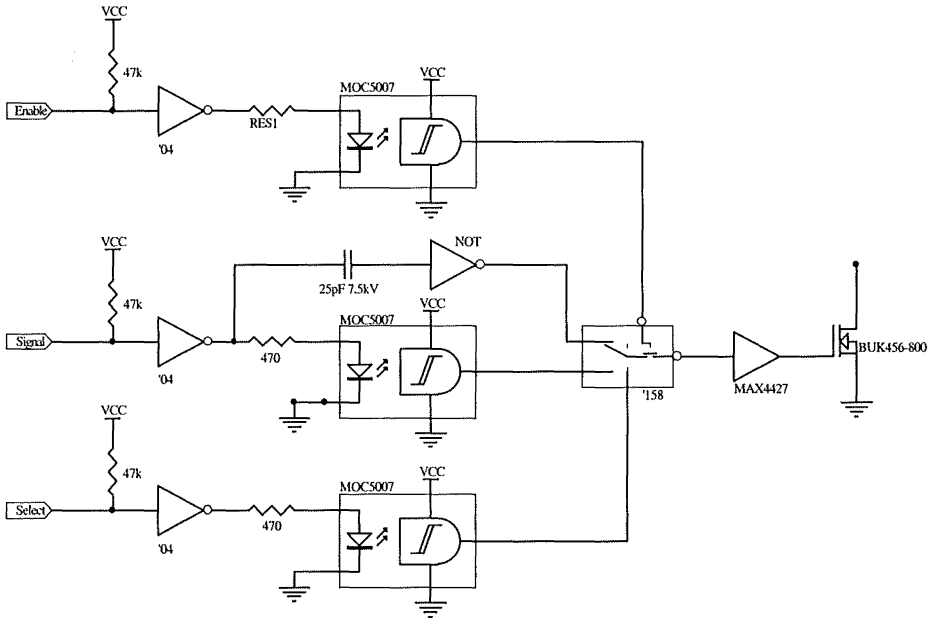

Figure 4.6: Opto-isolator section of the magnetron power supply/modulator.

Three signals are sent to the circuitry floating at -5 kV, SIGNAL (the required microwave pulse of set frequency and duty cycle), RUN/STOP (to start and stop the output) and SELECT (to select either an opto-isolated or capacitively coupled pulse signal). The choice of two pulse signals allows faithful reproduction of the pulse over a wide range of repetition frequencies. At low frequencies ($\sim$ 50 Hz) the capacitor cannot maintain the signal shape and at very high frequencies ($>$ 200 kHz) the opto-isolator cannot couple the signal fast enough. By having both options, good pulse shape can be maintained at all operational frequencies. The microcontroller can automatically select the correct coupling device for the pulse repetition frequency in use. After these signals have been elevated to -5 kV, a multiplexer with an enable line is used to select the correct signal and pass it on to the tube grid if RUN/STOP is set.

4.4.5 The grid driver

The triode tube is switched on and off via its grid. By setting the grid voltage to -30 V or $+90$ V relative to the cathode, the tube can be turned off (current

$< 1\,\mathrm{mA}$) or on (current up to 10 A). Figure 4.7 shows the circuit used to accomplish this. A $-30\,\mathrm{V}$ supply attached directly to the $-5\,\mathrm{kV}$ line lets all the grid control circuitry float at 30 V below the cathode voltage. This 30 V supply (and the 12 V and 120 V supplies) are floating supplies generated from the mains via isolating transformers. The isolated pulse signal is fed through a high speed FET driver to a high-voltage (800 V max) fast FET, which shorts the grid to $-30V$ (relative to the cathode) when on or lets it sit at 90 V (120 V-30 V) when off. The 12 V supply is only used to power the FET driver and thus the FET itself.

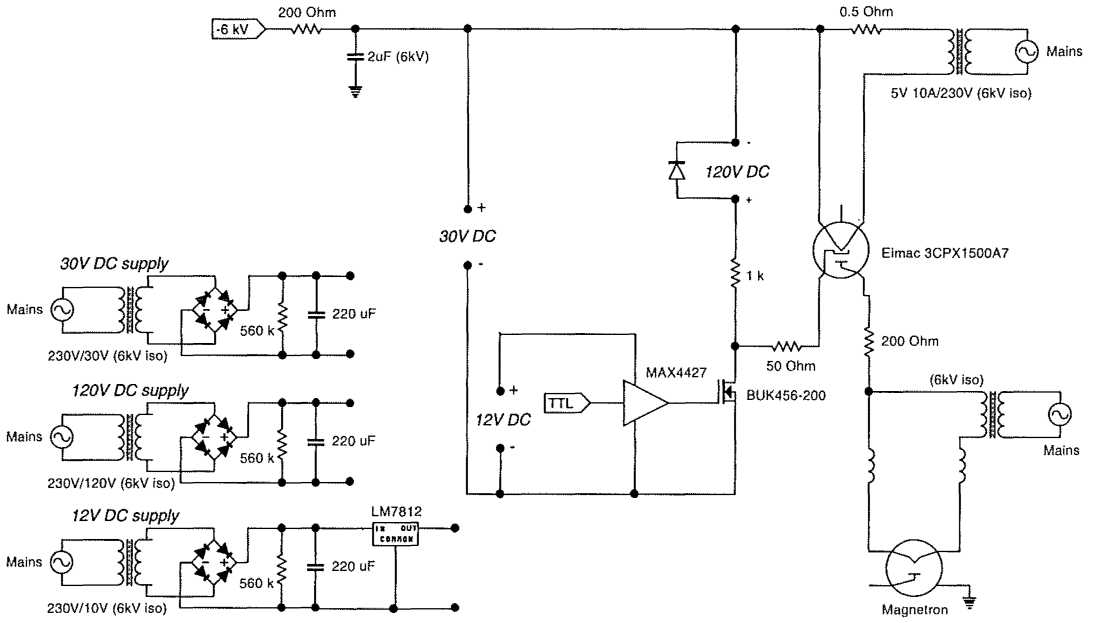

Figure 4.7: Schematic of the grid driving electronics.

One difficulty with this design is that it will not turn on especially fast due the non-negligible grid capacitance. This small grid capacitance means that there is a delay in turning on the tube while the grid charges via the 1 k resistor and the 120 V supply. This charging time could be diminished by reducing the resistor value, however there are practical limits to be observed regarding heat dissipation when the FET is on. A more elegant solution is presented in figure 4.8. In this case, no resistor is required as two FETs are used in a totem pole arrangement (when one is on the other is off). This means that the grid can be connected to the -30 or $+90$ V lines almost instantly. The extra logic circuitry allows the pulse sent to each FET to be delayed slightly. This means that the switching times of the particular FET can be taken into consideration and the circuit adjusted so that the one FET turns on coincidently with the other turning off.

The downside of this system is that another isolated supply is required to drive the top FET. Although the circuit board design contains facilities for this type of fast switching, such high speeds were not required during the laser experiments and this part of the circuit, although built and tested, was not used.

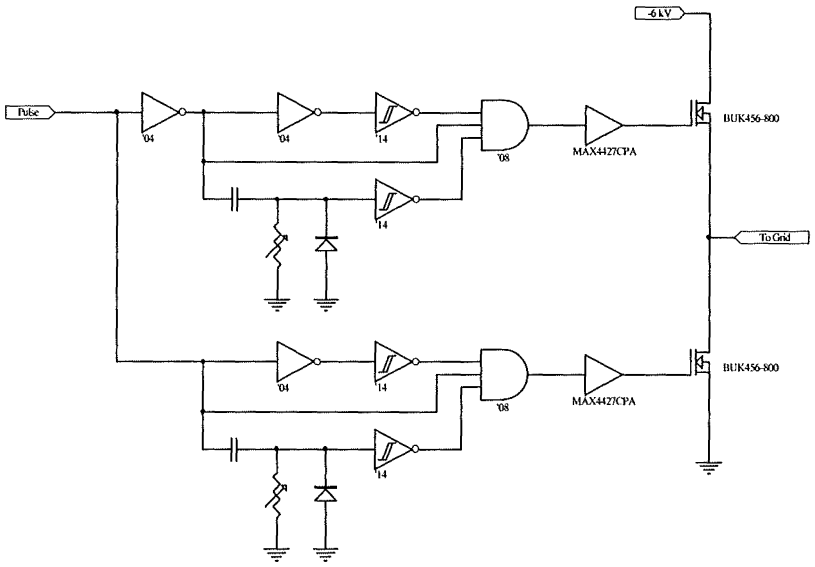

Figure 4.8: Schematic of the fast grid driving electronics.

4.4.6 The microcontroller and timer

The output pulse shape which the magnetron is to reproduce is created initially by a microcontroller and timer. A microcontroller was used instead of an analog system because the output pulse shape is binary (ie on or off), making it easy to control the device over a very wide range of operating parameters. It also allows the operator to select accurately the pulse length and period.

The microcontroller used was the Philips 80C552 which is a versatile single chip, 8-bit controller. As the controller has only 256 bytes of internal RAM and no internal ROM these have been added as external components. The processor is capable of addressing 64k of RAM and 64k of ROM in two separate address spaces. However, under normal circumstances only the ROM address space can be used to execute code. The configuration used here was 32k of RAM from 0 to 7FFF and 32k of ROM from 8000 to FFFF. In addition the two address spaces (data and code) were mapped together into a single data *and* code address space. This meant that the ROM section of memory, implemented as an EPROM, could contain a small amount of monitor code and the software necessary to run the supply under normal circumstances. New code could also be downloaded in to RAM and executed for debugging purposes or when some new feature was required. This reduced the need to erase and burn new EPROMs for every software revision and aided in code development. New software could be downloaded via the serial interface (MAX232) which allowed direct connection to a computer with an RS232 (or equivalent) port. Interaction with the operator was by four push buttons and a two line, 32 character display connected to the microcontroller via the I^2C bus.

The output pulse train was created by an 82C54 programmable interval timer and a EXO-3 crystal oscillator. The EXO-3 is a 16 MHz oscillator with a programmable divisor which is what allows the instrument to function over a wide range of time scales. The output from the oscillator is feed into the interval timer which creates a pulse train according to instructions from the microcontroller.

The circuit diagram for the microcontroller and timer is shown in figure 4.9. Also shown in the figure is the power supply for the controller. It filters and regulates the output from a simple 10V power pack. The circuit board layout (check plot) for these circuits is shown in figure 4.10.

4.5 The electric field probe

An electric field probe was used through out these experiments in order to make measurements of the standing waves in various waveguide configurations. A circuit diagram for the probe used is shown in figure 4.11. The time constant used was fast enough to give a faithful representation of the microwave pulse while eliminating higher frequency noise from the rest of the electronics.

The probe end of the diode was inserted about 2 mm into the centre of the waveguide as shown in figure 4.12. The probe could then be moved along the waveguide and the slotted line technique [65] used to measure the the standing wave ratio and thus the ratio of transmitted to reflected power.

The circuit configuration used for the probe is not a high gain configuration because of the relatively high powers (for the 1N23) present in the waveguide. The 1N23 diode is a square law detector [94, Chapt. 2] which means that its response is proportional to the square of the electric field.

It is worth noting that the voltage measured by the probe as a function of position along the waveguide is not a simple sine wave. It it easily calculated, however. Take a standing wave configuration with two waves travelling in opposite directions denoted by the subscripts + and −. The voltage in the guide as a function of position and time is given by,

$$V = A_+ e^{i(\omega t + kx)} + A_- e^{i(\omega t - kx)} \tag{4.16}$$

Because the probe averages the positive part of the signal (it is a diode) over a number of cycles the $e^{i\omega t}$ factor will average to a constant leaving the positive part of the amplitude envelope. This envelope is given by,

$$\begin{aligned} |V_{env}| &= |A_+ e^{+ikx} + A_- e^{-ikx}| && (4.17)\\ &= \sqrt{A_+^2 + A_-^2 + A_+ A_- e^{2ikx} + A_+ A_- e^{-2ikx}} && (4.18)\\ &= \sqrt{A_+^2 + A_-^2 + 2A_+ A_- \cos(2kx)} && (4.19) \end{aligned}$$

The probe response is proportional to the square of the voltage in the guide.

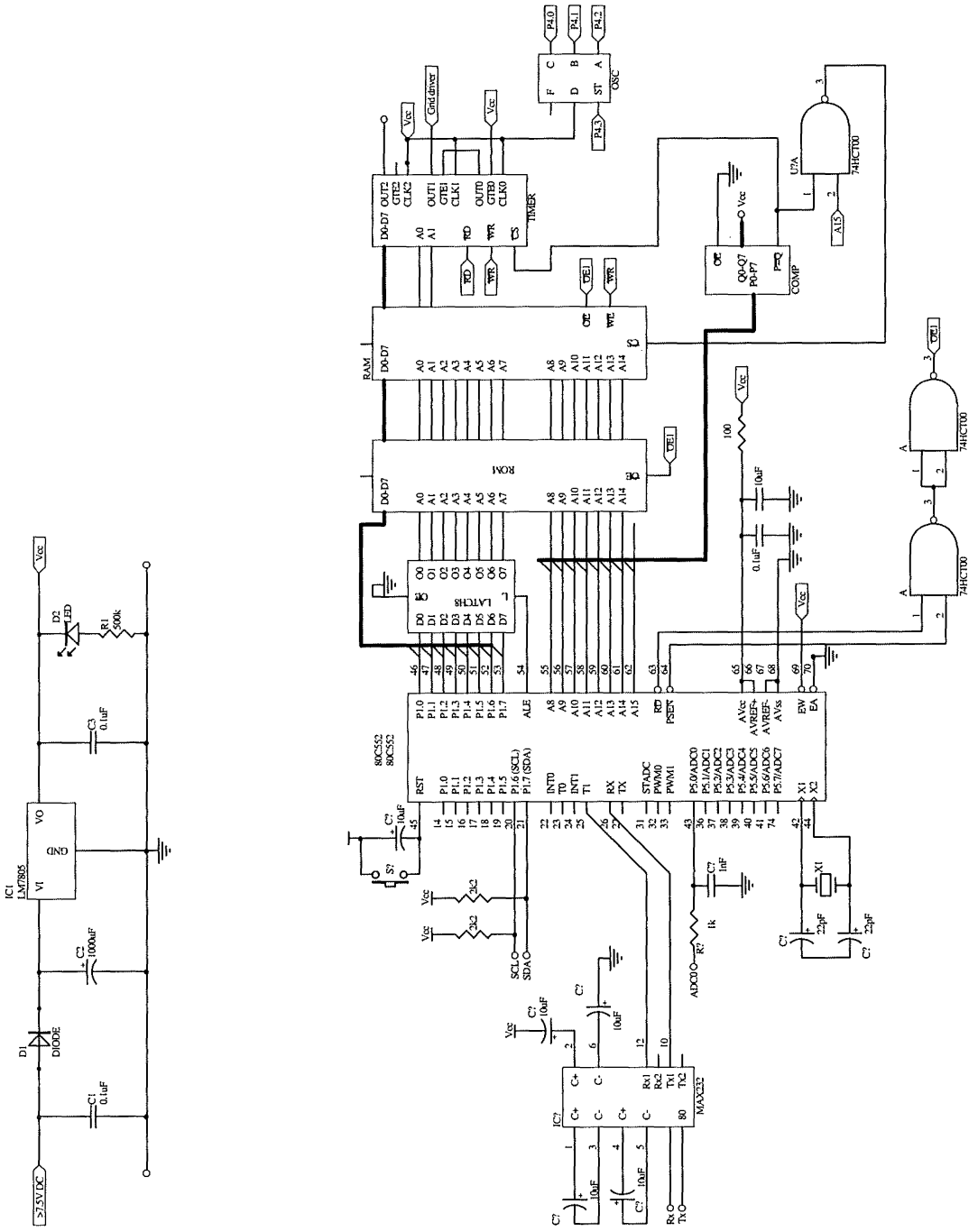

Figure 4.9: Microcontroller and timer schematic.

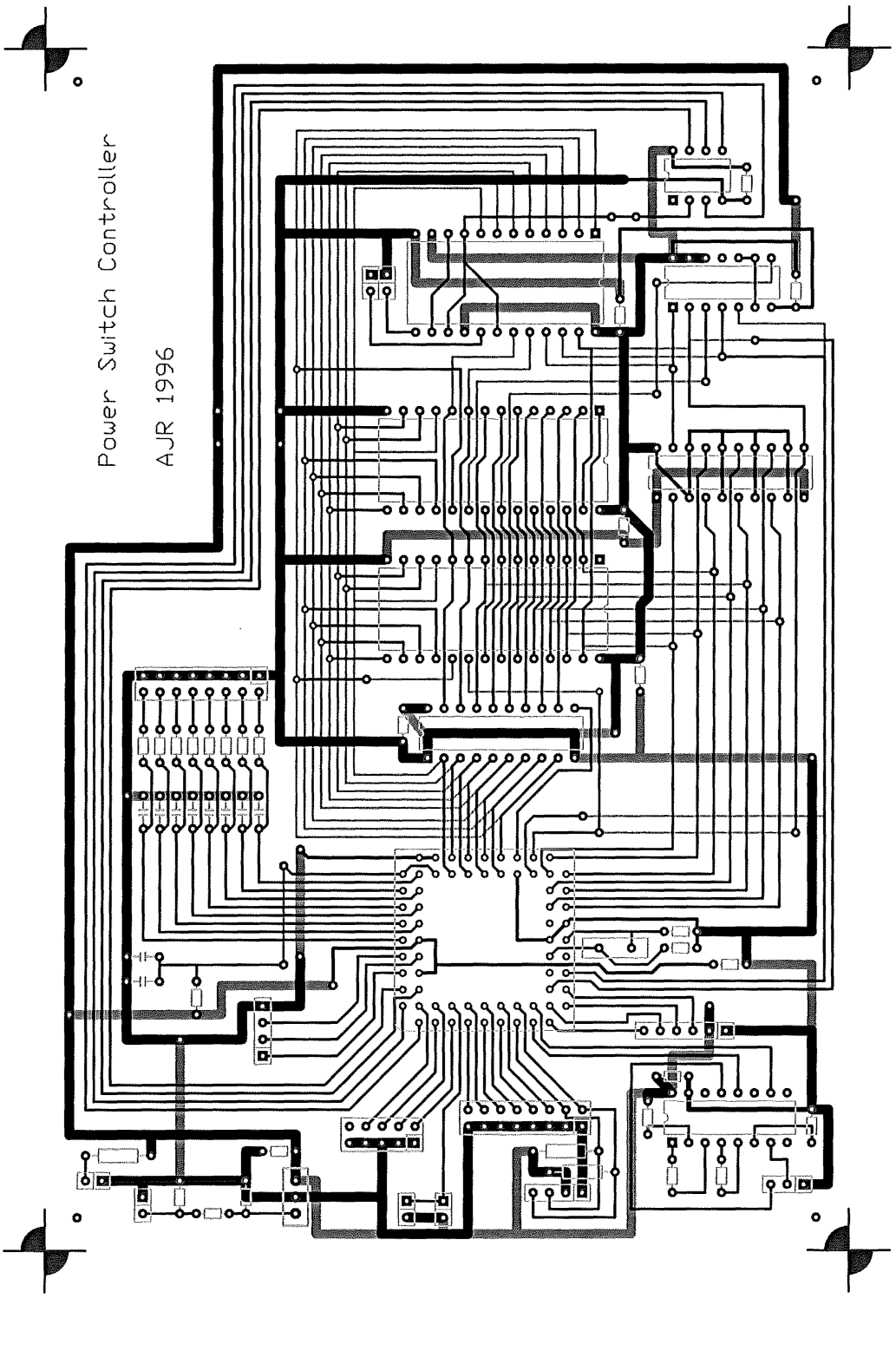

Figure 4.10: PCB layout (check plot) of the microcontroller and timer.

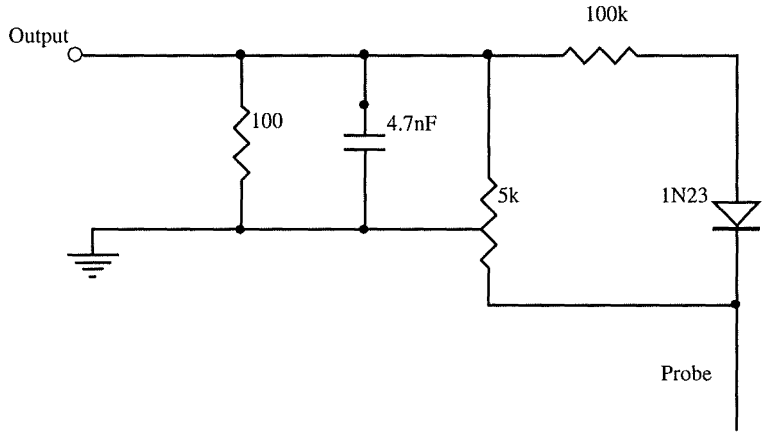

Figure 4.11: Circuit diagram for the electric field probe

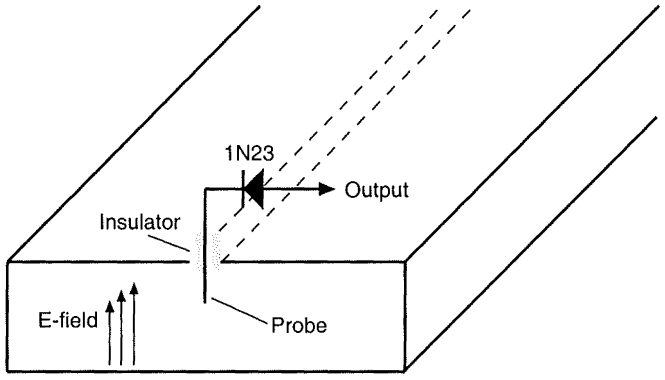

Figure 4.12: Electric field probe configuration

Thus the probe response as a function of position is given by,

$$V_{probe} = (A_+^2 + A_-^2 + 2A_+A_- \cos(2kx))^{\frac{1}{4}} \tag{4.20}$$

if the diode is operated in its square-law region. The typical response of the probe as calculated from equation 4.20 is shown in figure 4.13.

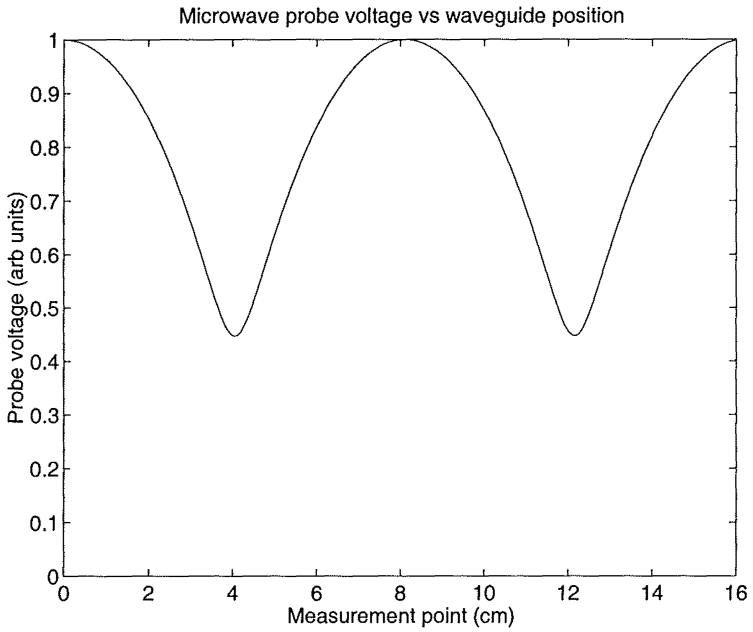

Figure 4.13: The voltage response of the microwave probe as a function of position for $\lambda = 16\,\text{cm}$. The incident and reflected waves have amplitudes of 0.6 and 0.4 respectively.

As a fast method of measurement, it was hoped that situating a few microwave diodes along the waveguide at fixed positions could be used in conjunction with equation (4.20) and a numerical optimisation technique used to measure the SWR in real time. In theory (and simulation) the technique works very well. In practice the shape of the curve in figure 4.13 and the degree of calibration of probe separation and response made estimating the position and therefore value of the maximum and minimum very difficult. For this reason the multi-probe detector was discarded and the more conventional single probe technique was used.

4.6 Microwaves at 2.45 GHz

Microwaves at 2.45 GHz have a wavelength in free space of 12.2 cm. In a waveguide, the wavelength is altered according to,

$$\lambda_g = \frac{\lambda}{\sqrt{1 - \left(\frac{\lambda}{2a}\right)^2}} \tag{4.21}$$

where a is the width of the waveguide.

A waveguide of width 95 mm and height 44 mm, made of readily available aluminium box-section, was used. This leads to a waveguide wavelength of λ_g = 16 cm. The dimensions of this waveguide are such that no modes except the TE_{10} mode will propagate along the guide. Table 4.1 shows the cutoff frequencies or minimum frequencies required for a mode to propagate along the box-section used. These cutoff frequencies can be calculated from equation (4.7).

f_{mn}	n=0	1	2	3
m=0		3.4	6.8	10.2
1	**1.6**	3.8	7.0	10.3
2	3.2	4.6	7.5	10.7
3	4.7	5.8	8.3	11.3

Table 4.1: Waveguide cutoff frequencies in GHz for TE_{mn} modes in a 95 mm × 44 mm waveguide.

4.7 Microwave excitation

The ultimate objective of the high voltage power supplies and waveguides is to create a strong electric field that is capable of creating a gas discharge between two parallel plates separated by a gap of approximately 2 mm. Optimally the plasma should be uniform [32] throughout the entire length and width of the electrode. It should also be resistant to small changes in gas flow and power. In order to create such a discharge, an effective method of coupling the microwave radiation into the small discharge region was required, such that a uniform electric field was produced.

The microwave excitation system involves the design of two main systems: the laserhead and the microwave coupling waveguide. The laserhead must house the thin discharge channel and associated optics under vacuum. The coupling waveguide is responsible for taking microwaves from the magnetron and coupling them efficiently into the laserhead while minimising reflections back to the magnetron and maximising discharge uniformity.

An effective microwave applicator is shown in figure 4.14. This waveguide setup introduces a TE_{10} mode to the laserhead. Note the choice of axes used here (and later) differs from section 4.2. The magnetron is an AWI BL750J (or similar) microwave oven magnetron which operates at 2.45 GHz and delivers 1200 W at full duty cycle into a matched load. The initial section of the waveguide (B) is the manufacturer-recommended "launcher" section to couple microwaves from the magnetron to a TE_{10} waveguide. The width of the first two sections of waveguide (B and C) is such that it will accommodate only the TE_{10} mode. The cutoff frequency for this mode is 1.6 GHz, with the cutoff for the next highest

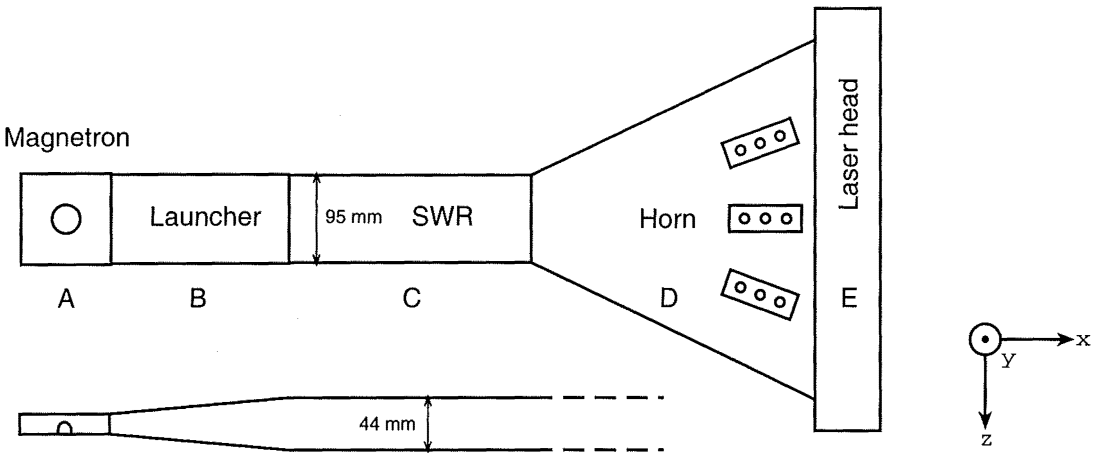

Figure 4.14: Schematic of the magnetron-waveguide-horn section.

mode at 3.2 GHz, well above the 2.45 GHz of the generator. Section C is a plain TE_{10} waveguide with a thin slot milled along the centre of the top surface. This groove can be used to sample the electric field and thus produce an estimate of the voltage standing wave ratio (VSWR) via the slotted line technique [26]. This measurement reveals information about transmitted and reflected power in the guide as well as the phase of the wave. It is a useful diagnostic section for determining how efficiently the microwaves are being coupled into the laser. Section D provides a relatively smooth transition from the 95 mm width of the TE_{10} guide to the 400 mm width, which is the length of the discharge cavity. As the transition is smooth, the mode incident on the laserhead should remain pure TE_{10}. Experimental observations confirm that the electric field pattern across the laserhead end of the horn is the half sinusoidal form of a TE_{10} mode. Tuning stubs on the horn section help to match the laserhead and plasma impedances to that of the waveguide.

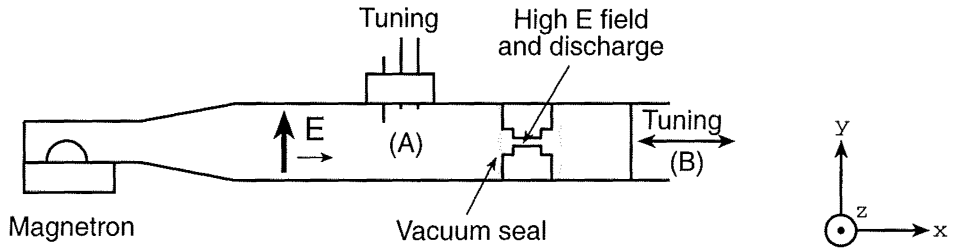

Figure 4.15: Cross section (side view) horn configuration of the brass laser.

A cross-section of the waveguide and V1 laserhead is shown in figure 4.15. The electric field is perpendicular to the top and bottom of the guide. Initially a standing wave is present in the guide, the phase of which may be adjusted by the trimmers (A) or the tuning stub (B). Correct placement of the E-field maximum in the discharge area results in a field which causes breakdown in the gas. Once

the discharge is lit the conductivity of the gas changes considerably requiring further tuning of the cavity for optimum excitation. At this point much of the energy is being absorbed by the gas before it reaches the tuning stub (B) and the standing wave ratio drops. In practice a high standing wave ratio is present with typical values or the order of 10. At low pressures the conductivity of the plasma is such that reflections from the plasma/electrode section are very uniform. However, at higher pressures, changes in the conductivity of the plasma and higher breakdown voltages result in non-uniform reflections which can generate higher order microwave modes in the horn section [88, pg. 356]. These reflections lead to an electric field which is not sinusoidal along the length of the discharge as it contains components of other modes. In this state the excitation of the discharge in a specific region depends on many parameters including: the microwave modes incident (local E field), the plasma conductivity, gas and electrode temperature, gas velocity and the gas pressure. If any of these parameters vary then so may the excitation of the discharge. This becomes a significant problem at high pressures where the incident power per gas molecule ratio drops and small fluctuations in discharge resistivity can lead to significant changes in the microwave characteristics of the system. The worst case scenario occurs when the discharge jumps continuously between several 'stable' microwave configurations. Apart from their uncontrollable nature, such discharges tend not to be uniform which is a serious impediment to high power output.

The results of microwave excitation for the three designs examined during this study, are detailed in the following sections. The main emphasis is on discharge quality (that is, its uniformity, the degree to which it fills the discharge area available and its resistance to instability) rather than direct lasing performance, although these are intimately related.

The brass V1 cavity

The brass cavity was the last discharge cavity studied by Jamison [72] (who used a different coupling waveguide) in earlier work on this project and became the first laserhead tested by the author. A diagram of the cross-section is shown in figure 4.16. The discharge occurs in the small evacuated 2 mm gap where the electric field is about 25 times that in the waveguide.

A series of discharge photographs from the brass V1 laser are shown in figure 4.17. Note that the axes have been scaled in a ratio $x : y$ of 1:3 for viewing purposes. The photographs cover a working pressure range of 10 to 25 torr in both flowing and non-flowing gas operation. The common dark region in the centre of all the photographs is due to an alumina spacer which maintains the electrode separation under vacuum. Several general trends are present in these photographs. Flowing gas tends to result in a more uniform discharge than in the non-flowing case. At low pressures the microwave mode pattern incident on the plasma appears to be TE_{10}, while at higher pressures the mode pattern breaks up into several regions of high intensity. The size and placement of these regions can be altered to a

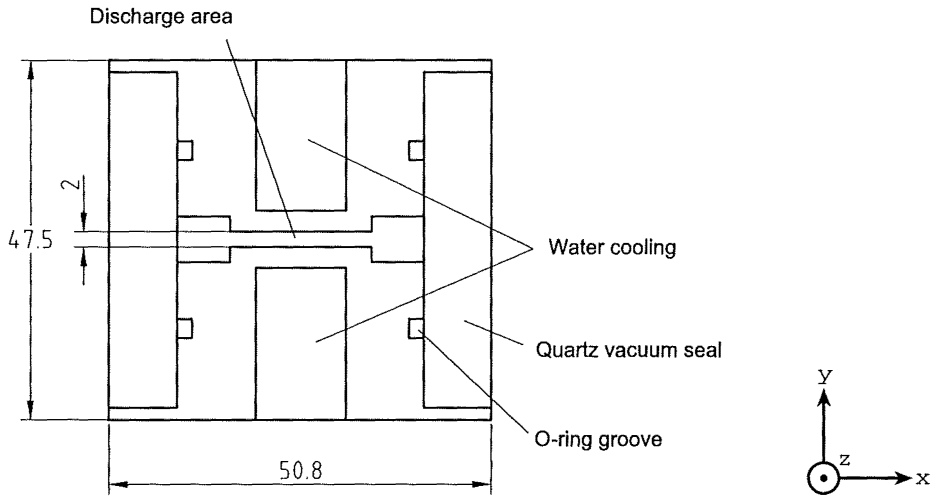

Figure 4.16: Scale cross section of the V1 cavity.

small degree by adjusting the tuning stubs (figure 4.15a) and the placement of the cavity termination (figure 4.15b). The pulse period and length of 400/40 μs was used as a base value because it has been found to be a good starting point for optimising laser output. In general, the discharge illumination pattern is insensitive to changes in the pulse period and length, tending to depend mainly on the gas pressure and microwave configuration. At pressures above 25 torr the discharge is very hard to light and the discharging section is always confined to a small area. At higher input powers (higher duty cycle) the discharge will light but tends to be unstable and regions flicker on and off as fluctuations in gas temperature and microwave configuration alter the impedance the plasma presents to the microwave cavity. Situations in which the discharge flickers are clearly unsuitable for lasing because (when they lase) the output power will also fluctuate with the discharge flicker. It is also impossible to optimise parameters such as pulse repetition rate under these conditions.

The V2 cavity

The second V2 laserhead was an attempt to create a more uniform discharge which could be excited at higher pressures. It incorporates a quartz dielectric to help stabilise the discharge. The design is elegant from a constructional point of view requiring only two vacuum seals, one for the discharge cavity and one more for the output coupler.

Discharge photographs of the aluminium V2 cavity are shown in figure 4.20. These photographs show clear evidence of the effectiveness of the quartz dielectric in generating a more uniform discharge. The mechanism for this is described in section 6.9. Unlike the brass (V1) cavity the microwave mode incident on the plasma is almost pure TE_{10}. Furthermore excitation at significantly higher pressures is possible whilst keeping the uniform discharge. However, when the

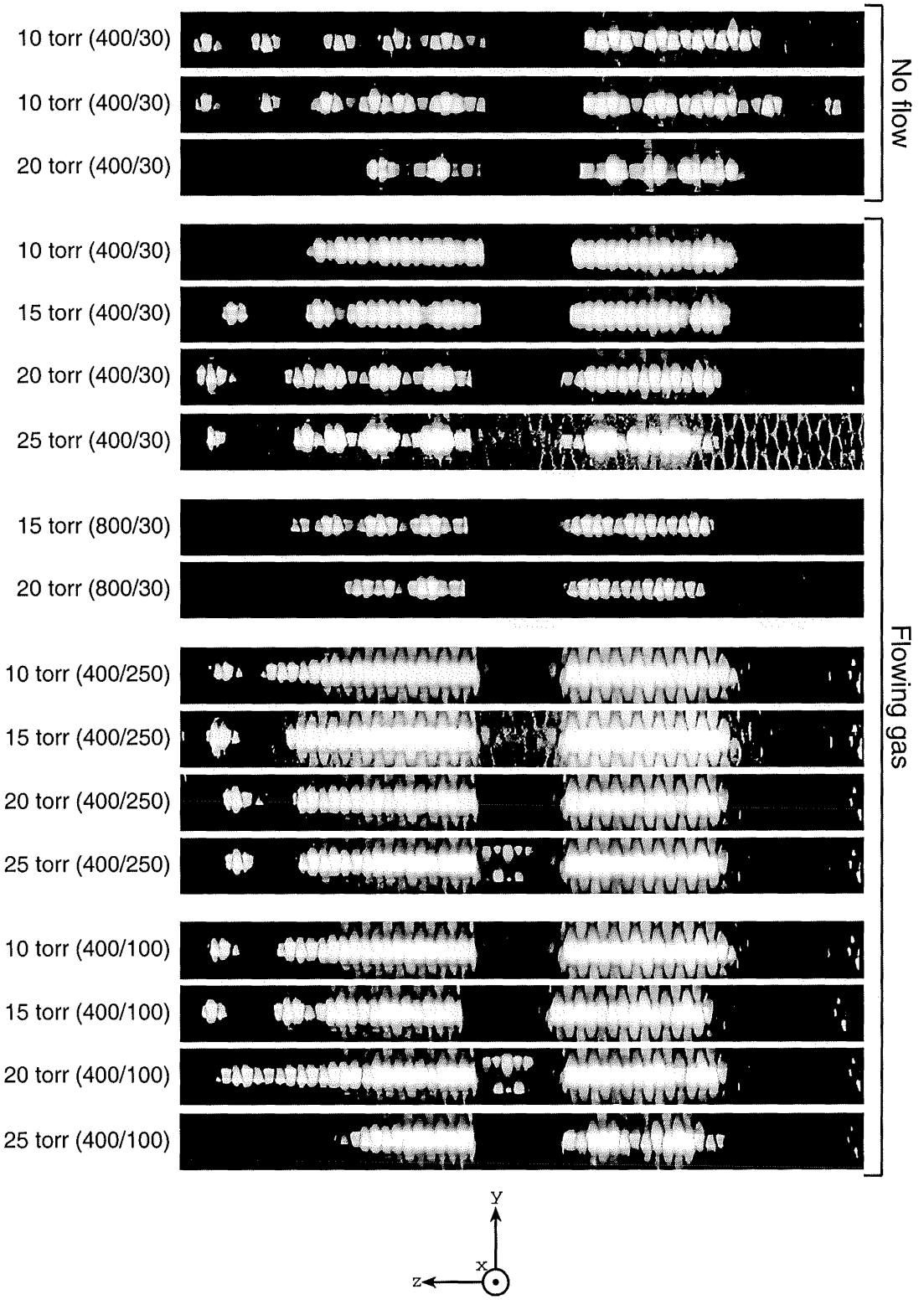

Figure 4.17: Microwave induced discharge in the brass V1 cavity as viewed from the side of the laser through the perforated metal microwave shield. The vertical (y) axis has been scaled by a factor of three with respect to the horizontal (z) axis. The numbers in brackets represent the period and pulse length respectively.

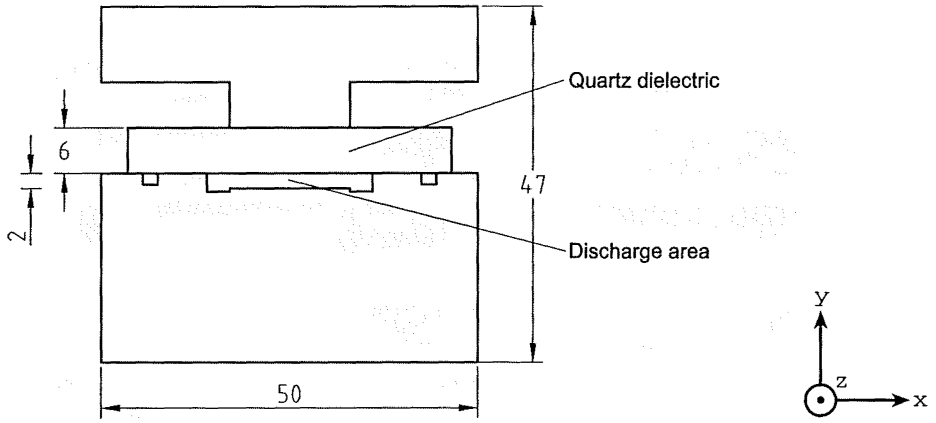

Figure 4.18: Scale cross section of the V2 cavity.

pressure reaches a value of around 50 torr the discharge has contracted to a small fraction ($\sim$ 20%) of the cavity length making it unsuitable for lasing.

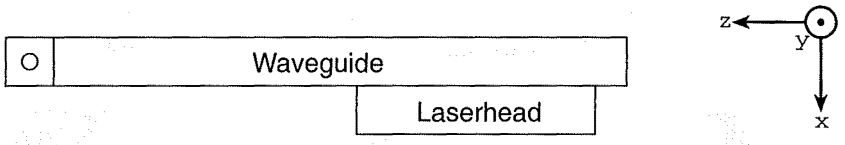

Figure 4.19: Parallel excitation method.

Another possible orientation of the device is shown in figure 4.19. Here a section of one side wall of a primary waveguide is removed and replaced by the laserhead. The energy is then coupled into the laserhead via this side wall. This is potentially a very compact design but does have one limitation compared to the horn excitation method. As the energy is being coupled into the laser from the side, the laserhead sees two and a half guide wavelengths which results in five distinct bright regions in the discharge as opposed to a single sinusoidal pattern produced by the horn. This pattern is therefore far from the uniform brightness discharge which is optimal.

The V3 cavity

The third V3 design was an attempt to incorporate the successes of the V1 and V2 designs while adding a number of features to make the cavity more versatile and user-friendly. This design, shown in figure 4.21, also incorporates the quartz dielectric for increased discharge uniformity. The optical configuration in this design is similar to the V1 design in that the mirrors are mounted almost directly on the ends of the infrared waveguide. Unlike the V1 design these mirrors are completely internal to the cavity so that their alignment is not affected by the presence of a vacuum.

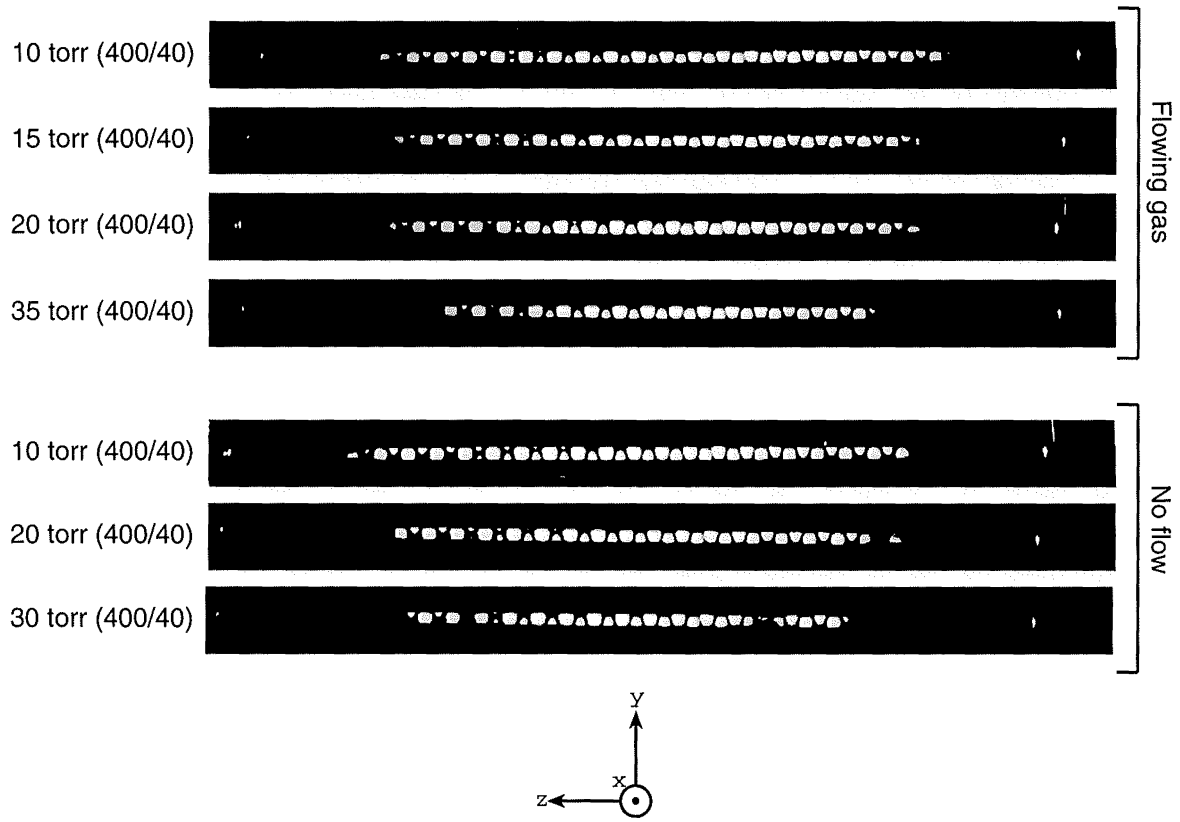

Figure 4.20: Microwave induced discharge in the aluminium V2 cavity as viewed from the side of the laser through the perforated metal microwave shield. The vertical (y) axis has been scaled by a factor of three with respect to the horizontal (z) axis. The numbers in brackets represent the period and pulse length respectively.

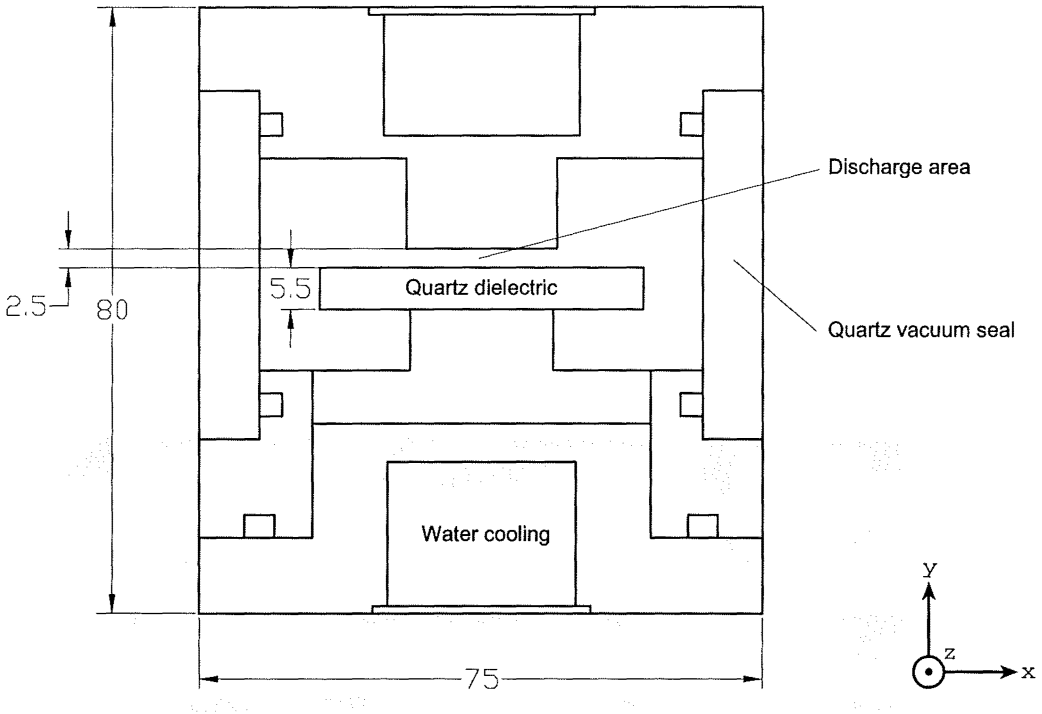

Figure 4.21: Scale cross section of the V3 laser.

Photographs of the V3 cavity discharge are shown in figure 4.22. The dark lines that run through the centre and just left of centre are due to vertical alumina rods which obscure the discharge. These rods prevent the laserhead from bending under pressure and ensure that the quartz slab is held firmly in place. The discharges created using this design are an obvious improvement over those produced by the brass (V1) cavity. It has a reasonably uniform glow which fills most of the length of the cavity. Once again higher pressure ($\sim$ 50 torr) operation is possible although the discharge has contracted to unuseably small regions. Higher duty cycle pulses tend to obscure drops in field intensity, however these are still present. The bright regions near the ends of the cavity are most likely the result of high fields due to end effects of the microwave cavity. Obviously the cavity cannot be a closed rectangular shape because of the requirement to situate mirrors very close to the end of the electrodes. Discharges with better filling of the available area are possible by tuning the cavity for a specific set of operational parameters (pressure, pulse length etc).

4.8 Resonant cavity approach

In the previous section, the high electric field required to cause a discharge was started by setting up a standing wave throughout the entire waveguide. When the discharge lights the wave becomes more of a travelling wave (still significant reflection). Another approach to cavity excitation is the resonant cavity approach where the laserhead is made into a resonant cavity which is tuned as closely

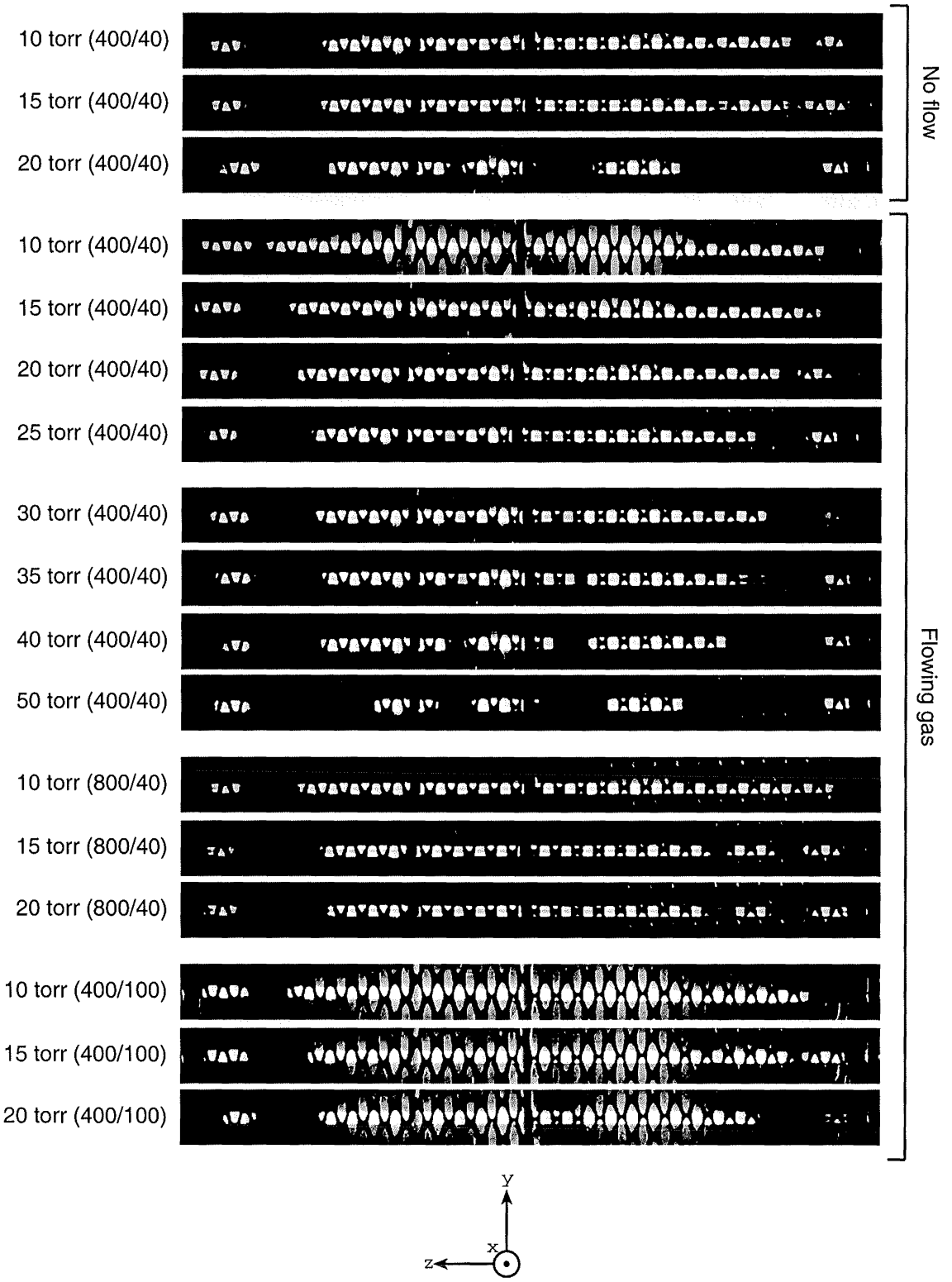

Figure 4.22: Microwave induced discharge in the brass V3 cavity as viewed from the side of the laser through the perforated metal microwave shield. The vertical axis (y) has been scaled by a factor of three with respect to the horizontal (z) axis. The numbers in brackets represent the period and pulse length respectively.

as possible to the excitation frequency of the magnetron. In this method the standing waves are confined to the laserhead at all times and the power fed in via a primary coupling guide. The laserheads can be viewed as ridge waveguides which have been studied extensively for specialist transmission applications [17]. The ridge waveguide has the general form shown in figure 4.23 and comes in two varieties, single and double ridged. In transmission applications ridge waveguides are characterised by lower cutoff frequencies, lower impedance and wider bandwidth. They are often used as filters, terminators, matching elements or where a wide frequency range is required in a single transverse mode. One unfortunate consequence of the ridge waveguide for microwave applications is that under certain conditions the central "ridge" section can develop very high electric fields, often enough to cause breakdown, a clearly undesirable feature in any power transmission waveguide. This "unfortunate" consequence can be exploited here to produce a discharge suitable for laser excitation between the ridges. A resonant microwave cavity, much like its electrical equivalent the LRC circuit, will oscillate with a high field when driven at its resonant frequency.

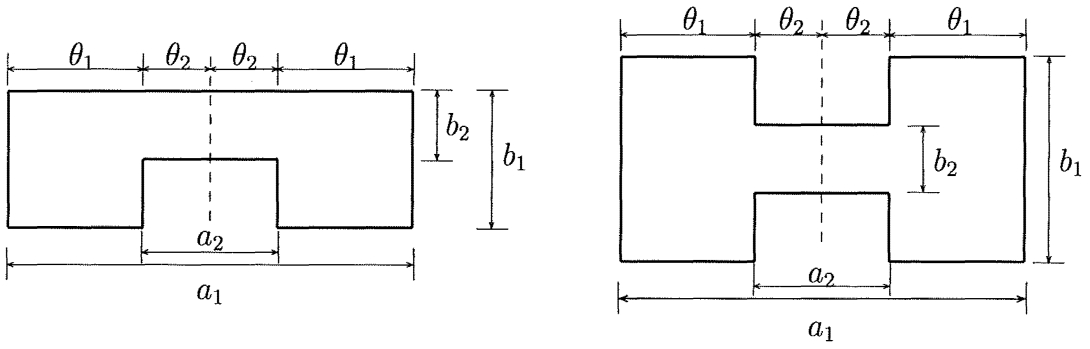

Figure 4.23: The ridge waveguide. (a) single ridge guide, (b) double ridge guide.

4.8.1 Resonant cavity design

The approximate dimensions for a cavity which will resonate at 2.45 GHz can be estimated from Hertz's approximation for a resonant loop,

$$f = \frac{c}{7.94D} \tag{4.22}$$

where D is the diameter of the loop. For 2.45 GHz the approximate value of D is 2×10^{-2} m. So a resonant cavity is expected to have characteristic cross-sectional dimensions of a few centimetres.

In order to describe the resonant frequency of the V1-V3 laserheads in a ridge waveguide configuration, The cavity is modelled using the duality principle [58] to supply equivalent inductances and capacitances for regions in the waveguide. A waveguide structure is capacitive when it consists of two closely spaced plates which are perpendicular to the electric field lines. The centre or ridge section of

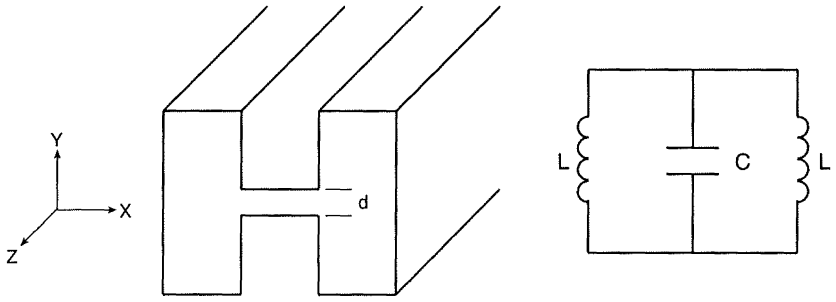

Figure 4.24: LC circuit representation of a double ridge waveguide.

figure 4.24 can be considered as a capacitor. The capacitance can be estimated in the same way as a conventional capacitor,

$$C = \frac{\epsilon_0 A_{xz}}{d} \tag{4.23}$$

Inductances (the dual of capacitance) arise from tall sections in a guide which enclose significant cross sectional area. The "wings" of the ridged guide in figure 4.24 can be modelled as single turn coils having an inductance given by,

$$L = \frac{\mu_0 A_{xy}}{l_z} \tag{4.24}$$

Thus, the ridge waveguide shown in figure 4.24 can be modelled by two inductors in parallel with a capacitance. The resonant frequency of the cavity can now be found using the standard electrical resonance formula,

$$f = \frac{1}{2\pi\sqrt{LC}} \tag{4.25}$$

In the notation of figure 4.23, L and C are given by,

$$C = \frac{\epsilon_0 a_2 l_z}{2b_2} \quad \text{and} \quad L = \frac{\mu_0 (a_1 - a_2) \cdot b_1}{l_z} \tag{4.26}$$

an the resonant frequency given by equation (4.25) is thus,

$$f_r = \frac{c}{\pi\sqrt{\frac{a_2(a_1-a_2)b_1}{b_2}}} \tag{4.27}$$

Note that in this analysis end-effects and field perturbations which arise from the sudden changes of height of the cavity are ignored, and although the variable l_z cancels out in this model, in practice the resonant frequency is affected by it, albeit at second order. This means that the resonant frequency arrived at for this cavity will be an approximate value only. However, a more detailed analysis is neither useful nor required due to the variable effect the plasma will have on

the system. The impedance which the discharge adds to the system is ignored as well as any screening effects it may introduce. In practice, instead of modelling the entire system it is better to design to an approximate geometry and then make small changes to either the frequency of the microwave generator or the dimensions of the cavity until it becomes resonant.

4.8.2 Resonant cavity modifications

The three laserheads are now examined for possible adaption to resonant cavities. The modification involves closing up the cavity into a waveguide by placing conducting walls on the outside of the quartz vacuum seals. As a result the cavity becomes a sealed section of waveguide. In order to excite the cavity a slot is cut down the centre of one of these walls and used to couple radiation from a secondary guide as shown in figure 4.25. Note that in theory these walls could have been located inside the vacuum, however, this is likely to cause unwanted discharges in the coupling slit due to the high local electric field.

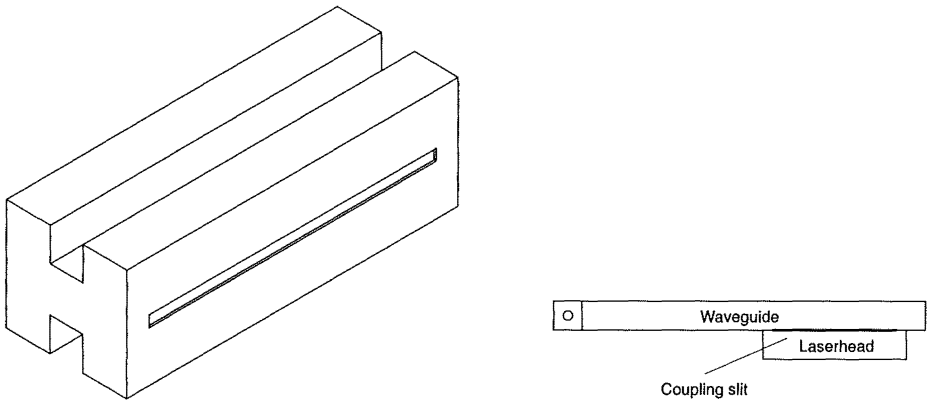

Figure 4.25: (a) Resonant waveguide and coupling slit. (b) Resonant waveguide excited by another waveguide.

The V1 cavity can be analysed using equation (4.27) and figure 4.23b. Using the following parameters: $a_1 = 50\,\text{mm}$, $a_2 = 32\,\text{mm}$, $b_1 = 45\,\text{mm}$, $b_2 = 2\,\text{mm}$, the resonant frequency is,

$$f_r = 0.8\,\text{GHz} \tag{4.28}$$

The analysis of the V2 cavity is slightly more complicated due to the presence of the quartz slab which adds another capacitive element to the circuit, as shown in figure 4.26. The addition of this series capacitance with relative permittivity ϵ results in the resonant frequency being given by,

$$f_r = \frac{c}{\pi\sqrt{\frac{\epsilon a_2(a_1-a-2)b_1}{\epsilon b_a+b_q}}} \tag{4.29}$$

Using parameters of $a_1 = 50\,\text{mm}$, $a_2 = 20\,\text{mm}$, $b_1 = 14\,\text{mm}$, $b_a = 2\,\text{mm}$, $b_q =$

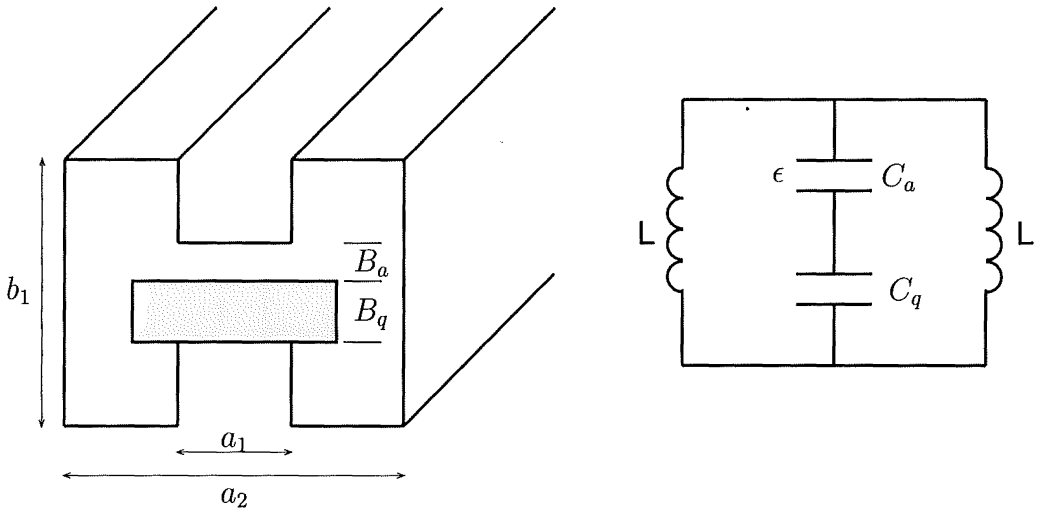

Figure 4.26: LC circuit representation of a double ridge waveguide with dielectric element as shown in figures 4.18 and 4.21.

5.5 mm and using a value of 3.85 for ϵ [62] the resonant frequency is,

$$f_r = 1.7\,\text{GHz} \tag{4.30}$$

where b_a and b_q are the heights of the 'air' and quartz gaps respectively.

A similar analysis is valid for the V3 cavity of figure 4.21. In this case, the parameters are $a_1 = 70\,\text{mm}$, $a_2 = 20\,\text{mm}$, $b_1 = 30\,\text{mm}$, $b_a = 2\,\text{mm}$, $b_q = 5.5\,\text{mm}$ and the resonant frequency is,

$$f_r = 1.0\,\text{GHz} \tag{4.31}$$

Obviously none of the above designs are candidates for modification to a resonant cavity as the changes in dimension must be quite large, as a result of the presence of the square root in the frequency formula. The changes in dimension are also limited by the need to have the coupling slit outside the vacuum as detailed above. In summary, a completely new design is required to utilise a resonant cavity. Such a design is presented in figure 4.27.

This model is described by the parameters $a_1 = 40\,\text{mm}$, $a_2 = 12\,\text{mm}$, $b_1 = 20\,\text{mm}$, $b_a = 3\,\text{mm}$, $b_q = 5.5\,\text{mm}$ and has a resonant frequency given by,

$$f_r = 2.5\,\text{GHz} \tag{4.32}$$

Although this cavity should result in a near resonant cavity it was not built for several reasons. It would not easily interface to our current waveguide feeders; for lasing purposes it would require custom optics and it has a limited number of free parameters. The discharge gap and width are set by cooling and optical requirements. The resonance, and other conditions such as cutoff, impose constraints giving the device very little flexibility for experimentation. A tunable microwave source would have been required for the device to be properly investigated.

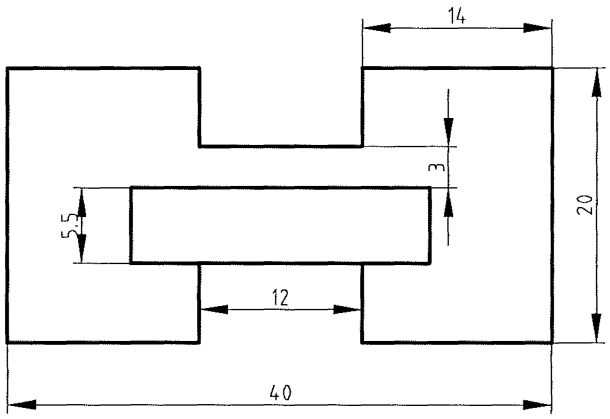

Figure 4.27: A new resonant cavity design.

4.9 Limitations

Although the microwave excitation approach used here results in some reasonably uniform discharges it is not an optimal solution especially when compared to its RF cousins.

All the designs presented above, including those from the literature described in the introduction, suffer from one fundamental restriction: the 16 cm wavelength of microwaves at 2.45 GHz. Any microwave cavity which is more than a few centimetres in length will house a significant fraction of a wavelength (if not many wavelengths). This means that due to the build up of transverse mode patterns and standing waves it is very difficult to get a uniform electric field. A non-uniform electric field results in a non-uniform discharge and therefore inefficient use of the available gain volume. Moreover, sections of extremely high field can result in gas heating and high rates of unwanted reactions such as dissociation, all of which are detrimental to the lasing process. The horn waveguide presented in this work goes some way towards creating a more uniform discharge by spreading a single 12 cm sinusoid over 40 cm. The fact still remains that the electric field profile is not flat.

In summary, while the excitation method developed here is effective, especially at low pressures, it would appear that due to the relatively small wavelength of microwaves compared to radio-frequency waves, a clever design will be required to achieve the discharge uniformity now possible in today's RF excited CO_2 lasers.

Chapter 5

Optics

The optics of a laser are the elements which harness the population inversion in the gain medium and couple the radiation out of the laser cavity where it can be put to use. Thus, efficient optics are essential for an efficient laser. The optics also have a role in determining the beam characteristics, such as focusability and mode pattern. The output of a high power CO_2 laser is most often used in highly localised heating or vaporisation applications. In these circumstances and many others, it is desirable to have an output beam which has a TEM_{00}-like mode pattern which is highly focusable.

The use of a slab discharge to excite a CO_2 laser brings with it the advantages of area-scaling of output power and compact design. From a Gaussian optics point of view, it is not obvious that such geometries lead to good beam quality. However, with the advent of the *waveguide laser* pioneered by Marcatili and Schmeltzer [56] it was shown that the waveguide geometry and good beam quality are compatible goals.

It should be stressed that the waveguiding referred to in this chapter relates to the waveguiding of infrared laser radiation and has no interaction with the microwave waveguiding being used to excite the discharge.

5.1 Waveguide lasers

An optical cavity in a laser may be said to be waveguiding when the optical mode passing through the gain medium is occluded to such a degree that the resonator modes are no longer the familiar Gaussian beams described by Kogelnik and Li [46] or those described by the numerical approach of Fox and Li [24]. The modes in these cavities are now being guided (in the waveguide sense) by the geometry through which they are passing.

A general optical waveguide resonator is shown in figure 5.1. Waveguide resonator refers to the whole optical cavity, including the end mirrors and free space as well as the centre section in which waveguiding occurs. Such resonators will have a set of *resonator modes* (self repeating field distributions) with associated round trip losses and resonant frequencies. An optical resonator may be said

to be waveguiding when the free space modes are significantly perturbed by the aperture of the waveguide. In practice the free space mode is said to be obstructed when the guide Fresnel number N satisfies $N < 1$ or when $a^2/\lambda L < 1$. Alternatively one can say that the beam is obscured if the $1/e^2$ beam intensity width of any free space mode is approximately the guide width.

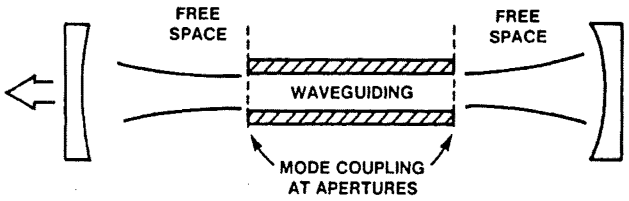

Figure 5.1: Schematic of a general waveguide resonator.

5.1.1 Waveguide propagation

Resonators which have their free space modes obscured possess a set of *waveguide modes* which are the solutions to Maxwell's equations with the new boundary conditions imposed by the waveguide. The lowest order waveguide mode for a rectangular waveguide is called an EH_{11} mode and its mode pattern has a 98% power overlap [1, 35] with the free space mode TEM_{00}. These solutions represent modes of the waveguide which are field patterns that keep their shape, but experience a mode dependent phase shift while propagating inside the guide. Typical guides in waveguide lasers have half-widths or radii of $a \simeq 100\lambda$ so it may be assumed that $a > \lambda$ and terms of order λ/a and higher can be removed. This reduces the complex formulae for the field amplitudes to first order ones. However, the corresponding simplified propagation constants include the essential terms of order λ/a and $(\lambda/a)^2$. Propagation of a waveguide mode along the guide z-axis may then described by $\exp(ikz)$ where $k = \beta + i\alpha$, β is a phase constant and α is an attenuation constant.

5.1.2 Field expressions

Although the waveguides used in this study are all rectangular, many of the early results in the field were formulated and explained in terms of circular geometries. For this reason expressions for circular guides are included. The values for mode losses under rectangular geometries are also of the same form as the losses found when circular coordinates are used. Generally there is little to be gained from recalculating these values under rectangular coordinates.

Circular guides

The first order field for the waveguide modes are given by,

$$E_{nm} = f_{nm} \mathrm{J}_n(\rho_{nm} r/a) \cos(n\psi) \quad 0 \leq r \leq a \tag{5.1}$$

where ρ_{nm} is the m^{th} root of the n^{th} order Bessel function, $\mathrm{J}_n(\rho_{nm}) = 0$ and

$$\begin{aligned} f_{nm} &= \sqrt{2}\left[\sqrt{\pi}a\ \mathrm{J}_{n+1}(\rho_{nm})\right]^{-1} && \text{if } n = 2, 3, 4, ... \\ &= \left[\sqrt{\pi}a\ \mathrm{J}_1(\rho_{om})\right]^{-1} && \text{if } n = 0 \end{aligned} \tag{5.2}$$

The normalisation and propagation constants are given by,

$$\int_0^{2\pi} \int_0^a \mathrm{E}_{nm}(r, \psi)\mathrm{E}_{n'm'}(r, \psi)\ r dr\ d\psi = \delta_{nn'}\delta_{mm'} \tag{5.3}$$

$$\beta_{nm} \simeq \frac{2\pi}{\lambda}\left[1 - \frac{1}{2}\left(\frac{\lambda\rho_{nm}}{2\pi a}\right)^2\right] \tag{5.4}$$

$$\alpha_{nm} \simeq \frac{1}{a}\left(\frac{\lambda\rho_{nm}}{2\pi a}\right)^2 \mathrm{Re}[\frac{1}{2}(\epsilon + 1)(\epsilon - 1)^{-\frac{1}{2}}] \tag{5.5}$$

Rectangular guides

Rectangular guides normally exist in two forms: single material or "hybrid" with one or two metal walls. The choice of wall composition is usually related to the excitation method being used. These rectangular guides support two sets of linearly polarised EH_{nm} hybrid modes and will not support circularly polarised modes. The first order fields for the linearly polarised EH_{nm} modes are given by,

$$\mathrm{E}_{mn}(x, y) = \sqrt{ab}\left[\begin{matrix}\cos \\ \sin\end{matrix}\left(\frac{m\pi x}{2a}\right)\right]\left[\begin{matrix}\cos \\ \sin\end{matrix}\left(\frac{n\pi y}{2b}\right)\right] \qquad m, n = \begin{matrix}\text{odd} \\ \text{even}\end{matrix} \tag{5.6}$$

with normalisation,

$$\int_{-a}^{a} \int_{-b}^{b} \mathrm{E}_{mn}(x, y)\mathrm{E}_{m'n'}(x, y)\ dx\ dy = \delta_{mm'}\delta_{nn'} \tag{5.7}$$

The propagation constants $k_{mn} = \beta_{mn} + i\alpha_{mn}$ are given by,

$$\beta_{mn} \simeq \frac{2\pi}{\lambda}\left[1 - \frac{1}{2}\left[\frac{m\lambda}{4a}\right]^2 - \frac{1}{2}\left[\frac{n\lambda}{4v}\right]^2\right] \tag{5.8}$$

and for x-polarised modes,

$$\alpha_{mn} \simeq \frac{m^2}{a}\left[\frac{\lambda}{4a}\right]^2 \mathrm{Re}(\epsilon_a(\epsilon_a - 1)^{-\frac{1}{2}}) + \frac{n^2}{b}\left[\frac{\lambda}{4b}\right]^2 \mathrm{Re}((\epsilon_b - 1)^{-\frac{1}{2}}) \tag{5.9}$$

where $2a$ is the width of the guide, $2b$ is the height and ϵ_a and ϵ_b are the relative permittivities of the horizontal and vertical walls respectively.

5.1.3 Resonator Modes

A waveguide resonator may be thought of as a free space resonator perturbed by a waveguide aperture or as a waveguide perturbed by free-space sections. A resonator mode, like a waveguide mode, is a field distribution which repeats itself in shape and phase after one round trip of the resonator.

Consider a free space or Gaussian resonator with two spherical mirrors which has its maximum field density near the axis and the dominant variation being the the axial propagation term $\exp(ikz)$. These are the TEM_{pq} free space modes of propagation. Their transverse shape is given by a simple Gaussian $\exp(-r^2/w^2)$, multiplied by Laguerre polynomials in cylindrical coordinates or Hermite polynomials in Cartesian coordinates. A common beam waist position z_0 and a common waist radius w_0 can then be defined for a whole orthonormal set of beams. The free-space field E_{fs} can then be expressed anywhere along the resonator axis as a linear combination of Gaussian beams,

$$E_{fs} = \sum b_{pq}\Psi_{pq}(z - z_0, w_0) \tag{5.10}$$

$$b_{pq} = \int E_{fs}\Psi^*_{pq}\, dA \tag{5.11}$$

where the Ψ_{pq} are the TEM_{pq} functions including the z dependent amplitude and phase factors and the integral is performed over the infinite cross-section through the axis. The b_{pq} are complex coefficients, which, during lossless free-space propagation do not depend on the axial position z. This analysis may be likened to a Fourier decomposition.

Resonator modes must be one of the self-repeating transverse modes of the cavity and the mode frequency must have an axial resonance. Two transverse mode numbers r and s and one longitudinal mode number j can be assigned where j is the number of 2π phase shifts in the cavity. A general resonator mode frequency can be written $\nu_{j,rs}$, for most real lasers $j > 10000$ and $r, s < 10$.

The above resonator mode conditions can be represented symbolically by a complex eigenvalue equation,

$$ME_{fs} = \gamma E_{fs} \tag{5.12}$$

where the round trip loss is $1 - |\gamma|^2$ and the relative phase shift is $\arg(\gamma)$. In practice equation (5.12) is difficult to solve. However, a judicious choice of w_0 and z_0 can minimise the number of off-diagonal terms in M.

5.1.4 Coupling and mode losses

In order to examine the effectiveness of a waveguide mirror combination (resonator) it is necessary to know how the guided radiation couples to the free-space section between the guide and the mirror (see figure 5.2). The amplitude coupling coefficient between EH_{11} and Ψ_{pq} is given by the overlap integral $c_{11} = \int \mathrm{E}_{11}\Psi^*_{pq}dA$ where the integral is performed over the interface between

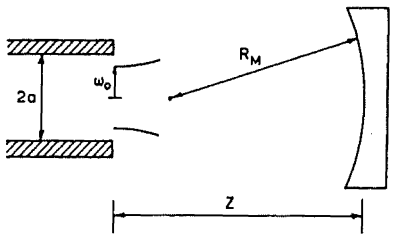

Figure 5.2: Waveguide and curved mirror.

the guide and free-space. The modulus squared of this quantity is the coupling efficiency. Of more use is the amplitude self-coupling coefficient. That is the amount of, say, EH_{11} which re-enters the guide after reflection from the mirror. This value is calculated by the overlap integral of E_{11} with the return field due to a launched E_{11} mode. A self coupling loss may then be defined for E_{11},

$$\Gamma_{11} = 1 - |c_{11}|^2 \tag{5.13}$$

In order to find the fields necessary to calculate these coefficients diffraction theory can be used or a linear combination of Ψ_{pq} can be tracked. This is not an easy task. The coupling efficiency for a certain combination of waveguide modes ($\sum a_{mn}\mathrm{E}_{mn}$) is not generally the weighted sum of the individual coupling efficiencies ($\sum |a_{mn}|^2|c_{mn}|^2$). This means that a multimode approach is necessary for all but the simplest of resonators. However a single-mode approach does provide some good physical insight into resonator design.

5.1.5 Single mode - first order theory

Although this approach does not lead to accurate results when applied to specific laser designs it does give a good qualitative description of the properties of certain configurations. The early work [1, 2, 20] on this subject established that there are three resonator configurations which have low coupling losses for the EH_{11} mode. For a circular guide of radius a where $E(r)$ is the field launched into the guide and $E'(r)$ is the returned field equation (5.13) may be rewritten as,

$$\Gamma_{11} = 1 - \left| \int_0^a E(r)E'(r)2\pi r \, dr \right|^2 \tag{5.14}$$

Figure 5.3 shows the value of this integral for a range of mirror curvature and spacing. The parameter α is given by ka^2/R_M and the γ value of 11 implies a mirror radius or half-width of $11a$. Note that the γ value of 11 is a coincidence and not related to the subscripted "11" which implies the mode numbers $n = 1$, $m = 1$. Three low loss configurations exist and have been named [20],

Case I	Large R mirrors very near the guide ($z \sim 0$, $z/R \sim 0$)
Case II	Large R mirrors centred near the guide entrance ($z \sim R$)
Case III	Mirrors with $R \sim 2b$ and $z \sim b$, where $b = \pi\omega_0^2/\lambda$

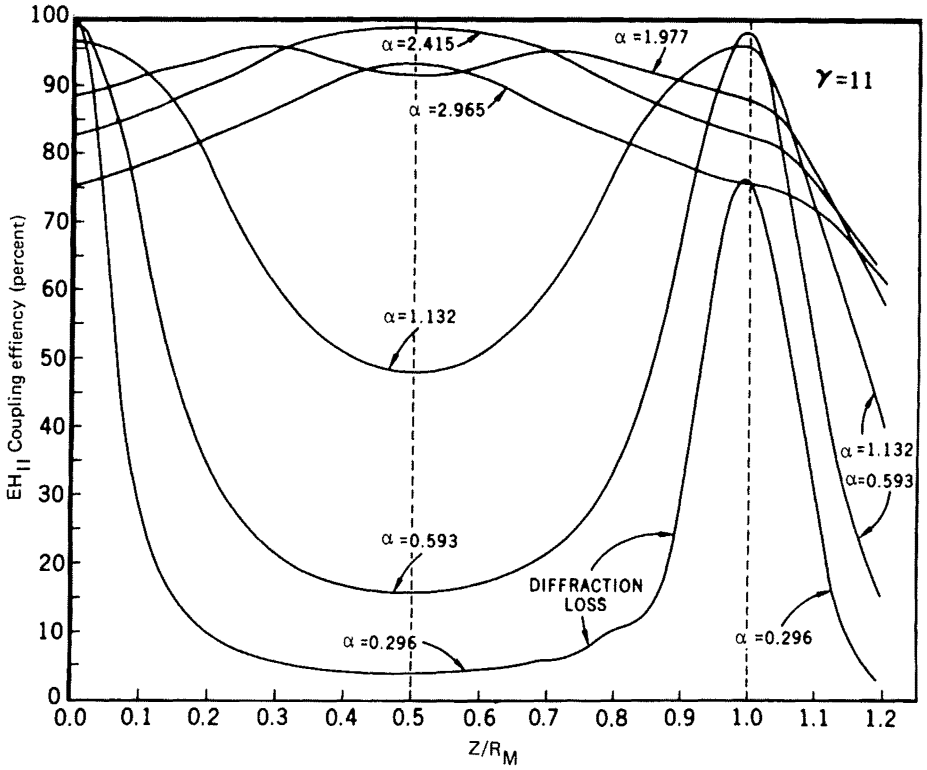

Figure 5.3: EH_{11} coupling losses as a function of distance and curvature of the mirror. (from [20])

The parameter b is the Rayleigh range of the EH_{11} modes approximating Gaussian. Schematics of the geometry for each case are shown in figure 5.4.

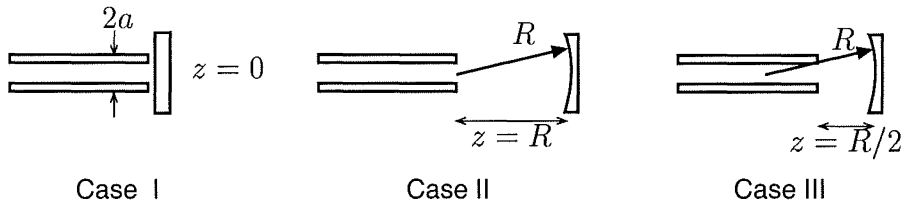

Figure 5.4: Three low loss coupling configurations for the fundamental waveguide mode. (Not to scale)

Case I

Case I is a simple and effective design in which the end mirror is placed as closely as possible to the waveguide. The simplicity and low coupling losses make this the favoured design for commercial waveguide lasers. In this situation the resonator exhibits nearly pure waveguide characteristics and all modes have low coupling losses.

Case II

Case II is a far-field phase-matched mirror, that is, the curvature of the mirror is chosen so that it matches the phase of the wave at a sufficient distance from the waveguide for the wavefront to be spherical. In this configuration any waveguide mode has a low coupling loss. This design is rarely used due to its poor mode discrimination and the complication of large z.

Case III

Case III is similar to Case II except that the mirror is positioned in the near-field. The term near-field is used to describe distances where the curvature of the exiting modes has not yet become spherical. This means that a near-field phase matched mirror will not couple all modes back efficiently. For a circular guide estimates [20] put $\Gamma_{11} \sim 1.38\%$ and $\Gamma_{12} \sim 78\%$ leading to excellent mode discrimination. It is the obvious choice where single, fundamental, mode behaviour is required.

5.1.6 Optics for slab lasers

The move from circular and square geometries to the rectangular slab configuration also requires a change in the optics [57, 48, 12]. Typical slab lasers have a discharge area with aspect ratio 8:1 width to height. This results in a discharge

width of the order of 20 mm. The approximate field descriptions for these wide cavities can be obtained by letting a or b tend to infinity in equation (5.6). This results in TE and TM waves respectively. For example, the transverse electric TE_m ($m \geq 0$) modes are of the form,

$$E_y = \left\{ \begin{array}{l} \cos \frac{(m+1)\pi x}{2a} \\ \sin \frac{(m+1)\pi x}{2a} \end{array} \right\} e^{i(\gamma_m z - \omega t)} \qquad \begin{array}{l} (m+1) \text{ odd} \\ (m+1) \text{ even} \end{array} \tag{5.15}$$

$$H_x = \sqrt{\frac{\epsilon_0}{\mu_0}} E_y \tag{5.16}$$

$$H_z = O\left(\frac{\lambda}{a}\right) \tag{5.17}$$

where $O(x)$ denotes a term of order x.

5.2 Optics design for a microwave pumped CO_2 laser

The optics used for this laser project differ slightly from the standard design used in RF lasers in that the side walls of the optical waveguide can be omitted on the V1 and V3 lasers. This means that there is no longer any waveguiding in the x-dimension. Such guides have been analysed [61, 67] and do not exhibit markedly different characteristics from the hollow slab guides above.

Both the V2 and V3 lasers replace one aluminium wall of the waveguide with one made of quartz. It it worth considering what effect this has on the properties of the guide. The reflectivity of quartz at normal incidence for 10.6 μm radiation is approximately 18% [66], much less than aluminium which is 98% (at 20-60°). The comparatively low reflectivity of quartz does not lead to severe attenuation in the waveguide. This is because the reflectivity of a surface at glancing angles ($\theta_i \rightarrow 90°$) goes to one by virtue of the Fresnel equations [34]. For this to be the case the surface must be flat so that specular reflection occurs. This requirement is easily met by the quartz slab which is optically flat and therefore more than sufficient at infrared wavelengths. For the other metal walls, a fine machine finish [85] is required to give efficient waveguiding properties. Generally, polishing is not necessary but may be convenient for other reasons such as alignment.

Regardless of the composition of the top and bottom walls, the side walls must be made from an insulator (ceramic), so that the electrodes are electrically separated in the case of RF and so that radiation can enter the discharge cavity in the microwave case. These ceramics often provide mechanical stability for the laserhead in addition to their electrical properties.

5.2.1 V1 optics

The basic optical design for the V1 (and V3) laser is shown in figure 5.5. The design is a Case I resonator consisting of a near total reflector at one end mounted

very close to the waveguide section in which the discharge occurs. On the other end of the waveguide is an output coupler which is also mounted close (< 2 mm) to the exit of the guide. The waveguide consists of two polished surfaces of brass. The mirror is a > 99% silicon, germanium or gold reflector, 25.4 mm in diameter. Two curvatures of this mirror were used: 3 m and flat. The gold mirrors used were glass coated with a layer of gold. While not as robust as commercially produced optics, these gold mirrors are relatively easy to make by flashing gold on to existing one inch glass optics. Having a mirror on a glass substrate obviously limits its ability to dissipate heat, however there has been no visible damage due to overheating shown in experiments to date. If this were to become a problem, a metallic substrate could be used - water cooled if necessary. The output coupler was a flat anti-reflection coated zinc selenide (ZnSe) mirror with 5% transmission and 0.08% absorption. Although zinc selenide is more expensive than the equivalent germanium and silicon mirrors it has the advantage of being transparent over part of the optical spectrum. This allows the use of a helium neon laser for the alignment of the mirrors.

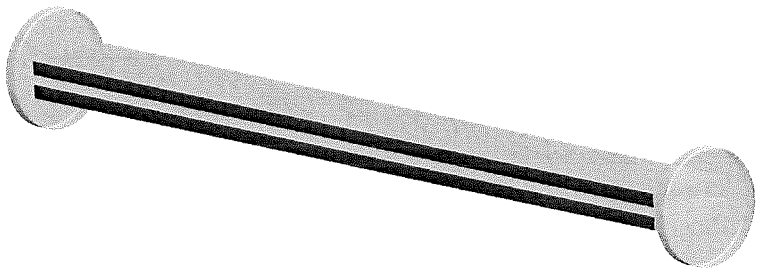

Figure 5.5: Basic optical design used in the V1 and V3 lasers.

The radius of curvature of the mirrors in gas lasers is in general large so that the highest possible fraction of the available gain medium is utilised. Often there is a trade off between maximising the gain volume and the optical stability of the system. Usually it is very difficult to align lasers which border on instability and a flat-flat configuration, although not actually unstable [24], is unlikely to lase at optical frequencies. However the waveguiding nature of the optical cavity means that small misalignments in the vertical direction can be tolerated. Even so, aligning the flat-flat configuration on the V1 laser was very difficult due the mirrors being mounted on the vacuum seal.

The EH_{11} coupling loss for a flat mirror in this Case I configuration is given [20] to a good approximation by,

$$\begin{aligned} \text{fractional loss (flat)} &\simeq 6.05\left(\frac{d}{ka^2}\right)^{\frac{3}{2}} \quad \text{for} \quad \frac{d}{ka^2} \lesssim 0.1 \qquad (5.18) \\ &= 6.05\left(\frac{d\lambda}{2\pi a^2}\right)^{\frac{3}{2}} \\ &= 0.1\% \end{aligned}$$

where the condition $d/ka^2 \lesssim 0.1$ is easily satisfied. Therefore a flat-flat setup therefore has low coupling loss and should allow lasing given suitable population inversion.

5.2.2 V2 optics

The V2 laser was originally designed to examine discharge properties when a dielectric slab was added. Its simple design makes it robust and easy to manufacture, however because of the location of the main o-ring (see figure 3.7) it is not a simple matter to incorporate optics. The only realistic solution is to use an L-shaped cavity, see figure 5.6, in which a 45° total reflector is added to the resonator so that the exit beam is now perpendicular to the waveguide. A U-shaped cavity is also a possibility but this would require an additional internal mirror. Such mirrors must be of the order of 3 mm in height which makes them difficult to manufacture and awkward to mount and align.

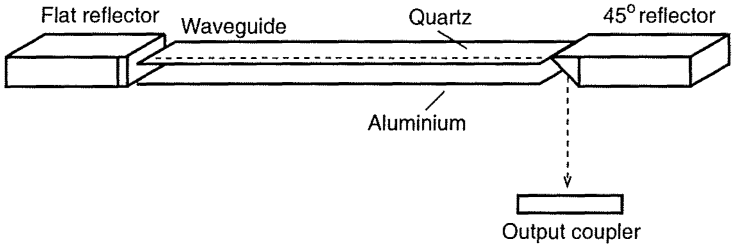

Figure 5.6: L-shaped optical optical cavity for the V2 laser.

The problem with this design is that the waveguide does not extend all the way to the output coupler. This means that there will be significant diffraction from the waveguide exit using the same mirror curvatures. If the beam 'diameter' D at the exit of the waveguide is assumed to be 2 mm and the distance z from the waveguide to the mirror is 25 mm, then the beam diameter when it returns to the waveguide can be calculated by assuming a diffraction limited beam. The diffraction angle is given by,

$$\theta_D \simeq \frac{\lambda}{D} \tag{5.19}$$

$$= 5.3 \times 10^{-3} \tag{5.20}$$

and diameter D' of the beam after it is reflected back onto the waveguide is then,

$$D' \simeq D + 2 \cdot 2z \tan\theta_D \tag{5.21}$$

$$\simeq D + 4z\theta_D \tag{5.22}$$

$$\simeq 2.5\,\text{mm} \tag{5.23}$$

This means that a significant amount of the beam will be occluded as it reenters the waveguide. Hence, without even considering the mode coupling between the

two regions, it can be seen that such a configuration will not lase due the losses involved.

In order to limit the losses in this situation the output coupler needs to be a mirror with a small radius of curvature. If the curvature of the mirror matches the curvature of the beam on the surface of the mirror then the beam should be reflected back along the path it came. This implies the use of a Case II or Case III resonator. The Case II resonator requires that the mirror is positioned in the far-field and for a guide height of 2 mm, this distance is of the order of one metre [20, 5] which would be awkward in most experimental situations. The Case III configuration offers the best solution. For a 2 mm discharge gap, a mirror with radius of curvature $\sim$ 30 cm should be placed $\sim$ 15 cm from the guide. This corresponds to $\alpha \simeq 2.4, z/R_M = 0.5$ in figure 5.3. Notice that small changes in mirror placement (z/R_M) make little difference to the coupling loss. Under optimum conditions coupling losses in this configuration are 1.4%. In addition, the Case III design has the previously mentioned benefit of good mode discrimination.

This optical design was not tested due to the lack of available ZnSe optics of this type.

5.2.3 V3 optics

The geometry of the V3 optics is similar to that of the V1 laser except that the mirrors have been situated inside the laser cavity so that they are no longer part of the vacuum seal. This makes alignment a simpler process and means that small modifications to the discharge cavity can be made without having to realign the mirrors. This design, like the V2 design, also incorporates a quartz dielectric as one of the walls of the waveguide. The internal positioning of the mirrors meant that the laser could be aligned much more accurately. Unlike the V1 laser, aligning a flat-flat configuration was reasonably straight forward.

5.3 Unstable optics

While the Case I configuration is a simple, compact design with efficient utilisation of the gain volume, in general, without special measures being taken it leads to poor mode quality due to the lack of any mode discrimination. One method to retain high quality output while utilising the entire gain volume and keeping the optics compact is to use an unstable resonator [96]. An unstable resonator in a slab laser configuration is shown in figure 5.7. The two mirrors are total reflectors with the radiation being coupled out of the cavity via a small gap on the edge of the convex mirror. Lasers using this technique [44, 68] have produced nearly diffraction limited output beams.

The problem with these types of optics, especially in the case of a slab laser, is

that they are difficult to manufacture (or buy) and alignment is often awkward. This is because such optics have to be designed to fit the laser rather than being off-the-shelf components.

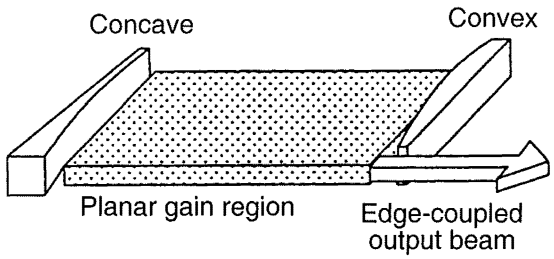

Figure 5.7: Slab waveguide employing an unstable resonator.

Chapter 6

Microwave-excited CO_2 laser discharges

This chapter examines the characteristics and behaviour of a microwave-excited discharge in CO_2 laser gas. A working definition of the terms DC, RF and microwave, in the CO_2 laser context, is required. It is assumed that,

- **DC-excitation** - refers to excitation by a constant potential. In fact, most 'DC' devices will operate at low frequency AC, typically 50 Hz or some multiple of the mains frequency. At these frequencies the electric field oscillates so slowly that there are no significant differences in the discharge characteristics from an actual DC potential (apart from making the discharge symmetrical to the eye). These slow oscillations help to make the electrodes wear more evenly.

- **RF-excitation** - refers to excitation in the range 1 - 300 MHz. RF-excited discharges behave in significantly different ways to DC discharges.

- **Microwave-excitation** - refers to excitation at frequencies above 1 GHz. Microwave-excited discharges share many characteristics with their RF counterparts.

The fundamental difference between DC- and RF- (or microwave) excited discharges is in the motion of the electrons in the plasma. In a DC discharge electrons are accelerated at a constant rate. In an RF discharge the electrons oscillate with the electric field. This leads to new discharge features. The physical geometries used to exploit these excitation mechanisms also differ significantly. DC lasers are usually excited longitudinally, that is, the electric field is applied across the long axis of the laser, whereas RF lasers are usually transversely excited (ie perpendicular to the long axis).

6.1 The high frequency advantage

Gas discharges excited by high frequency electromagnetic fields have a number of advantages over DC-excited discharges,

- In DC systems ignition (peak) voltages are often of the order of 15 kV for metre length tubes. As the output power in a DC laser is directly proportional to the tube length any increase in length must be accompanied by an increase in ignition voltage. These voltages are often unacceptably high in terms of user safety. RF-excitation avoids this problem by exciting the discharge transversely with electrode spacings often as small as 1 mm. This means the potential difference between the electrodes can be kept at acceptable levels, 400 V is typical.

- RF discharges have a positive voltage versus current slope whereas DC discharges have a negative resistance characteristic. This requires the use of a ballast resistor to make the overall resistance characteristic positive. Typically one third to one half of the power used by such lasers is dissipated as heat in the ballast resistor.

- RF-excited lasers are stable over a wider range of operating conditions (pressure, current, etc) which means that there is more opportunity to manipulate discharge conditions for optimum pumping of the gas.

- RF generators are easily modulated at several kilohertz (audio frequencies). This leads to the precise output power control required for many industrial applications.

- Secondary emission from electrode surfaces is not required to sustain the discharge. Consequently, the laser interior can be made of dielectric materials such as alumina or beryllia which suffer less electrode wear than metal electrodes and are chemically inert leading to long sealed-off lifetimes and are good infrared reflectors.

6.2 DC gas discharges

Before examining the details of a microwave-excited discharge it is useful to review the concepts used to describe DC- and RF-excited lasers. This section follows, for the most part, the definitions and notation of Verdeyen [96] where further details can be found.

An example of a DC discharge is shown in figure 6.1. It shows a strong correlation between the potential and the "dark" and "light" regions of the discharge. These regions are called the cathode "dark" space (dimmer, not dark), the negative glow and the positive column. From figure 6.1c it can be seen that the total current is constant independent of x. However the current is not always carried predominantly by electrons. If the cathode does not emit many electrons then ions must carry most of the current. This requires a large potential to accelerate the comparatively massive ions. If the cathode emits many electrons then the potential required falls to just above the ionisation potential of the gas.

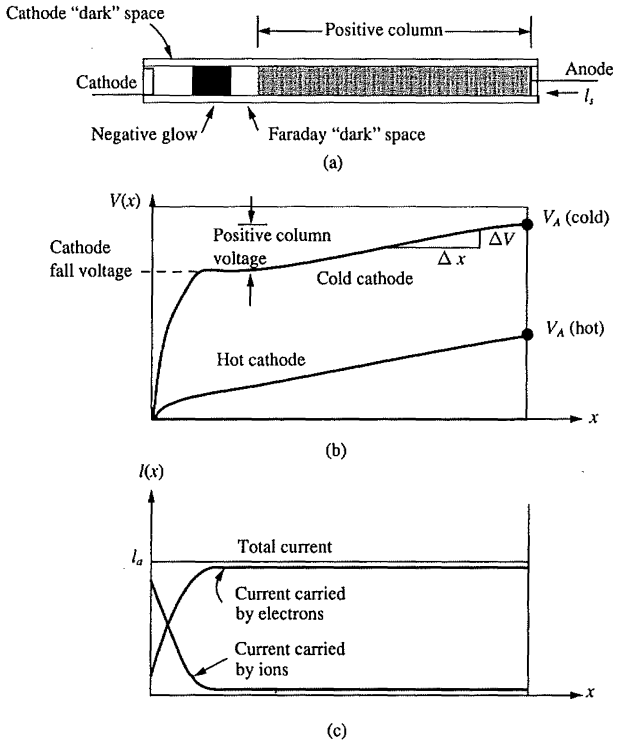

Figure 6.1: Characteristics of a DC discharge

The negative glow is caused by those electrons which have accumulated energy from a significant fraction of the cathode fall potential. These electrons then slow down by exciting and ionising collisions.

In the positive column the E field is constant. It can be shown using Gauss's law that such a region has *space-charge neutrality*. That is, there are equal numbers of negative and positive charges so that the net charge is zero.

6.2.1 The electron gas

In a typical gas laser electron densities range from $10^{10} - 10^{13}\,\mathrm{cm}^{-3}$ for low pressure systems (tens of torr) and $10^{15} - 10^{17}\,\mathrm{cm}^{-3}$ for high pressure systems (atmospheric). Despite this, ionisation seldom exceeds 0.1%.

In the time interval between collisions with atoms or ions, an electron in an electric field will experience a force due to the field,

$$m\frac{dv}{dt} = -e\mathbf{E} \tag{6.1}$$

$$\mathbf{v} = \mathbf{v}_i - \frac{e}{m}\mathbf{E}t \equiv \mathbf{v}_i + \mathbf{v}_{ord} \tag{6.2}$$

where $\mathbf{v}_i$ is the initial thermal velocity which has random orientation with respect to the ordered velocity $\mathbf{v}_{ord}$ induced by the electric field. For n_e electrons the

current is,

$$\mathbf{i} = \sum_{j=1}^{n_e} -e\mathbf{v}_j \tag{6.3}$$

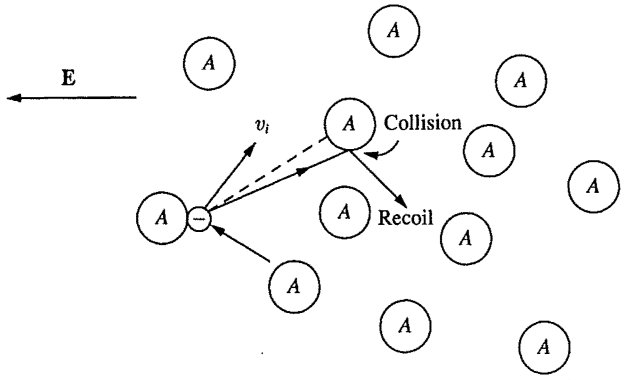

Figure 6.2: Trajectory of a typical electron

To take account of collisional interruptions during the electron's acceleration in the field, equation (6.1) can be modified to include a damping term,

$$m\frac{d\mathbf{w}_d}{dt} = -e\mathbf{E} - m\mathbf{w}_d\nu_c \tag{6.4}$$

where ν_c is the collision frequency for momentum scattering and $\mathbf{w}_d$ represents the average drift velocity of the electrons. For DC fields $\mathbf{w}_d$ is constant and,

$$\mathbf{w}_d = -\frac{e\mathbf{E}}{m\nu_c} = -\frac{e\tau}{m}\mathbf{E} \tag{6.5}$$

where $\tau = 1/\nu_c$ is the mean free time between collisions. The drift velocity per unit electric field is the mobility,

$$\mu_e = -\frac{w_d}{E} = \frac{e}{m\nu_c} = \frac{e\tau}{m} \tag{6.6}$$

The collision rate of the electrons in the gas depends on the number density of scattering atoms (N_A), the size or collision cross-section of the atom (σ_c) and the relative velocity between the atom and the electron. This velocity is almost entirely caused by the random thermal speed of the electron v_{th},

$$\nu_c = N_A\sigma_c v_{th} \tag{6.7}$$

The net electrical current carried by this drift is,

$$\mathbf{J} = n_e e\mathbf{w}_d \tag{6.8}$$

Energy is transferred to the electron gas, via the electric field, at a rate,

$$P_{el} = \mathbf{E}\cdot\mathbf{J} = \frac{n_e e^2}{m\nu_c}E^2 \quad [\mathrm{W/vol}] \tag{6.9}$$

The kinetic energy is related to the $\mathbf{v}$ of equation (6.2) by,

$$E = \frac{1}{2}m\mathbf{v}\cdot\mathbf{v} = \frac{1}{2}m(\mathbf{v}_i^2 + 2\mathbf{v}_i\cdot\mathbf{v}_{ord} + \mathbf{v}_{ord}^2) \tag{6.10}$$

in which the second term averages to zero because of the random orientation of the initial velocity with respect to the electric field. The evolution of the kinetic energy for a single electron is sketched in figure 6.3. It can be seen that the electron gaining energy from the field and undergoing collisions, which are (primarily) elastic, until it has sufficient energy to undergo an inelastic collision in which the internal state of the atom is changed.

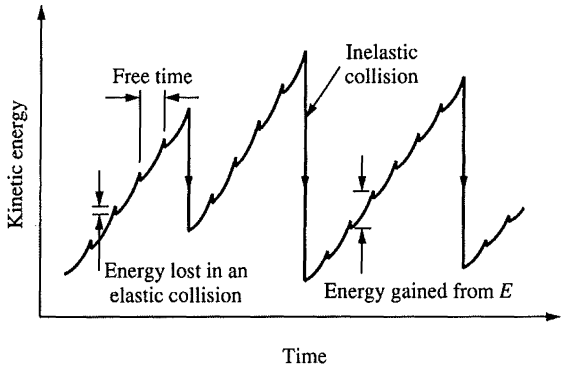

Figure 6.3: Evolution of the kinetic energy of an electron

These concepts can be used to describe how the mean kinetic energy of the electron gas changes with time,

$$\frac{dw_e}{dt} = p_{el} - \underbrace{\nu_c\delta n_e(\frac{3}{2}\epsilon_k - \frac{3}{2}\epsilon_A)}_{\text{gas heating}} - \sum_j \underbrace{n_e\nu_{inel}\Delta W_j}_{\text{excitation}} \tag{6.11}$$

where,

w_e	=	density of electron $\times$ the average energy of the typical electron
	=	$n_e(\frac{3}{2}\epsilon_k)$
ϵ_k	=	a characteristic energy of the electrons (kT_e)
ϵ_A	=	a characteristic energy of the atoms (kT_A)
δ	=	fraction of the excess energy lost per elastic collision = $2m/M$
ν_{inel}	=	inelastic collision rate
ΔW_j	=	energy lost in an inelastic collision

After some algebra and simplifying assumptions, equation (6.11) can be reduced to,

$$\frac{3}{2}(\epsilon_k - \epsilon_A) = \frac{2}{\delta}\frac{1}{2}m\left(\frac{e}{m\sigma_A v_{th}}\right)^2\left(\frac{E}{N}\right)^2 \tag{6.12}$$

which shows that: *The characteristic energy ϵ_k (or temperature) of the electron gas is a monotonically increasing function of the ratio of electric field to neutral*

gas density, or

$$\epsilon_k = f\left(\frac{E}{N}\right) \tag{6.13}$$

This general trend is very important to laser physics as it relates two (usually) measurable parameters (E and N) to the characteristic energy of the electrons.

While this "average electron energy" approach is sufficient to describe the basics of many systems, serious modelling attempts must take account of the fact that there is actually a distribution of electron energies which is unlikely to conform to a Maxwell-Boltzmann distribution.

6.2.2 Electron balance

The continuity equation for electrons may be written,

$$\begin{aligned} \frac{dn_e}{dt} = & \quad \text{production of electrons by those present} \\ & + \text{production of electrons by external sources} \\ & - \text{losses of electrons by various processes} \end{aligned} \tag{6.14}$$

This equation can be simplified if external sources are ignored and a simple lifetime model is used for electron losses, that is, the loss is proportional to n_e divided by some lifetime τ_e. Similarly the first term can be handled by multiplying n_e by some ionisation frequency ν_i. The equation becomes,

$$\frac{dn_e}{dt} = +\nu_i n_e - \frac{n_e}{\tau_e} \tag{6.15}$$

A steady-state discharge where $dn_e/dt = 0$ is produced via the following mechanism. An initially high electric field ionises the gas and creates a large number of electrons. As more electrons are produced the current through the discharge tube increases, this lowers the voltage across the tube which lowers the E/N which in turn lowers ν_i until the rates of electron production and loss are equal.

Another important gas discharge result which is related to this electron balance equation is the following. For a given gas at a specified pressure there is a unique value of the characteristic energy which satisfies the ionisation balance equation. Assuming a direct relationship between ϵ_k and E/N then: *there is a unique value of E/N for a self-sustained steady-state discharge.*

6.3 Alpha and Gamma discharges

In RF-induced gas discharges, there are two possible types of discharge configurations. These discharge types, called *alpha* and *gamma*, describe the low and high current forms of the discharge. The names relate to the first and second Townsend ionisation coefficients. In the low current density alpha discharge,

volume ionisation is the dominant form of ionisation whereas in the high current density or gamma discharge, electron generation occurs mainly in the plasma-electrode boundary region.

The transition from alpha to gamma discharge is characterised by a sharp increase in the discharge current, indicating a drop in the plasma impedance and the physical contraction of the discharge to occupy a much smaller cross-sectional area of the electrodes. This transition is thought to occur as a result of the neutralisation of the positive ion plasma sheaths by secondary emission from the electrodes.

In the context of CO_2 lasers the transition to gamma discharge is fatal to the lasing process, because the electrons produced in a gamma discharge have much higher energies. This dramatically changes the cross-section for excitation of the upper lasing level (see figure 2.9).

Some spectroscopic tests for alpha and gamma discharges are discussed in section 8.11.

6.4 Electron oscillation amplitude and plasma sheaths

The excitation process starts with the electromagnetic field causing free electrons in the gas to oscillate. These electrons then collide with neutral atoms and excite them. This excitation can take one of many forms, such as, vibrational or electronic excitation or ionisation.

The motion of electrons in a high frequency electric field may be described by,

$$m\frac{dv_D}{dt} + mv_D\nu_c = eE_0e^{i\omega t} \tag{6.16}$$

where m and e are the mass and charge of the electron, v_D is the electron drift velocity and ν_c is the electron-molecule collision frequency. The solution to this equation is,

$$v_D = \frac{eE_0e^{i\omega t}}{m(i\omega + \nu_c)} + c_1e^{-t\nu_c} \tag{6.17}$$

$$= \frac{eE_0e^{i\omega t}}{m(i\omega + \nu_c)} \quad \text{when} \quad c_1 = 0 \tag{6.18}$$

The second term is a transient term and so c_1 may be set to zero for a steady-state solution. This equation may then be integrated to give,

$$x = \frac{eE_0e^{i\omega t}}{m(i\nu_c\omega - \omega^2)} \tag{6.19}$$

From this an estimate of the electron oscillation amplitude in a field of amplitude E_0 may be obtained,

$$|x_0| = \frac{eE_0}{m\omega(\nu_c^2 + \omega^2)^{\frac{1}{2}}} \tag{6.20}$$

This is the oscillation amplitude of the electrons when they are not close to the electrodes. Electrons oscillating near an electrode are quite likely to be captured, resulting in an electron deficiency or positive charge near the electrode. The resulting internal field attracts electrons away from the electrode and repels ions towards the electrode. These ions can lead to secondary emission.

In a typical RF discharge at 52 MHz, 100 torr, 2 mm electrode separation and 200 V RMS across the electrodes gives $|x_0| = 0.35$ mm. In contrast, under the same conditions at 2.45 GHz, $|x_0| = 7\,\mu$m.

A schematic of a simple discharge model is shown in figure 6.4. The discharge of width L can be divided into two sheath zones, located at positions $x = s$ and $x = L - s$ and a positive column located between the two sheaths. As an oscillating potential is applied to the electrodes the sheath regions oscillate with an amplitude of $|x_0|$. As the electrons move much faster than the ions, significant charge separation can occur which is not neutralised by the back diffusion of electrons. This, coupled with the ability of the electrodes to capture nearby electrons, leads to the initial formation of the sheath regions. From this model much of what is observed in an RF discharge can be understood.

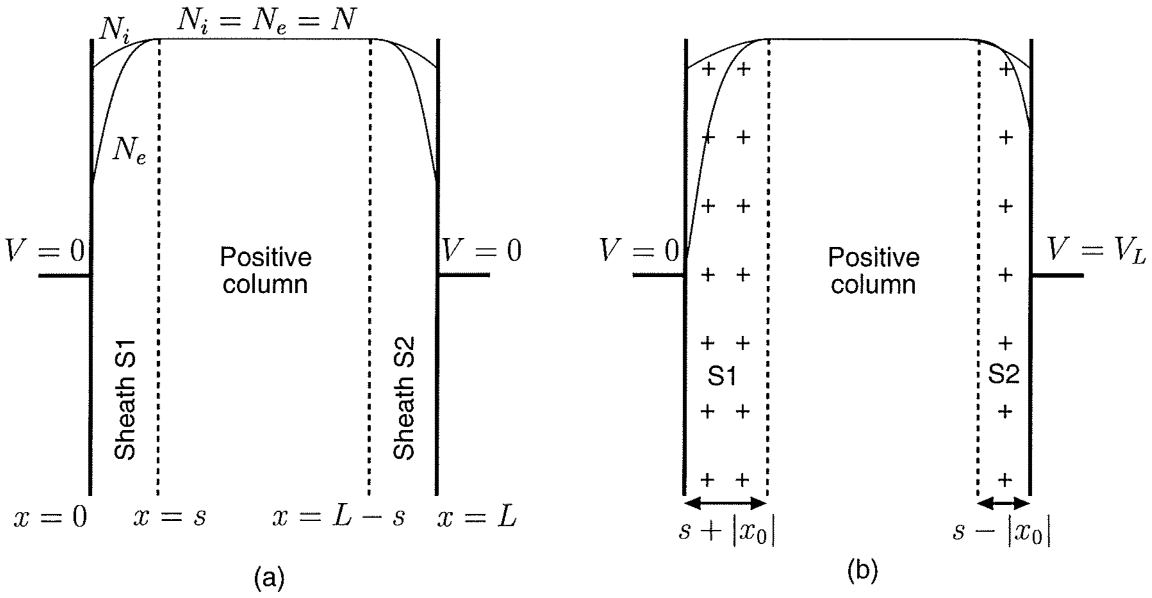

Figure 6.4: Charge distribution for a simple (alpha) discharge model. (a) zero applied voltage. (b) RMS voltage V_L applied between the electrodes

Figure 6.5 shows an RF discharge viewed end on. The discharge is symmetrical because the electric field is oscillatory. When viewed by eye or with a camera one is actually seeing a time average of the real picture. The dark bands near the electrodes are due to low electron density in that area. When the electric field which created the positive space charge region reverses, the two fields add and accelerate electrons away from the wall (through the positive region) where they excite neutral species. It is the decay of these excited species which results

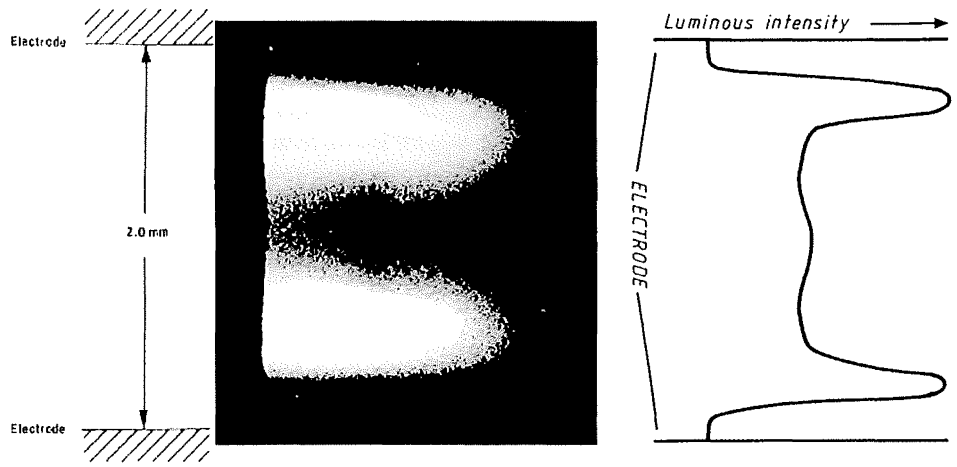

Figure 6.5: (a) An alpha RF discharge view from one end. (b) Diagram showing the variation in luminous intensity across the discharge.

in the high intensity peaks shown in the figure. The intensity of the discharge decreases and levels off towards the centre of the discharge indicating a decrease in the electron energy away from the positive regions.

The vastly reduced electron oscillation amplitude at microwave frequencies (7 μm compared with 0.35 mm) means that the plasma sheaths present in a microwave-excited discharge are smaller and less significant than in RF discharges.

6.5 Critical electron density and plasma resonance

Plasmas can often exhibit instability, that is, the parameters which describe the discharge fluctuate leading to erratic and unpredictable behaviour. Such instabilities are often visible as changes in intensity of the discharge. The major factors affecting instability are inhomogeneous processes related to the density of electrons and their production, removal and diffusion. In a steady-state discharge the production and removal rates of electrons Z_+ and Z_- are equal,

$$\frac{dn_e}{dt} = Z_+ - Z_- \tag{6.21}$$

The criterion for stability in a "steady-state" discharge can be deduced from the relative gradients of the rates Z_+ and Z_- when plotted with respect to n_e. In a steady-state discharge $dn_e/dt = 0$ or $Z_+ = Z_-$. In general, the discharge will be stable if small fluctuations in the electron density are self correcting. In terms of Z_+ and Z_- this means that the curve for Z_- must cross above Z_+ as the electron density increases (see figure 6.6). Therefore, any small increase in the electron density n_e will result in an increase in the removal of electrons Z_- which in turn limits the increase in n_e, resulting in a steady-state discharge.

As the rate of production of electrons in a plasma is a function of the electric

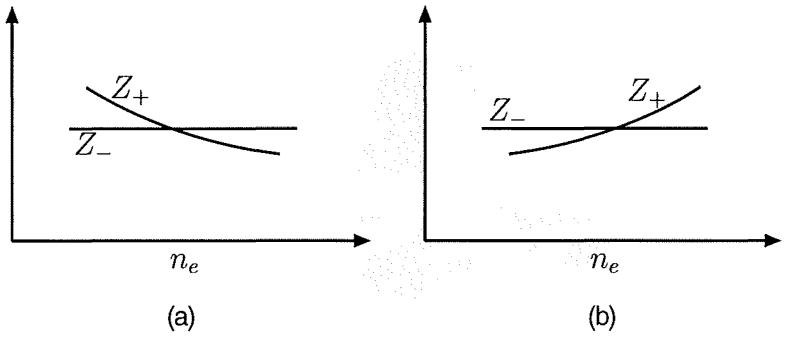

Figure 6.6: Variation of electron production and removal with electron density. (a) stable situation, (b) unstable situation

field, the stability criterion above may be rephrased in the following manner. The plasma is stable if the electric field within the plasma decreases with increasing electron density. Assuming a constant applied field E_a, the electric field inside the plasma conforms to the relation,

$$|\epsilon_p| E_p = \text{constant} \tag{6.22}$$

where ϵ_p is the dielectric permittivity of the plasma. The electric field inside the plasma is therefore inversely proportional to the magnitude of the plasma dielectric constant. This dielectric constant is given by [11],

$$\epsilon_p = 1 - \frac{\omega_p^2}{\omega^2 + \nu_c^2} + i\frac{\nu_c}{\omega}\frac{\omega_p^2}{\omega^2 + \nu_c^2} \tag{6.23}$$

where,

$$\omega_p^2 = \frac{e^2 n_e}{m_e \epsilon_0} \tag{6.24}$$

and ω_p is the electron plasma frequency, ν_c is the electron momentum transfer frequency, m_e is the electron mass and ϵ_0 is the vacuum dielectric constant. The variation of the electric field in the plasma with electron density can now be found by plotting $1/|\epsilon_p|$ versus electron density. Figures 6.7a and 6.7b show this variation for 100 MHz and 2.45 GHz respectively. The point on each graph where the maximum occurs is called the critical electron density n_{ec} and occurs when the excitation frequency equals the plasma frequency, $\omega = \omega_p$. For electron densities above the critical density the electric field in the plasma decreases as the electron density increases, therefore the plasma is stable. Note that the pressure has no effect on the critical electron density. It determines only the magnitude of the electric field in the plasma. For the cases presented here, the critical density occurs at $n_{ec} = 1.2 \times 10^8\ \text{cm}^{-3}$ for 100 MHz excitation and at $n_{ec} = 7.4 \times 10^{10}\ \text{cm}^{-3}$ for 2.45 GHz. Most laboratory plasmas in the pressure range 10-50 torr will have electron densities in the range $10^{10}-10^{13}\ \text{cm}^{-3}$. The stability condition is therefore satisfied at RF and is likely to be satisfied at 2.45 GHz. Conversely, from an experimental point of view, one could observe that stable discharge operation at 2.45 GHz is achieved (at least at low pressures) and thus infer that the electron density in these discharges exceeds $7.4 \times 10^{10}\ \text{cm}^{-3}$.

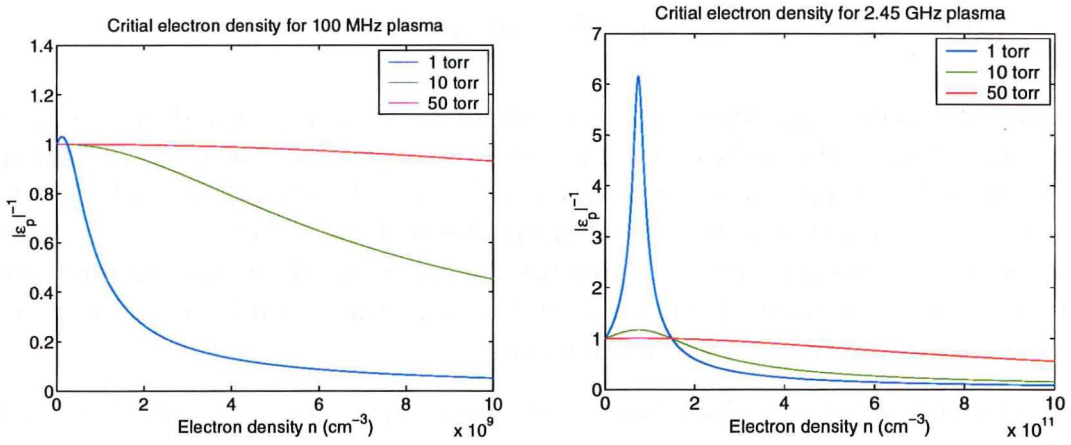

Figure 6.7: Variation of the electric field in the plasma with respect to electron density. (a) 100 MHz, (b) 2.45 GHz.

6.6 Thermal instability

Thermal instability is another type of discharge instability which could potentially affect the discharge more seriously than issues relating directly to electron density. Thermal instabilities result in plasma filaments which greatly increase the power density in localised regions of the discharge. This increase in power density results in overheating of the gas which severely affects lasing performance. Loosen and Wester [54] have developed a model which gives parameter limits for stable operation with respect to thermal instabilities. The discharge is shown to be stable if,

$$Nd < \left(\frac{\lambda T \pi^2}{2|\alpha|\epsilon_0 \omega (E/N)^2} \right)^{1/2} \tag{6.25}$$

where N is the neutral gas density, d is the discharge width, λ is the thermal conductivity of the discharge, α is a parameter of the system which has a worst case value of -0.75, T is the gas temperature, N is the neutral particle density and E is the electric field.

Although there is insufficient information to evaluate whether this condition is satisfied for the lasers examined in this research, a comparison with RF-excited lasers is instructive. If a 100 MHz discharge is compared to a discharge excited at 2.45 GHz, the right hand side of equation (6.25) is found to be five times greater at 2.45 GHz than at RF. While no firm conclusions can be drawn from this, it is a warning that the parameter space which avoids thermal instabilities is smaller in a microwave-excited CO_2 laser than it is in a similar RF-excited laser. It should be mentioned that this model applies to bare electrode lasers like V1 and neglects any effects due to plasma sheaths. Consequently, the V2 and V3 lasers which incorporate a quartz dielectric may not be well described by this relation.

6.7 The electron density in the plasma

Inside any gas discharge there is a balance between electrons created by ionisation and those lost to the walls by diffusion and other processes such as recombination. In order to understand more about the internal state of the discharge the electron density between two metal electrodes will be modelled. As electrons are the basic "moving-parts" or most active species the discharge, finding their distribution between the electrodes should go some way towards explaining some of the observed characteristics of the plasma.

The electron density at which plasma resonance occurs for an applied frequency ω is [4],

$$n_r = \frac{m\omega^2\epsilon_0}{e^2} \tag{6.26}$$

To simplify the mathematics it is convenient to measure the electron density in terms of its value at resonance. That is,

$$r = \frac{n}{n_r} = \frac{ne^2}{m\omega^2\epsilon_0} \tag{6.27}$$

where $r = 1$ at resonance. A damping constant β for the plasma is given by,

$$\beta = \frac{\nu_c}{\omega} \tag{6.28}$$

where ν_c is the electron-molecule collision frequency. The total current density may be derived from equation (6.18) using $J = nev$, $J = \sigma E$ and including the displacement current modification. The result is,

$$J = \left[\frac{ne^2}{m(\nu_c + i\omega)} + i\omega\epsilon_0\right] E \tag{6.29}$$

$$= \left[\frac{r(\beta - i)}{\beta^2 + 1} + i\right] \omega\epsilon_0 E \tag{6.30}$$

The magnitude of the resistivity may be calculated as,

$$\left|\frac{E}{J}\right| = \frac{\sqrt{\beta^2 + 1}}{\omega\epsilon_0\sqrt{(r-1)^2 + \beta^2}} \tag{6.31}$$

The ionisation process is modelled by assuming [36, 37] that the ionisation frequency per electron ν_i depends on the applied field about a central value E_0 and that it varies as a power of 2α with respect to the field. That is,

$$\nu_i = \nu_0 \left|\frac{E}{E_0}\right|^{2\alpha} \tag{6.32}$$

where the parameter α is an experimentally determined constant for the gas which is related to the product of the pressure and the electrode spacing. Equation (6.31) is substituted into equation (6.32) to obtain an expression for ν_i,

$$\nu_i = \frac{\nu_0 \left|\frac{J}{\omega\epsilon_0 E_0}\right|^{2\alpha} (\beta^2 + 1)^\alpha}{((r-1)^2 + \beta^2)^\alpha} \tag{6.33}$$

This implies that the ionisation rate is a function of the electron density with a maximum at the plasma resonance ($r = 1$).

6.7.1 The diffusion equation

The electron density distribution may now be found by the solution of a differential equation which balances the rate of production of electrons with the dominant loss mechanism, diffusion. The diffusion is assumed to be ambipolar due to the relatively high electron-ion concentrations. If one examines a pair of infinite parallel plates separated by a distance d then the diffusion equation is,

$$\frac{d^2n}{dz^2} + n\frac{\nu_i}{D} = 0 \tag{6.34}$$

where the position across the gap is measured by z and D is the ambipolar diffusion coefficient. After making a change of variables $u = 2z/d$ and substituting equation (6.33) we have, in terms of r and u,

$$\frac{d^2r}{du^2} + \frac{k^2}{(r^2 - 2r + 1 + \beta^2)^\alpha} = 0 \tag{6.35}$$

where,

$$k^2 = \left[\frac{d^2\nu_0(1+\beta^2)^\alpha}{4D}\right]\left|\frac{J}{\omega\epsilon_0 E_0}\right|^{2\alpha} \tag{6.36}$$

is a constant and u (and z) is measured from the centre of the discharge. The boundary conditions are,

$$r = r_0 \quad \text{and} \quad \frac{dr}{du} = 0 \quad \text{at} \quad u = 0 \tag{6.37}$$

$$r = 0 \quad \text{at} \quad u = \pm 1 \tag{6.38}$$

The first condition sets the peak value of the electron density at the centre of the discharge and requires that the solution be symmetric. The second condition requires that the electron density goes to zero at the walls.

To solve this diffusion equation, subject to the constraints above, values for α, β and a central value for r are required. Of these, α is the quantity which is most difficult to estimate. Generally, experimentally measured values are used for this quantity, however, the value is likely to reside between 2 and 5 [37].

Numerical solutions of equation (6.35) are plotted in figure 6.8 for frequencies of 100 MHz and 2.45 GHz. The gas pressure is 20 torr. Near resonance ($r = 1$) or when α is small, the distribution can be described by a sine function. Further away from resonance (larger r) the distribution becomes more rounded and semicircular in the limit of large r. Increasing α also leads to a more rounded distribution. However, in the limit of large α the distribution takes on a rectangular box shape. As an electron density of $10^{11}\,\mathrm{cm}^{-3}$ is somewhat high for an RF discharge at 20 torr, a value of $10^{10}\,\mathrm{cm}^{-3}$ has been used to calculate the curves

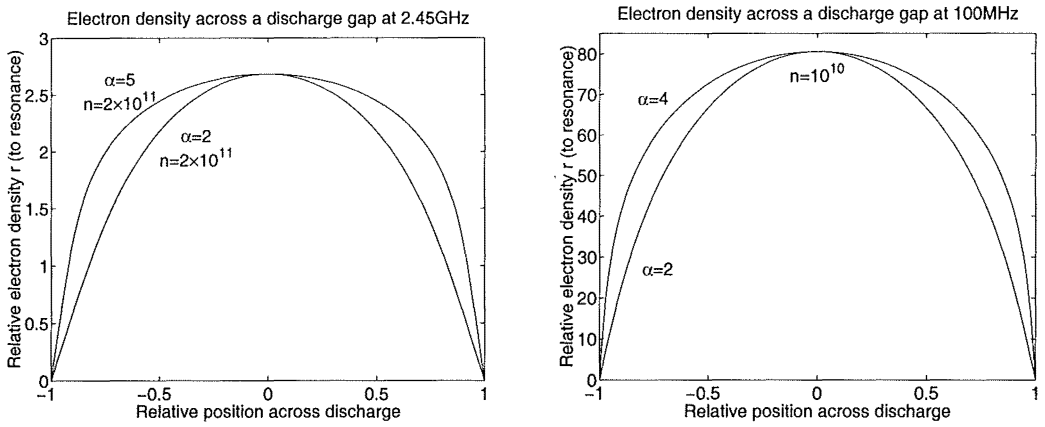

Figure 6.8: Variation of the electron density across the discharge gap. (A) 2.45 GHz, (B) 100 MHz

in figure 6.8b. In practice this change makes little difference to the shape of the distribution as both values are well above resonance.

From these solutions it may be concluded that the shape of the electron density distribution across the discharge gap is not significantly different under the assumptions used. There are two limitations to this model which should be considered. The first is that it applies only to the case where the electrodes are bare. In the V2 and V3 lasers where a quartz dielectric is present, it is unlikely that the condition (6.38) is rigidly enforced on the quartz-plasma boundary because the dielectric is unable to remove excess electrons by conduction, as would be the case in a metal. This means that the addition of the dielectric might lead to a more uniform electron distribution across the gap. Another discharge feature which is ignored by this model is the possibility of plasma sheaths. These are especially important at RF frequencies due to the larger electron oscillation amplitude. While these positive sheath layers will compress the electron distribution curves so that they occupy of smaller portion of the discharge gap, it is unlikely that there will be other significant changes in the shape of the curve.

Verifying that the model is a good description of the physical situation requires some comparison with experimental observation. The simplest way to accomplish this experimentally is by direct observation of the discharge. In terms of the model, the visible brightness of the discharge is proportional to ionisation rate. As this rate is strongly dependent on α (see equation (6.32)) it becomes difficult to estimate the ionisation with any accuracy. However, the results appear to follow a general trend. The ionisation at a particular point in the discharge can be found from the electric field, which is related to the electron density by,

$$E(u,r) = \frac{((r-1)^2+\beta^2)^{-\frac{1}{2}}}{((r_0-1)^2+\beta^2)^{-\frac{1}{2}}} \tag{6.39}$$

Once $E(u,r)$ is known the ionisation per electron can be found from equation (6.32). Therefore the ionisation rate is the ratio of the ionisation rate per electron

to the electron density. Plots of these three quantities, as well as the electron density, are presented in figure 6.9 for $n = 2 \times 10^{11}\,\mathrm{cm}^{-3}$ and $\alpha = 2$ at 20 torr. This ionisation (intensity) profile has a strong resemblance to observed intensity profiles.

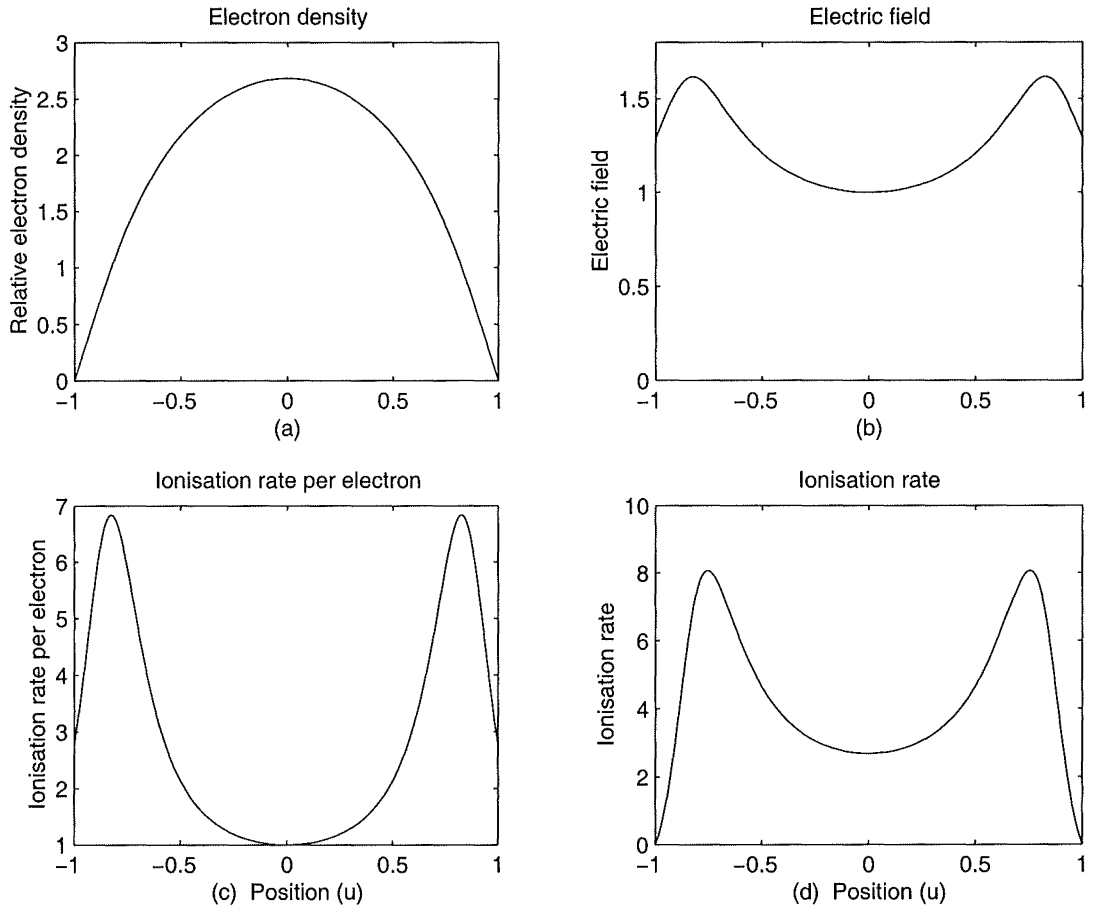

Figure 6.9: Model results for a 2.45 GHz discharge at 20 torr. All magnitudes are relative. Parameters: $n = 2 \times 10^{11}\,\mathrm{cm}^{-3}$, $\alpha = 2$. Note that (d) should represent the observed brightness of the discharge.

6.8 Plasma circuit model

In this section a circuit model is developed to describe the electrical properties of the laserhead. This model describes the behaviour of the quartz dielectric. The configuration without the dielectric will be shown to be a special case of the model.

A diagram of the model is shown in figure 6.10. A second dielectric has been added to keep the model symmetrical and reduce the number of equations. Moving to a single dielectric system requires a trivial alteration to the equations at a later stage. The plasma is taken to be occurring in one-dimension between two

metal electrodes. Positioned between these electrodes are two quartz dielectrics with permittivity ϵ_q, internal electric field E_q and width d_q. The plasma has permittivity ϵ_p, internal electric field E_p and width d_p. The conduction current density in the plasma is j_{pc} and the total current in the circuit is denoted by i. At any instant in time, charge densities are assumed to be present at the interfaces between each region. The charge density for the model as a whole is represented by ρ. There is a charge density of q_p at the interface between the dielectric and the plasma and a density q between the electrode and the dielectric. This is equivalent to assuming that the plasma is electrically neutral with an applied potential. While this is not strictly true due to the presence of sheath regions (see section 6.4) and the varying density of electrons across the gap, the assumption is reasonable as the plasma is electrically neutral as a whole. If necessary the sheath regions could be added to the model as an extra layer. However in microwave-excited discharges these areas are very thin due to the small electron oscillation amplitude.

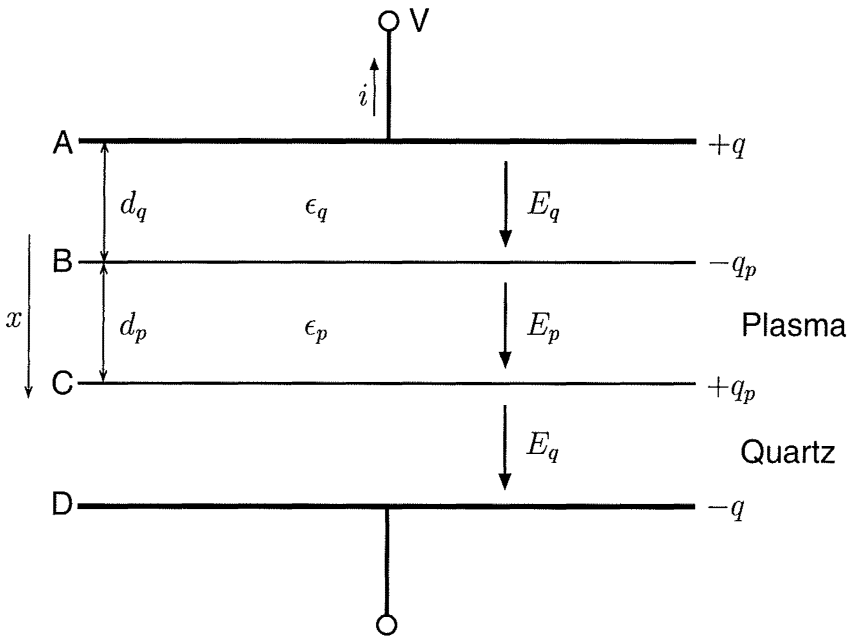

Figure 6.10: Discharge model.

Maxwell's equations may now be applied to the plasma to determine the conduction current.

$$\frac{\partial \rho}{\partial t} + \frac{\partial j_{pc}}{\partial x} = 0 \qquad \text{(Continuity equation)} \tag{6.40}$$

$$\epsilon_p \frac{\partial E_p}{\partial x} = \rho \qquad \text{(Electrostatics)} \tag{6.41}$$

$$j_{pc} = \sigma_p E_p \qquad \text{(Ohms law)} \tag{6.42}$$

If the right hand side of the Maxwell equation,

$$\nabla \times \mathbf{H} = \mathbf{j} + \frac{\partial \mathbf{D}}{\partial t} \tag{6.43}$$

is taken to be a current density, one may write,

$$j_{\text{total}} = j_{pc} + j_{pd} \tag{6.44}$$

where j_{pd} is the displacement current. If equation (6.41) is integrated between the boundaries of two layers over an infinitesimally small region it is found that,

$$\lim_{\delta x \to 0} \int_{A-\delta x}^{A+\delta x} \epsilon \frac{\partial E}{\partial x}\, dx = \lim_{\delta x \to 0} \int_{A-\delta x}^{A+\delta x} \rho\, dx \tag{6.45}$$

$$\epsilon_q E_q = +q \qquad \text{(At A and D)} \tag{6.46}$$

$$\epsilon_p E_p - \epsilon_q E_q = +q_p \qquad \text{(At B and C)} \tag{6.47}$$

If the charge continuity is applied at the boundaries, then,

$$\frac{dq_p}{dt} = j_p c \qquad \frac{dq}{dt} = j_{\text{total}} = \frac{i}{A} \tag{6.48}$$

where A is the area of the electrode. The voltage across the electrodes can now be calculated from the electric fields,

$$\begin{aligned} E &= 2E_q + E_p \\ V &= 2E_q d_q + E_p d_p \\ &= \frac{2qd_q}{\epsilon_q} + \frac{j_{pc} d_p}{\sigma_p} \qquad \text{where} \qquad j_{pc} = \frac{\sigma_p (q - q_p)}{\epsilon_p} \end{aligned} \tag{6.49}$$

where Ohms law $j = \sigma E$ has been used. These equations may now be changed to "circuit" form by converting the densities to the total quantities they represent, ie,

$$Q = qA \qquad Q_p = q_p A \qquad R_p = \frac{D}{\sigma_p A} \tag{6.50}$$

Capacitances for the dielectric and plasma can be introduced,

$$C_q = \frac{\epsilon_q A}{d_q} \qquad C_p = \frac{\epsilon_p A}{d_p} \tag{6.51}$$

After substitution, equations (6.48) and (6.49) become,

$$V = \frac{2Q}{C_q} + i_{pc} R_c \qquad i_{pc} R_p = \frac{Q - Q_p}{C_{pc}} \qquad \dot{Q}_p = i_p \qquad \dot{Q} = i \tag{6.52}$$

The equations (6.52) have an obvious circuit representation shown in figure 6.11. It now clear that the situation without the dielectric slab can be modelled by removing the capacitance C_q from the circuit and that the removal of one of the dielectrics may be accomplished by replacing $C_q/2$ with C_q. Note that the displacement current in the plasma i_{pd} is equal to the difference between the total current i and the conduction current i_{pc}.

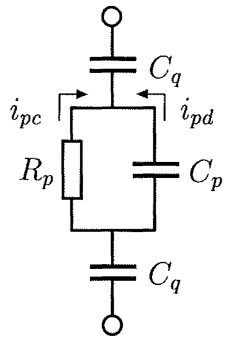

Figure 6.11: Circuit model for equations (6.52).

6.8.1 Circuit solution

To solve equations (6.52) it is assumed that a potential of the form $V = V_0 \sin(\omega t)$ is applied to the *electrodes*. It is also assumed that ϵ_p and R_p are constant throughout the period of the high frequency cycle. This is reasonable at the frequencies of interest (≥ 10 MHz) as the characteristic frequency for the removal of electrons does not exceed $10^5\,\mathrm{s}^{-1}$ whereas ionisation occurs at the frequency of oscillation ω. This means that in a steady-state discharge, n_e and hence R_p and ϵ_p should not be strongly affected by the phase of the field. Therefore the equations can be solved using standard electrical circuit techniques. The voltage across the plasma V_p is given by,

$$V_p = E_p d_p = i_p R_p = V_o \frac{C_q R_p \omega}{2\sqrt{1+\omega^2\tau^2}} \sin(\omega\tau + \phi) \tag{6.53}$$

where,

$$\tau = R_p \left(\frac{C_q}{2} + C_p\right) \quad \text{and} \quad \phi = \tan^{-1}\left(\frac{1}{\omega\tau}\right) \tag{6.54}$$

The current i which is seen by the external circuit can be written,

$$i = V_o \frac{C_q \omega \sqrt{1+\omega^2\tau_p^2}}{2\sqrt{1+\omega^2\tau^2}} \sin(\omega t + \phi + \Delta\phi) \tag{6.55}$$

where,

$$\tau_p = R_p C_p \quad \text{and} \quad \Delta\phi = \tan^{-1}\left(\frac{1}{\omega\tau_p}\right) \tag{6.56}$$

The time constants τ_p and τ characterise the charging time for the plasma and for the circuit as a whole. The phase constants ϕ and $\Delta\phi$ give the phase difference between the plasma voltage and the applied voltage, and the total circuit current and the applied voltage, respectively.

6.9 The quartz dielectric

Having shown that the addition of the dielectric to the discharge circuit can be modelled by adding a capacitance in series with the plasma, it is possible to see

how the apparently arbitrary introduction of the quartz dielectric in section 3.3 leads to a more uniform discharge. It operates in a similar manner to the resistive ballast added to DC lasers to make the overall resistance characteristic of the circuit positive. Although plasmas at DC have a negative resistance characteristic, at high (RF and microwave) frequency the characteristic is positive. This means that a ballast is not required to prevent an avalanche in the current but is of considerable help with respect to uniformity. To understand why, imagine a discharge situation like V1 without any dielectric. The voltage induced across the electrodes by the feeder waveguide will be set by the E/N for the particular gas mix and pressure involved (see section 6.2.2). Any localised changes in the plasma characteristics will result in localised changes in the current through the plasma. In this configuration the only element limiting the current through the discharge is the reactance of the plasma itself. Large increases in the discharge current in a small region will lead to an increase in the electron density there. If the increase is significant it will begin to affect neighbouring regions by diffusion, resulting in non-uniform current flow in the discharge. The operation of the dielectric slab can be understood in the circuit context. While the voltage across the discharge will be the same as in the bare electrode case, the total voltage between the metal electrodes will have increased due to the voltage drop across the quartz. The relation between these voltages is given by equation (6.53). In addition to providing a better impedance match between the waveguide and the laserhead the quartz adds a constant reactance to the discharge circuit which limits the current able to be drawn. This prevents regions of high current (and thus electron density) in the discharge and leads to a more controlled uniform discharge.

The current-limiting feature of the dielectric does come at the cost of reduced power input if the capacitance severely limits the current. While currents in the discharge are difficult to estimate, due the need to know accurately the E/N and electron density, the ratio of the voltage across the plasma to the voltage across the metal electrodes can be estimated. Given that the voltage across the quartz is of the same order of magnitude as the voltage across the plasma, then it is reasonable to assume that a significant amount of power will still reach the discharge. In order find a value for V_p/V_0 estimates are required for: n, ν_c, ϵ_p, ϵ_q and R_p.

The electron density n for CO_2 laser discharges is typically between 10^9 and $10^{12}\,\mathrm{cm}^{-3}$. In section 6.5, a minimum electron density of $7.4\times10^{10}\,\mathrm{cm}^{-3}$ was found to be required for a stable discharge operation. A value of $n = 10^{11}\,\mathrm{cm}^{-3}$ might therefore be a realistic estimate of the electron density. The collision frequency for momentum transfer from electrons can be calculated [6] from,

$$\nu_c = \sum_i N_i Q_{mi} \tag{6.57}$$

where N_i is the particle density and Q_{mi} is the cross-section for momentum transfer by electrons for gas species i. For the gas species present this can be

expressed,

$$\nu_c = 10^9 p\,(1.8 f_{CO_2} + 4.2 f_{N_2} + 2.0 f_{He}) \tag{6.58}$$

where f_x is the fraction of gas species x in the mixture and p is the pressure in torr. For a 1:3:18 mixture at 20 torr,

$$\nu_c = 2 \times 10^{10}\,\text{Hz} \tag{6.59}$$

The dielectric permittivity of quartz [45] is,

$$\epsilon_q = 4.5\epsilon_0 \tag{6.60}$$

The dielectric permittivity ϵ_p can be calculated from the conductivity of the plasma via the relation,

$$\epsilon_p = 1 + \frac{\sigma_p}{i\omega\epsilon_0} \tag{6.61}$$

where the conductivity σ_p can be estimated [22] from,

$$\sigma_p = \frac{ne^2}{m}\frac{\nu_c - i\omega}{\nu_c^2 + \omega^2} \tag{6.62}$$

This leads to a permittivity,

$$\epsilon_p = (1 - \frac{\omega_p^2}{\nu_c^2 + \omega^2})\epsilon_0 \tag{6.63}$$

where the complex part of the permittivity has been dropped as the attenuation of the medium is handled by the resistive term in the circuit model. This resistive term may be calculated from the complex conductivity above,

$$R_p = \frac{d_p}{\sigma_p A} \tag{6.64}$$

$$= \frac{d_p}{A}\frac{\nu_c m}{ne^2} \tag{6.65}$$

The capacitances C_p and C_q resulting from the permittivities above are of the same order of magnitude. However, the capacitance of the dielectric is not affected by the electron density (or current).

Practical concerns dictated that quartz be the material used for the dielectric spacer. It can be polished flat so that it will perform well as part of the optical waveguide. It can handle the high thermal stress from plasma heating, without fracturing. Quartz is also readily available. Other options included alumina or beryllia which have better thermal conductivity, however, these are difficult to acquire in the required shape and troublesome to machine.

There is now sufficient information to calculate the voltage across the plasma V_p in relation to the applied voltage V_0. Using the following values,

$$\begin{array}{llll} n = 10^{11}\,\text{cm}^{-3} & \nu_c = 2 \times 10^{10}\,\text{Hz} & \epsilon_q = 4.5\epsilon_0 & \epsilon_p = 0.51\epsilon_0 \\ \omega = 2\pi \times 2.45\,\text{GHz} & d_q = 5.5\,\text{mm} & d_p = 2\,\text{mm} & R_p = 3\Omega \\ A = 16\,\text{mm} \times 300\,\text{mm} & p = 20\,\text{torr} & & \end{array} \tag{6.66}$$

it is found that,

$$V_p = 0.69V_0 \tag{6.67}$$

So a considerable fraction of the voltage is being dropped across the quartz dielectric ($V_q = V_0 - V_p$). Table 6.1 indicates how this fraction changes when various plasma parameters are altered. As expected, alteration of the dielectric thickness and discharge gap result in significant changes to the ratio. Most notably, a dielectric 2-3 mm in thickness still results in a significant drop across the dielectric but would have the advantage of significantly improving heat extraction from the discharge. Unfortunately quartz slabs of this size and thickness are very brittle and difficult to obtain commercially. The ratio is relatively unaffected by changes in pressure. Only a small change is observed when the pressure is set to 100 torr. The ratio also appears to be insensitive to electron density.

n_e (cm^{-3})	p (torr)	d_q mm	d_p mm	V_p/V_0
10^{11}	20	5.5	2	0.69
10^{11}	20	5.5	3	0.78
10^{11}	20	5.5	4	0.83
10^{11}	20	5.5	5	0.87
10^{11}	20	10	2	0.52
10^{11}	20	2	2	0.88
10^{11}	20	3	2	0.75
10^{9}	20	5.5	2	0.62
10^{11}	100	5.5	2	0.63

Table 6.1: The variation in the ratio V_p/V_0 when various plasma parameters are altered.

6.10 The electron energy distribution function

The correct distribution of electron energies is crucial to the excitation process in a CO_2 laser (see section 2.7). Closely related to the electron energy distribution function (EEDF) is the plasma parameter E/N which plays the most significant role in determining the electron energies. At high frequencies the parameter E in E/N should be replaced by an effective DC electric field E_{DC} given by,

$$E_{DC}^2 = E_{AC}^2 \left(1 + \frac{\omega^2}{\nu_c^2}\right)^{-1} \tag{6.68}$$

where E_{AC} is the high frequency electric field. At RF frequencies the ratio ω^2/ν_c^2 is less than 10^{-4} and there is no significant difference between the effective field and the AC field.

When the system is excited by microwaves at 2.45 GHz, the excitation frequency becomes comparable to the electron collision frequency ν_c and the effective field is

no longer identical to the AC field. At 20 torr ($\nu_c = 2 \times 10^{10}\,s^{-1}$) the relationship is,

$$E_{DC} = 0.79 E_{AC} \tag{6.69}$$

so the difference is significant now, but not extreme. A higher electric field will be required to induce the same excitation (EEDF) in a microwave-excited plasma than in the equivalent plasma excited by RF. A study of electron excitation rates by Baker *et al.* [6] briefly examined the effects of increased excitation frequency on the electron energy distribution. The results, shown in figure 6.12, show that the average energy of the electrons moves towards 0 eV as the frequency is increased. Note however, that the curve (B), for 10 GHz, (four times 2.45 GHz), is not drastically different than curve (C) at 400 MHz. RF behaviour only starts to deviate from the DC behaviour above 400 MHz.

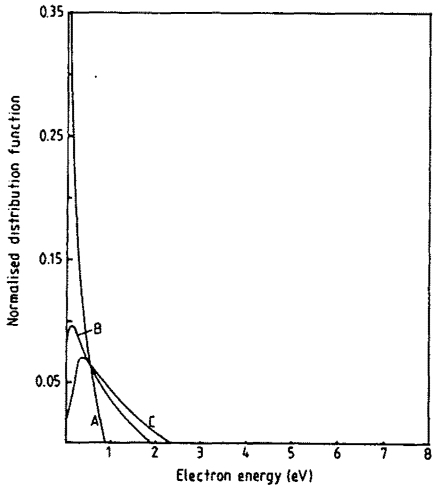

Figure 6.12: Electron energy distributions for various excitation frequencies (1:1:3 CO_2:N_2:He). Excitation frequencies of: (A) 30 GHz, (B) 10 GHz, (C) 400 MHz

6.11 Conclusion

In conclusion, although there are some significant differences between RF- and microwave-excited discharges there does not appear to be any significant reason why microwave-excitation of a CO_2 laser should result in a discharge that is so different in nature that lasing cannot be induced.

Chapter 7

Experimental Results

The experimental characteristics of the three lasers are investigated in this chapter.

The experimental setups for the three lasers are basically identical except for the substitution of the laserheads. A schematic of the setup is shown in figure 7.1. The magnetron used was obtained from a conventional microwave oven, AWI-BL750J or similar. The magnetron was powered by a modified Quentron 7000A DC power supply modulated by the fast high voltage switch described in section 4.4. The gas was a 1:3:18 (CO_2:N_2:He) pre-mix from BOC gases. The vacuum pump was a Leybold-Heraeus D8A rotary pump capable of pumping at 3.25 L/s. The calorimeter consisted of two well calibrated temperature sensitive ICs connected to a computer. Flow measurement was performed manually with a measuring cylinder. The IR output power was measured by a Scientech 364 laser power meter. High speed laser pulse measurements were made by a HgCdTe detector optimised for 10.6 μm. All oscilloscope traces were taken by a Hitachi VC-6275 digital storage oscilloscope.

7.1 The V1 laser

In section 4.4 a power supply for the magnetron was described as were some other simpler designs akin to a conventional microwave oven magnetron. Although these simpler designs were successful, in that they could excite a discharge which was capable of producing laser output under certain conditions, they lacked versatility for experimental investigation and were superseded by the DC switch supply. Thus experiments involving this newer supply will be reported in favour to those involving the simpler less controllable devices.

7.1.1 Basics

Striking a discharge in the V1 laserhead at pressures of less than 20 torr was relatively trivial. Above 25 torr, however, it was increasingly more difficult. In addition, the discharge 'mode' pattern became very unstable, jumping from one configuration to another resulting in erratic laser output. For this reason these

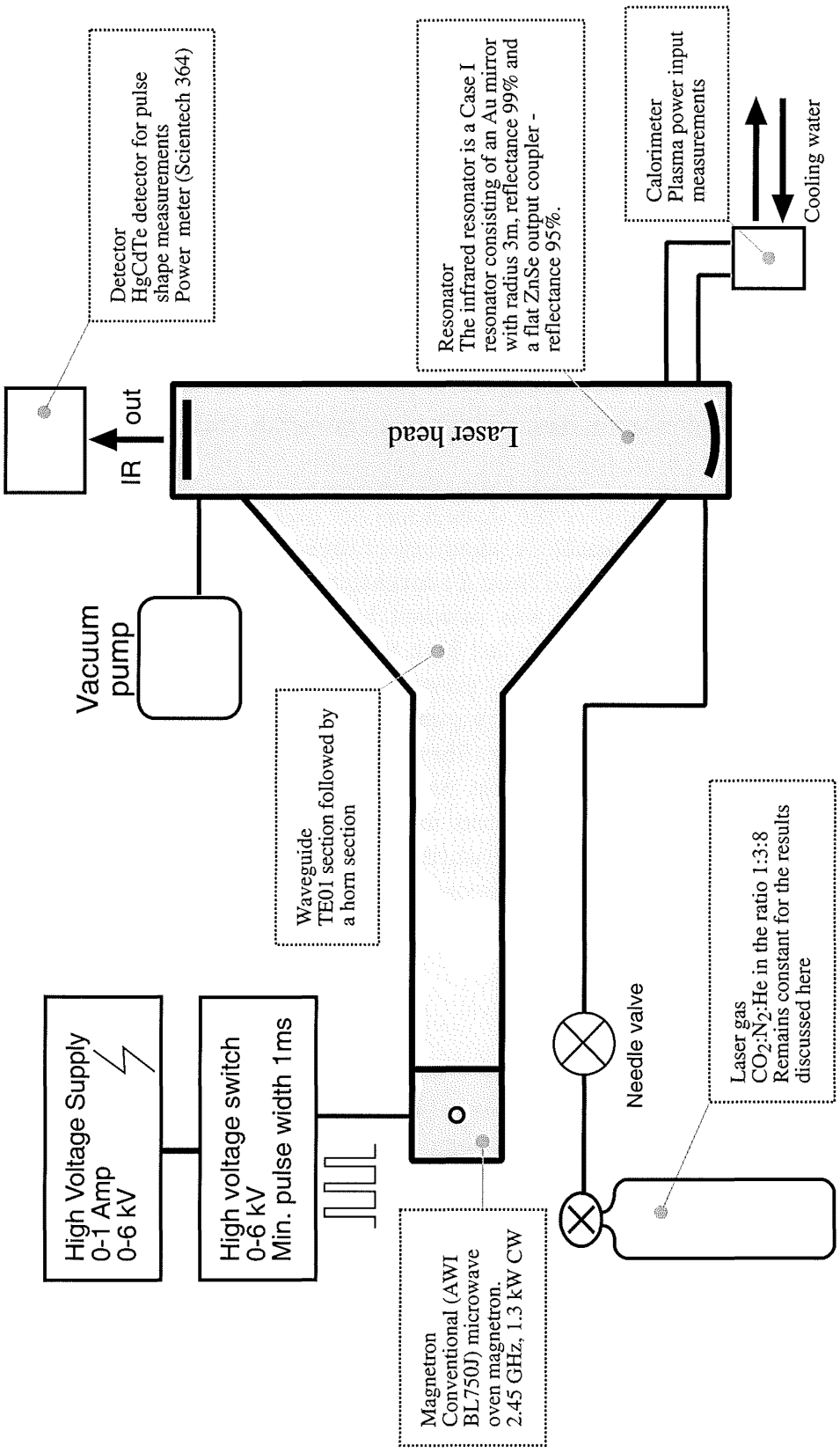

Figure 7.1: Basic experimental setup used for the experiments. The laserheads V1,V2 and V3 can interchanged.

experiments have been limited to pressures below 25 torr. Sealed-off operation was possible with this design but only for short periods of time and under a very limited range of power and pressure. In general, sealed-off operation led to poorer discharge quality and lower, if any, output power. A survey of mark/space timings for the microwave input pulse was made in relation to the laser output power under conditions of good discharge stability. It was found that the region of highest output power and efficiency occurred at a pulse width of 35 μs with 400 μs between each pulse (2.5 kHz). These timings were found to be a good starting point for the optimisation. Standing wave ratios in the microwave cavity tended to be of the order of 10, a problem resulting primarily from the drop from 50 mm to 2 mm in the microwave cavity height. A number of methods were employed to achieve lower standing wave ratios (SWR) but none of them resulted in a significantly lower value. Despite this high figure a reasonable amount of power can be extracted by the discharge and, in general, other limitations were more significant.

7.1.2 Output power

The laser output power extracted, while keeping the microwave input power constant, is shown in figure 7.2. The pulse length was set to 30 μs, with a period of 400 μs. Over this range the pulse length and and period used were near optimal. Higher average, but more erratic, output powers ($\sim$ 2 W) were achievable at the cost of discharge quality and efficiency.

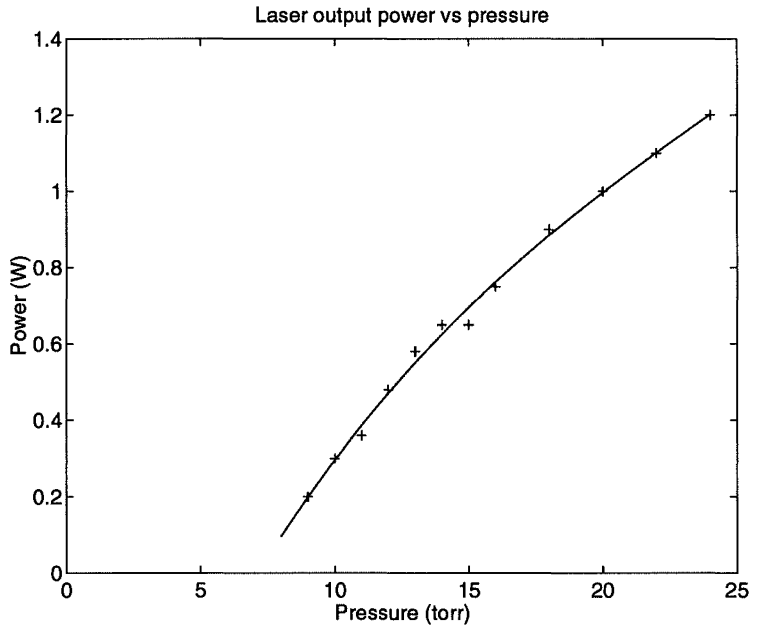

Figure 7.2: Laser output power vs pressure for constant input power ($\sim$ 50 W), PRF 2.5 kHz (400 μs) and pulse width 30 μs.

When the pulse repetition frequency was held constant and the pulse width

varied, an optimum was found near 30 μs. This width increases slightly at higher pressures. Figure 7.3 shows the general trends between 12 and 24 torr.

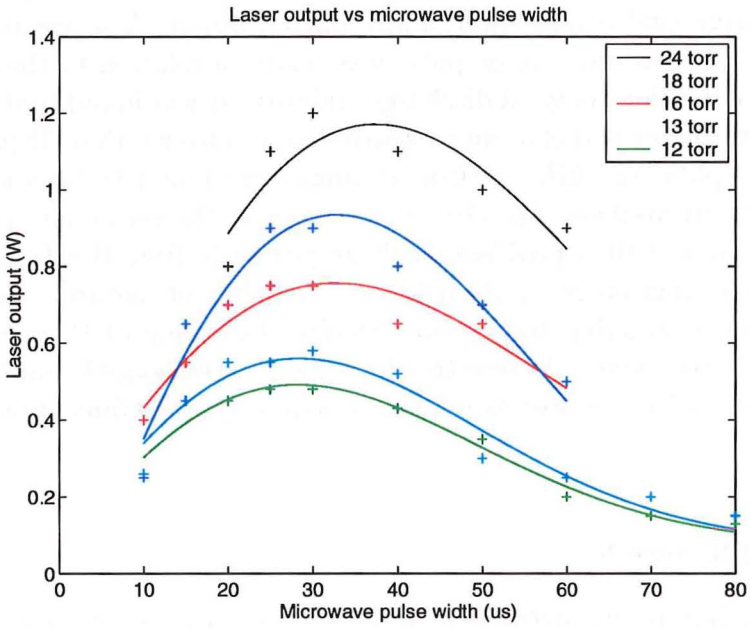

Figure 7.3: Output power versus microwave input pulse width for a 400 μs period (2.5 kHz)

7.1.3 Efficiency

Efficiency is a practical design goal in any laser as increases in efficiency can often lead to significant increases in output power. For the purposes of these experiments the efficiency figure has been defined to be the percentage conversion of power transferred to the discharge, to the laser output power. Measuring the laser output power is a simple matter of using a laser power meter. Measuring the microwave input to the discharge is more complicated. One may either measure or estimate the net microwave power entering the laserhead or, alternatively, measure the temperature rise in the laserhead as a result of cooling the discharge. Estimation of the microwave input power requires a great deal of knowledge about the system which was not available. Direct measurement would require a directional coupler and power meter which were also unavailable. The second, calorimetric, method can be implemented by measuring the temperature change in cooling water passing through the device and then estimating input power from the water flow. While reasonably easy to implement, this system requires that all heat is extracted from the discharge by the cooling. This rules out input power measurements when gas flow rates are sufficiently high that heat removal by gas transport is significant compared with the diffusion cooling rate.

As was mentioned in the previous section, operation in sealed-off mode alters the discharge shape and the lasing characteristics of the device. Fortunately, while the

discharge and lasing characteristics are altered the microwave input power appears to remain unchanged for a given pressure and magnetron voltage over the range of pulse width/period used. This can be understood by considering three empirically observed results. First, input power is directly proportional to pulse width when the magnetron voltage is fixed, see table 7.1. Second, the only electrical changes in the microwave cavity between flowing and non-flowing operation can be in the gas itself. Third, these changes appear to be small in comparison to the system as a whole as no changes in SWR are observed. This leads to the conclusion that although the shape of the discharge is changing slightly between flowing and non-flowing operation the input power to the discharge remains unchanged. Note that the change in shape of the discharge may make it unsuitable for laser action if, for example, all the energy is concentrated in very localised regions.

Pressure (torr)	Pulse period/width (μs)	Power in (W) $\pm$4
10	400/40	45
15	400/40	47
15	400/60	72
20	400/40	51
20	400/60	74

Table 7.1: Microwave input power to the V1 discharge. Measured calorimetrically at various pressures and pulse shapes. Note that widening the input pulse by a factor of 1.5 results in an increase in input power of 1.5.

As confirmation of the above, power input measurements under flowing and non-flowing conditions give very similar results suggesting that the gas flow (on this laser, at this flow-rate) only plays a small role in cooling the discharge. This is not too surprising considering the cooling results described in section 3.5.7 and the flow rate of $\sim$ 25 mL/s at 760 torr. Given this flow rate, a pressure of 15 torr and a laser gas volume of 40 mL it is found that the gas is exchanged 32 times every second. This may appear to be a fast rate of gas removal, however, considering that the characteristic cooling time of the gas is of the order of 60 μs, one finds that the gas has been cooled to $1/e$ of its initial temperature after it has moved only 0.7 mm.

The highest observed efficiency of the device was approximately 2.5%. This figure, while low for a CO_2 laser, is reasonable considering the non-uniformity of the discharge - a problem discussed in more detail in section 8.10.

Area-cooled RF CO_2 lasers running under optimum conditions are capable of extracting approximately 20 kW/m^2 from a discharge with typical efficiencies ranging from 10 to 15% [3]. Using the geometry of the V1 laser this would translate to 120 W for a discharge running at 75 torr with an input power of 1 kW. Therefore, given the input power of 50 W, an output power of 5 W might be a reasonable goal. Even then, an RF laser would have to be running at about 75 torr (cf. 30 torr) to achieve this figure. Given the non-uniform nature of the

discharge, the output powers achieved here may be viewed as encouraging.

7.1.4 Mode pattern

Mode output mode patterns from the V1 laser are shown in figure 7.4. These mode patterns which were created using thermally sensitive paper show that the laser is running with a high order transverse mode which is waveguided in the transverse (narrow) dimension but is a high order gaussian in the lateral (wide) dimension. Although unsuitable for most applications no attempt has been made to correct this. Waveguide optics have been studied in great depth by others (see chapter 5).

Figure 7.4: Five typical mode patterns from the V1 laser output. These patterns were rendered using thermally sensitive paper. Scale 1:1.

7.1.5 Laser pulse shape

In this section the pulse widths of the microwave input pulse and the laser output pulse are examined as they relate to average laser output power. The laser output pulse shape has been measured using a fast HgCdTe detector. Figure 7.5 shows how the laser output pulse changes as the input microwave pulse is varied from 16 to 72 μs in steps of 8 μs. The graphs show that the energy in the output pulse increases with the increase in input energy. However, the relationship is not linear and it becomes counter productive to continue to increase the input pulse width beyond a certain point.

For these measurements the period was set to 2 ms which resulted in poor average output power but showed the entire laser pulse which lasted $\sim$ 0.5 ms. Note that the laser pulse was delayed until approximately 30 μs after the end of the microwave pulse. This means that lasing is not possible during plasma excitation and it is a good indication that the value of E/N is far from optimum. More practically it means that continuous-wave (CW) operation is not possible.

A useful quantity to examine is the output pulse energy divided by the input pulse energy. This figure, which is the conversion efficiency for a single pulse, is shown in figure 7.6 plotted against input pulse width ($\propto$ pulse power). The graph shows that microwave pulse widths greater than 30 μs start to become less efficient. This drop in efficiency will result in extra heating of the discharge possibly making future pulses less efficient. In this case, however, there is a long (2 ms) delay between pulses so there is ample time for the discharge to cool.

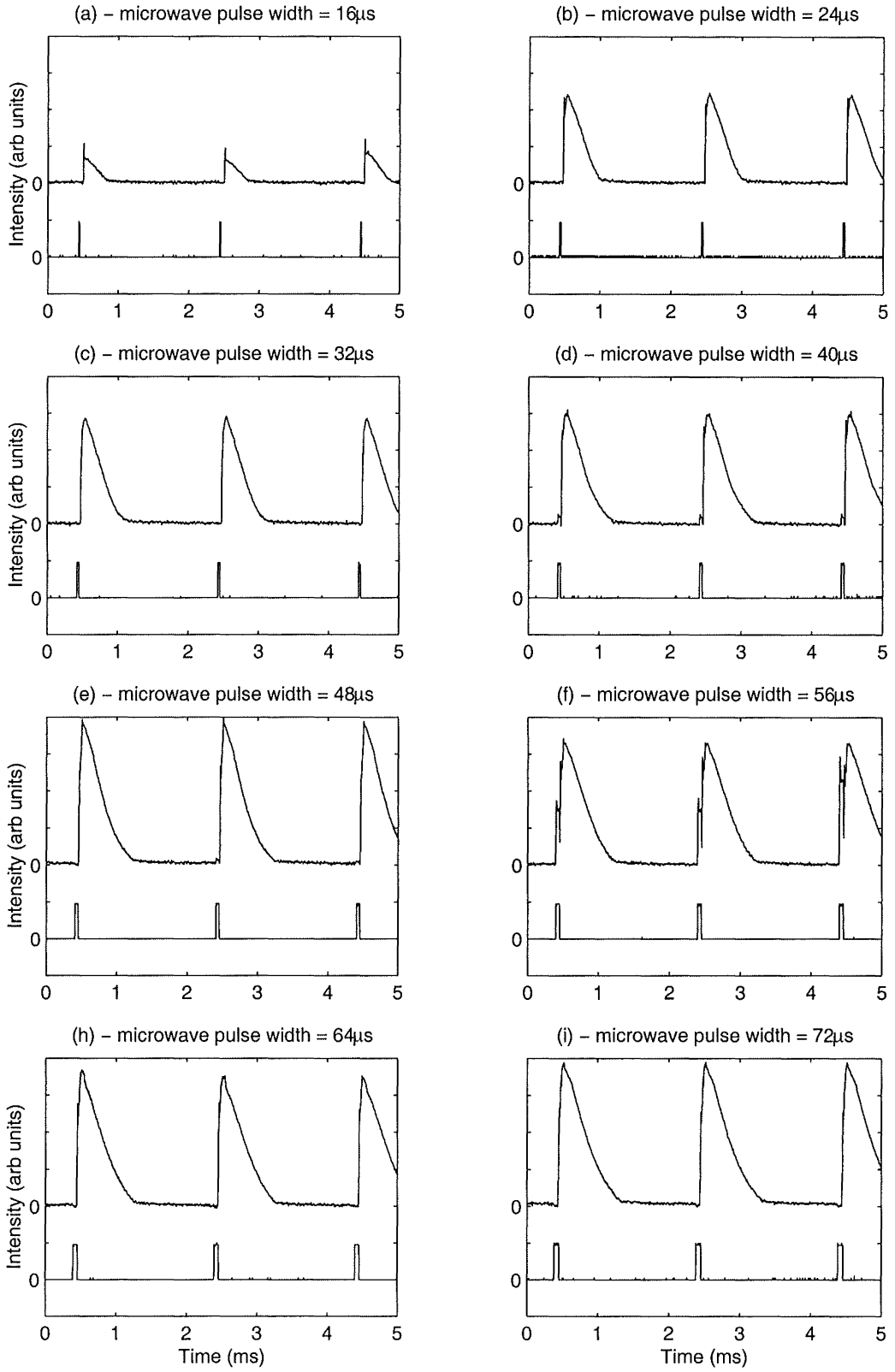

Figure 7.5: Laser output pulse (upper trace) relative to the microwave input pulse (lower trace) at 15 torr for input pulse widths between 16 and 72 μs. Pressure 15 torr.

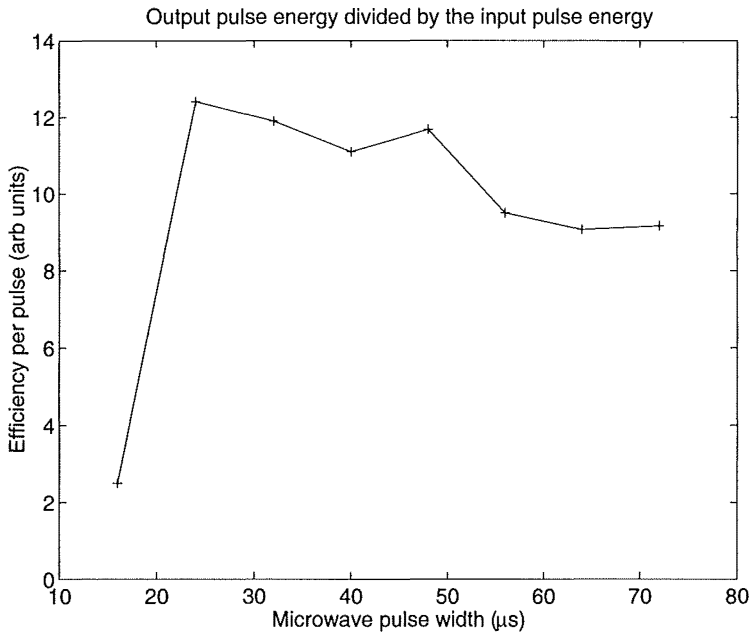

Figure 7.6: Relative efficiency per pulse plotted versus pulse width. Pressure 15 torr. Pulse period 400 μs.

In order to optimise the average output power the pulse period needs to be reduced to a value lower than 2000 μs. Figure 7.7 shows how changing the microwave pulse period affects the output pulse. Reducing the period to 1000 μs makes no detectable change to the shape of the laser pulse as the system has had sufficient time to return to its initial state. At 500 μs the output pulse is definitely shortened but the average output power has also risen significantly. At 250 μs pulses are being severely truncated and the output power has not increased. The efficiency has therefore dropped.

From the preceding observations it would appear that an input microwave pulse width of 30 μs with a period of 500 μs would lead to the most efficient laser output. General observations during experimentation confirm this. These figures do vary slightly with pressure but are generally a good point at which to start the optimisation process.

In addition to the experimental measurements above, a number of optical spectra were taken from the discharge in order to determine its suitability as a CO_2 laser gain medium. These measurements are discussed in chapter 8.

7.2 The V2 Laser

The V2 cavity, for which the design is detailed in section 3.3, was designed to test the effectiveness of inserting a dielectric slab (see section 6.9) in series with the discharge. Although it is a simple and easily fabricated geometry, which

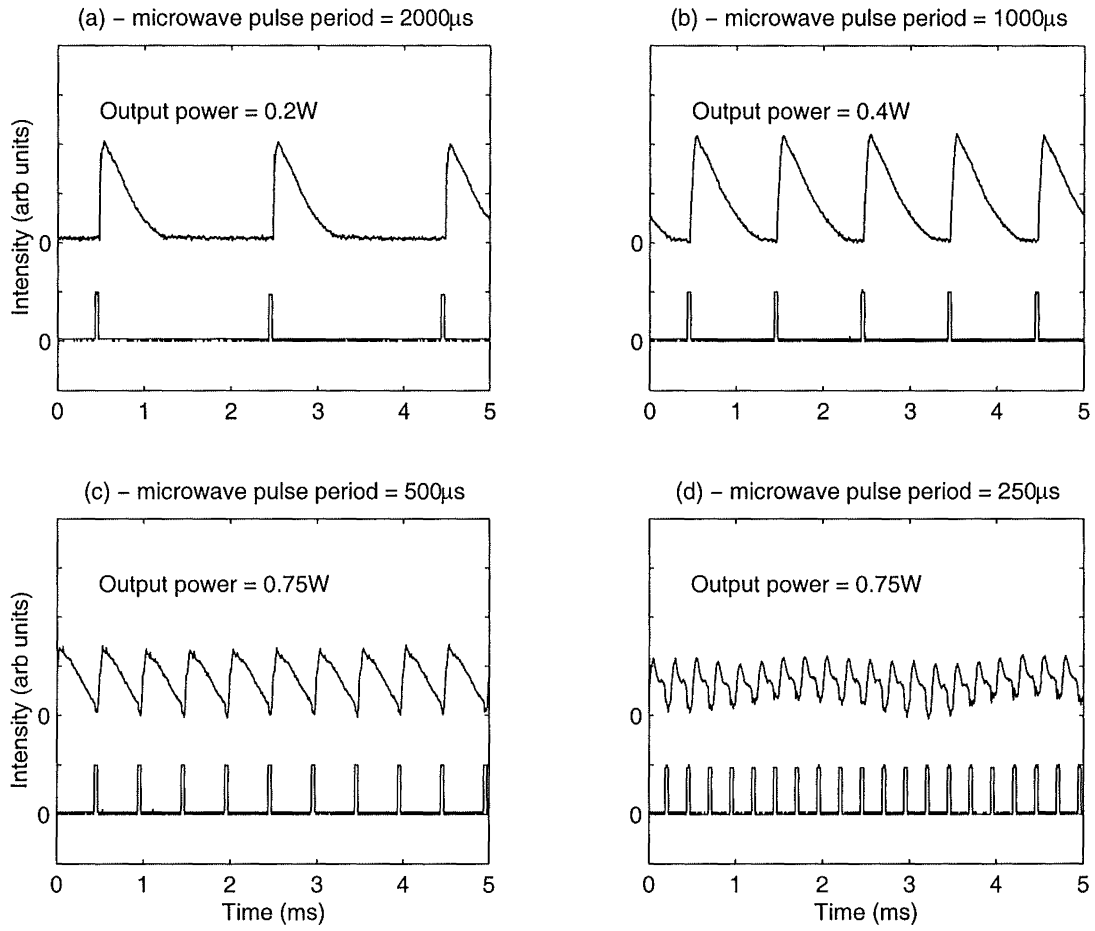

Figure 7.7: Change in laser pulse shape when the microwave pulse period is reduced from 2000 μs to 250 μs. Pressure 15 torr. Pulse width 40 μs.

was never intended to produce laser output, it has produced the most uniform discharges of the three designs tested. The possibility of adding optics to this design to convert it into a laser was discussed in section 5.2.2.

The improvement made by adding the quartz dielectric to the discharge circuit is clearly observable. At low pressures (< 15 torr) the discharge fills most of the discharge cavity and consists of a single region of plasma. In contrast to V1, this holds true for flowing and non-flowing gas. Furthermore, the discharge remains uniform, and is able to be excited, at much higher pressures than was possible with the V1 design. Operation with reasonable discharge uniformity was possible up to 30 torr. However, above that, the plasma separated into several bands and the discharge became increasingly hard to strike.

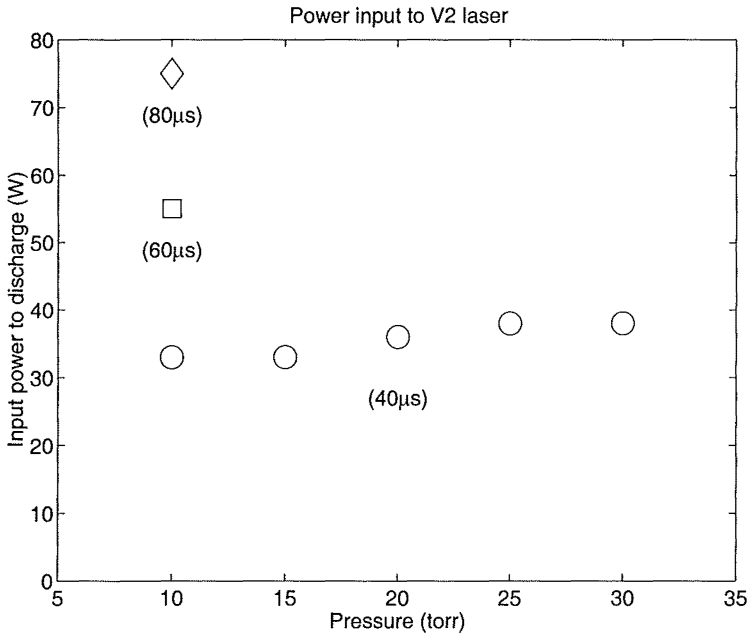

Figure 7.8: Power input to the V2 discharge. Pulse period 400 μs. Pulse widths are indicated in brackets.

The input power to the discharge is plotted in figure 7.8 under conditions similar to those used in the V1 laser. The power deposited in the discharge scales linearly with pulse width and appears to be independent of pressure between 10 and 30 torr. It should be noted that because only the bottom (aluminium) electrode is water cooled, only the heat removed from the lower electrode will contribute to the calorimetric measurement of the input power. The input power measurements may therefore be up to twice the figures given here. Realistically, the rise in temperature of the quartz and its lower thermal conductivity will mean that the aluminium electrode will remove the majority of the heat energy. It is therefore not unreasonable to assume that the power input to the V1 and V2 lasers is similar under the same operating conditions.

This laser design showed that the addition of a dielectric resulted in a distinct

improvement in the discharge quality. A number of optical observations of the V2 discharge, covered in chapter 8, also confirm the improvement due to the dielectric. Also, its ability to produce uniform discharges without gas flow makes it suitable for running in sealed-off mode. This, in addition to its simple and compact design, would make it a good starting point for a production laser once the problem of optics had been addressed (section 5.2.2).

7.3 The V3 Laser

The V3 laserhead (design is detailed in section 3.4) incorporated the quartz dielectric in a configuration which included an optical resonator. The design was therefore capable of lasing. In general the V3 laser out-performs V1 and produces more consistent (repeatable) results. Under the same operating conditions as the V1 laser, V3 will generally produce output powers a factor of two greater. Sealed-off operation was possible and, in fact, at the gas flow rates used V3 was fairly insensitive to changes in rate. Discharges could be produced at pressures up to 40 torr, with reasonable uniformity up to 30 torr.

The complex internal structure of the V3 laser meant that it was susceptible to discharges in undesirable places such as between the mirror holder and the electrode. While these discharges did not directly affect lasing their erratic nature could cause the field configuration within the cavity to change. This is especially noticeable at higher pressures (> 30 torr). In this respect the V2 laser fared better because of its simple internal structure. The insertion of a shield in front of the mirror holder should eliminate this problem.

7.3.1 Interesting gas phenomena

Initial experiments with the V3 laser led to variable and somewhat confusing output power results. It appeared that when the laser was set up under apparently the same initial conditions, the laser output would be at a random level. Further investigation showed that laser performance varied as a function of time. After filling the laser with gas to a certain pressure and starting the discharge, the laser output would rise to a level, stay constant for 20 to 30 seconds and then slowly drop back to zero or near-zero. If the discharge was continued for 10 and 20 minutes the power would at some point rise again to an almost constant value. Furthermore, after this process had been completed once, the laser output from a newly lit discharge would then stabilise after 30 to 40 seconds. The fact that the initial discharge process needed to be performed only once suggested that a change in the gas chemistry was occurring. To further investigate this phenomenon a mass spectrum analyser was attached to the laser vacuum system and the gas content analysed.

The setup of the mass spectrum analyser (mass spec) is shown in figure 7.9. The analyser being used (Spectramass Dataquad) required pressures less than

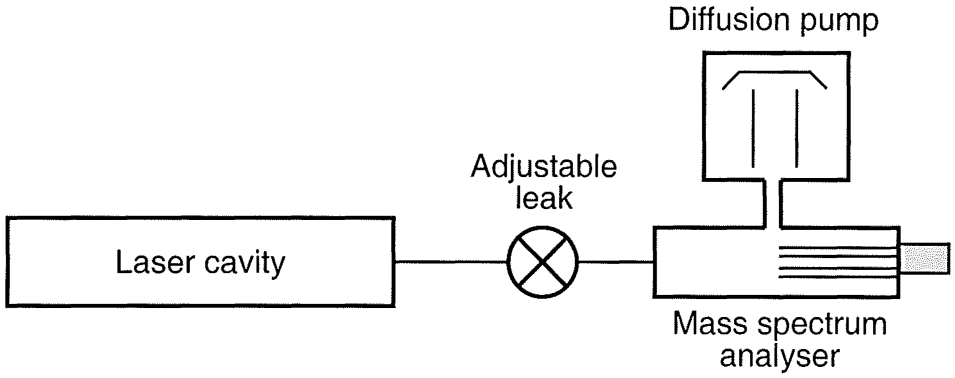

Figure 7.9: Setup of mass spectrum analyser system.

10^{-5} torr for safe operation. This required a very small quantity of gas to be leaked into an auxiliary vacuum chamber which was at a much lower pressure ($\lesssim 10^{-6}$ torr) than the laser. This auxiliary chamber was pumped continuously by a diffusion pump to prevent outgassing or gas from the leak raising the pressure above the safe limit for the mass spec. Pumping this chamber continuously rather than introducing discrete volumes of gas meant that fast moving (lighter) species would be removed from the gas more quickly than slower moving (heavier) species. Consequently the following numerical results should be viewed in a qualitative manner only. As the analyser was borrowed on a strictly short-term loan there was insufficient time to attempt to calibrate for this differential pumping or for the response of the instrument to various species.

Investigation of the phenomenon proceeded as follows. A background reading of residual gases in the auxiliary and laser chambers was taken (see figure 7.10) so that it could be subtracted from subsequent measurements. This background consists of components commonly found in vacuum systems that have been exposed to the atmosphere at some point. They can be identified as: hydrogen (mass 2), water (17 and 18), nitrogen (14 and 28), argon (40) and carbon dioxide (15, 28 and 44). The laser cavity was then filled with gas and a mass spectrum of the initial conditions taken, see figure 7.11a (background subtracted). Note that the peaks for He, N_2 and CO_2 do not appear in the same ratios as those present in the gas. This is due to the differential pumping and response issues discussed earlier.

The discharge was then started and run for approximately 30 minutes after which another spectrum was taken. Figure 7.11b shows the mass spectra taken after the 30 minute discharge period. The differences between the initial and final spectra can be highlighted by subtracting one from the other. The results are shown in figures 7.12a and 7.12b. In the second figure (b) the axes have been cropped so that changes in masses other than 28 may be more easily observed.

In general the results did not depend strongly on pressure or the power input except that some circumstances lead to faster establishment of conditions suitable

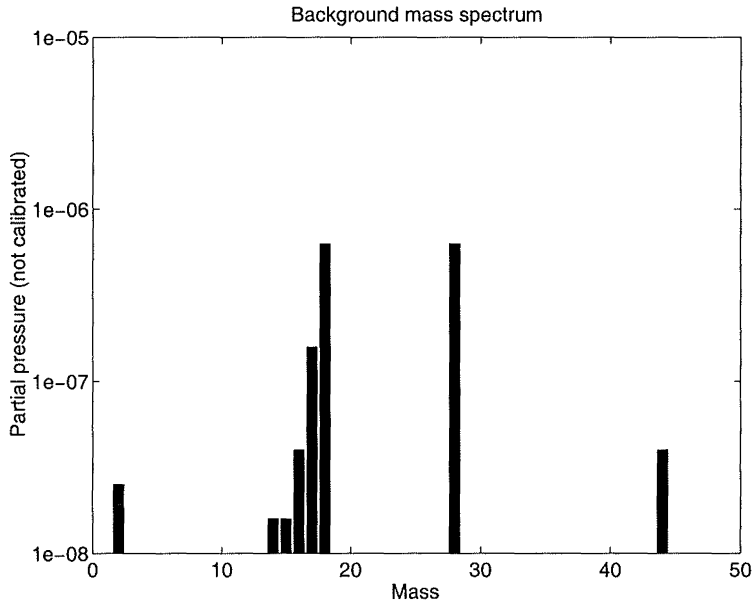

Figure 7.10: Background mass spectrum of the laser cavity and auxiliary chamber. The peaks represent: hydrogen (mass 2), water (17 and 18), nitrogen (14 and 28), argon (40) and carbon dioxide (15, 28 and 44)

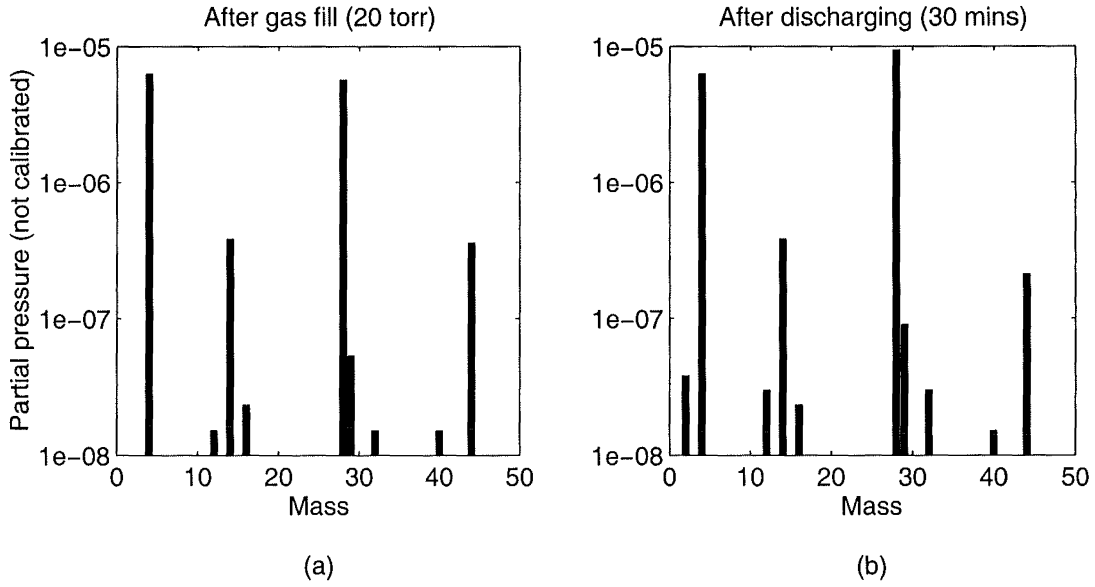

Figure 7.11: (a) Mass spectrum of the cavity after it has been filled to 20 torr with the laser gas (log scale, background subtracted). (b) Mass spectrum after the laser has been discharging for 30 minutes.

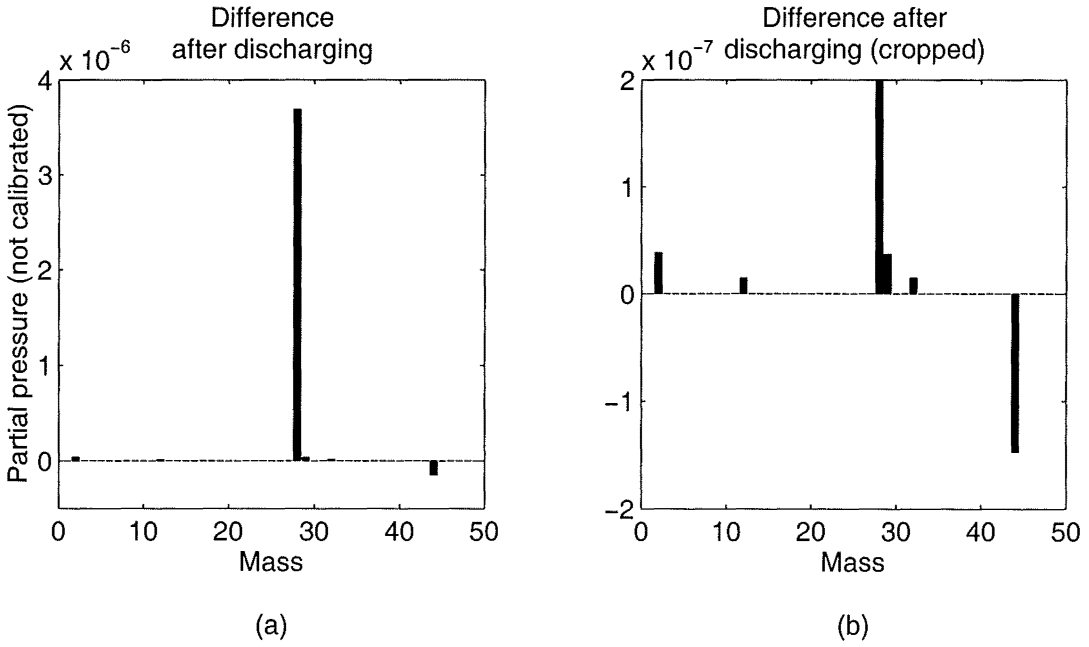

Figure 7.12: (a) Change in the mass spectrum of the cavity after discharging for 30 minutes (linear scale). (b) Graph (a) cropped to expose the smaller detail.

for lasing. All followed the general trends shown in figure 7.12. It appears that a significant fraction of the CO_2 (44) has dissociated into carbon monoxide (CO, 28) and oxygen (O_2, 32). Some carbon (C, 12) also appears to be present. The change in hydrogen (H_2, 2) is probably due to dissociation of the trace amounts of water or hydrocarbons (such as rotary pump oil) and is unlikely to be significant. Even though N_2 and CO share the same atomic mass, changes in the level of N_2 are very unlikely due to its non-reactive nature.

The fact that an increase in CO appears to aid the lasing is quite perplexing. While it is well known that CO does not seriously affect the lasing process, as it also has a near resonance with the upper lasing level, the excitation pathway it provides is not as efficient as excitation via N_2. For this reason small amounts of H_2O or H_2 are often added to sealed-off CO_2 lasers to aid in the recombination of dissociation products. Normally laser output is observed to drop as the CO faction rises [100, pg 104]. The most likely reason that the CO is improving the laser output in this case is that it is providing a more efficient excitation pathway for a discharge which has an non-optimum E/N value. Optimum E/N values result in electron energies of between 2 and 2.5 eV. In this energy range the excitation cross sections for CO_2 and N_2 lead to optimum excitation of the upper lasing level. At electron energies outside this range the cross section drops rapidly (see figure 2.6). However, CO has a higher peak cross-section and does not fall off so rapidly (see figure 2.8). The CO may therefore be providing an alternative excitation method for plasma with a non-optimum electron energy.

7.3.2 Input power

The power deposited in the discharge by the microwaves using the same settings as those used for figure 7.8 is about 38 W, the same as in the V2 laser. Once again the power deposition is linear with microwave pulse width and has no obvious pressure dependence. Measurements of input power are graphed in figure 7.13.

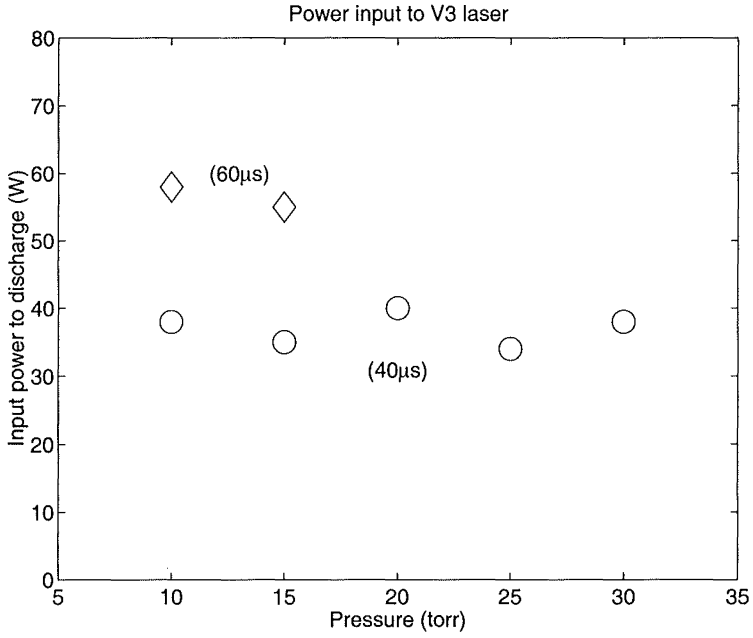

Figure 7.13: Power input to the V3 laser for a period of 400 μs. Pulse widths are indicated in brackets. No gas flow.

7.3.3 Output power and efficiency

For comparison with the V1 laser, a number of output power measurements were made under similar conditions to those used for the V1 measurements of section 7.1.2. As the V3 laser is capable of being operated in sealed-off mode, at least for short periods of time (many hours), with relatively little effect on output power, the following power measurements were made with no gas flow.

Figure 7.14 shows how the laser power varies with pressure for an input power of $\sim$ 35 W and pulse period and width of 400 μs and 40 μs respectively. These are similar conditions to those used in figure 7.2. The most notable difference between the two graphs is that the output power has doubled even though the input power has been reduced by approximately 30%. This obviously represents a significant rise in efficiency ($\sim$ 5% at 20 torr). The flattening-out of the curve for pressures greater than 20 torr is due to the reduced gain volume presented to the optics when the discharge length contracts. Above 20 torr, the discharge had contracted to fill only two thirds of the available cavity. Power measurements at 25 and 30 torr are quite variable due to this change in discharge length.

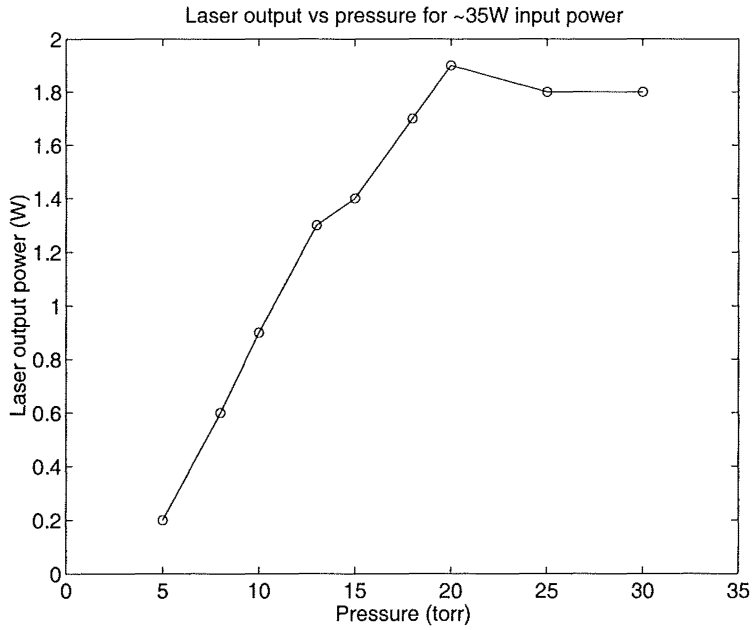

Figure 7.14: Output power of the V3 laser versus pressure in sealed-off mode when operated with a microwave pulse period of 400 μs and a pulse width of 40 μs. The input microwave power was $\sim$ 35 W.

A survey of laser output power measurements at different pressures and microwave pulse shapes was made in order to determine optimum conditions for laser output. These measurements were made after the gas had been discharged for 20 minutes as described in section 7.3.1 above. Each reading was obtained from the power meter after the discharge had been running for one minute. There was a gap of one minute between each measurement where the discharge was turned off so that the initial conditions would be restored. The results of the survey are shown in figure 7.15. Although the general trends and relative amplitudes in these graphs are repeatable from one day to the next the measured output power can often vary by as much as 0.25 W. Even so, there are a number of general trends which can be observed from these readings.

Laser output generally increases with pressure and the maximum output occurs at a pressure of 25 torr. It is likely that the reduction in output power at 30 torr is due to the lack of discharge uniformity and available gain volume rather than 25 torr being the true optimum pressure for this input power and gas mix.

The duty cycle of the microwave pulse appears to be optimum between 10 and 20%. This can be observed more easily in figure 7.16 where the data from figure 7.15 has been re-plotted as output power versus duty cycle.

High efficiency is generally obtained at lower microwave pulse widths as shown in figure 7.17, where efficiency has been plotted versus pulse width. Note that the efficiency values shown in these graphs are estimates based on the assumption that the microwave input power is 38 W in each case. The value of 38 W has been

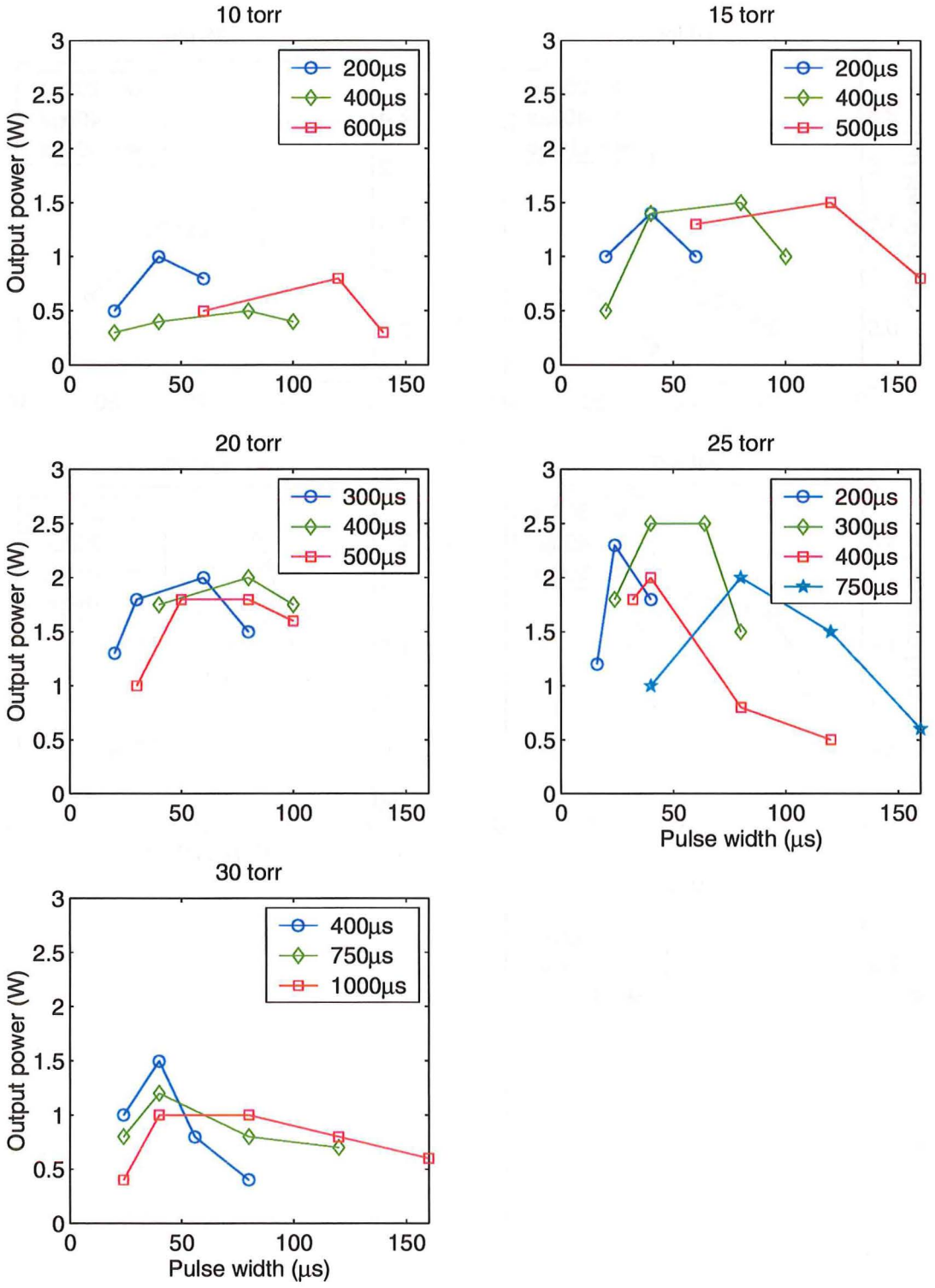

Figure 7.15: Output power versus pulse width for pressures between 10 and 30 torr. Input pulse period 400 μs. Input power $\sim$ 38 W for a 40 μs pulse width.

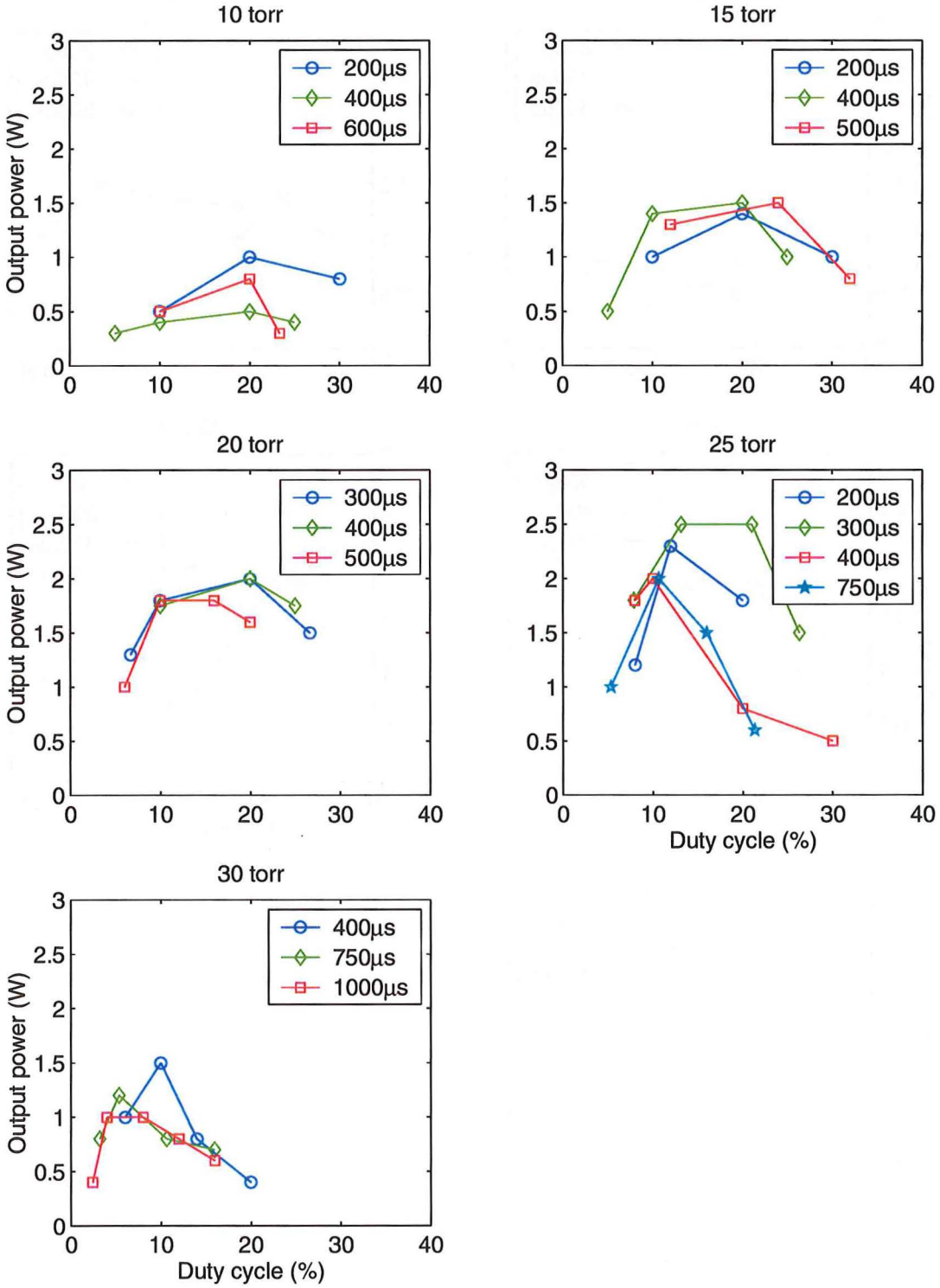

Figure 7.16: Data from figure 7.15 re-plotted as output power versus duty cycle.

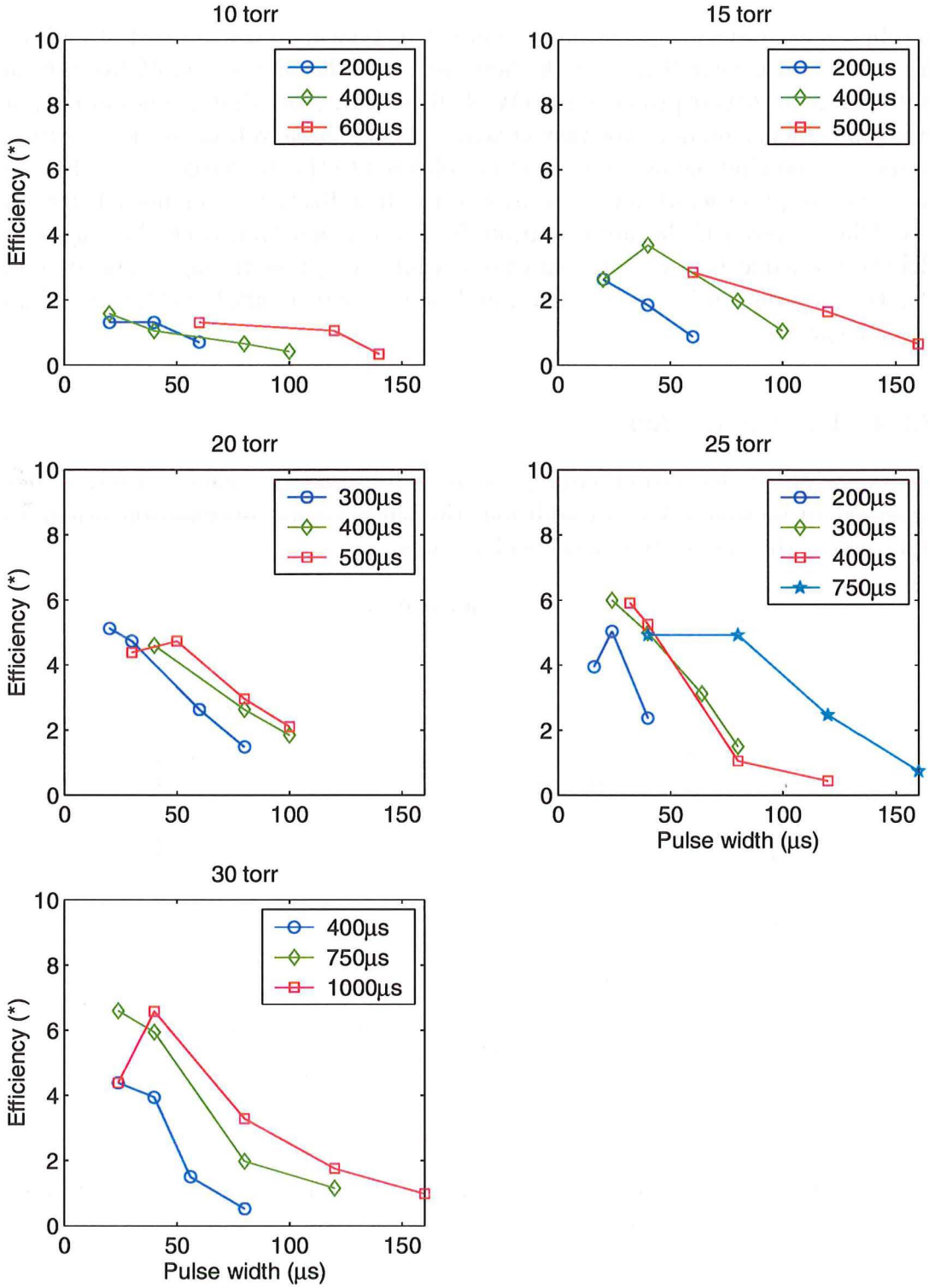

Figure 7.17: Data from figure 7.15 re-plotted as efficiency versus pulse width.

shown to be relatively constant (see figure 7.13) for the settings used to conduct these experiments.

Explicit measurements of efficiency resulted in typical values between 4 and 5% for pulse widths near 40 μs. The highest recorded efficiency was 6.5% taken from a discharge at 20 torr producing 1.5 W of IR output. Note that the power output from the magnetron does not vary greatly with the input voltage so there is little scope for changing the amount of power delivered to the discharge, other than by altering the pulse width and repetition rate. It is likely that higher efficiencies could be achieved if the power output from the magnetron could be varied to deliver the same power to the discharge while the pulse timings were altered. Another way of implementing this would be to insert a variable attenuator into the waveguide.

7.3.4 Laser pulse shape

Examination of the output laser pulse of V3 reveals the same general trends observed in section 7.3.3. In addition, the time-domain information brings to light some other interesting aspects of the laser.

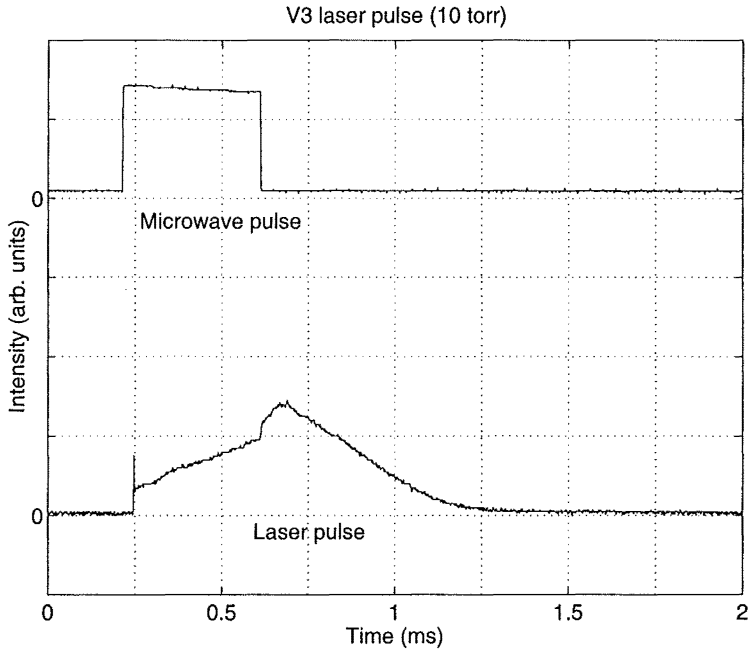

Figure 7.18: Output laser pulse in relation to the input microwave pulse. (10 torr, 400 μs width, 2000 μs period)

Figure 7.18 shows an output laser pulse from the V3 laser relative to its microwave input pulse. One detail to note is the delay between the start of the microwave pulse and the start of the laser pulse. This delay (30 μs here) increases with both pulse width and pressure although not rapidly. Typical values reside between 20 and 40 μs for the pressure range used here (10 to 30 torr). The more obvious

difference between this laser pulse and those produced by the V1 laser (figures 7.5 and 7.6) is that laser output now occurs during the microwave pulse. This is a very important difference and suggests that the configuration of the laser is near the point where CW operation is possible.

It is very likely that this change in behaviour is due to a more favourable E/N ratio brought about by the new geometry of the V3 laser. Optimum lasing occurs in a discharge when the ratio E/N is such that significant contributions to the excitation of the upper lasing level come from both electronic excitation and indirect excitation via N_2 (see section 2.7).

Recall that in the V1 laser there was no lasing until the termination of the microwave input pulse at which point laser pulses of the order of 500 μs were typical. The relatively short lifetime of the upper lasing level suggests that it is being excited long after the input pulse. The obvious source of this excitation is N_2 with its long (metastable) lifetime. It is likely that during the power input stage the vibrational levels of the gas species are being excited somewhat indiscriminantly. This would account for the lack of population inversion (and lasing) during the microwave pulse. Then after the pulse ends normal decay processes occur de-populating the excited CO_2 states, including the lower lasing level. However, N_2 remains excited longer due to its metastable nature and finds a de-excitation pathway via the CO_2 molecule in the normal (laser) manner.

In the V3 laser the fact that lasing occurs during the input pulse means that a population inversion is being created during the pulse and that the excitation is targeted more to the upper lasing level. From this it may be inferred that the E/N (which is related to the electron energy distribution) is at a more favourable value. Although it is difficult to modify separately the value of E or N due to the the contraction of the discharge at higher pressures (leading to increased E), some systematic change in the ratio E/N should be expected as the pressure is increased. Experimentally this change should be most obvious during the microwave pulse and would manifest itself as a change in the level of laser output as the pressure is changed. Figure 7.19 shows how the laser pulse changes with increasing pressure under similar excitation conditions. The laser output during the microwave pulse drops to zero as the pressure ($\propto N$) is increased from 15 to 30 torr.

Given that the E/N ratio is still not optimum for the conditions presented here, it is worth examining what can be done to improve the situation. Obviously varying the pressure which is directly proportional to N is of limited use as, in general, higher output powers are achieved at higher pressures due to the increase in the number of possible lasing states. In order to maintain optimum excitation conditions E must increase with N to keep the ratio constant. One possibility is to change the value of E/N which leads to optimum output. This can be accomplished by altering the ratio of the gases in the mixture, although there is only a limited range about which the value can be shifted. Detailed numerical simulations [92] of RF discharges can predict optimum E/N values for given gas

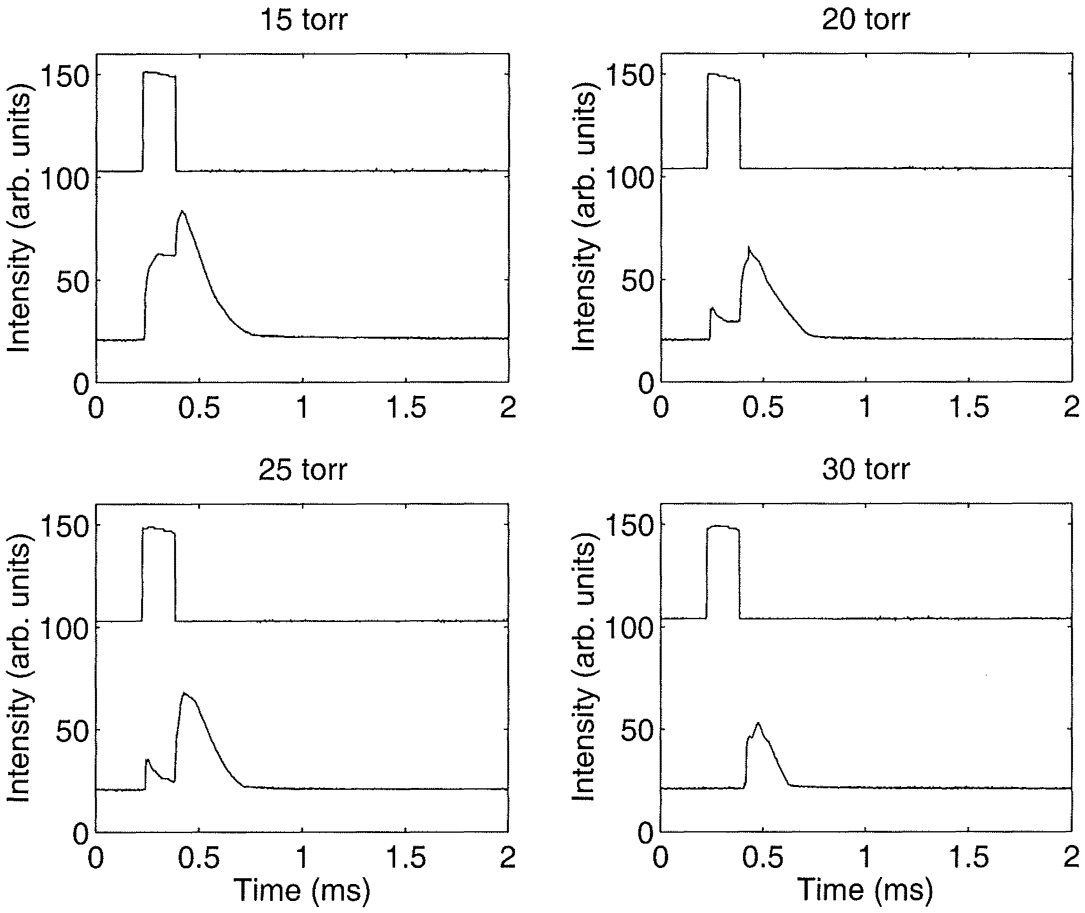

Figure 7.19: Change in laser pulse shape as the pressure is increased.

ratios however these models were not specifically designed to work at microwave frequencies. An empirical investigation of the several gas mixes is presented in section 7.3.5.

7.3.5 Gas mixing

In all the experiments discussed in this thesis, except for those in this section, a readily available gas pre-mix designed for DC lasers was used. The ratio of CO_2:N_2:He in this mixture was 1:3:18. The literature indicated that in general, altering the ratios of the gases only leads to a moderate improvement in the laser output power as long as the initial ratios are in a generally accepted range. As a rule of thumb, similar amounts of CO_2 and N_2 should be present and significantly more He should be present than either of these. RF-excited lasers commonly use the ratios 1:1:8 and 1:1:3. Even though the expected gains in output power would be small it was felt that some investigation of different gas ratios should be made, firstly due to the findings of section 7.3.1 concerning dissociation effects and secondly the excitation frequency is somewhat higher than RF frequencies.

The output power produced for various gas ratios at 15 torr is presented in table 7.2 along with some general observations.

Ratio (CO_2:N_2:He)	Power (W)	Comment
1:3:18	0	std DC mix (poor output due to short discharge time)
1:1:8	0.8	reasonably uniform discharge (std RF mix)
1:1:3	2.0	reasonable discharge (std RF mix)
1:1:1	1.7	poor discharge, high initial power, better at high PRF
3:1:1	1.0	broken discharge
3:1:8	1.25	reasonable discharge
3:1:20	0.5	good discharge
1:3:8	0	good discharge

Table 7.2: Output power for various gas ratios at 15 torr. The power measurements were made after the discharge had been running one minute. The pulse period and width were 400 and 40 μs respectively.

The table shows that the standard gas mix of 1:3:18 was a poor choice for initial studies of a microwave-pumped laser in that the power output from this gas is low until the dissociation process described in section 7.3.1 has occurred. In most of the other cases examined here, where the CO_2 and N_2 levels are similar, the gas is suitable for producing a population inversion immediately. Even so, the output power does not increase dramatically due the use of these new gas ratios. The uniformity of the discharge depends strongly on the relative abundance of He in the mixture. The higher the proportion of He present, the more uniform the discharge. Best results are found when CO_2 is present in similar quantities to N_2. Lower CO_2 levels tend to result in output which is initially very poor.

Increasing the level of CO_2 above that of N_2 appears to have little effect on the output power or discharge uniformity. In summary, the standard RF mixes 1:1:8 and 1:1:3 would also appear to be appropriate for microwave-pumped CO_2 lasers, at least within the operational parameters of the V3 laser.

7.3.6 Flowing gas versus sealed-off operation

All of the laserheads used in these experiments were capable of being run in either a flowing-gas or sealed-off mode. Sealed-off operation of the V1 laser led to non-uniform and erratic discharge behaviour. Little, if any, output power was observed. When gas was flowed through the discharge chamber, significant improvements in discharge uniformity and output power were observed. These improvements can be attributed to the turbulence in the gas preventing plasma filaments from forming [54]. Such filaments, which draw high currents in localised regions, have a significant impact on the performance of the laser.

In the V3 laser, only minor differences in discharge uniformity were observed between flowing and sealed-off operation, due to the presence of the quartz dielectric. Therefore, the sealed-off mode was used for most of the experiments conducted using this laserhead. There was little difference in output power measurements between the two operational modes apart from changes related to gas composition (see section 7.3.1), which affected initial readings.

While no attempt was made to prepare the discharge cavity for sealed-off operation, output power did not drop after several hours operation. A number of techniques can be employed to a ensure long sealed-off lifetime. Baking the cavity under vacuum reduces volatiles embedded in the metal surfaces which would normally outgas into the discharge after the device is sealed. The addition of xenon has been shown to increase sealed-off lifetimes and output power [16, 33] by lowering the E/N of the discharge. Small amounts of H_2O or H_2 aid in the recombination of CO_2 in addition to increasing the depopulation rate of the lower lasing level [99]. All these techniques could be applied to the V3 laser to promote a long sealed-off lifetime.

7.3.7 Gap spacing

The spacing of the discharge gap is an important factor in slab cooled lasers. In general smaller gaps lead to more rapid cooling of the discharge and consequently higher output power. At RF frequencies the electron oscillation amplitude places a limit on the minimum gap spacing which can be used. When this amplitude is comparable with the discharge gap, the plasma sheaths form in the centre of the discharge. The high electron energies in these regions are unsuitable for inducing a population inversion.

As the excitation frequency is increased, the electron oscillation amplitude decreases. This reduces the size of the plasma sheaths in addition to moving them

towards the electrodes. For small gap spacings, this can represent a significant increase in gain volume. Discharge similarity laws for RF have shown that changes to gap spacing should be inversely proportional to changes in gap spacing [13] or,

$$\omega d = \text{constant} \tag{7.1}$$

The pressure should also be increased as the gap is decreased. While these similarity laws dictate how various parameters should scale, in practice, implementation can be challenging. At spacings of the order of 1 mm variations in gap due to mechanical deformation by vacuum pressure, for example, can be a significant faction of the total gap spacing. Great care must be taken to avoid the non-uniform plasmas such variations will induce.

A 2 mm gap spacing was used for all experiments detailed thus far. A spacing of 2 mm was chosen as a starting point because it did not over-complicate the design. Experiments with gap spacings of 3 mm and 4 mm gave inferior results. The discharge became harder to strike at lower pressures than with the 2 mm spacing and resulted in poor uniformity even at pressures of 10 torr. Consequently output power was significantly reduced ($\sim$ 0.5 W max).

A gap spacing of 1 mm was also investigated. Due to the increase in mismatch in impedance between the laserhead and waveguide, discharges were hard to strike. However once initiated the discharge appeared relatively uniform, except at the centre where the plasma appeared brighter. This high intensity region can be attributed to a slightly narrower gap at the centre of the cavity due to mechanical flexure under vacuum. For this reason, no attempt was made to align the optics precisely and output powers were modest ($<$ 0.5 W). Despite these mechanical difficulties, discharges at this gap spacing appeared promising.

Chapter 8

Optical Diagnostics

Measurement of laser and plasma parameters in a microwave-excited CO_2 laser is more difficult than in conventional RF and DC excited lasers. This is because one of the fundamental plasma parameters, E/N, is difficult to measure. This parameter, which is proportional to the ratio E/p, is easily obtained in RF and DC plasmas by measuring the interelectrode voltage and the pressure. Unfortunately in microwave-excited systems the two electrodes are in direct electrical connection and the supplied power does not flow through a cable, for which the current can be measured. This makes it very difficult to get measurements of the applied voltage, current and input power. Measurement of other plasma parameters can also be difficult. The gas temperature is awkward to measure because of the small gap ($\sim$ 2 mm) in which a measuring device must be placed. In addition to the perturbing effect these probes have on the discharge, such devices have to be well shielded from microwaves in order to produce accurate and reliable results.

One method of interrogating the discharge which does not suffer from microwave interference or awkward geometries, is sidelight spectroscopy. As the sidewalls of the laser are vacuum-sealed by fused-quartz, they provide an optical window through which the discharge may be observed. Quartz windows have a large pass-band which extends well into the ultraviolet. This means that the discharge can be observed spectroscopically by making a small hole in the waveguide structure and placing an optical fibre through it. Small holes in the waveguide structure do not significantly affect the microwave cavity because the holes are much smaller than the wavelength of 12 cm. In fact a mesh wall was used for most experiments.

8.1 The optical spectrum of a CO_2 laser discharge

The optical spectrum available from sidelight emissions of CO_2 lasers consists primarily of transitions from the second positive system of nitrogen ($C^3\Pi_u - B^3\Pi_g$). These transitions are vibronic or vibrational-rotational which means that a rotational band structure is present about every vibrational transition. A typical CO_2 discharge spectrum is shown in figure 8.1. The main vibrational transitions have been labelled with their initial and final vibrational states, and associated wavelength. The decay into the ultraviolet of each line is due to the rotational

fine structure of each vibrational transition.

8.2 Optical spectra as a diagnostic tool

Given a discharge spectrum of the form shown in figure 8.1 it should be possible to infer information about the state of the plasma, specifically, the rotational temperature of the laser gas and the populations of the vibrational states. The rotational temperature is of interest because it is equivalent to the thermal temperature of the gas due to the very fast thermalisation between rotation and translation ($\sim 10^{-8}$ s). Measurement of the rotation temperature from discharge spectra is discussed further in section 8.9.

8.3 Vibrational temperature

Using estimates of the vibrational populations of the second positive system of nitrogen ($C^3\Pi_u - B^3\Pi_g$) and an excitation model, it is possible to estimate the vibrational populations of the electronic ground state of N_2 ($X^1\Sigma_g^+$). With this information a "vibrational temperature" for the ground state of N_2 can be estimated. The words "vibrational temperature" are in inverted commas as the concept of temperature must be well defined for any values to be meaningful or suitable for comparison with the work of others. The specific method of calculating a vibrational temperature for N_2 will be detailed later; for the moment the "vibrational temperature" can be taken to imply that the populations of the vibrational states form a Boltzman distribution.

Knowledge of the vibrational temperature of the gas is of interest because it is directly related to the vibrational temperature of the ground state of the CO_2 molecule, and its relationship to other plasma parameters has been examined theoretically. High vibrational temperatures have also been linked to poor laser output so this temperature can be used to some degree to characterise how well one section of the gain medium is performing in relation to another. In general, having an estimate of the populations of the ground state of nitrogen should be a useful tool with which to characterise and optimise the laser.

Given discharge parameters in the range $N_e = 1 \times 10^9 - 2 \times 10^{10}\,\mathrm{cm}^{-3}$, $T_e = 0.2 - 1.6\,\mathrm{eV}$, $\delta = 0 - 0.6$ (CO_2 dissociation fraction), $F = 0 - 30\%$ (percentage ratio of CO_2 in gas mix), $P = 10\,\mathrm{torr}, T_g = 450\,\mathrm{K}$ (gas temperature), theoretical analysis [70, 71] of the vibrational temperature T_v of N_2 versus other plasma parameters has shown the following general trends. T_v ranges from 1000-7000 K, increasing with increasing n_e and decreasing P for otherwise fixed discharge conditions. For fixed n_e, T_v increases with increasing δ for $T_v \lesssim 2000\,\mathrm{K}$ and decreases with increasing δ for $T_v \gtrsim 2000\,\mathrm{K}$. T_v increases with increasing T_e and has a saturation value at $T_e \gtrsim 0.8\,\mathrm{eV}$. For fixed P, T_g, n_e, T_e and N_2 concentration in the gas mixture, T_v decreases rapidly as the CO_2 fraction is increased up to 10%

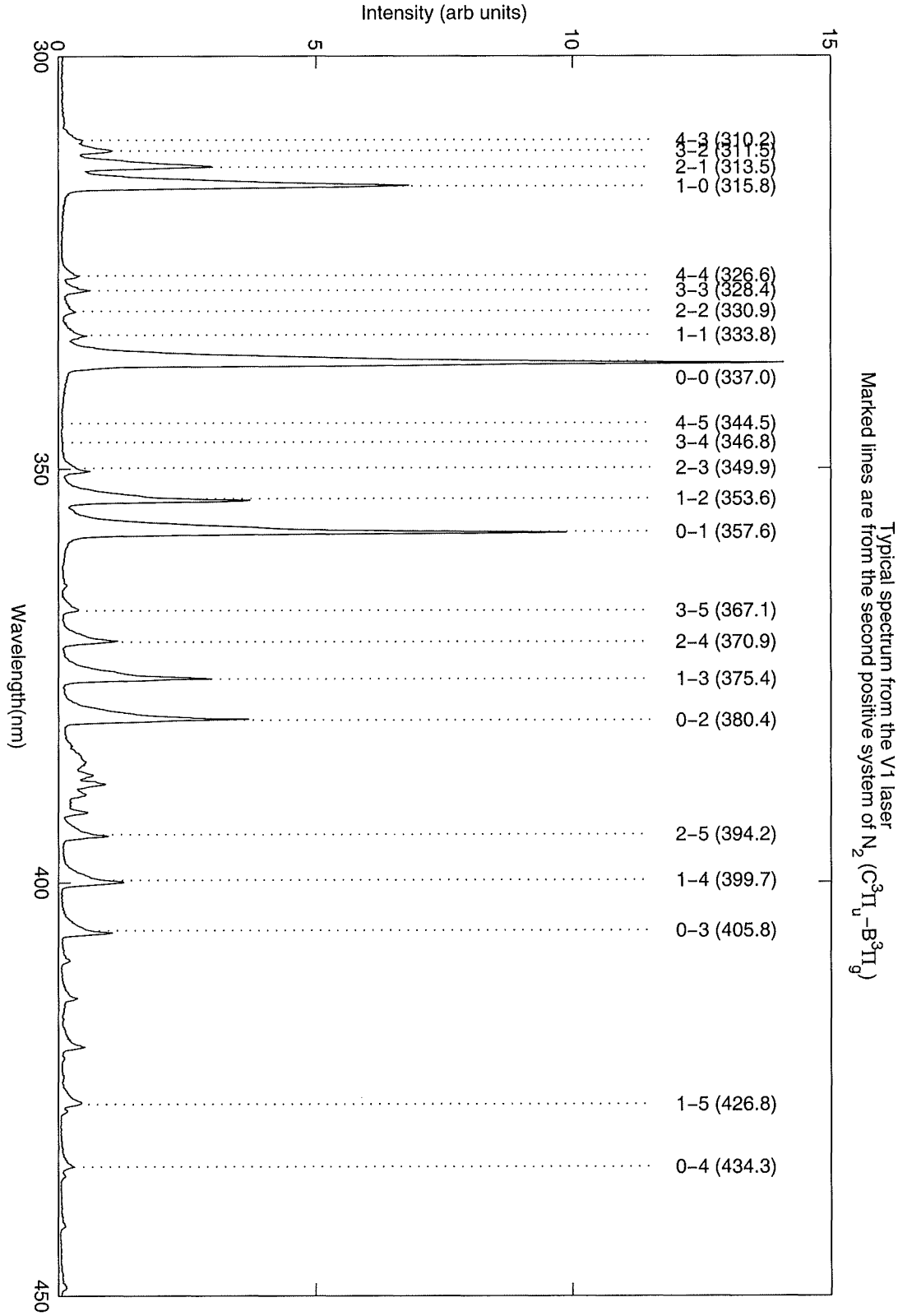

Figure 8.1: Typical spectrum from the V1 laser. The main lines are due to the second positive system of nitrogen ($C^3\Pi_u$–$B^3\Pi_g$) which have been labelled by the vibrational transition and the wavelength of the band origin.

of the gas mixture due the resonant energy transfer from vibrationally excited N_2 molecules to CO_2 molecules.

8.4 Vibrational temperatures via spectroscopy

The first step in determining the populations of the electronic ground state ($X^1\Sigma_g^+$) of N_2 is to find the populations of the states of the second positive system ($C^3\Pi_u$) via a spectroscopic method. These populations can then be used to determine the populations of the $X^1\Sigma_g^+$ state. The method used here is an extension of the method of Bleekrode [10] incorporating some observations made by Kosoruchkina and Trekhov [47] and others [63, 39].

There is a relationship,

$$I_{vv'} \propto N_v A_{vv'} \nu_{vv'}^4 \tag{8.1}$$

between the band head intensity $I_{v'v''}$ for a transition between the vibrational energy levels E_v and $E_{v'}$ of the $C^3\Pi_u$ and $B^3\Pi_g$ electronic states of N_2 (see figure 8.2). N_v is the population of vibrational energy level E_v, $A_{vv'}$ is the Frank-Condon factor [7, 9] of the $v-v'$ transition and $\nu_{vv'}$ is the transition frequency [8]. Since $A_{vv'}$ and $\nu_{vv'}$ are known, one can calculate N_v from the measured band head intensities.

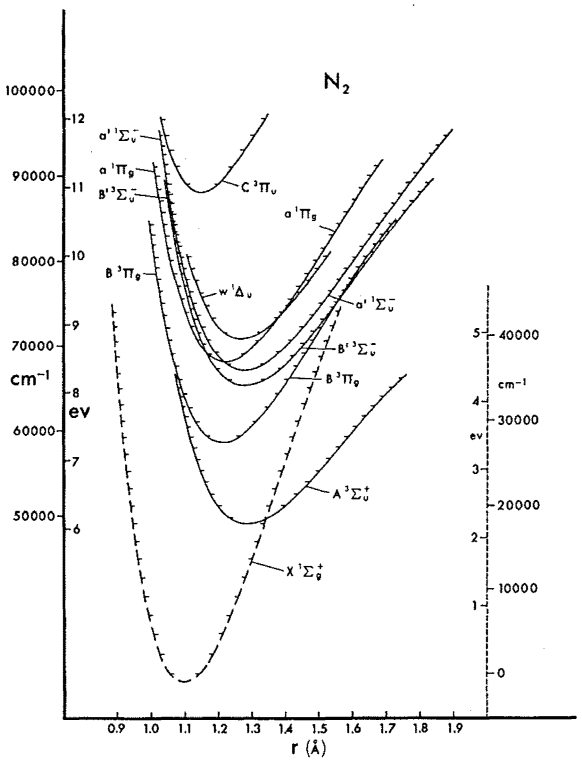

Figure 8.2: Energy level diagram for observed states of N_2 below 12 eV. Note that the ground state $X^1\Sigma_g^+$ is drawn with respect to the scale on the right.

If the vibrational energy levels are assumed to be thermally distributed (ie. a Boltzmann distribution) the populations are given by,

$$N_v = \frac{N_\pi}{Q_\pi} \exp\left(\frac{-E_v}{kT_v}\right) \tag{8.2}$$

where N_π is the total population of the $C^3\Pi_u$ electronic state, Q_π is the vibrational partition function, k is Boltzmann's constant and T_v is the vibrational temperature of the $C^3\Pi_u$ electronic state.

According to equation (8.2) a plot of $\ln N_{v'}$ versus energy level ($\simeq$ vibrational quantum number) should give a straight line. Any nonlinearity means the distribution deviates from a Boltzmann distribution. Table 8.1 lists the vibrational energy levels of the $C^3\Pi_u$ state.

$C^3\Pi_u$			
v	ν (cm^{-1})	$\nu_n - \nu_{n-1}$	$\nu_n - \nu_0$
0	88978		
1	90972	1994	1994
2	92913	1941	3935
3	94787	1874	5809
4	96568	1781	7590

Table 8.1: Vibrational energy levels for N_2 (from [8]).

Equation (8.2) can be used to determine a vibrational temperature by examining two vibrational levels of the electronic state in question,

$$N_{v1} = \frac{N_\pi}{Q_\pi} \exp\left(\frac{-E_{v1}}{kT_v}\right) \tag{8.3}$$

$$N_{v2} = \frac{N_\pi}{Q_\pi} \exp\left(\frac{-E_{v2}}{kT_v}\right) \tag{8.4}$$

The solution for T_v is,

$$T_v = \frac{E_{v1} - E_{v2}}{k(\ln N_{v1} - \ln N_{v2})} \tag{8.5}$$

This amounts to finding the gradient of the graph when vibrational energy level is plotted versus log population. If the populations of the levels all lie on a straight line when plotted this way, the distribution is Boltzmann and assigning a temperature to the state makes sense. However, more often than not in laser plasmas this distribution will not be Boltzmann and the assignment of a temperature is not so meaningful. This "problem" and the fact that two sets of vibrational levels are involved ($C^3\Pi_u$ and $X^1\Sigma_g^+$) has lead to varying results and some confusion about the meaning of vibrational temperatures. The vibrational populations of the $C^3\Pi_u$ state are plotted for a typical CO_2 discharge in figure 8.3.

A solution to the problem of assigning a meaningful temperature was provided by Kosoruchkina and Trekhov [47] who noted that although the gradients between

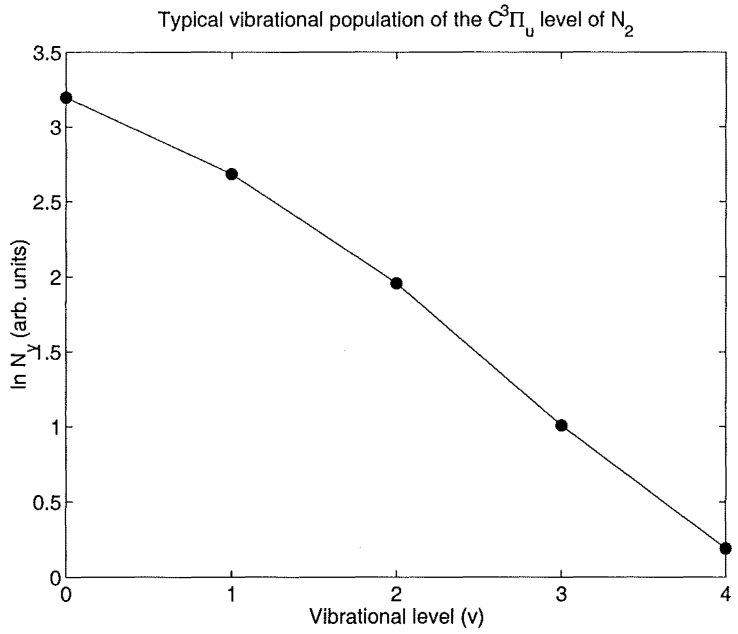

Figure 8.3: Typical population of the $C^3\Pi_u$ level of N_2 as the result of microwave discharge excitation in a CO_2 laser.

the first three levels ($v = 0, 1, 2$) are often non-Boltzmann, the gradients between levels 2,3 and 4 do normally follow the Boltzmann distribution. They showed that if these levels were used to determine an "effective temperature" of the $C^3\Pi_u$ state many of the conflicting results of others could be reconciled.

8.4.1 Calculating the temperature of the $X^1\Sigma_g^+$ state

Ultimately the temperature of the ground state ($X^1\Sigma_g^+$) is of interest to the designers of CO_2 lasers. In order to get this information from the populations of the $C^3\Pi_u$ state an excitation model needs to be developed. Howorth [39] showed that the dominant excitation mechanism for the $C^3\Pi_u$ state was by direct electronic excitation from the ground $X^1\Sigma_g^+$ state. Using this fact it is possible to predict the populations of the $C^3\Pi_u$ state given the $X^1\Sigma_g^+$ state.

If it is assumed that the excitation rate constants $k_{vv'}$ for $X^1\Sigma_g^+ \rightarrow C^3\Pi_u$ are proportional to the Frank-Condon factors $A_{vv'}$ [10] then the populations of the $C^3\Pi_u$ state can be estimated from a given $X^1\Sigma_g^+$ populations via,

$$N_{v'_C} \propto \sum_v k_{vv'} N_v \tag{8.6}$$

$$\propto \sum_v A_{vv'} N_v \tag{8.7}$$

If it is assumed that the $X^1\Sigma_g^+$ state has a Boltzmann distribution,

$$N_{v'_C} = \frac{N_x}{Q_x} \exp\left(\frac{-E_v}{kT_{v_X}}\right) \tag{8.8}$$

then the populations of the $C^3\Pi_u$ state are given by,

$$N_{v'_C} \propto \sum_v A_{vv'} \exp\left(\frac{-E_v}{kT_{v_X}}\right) \tag{8.9}$$

Using equation (8.9), populations of the $C^3\Pi_u$ state have been calculated for temperatures ranging from 500 to 10000 K of the $X^1\Sigma_g^+$ state. The results are plotted in figure 8.4. Note that the resulting distribution in the $C^3\Pi_u$ state is not a Boltzmann distribution for temperatures $T_{v_x} \lessapprox 6000$ K. In fact the curves bear strong resemblance to the experimentally observed populations which suggests that the model adequately describes the physical situation.

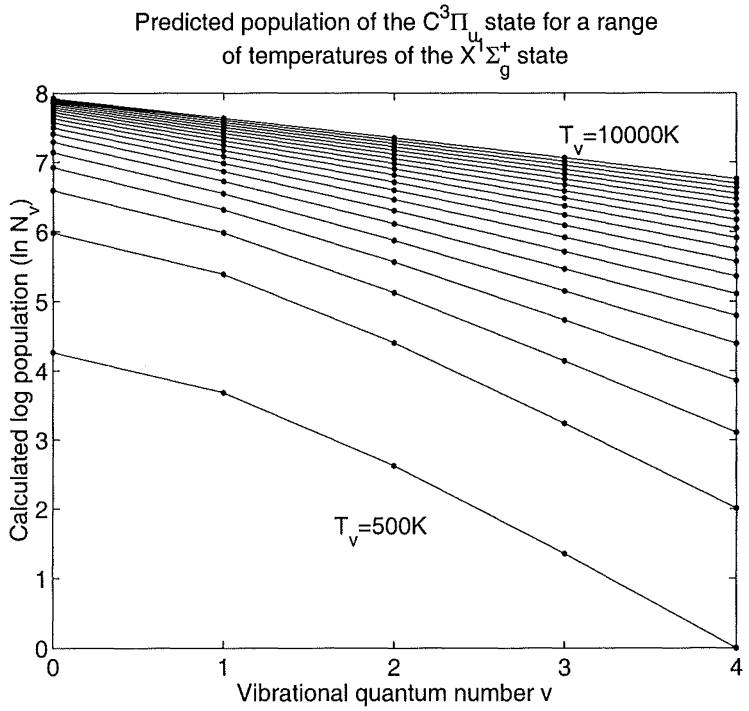

Figure 8.4: Predicted population of the $C^3\Pi_u$ state of N_2 as calculated from a Boltzmann distributed $X^1\Sigma_g^+$ state using the excitation model. Each line represents and increase of 500K in the temperature of the $X^1\Sigma_g^+$ state.

Having calculated the populations of the $C^3\Pi_u$ state, its temperature can then be measured using the gradient of levels 2, 3 and 4 which are co-linear even at low values of T_{v_x}. If T_{v_x} is plotted versus T_{v_c} the temperature of the $X^1\Sigma_g^+$ state can be estimated from the measured temperature of the $C^3\Pi_u$ state. The temperature map is shown in figure 8.5.

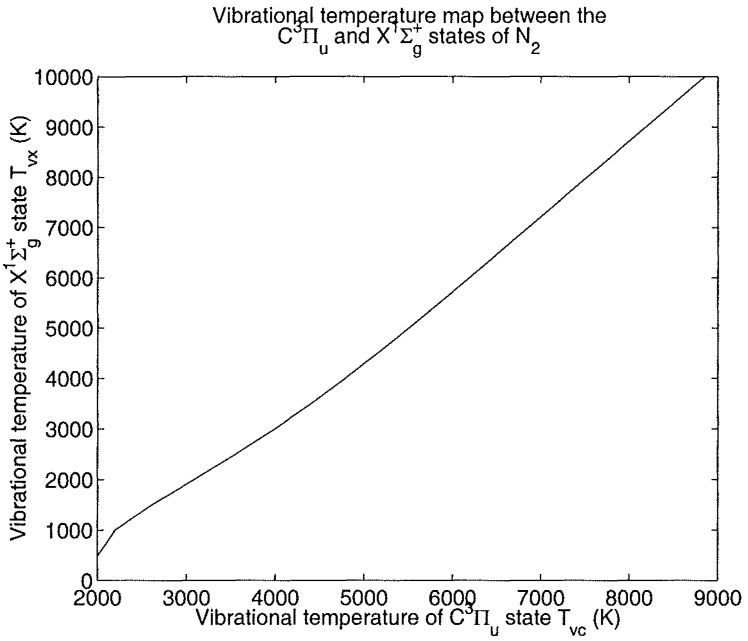

Figure 8.5: Temperature map between the $C^3\Pi_u$ and $X^1\Sigma_g^+$ states of N_2 created by calculating the temperature of the estimated populations of $C^3\Pi_u$ derived from the $X^1\Sigma_g^+$ state using an excitation model.

Another method of finding the temperature of the $X^1\Sigma_g^+$ state would be to numerically solve the equation,

$$n_{v'_C} = c \sum_{v_x} A_{vv'} n_{v_x} \tag{8.10}$$

where k is a constant and the n_{v_x} are assumed to have a Boltzmann distribution. While this method is feasible, practical concerns discussed in the next section make it less reliable than the method described above.

8.5 Practical experimental issues

In addition to setup and calibration a number of experimental issues need to be examined. The first is the validity of taking time-averaged spectra from a pulsed discharge. Time averaging (see later) is required to get the necessary resolution and accuracy. For a time-averaged spectrum to be useful for calculating information about the discharge, the spectrum must be 'constant' during the period it is being measured. To ensure this, all vibrational lines used in this experiment were checked for linear response by checking that the intensity profile of the line in the time domain was a rectangular pulse shape with the same width as the microwave pulse. This check was made by connecting the photomultiplier output to an oscilloscope and observing the intensity of each line in the time domain. Considering the radiative lifetime of the $C^3\Pi_u$ state is $\lesssim 10^{-7}$ s [39] any

changes in the populations of the $X^1\Sigma_g^+$ state during the pulse would have been obvious.

In principle lines from any of the sequences can be used to estimate the populations of the $C^3\Pi_u$ state and all should give the same results. In practice technical concerns dictate which lines should be used. The limited dynamic range of the instruments in use meant that it was difficult to measure line intensities which varied over much more than two orders of magnitude. Therefore, it is preferable to use lines which have values of v and $A_{vv'}$ (see equation 8.1) which result in strong lines of similar intensity. A complication is that the $v = 4$ line is very weak in all cases and often obscured by overlap of an adjacent band. This led to variable results unless extreme care was taken. For this reason it was decided that the temperature would be determined entirely from the $v = 2$ and $v = 3$ populations.

Of the available transitions (see figure 8.1) only the $\Delta v = -1$ and $\Delta v = 2$ sequences were candidates for thermometry, other sequences were ignored due to the weak nature of transitions from $v = 2, 3$ states or because of overlap with some other discharge feature. Finally the $\Delta v = -1$ sequence (1-0, 2-1, 3-2, 4-3) was chosen which, even though it does have more overlap than the $\Delta = 2$ sequence, has more favourable $A_{vv'}$. Experimentally both the $\Delta v = -1$ and $\Delta v = 2$ sequences produced similar values of T_v but the using the $\Delta v = 2$ sequence meant that the equipment gain had to be adjusted each run to avoid clipping.

8.6 Experimental setup and calibration

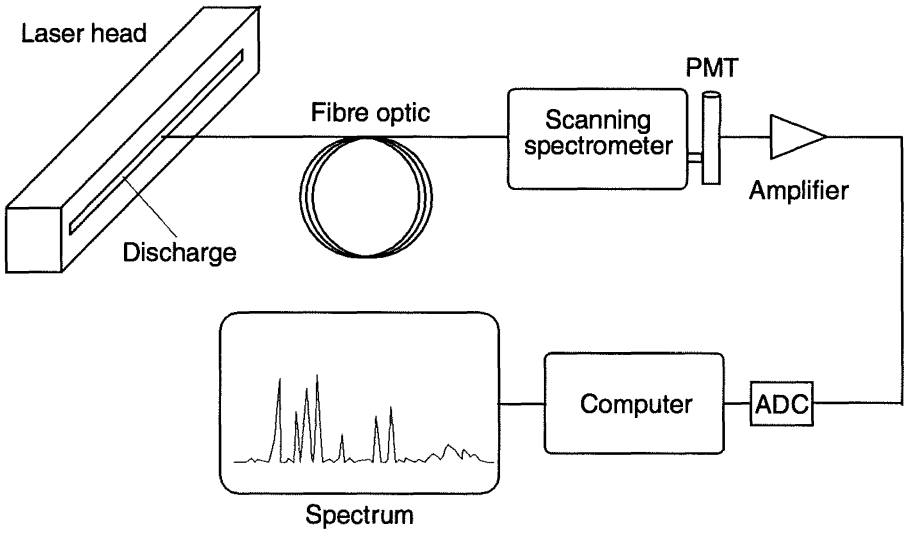

Figure 8.6: Optical emissions from the discharge are fed into a spectrograph by fibre optic. Wavelength ranges were then scanned and digitised by the computer.

The experimental setup used is shown in figure 8.6. Light from the discharge is fed

through a fibre optic cable to a Digikrom 240 which is a Czerny-Turner scanning monochromator with a 1200 lines/mm grating. The monochromator is capable of selecting wavelengths to a resolution of 0.1 nm. The selected wavelength is then detected by an RCA 1P28 photomultiplier tube (PMT) and the output amplified by transimpedance (current to voltage) amplifier. The resulting voltage is then digitised by an 8-bit analog to digital converter (ADC).

As the scanning speed of the spectrograph is slow compared to the digitisation rate, the output signal from the PMT amplifier can be sampled many times per wavelength bin. By adding one ADU (A to D unit - the voltage required to make the output of the ADC increase by one) of white noise (peak to peak) to the signal level, the resolution of the 8-bit ADC can be effectively increased to 12-bits by averaging the value acquired over many samples. The digitisation rate was 35 kHz with a sample time per bin typically ranging from 6-60 ms. An example of the effectiveness of this technique is demonstrated in figure 8.7. Here, in a somewhat contrived, but not unrealistic situation, the spectrum of a tungsten lamp has been sampled using a gain resulting in a dynamic range of 5 ADU. The undithered (blue) signal shows clearly the discrete ADC steps whereas the dithered (green) signal removes these steps revealing features of the spectrum which were previously unobservable.

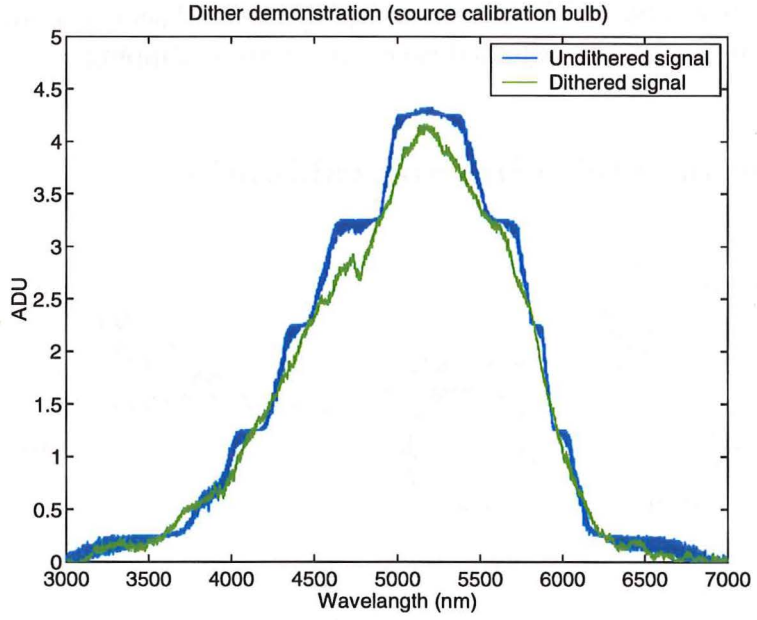

Figure 8.7: Dither demonstration. The spectrum in blue was acquired without adding any dither to the signal. The result is discrete steps in the spectrum where the A to D converter jumps to the next value. The rounding of the steps is due to a small amount of noise already present in the signal. The green spectrum was acquired with the addition of dither.

The PMT amplifier is a simple transimpedance amplifier which incorporates a low pass filter to smooth the photon noise while still allowing fast response during scanning. The 3 dB point for the filter was set at approximately 30 kHz.

The 1P28 photomultiplier is a nine dynode side-on type with ultraviolet transmitting glass designated as having S5 response. The S5 response curve is shown in figure 8.8.

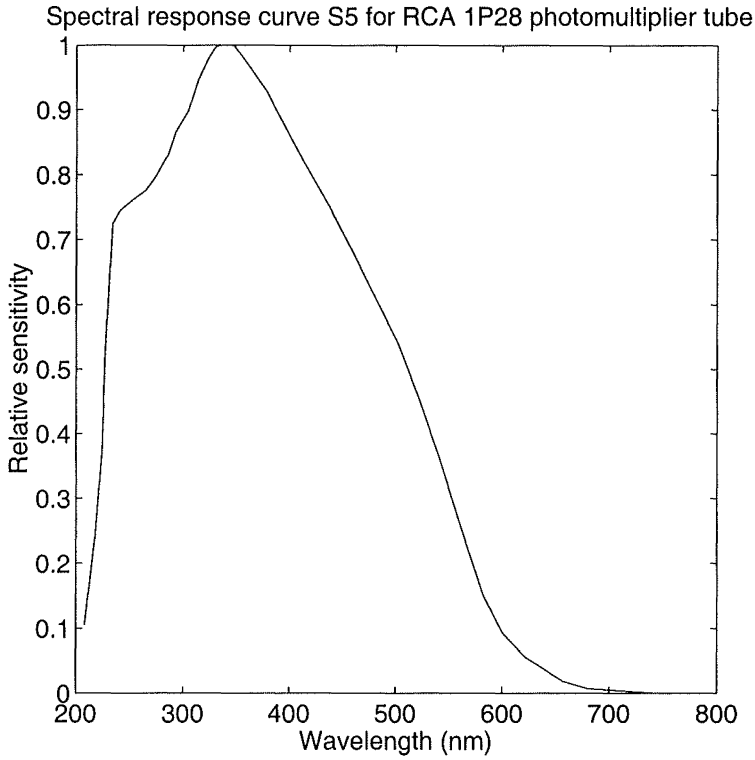

Figure 8.8: Spectral response curve for the 1P28 photomultiplier. S5 curve - digitised from the RCA phototubes and photocells technical manual [80].

8.6.1 Calibration

In order to use the monochromator for spectroscopy it must be calibrated. Although all elements in the system behave in a linear fashion, the filter functions associated with various elements and the photomultiplier response curve mean that, in general, the ratio of readings at two different wavelengths is not equal to the ratio of spectral intensities at those wavelengths. Therefore, an overall response curve for the whole system must be created which can be applied to any measurements to give correct intensity. Fortunately only relative spectral calibration is required. This means that the output must be proportional to the actual intensity at any wavelength and that the proportionality constant must be the same for all wavelengths. The normal way to accomplish this calibration is by observing a source of known spectral content. In this way a table of correction factors can be calculated which, when applied to the observed data, result in the real intensities.

Unfortunately the only calibrated spectral lamp available for these experiments was calibrated down to a wavelength of 400 nm and much of the relevant spec-

troscopic information resides between 300 and 400 nm. However, it is a possible to extrapolate the data back to 300 nm given what is known about the various elements of the system.

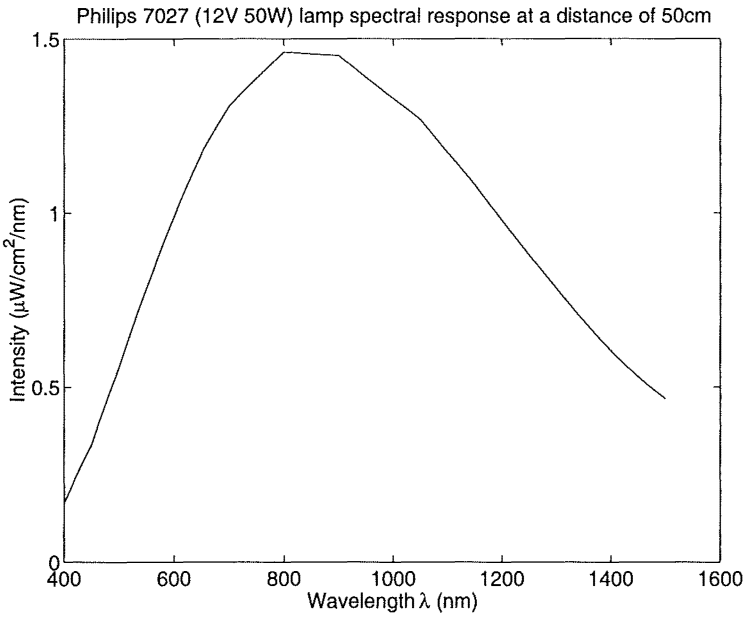

Figure 8.9: Philips type 7027 tungsten halogen lamp spectral emission curve. Calibration is relative to a secondary standard lamp.

The spectral response of the calibrated lamp (Philips Type 7027) is shown in figure 8.9. This curve was deduced from the comparison of the spectral response of this lamp with a secondary standard lamp. Tungsten halogen lamps, like most other incandescent light sources, behave primarily like black bodies. However, the response of such light sources is not strictly black body because it is not observed through a small hole into an enclosed volume. To correct for this emissivity values may be applied to the black body data. The emissivity of a body at a certain wavelength and temperature is the ratio of the measured intensity to that of the black body intensity at the same wavelength and temperature. Emissivity values vary with the shape and surface finish of the particular material and also with wavelength and temperature. There have been many studies of the emissivity of tungsten [95] although few at temperatures higher than 2800 K. Although the nominal temperature of the calibrated bulb is 3000 K there is not a significant change in the emissivity ($\sim$ 2%) between 2800 K and 3000 K for the values that were available. Emissivity values at a temperature of 2800 K will therefore be used for what follows. The available data also shows that the particular surface finish of the material starts to affect the emissivity values at wavelengths over 1000 nm. For this reason the range of wavelengths used was limited to values less than 1000 nm.

A black body curve with emissivity corrections can be fitted to the calibrated data so that the curve can be extended down to 300 nm. This fitted curve can

then be used for values between 300 and 400 nm. The spectral emittance of a black body at a temperature T and wavelength λ is given by,

$$S_\lambda = \frac{2\pi c^2 h}{\lambda^5} \frac{1}{e^{hc/kT\lambda} - 1} \tag{8.11}$$

S_λ has been evaluated for wavelengths between 300 and 1000 nm and the results plotted in figure 8.10 along with the curve after it has been modified to account for the emissivity of tungsten. The next step in the process is to find the operating

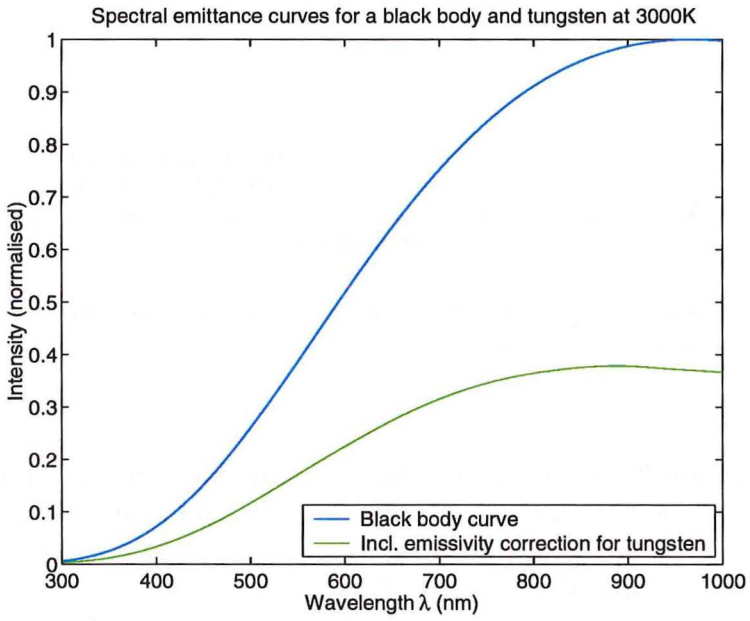

Figure 8.10: The blue curve shows the spectral emittance of a black body at a temperature of 3000 K normalised so that the maximum intensity is unity. The green line shows the same curve modified to include the emissivity of tungsten.

temperature of the tungsten bulb. The easiest way to accomplish this is to vary the temperature of the black body curve until it fits the calibration curve. Figure 8.11 shows a black body curve at 3170 K adjusted for the emissivity of tungsten with the lamps calibration curve superimposed. Measurements with an optical pyrometer, again adjusting for the emissivity of tungsten, confirm a temperature near 3200 K. The lamp calibration curve may now be extended by using the adjusted black body curve for wavelengths between 300 and 400 nm.

8.7 Preliminary spectra

A number of spectra from a stable discharge were taken under normal operating conditions to check for the presence of any systematic errors in the equipment and measurement procedures. Runs made at different scanning speeds produced spectra which were almost identical. The linearity of the PMT - amplifier - ADC

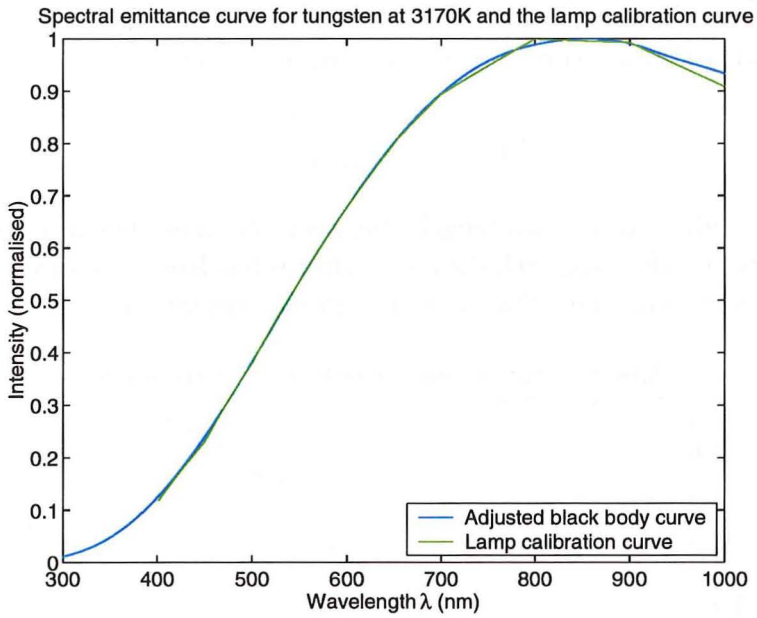

Figure 8.11: Black body curve at 3170 K adjusted for the emissivity of tungsten (blue) and the lamp calibration curve (green)

system was checked by observing the same spectrum at a number of different gains (set via the PMT voltage) and the results found to be linear. Several runs on the same discharge were made to gauge the repeatability of the results with respect to temperature measurement. The results are plotted in figure 8.12. The span of the measured temperatures under "identical" discharge conditions was typically 500 K. The uncertainty in these vibrational temperatures should therefore be taken to be ± 250 K.

8.8 Experimental results

A large number of optical spectra where taken from the three laserheads during the course of these experiments. Figures 8.13, 8.14 and 8.15 show the vibrational temperatures inferred from these spectra versus pressure for a range of microwave pulse widths.

The most obvious trend is that the vibrational temperature increases with input power (pulse width). This can be understood in terms of a simple power excitation model. Of more interest is the difference in this increase between the laserheads. Increases in pulse width lead to large increases in vibrational temperature in the V1 laserhead but the increase in the V2 and V3 laserheads is much more moderate. Probably the most significant factor affecting this is that lasing occurred during the microwave pulse in the V3 laserhead which provided a de-excitation pathway for vibrationally-excited N_2. In the V2 laserhead where no lasing took place, the vibrational temperatures obtained also increased with power input, however not

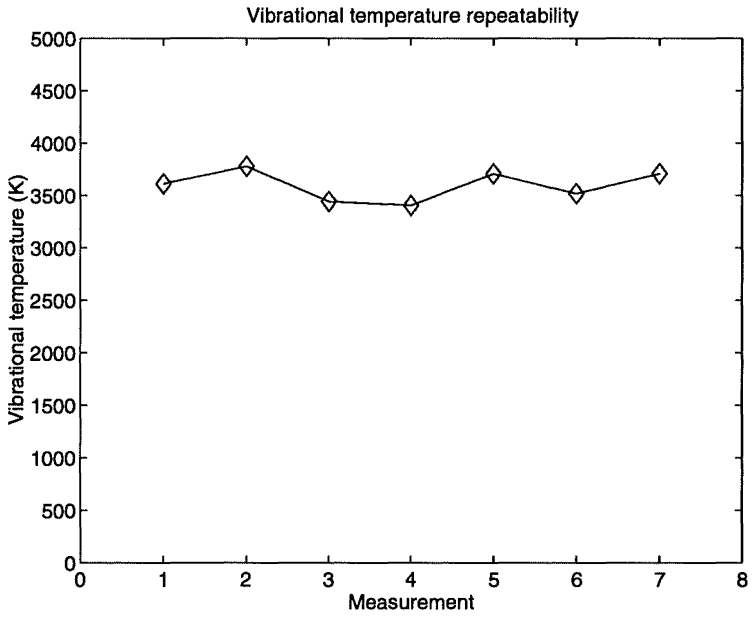

Figure 8.12: Vibrational temperatures inferred from several spectra taken in rapid succession from a 10 torr discharge.

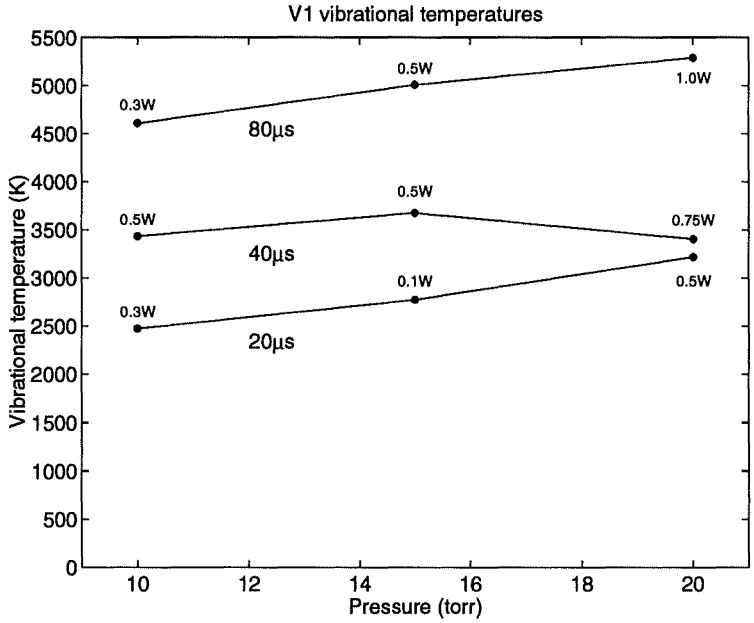

Figure 8.13: Vibrational temperature estimates of the V1 laser as a function of pressure for various microwave input pulse widths.

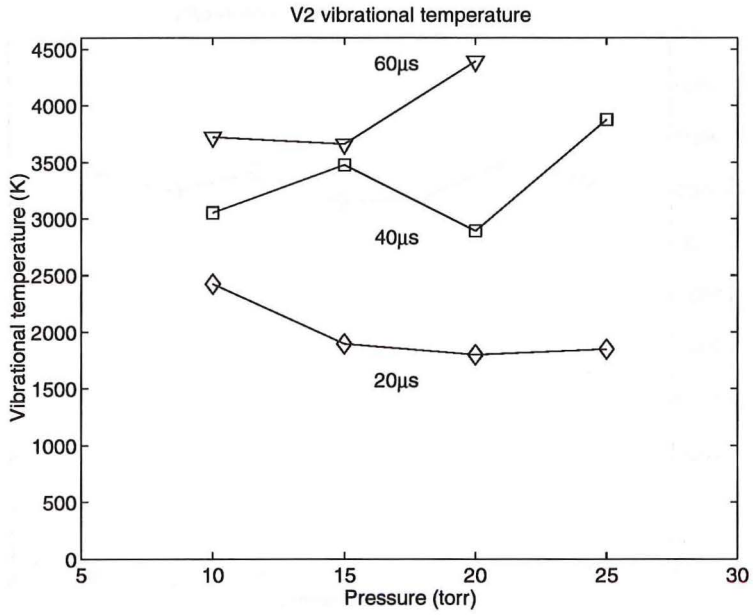

Figure 8.14: Vibrational temperature estimates of the V2 laser as a function of pressure for various microwave input pulse widths.

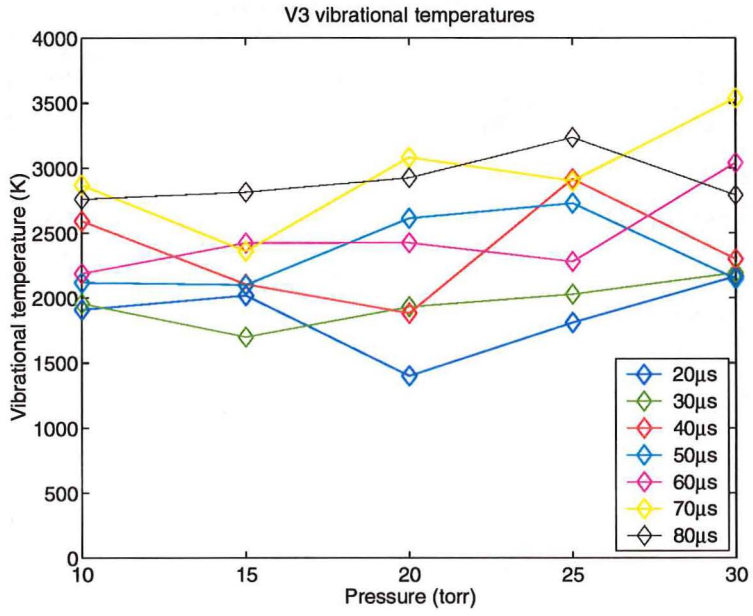

Figure 8.15: Vibrational temperature estimates of the V3 laser as a function of pressure for various microwave input pulse widths.

as rapidly as in the V1 laser. This difference may be explained by the lower power input the the V2 head. No other general trends were observed.

Vibrational temperatures are of greatest diagnostic value when coupled with measurements of other plasma parameters such as T_r, T_e and n_e (see section 8.3). Alternatively, comparison of vibrational temperature measurements made on other lasers operating under similar conditions should lead to some useful insights. It was hoped that the vibrational temperatures measured in this work could be compared with measurements made by by Ikeda and Danno [41], who examined the vibrational temperature in a discharge tube filled with a CO_2 laser mixture which was excited at 2.45 GHz. However, if the method used to determine vibrational temperatures described in their paper is the one actually employed, then it is inappropriate in a number of aspects and not suitable for comparison with the results found here. Measurements made in this work must therefore serve as a reference for future investigation.

8.9 Rotational temperature

The CO_2 laser requires low gas temperatures in order to sustain a population inversion. Knowledge of the gas temperature is therefore important for improving output power and efficiency. Measurement of the rotational temperature of N_2 would be of considerable interest as the kinetic temperature of the gas is in thermal equilibrium with the rotational temperature of the various gas species. As the spectrum of N_2 is the result of vibronic (vibrational-rotational) transitions, it should be possible to estimate the rotational (and therefore kinetic) temperature of the gas via spectroscopy. The rotational transitions of the N_2 spectrum appear as a broadening of the vibrational transitions (see figure 8.1). The populations of the rotational levels thermalise rapidly ($< 10^{-8}$ s) which means that they form a Boltzmann distribution. Therefore, it should be possible to estimate the rotational temperature of the gas by examining the rotational broadening of the vibrational temperatures. The most reliable method of accomplishing this would be to fit synthetically-generated line shapes to measured spectra.

Changes in line shape as the temperature was increased were found to be relatively subtle. This meant that small uncertainties in the fit led to large uncertainties in the estimated temperature. Variations between two sets of similar spectra were often as much as 200 K. As the temperature range of interest only varies over 450 K these measurements were of limited use. The fitting routine may have been improved by implementing a more sophisticated error measure than the simple least-squares method used. However, the main problem was due to the lack of data points on the wavelength axis. A higher resolution spectrum would have made the fitting process much more reliable and given lower uncertainties in the temperature measurements.

8.10 Discharge uniformity

Throughout this work discharge uniformity has been discussed in relation to its importance for the efficient running of a high power CO_2 laser. Considerable efforts [32, 18, 52, 89] have been made to minimise longitudinal voltage variations in the applied electric field of RF-excited lasers. If uncorrected, variations of up to 30% in discharge intensity are observed in cavities having RF wavelengths five times the length of the discharge channel [32]. Generally inductances are added to the cavity in the style of a transmission line to minimise these variations. Such tunings can be very sensitive to variations in frequency, changes of 1% can often result in regions of "drop-out" where the field is too low for a self-sustained discharge to operate [18].

In a microwave-excited CO_2 laser, where the discharge cavity may be a few wavelengths long, voltage-uniformity corrections are very difficult to compensate for. This is a significant disadvantage of microwave excitation.

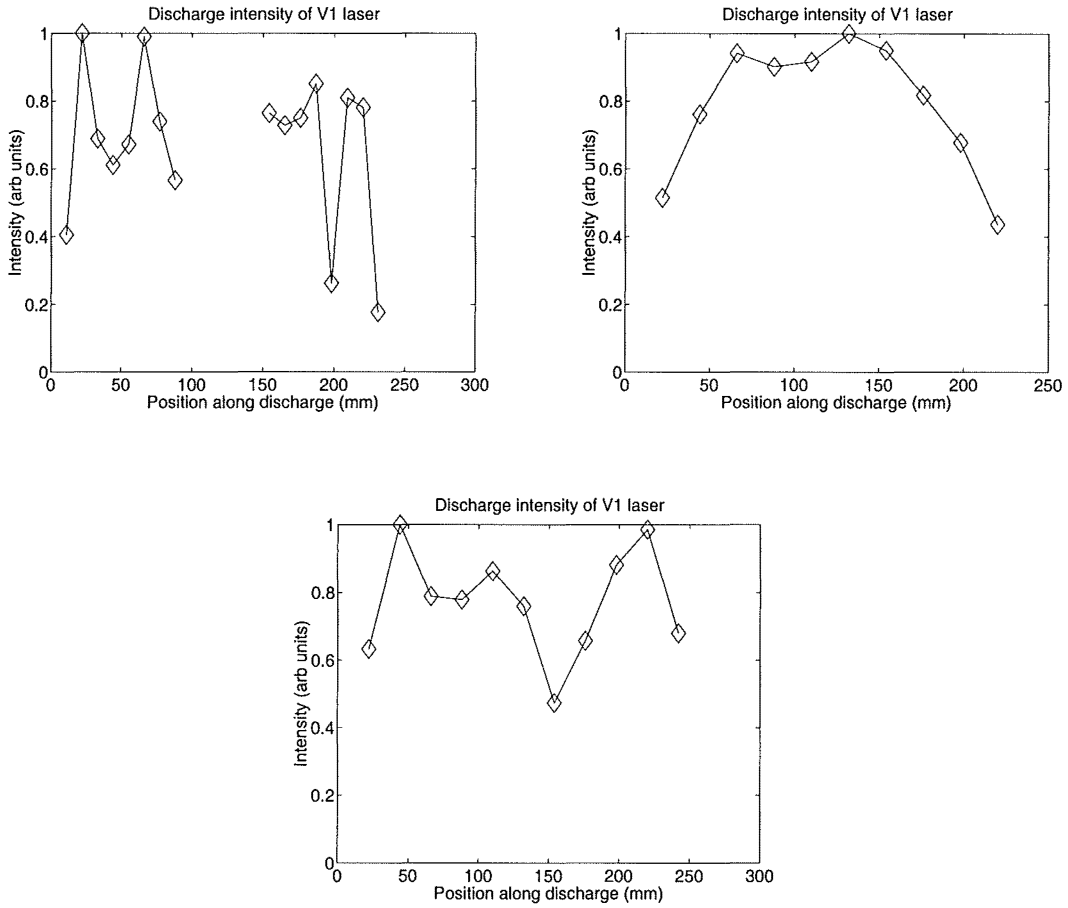

Figure 8.16: Discharge intensity as a function of position for each of the laserheads.

The discharge intensity and electric field vary along the length of the discharge cavity. In order to be more quantitative than the photos of the discharge in

figures 4.17, 4.20 and 4.22, intensity measurements have been made at equally spaced intervals along the cavity. These intensity measurements were made by integrating a spectrum taken at each point. Unlike the human eye or photographic film, this method responds linearly with respect to intensity and frequency. In addition, ultraviolet wavelengths make a significant contribution. The results, shown in figure 8.16, are consistent with observations made with the naked eye but the variation in brightness is much more apparent. The intensities have been scaled so that the maximum occurs at unity. The curve for the V1 shows marked changes in discharge uniformity along the laser. The missing central region is due to the structural spacer which obscures the discharge there. The curve for V2 shows a smoother curve with more gradual changes in intensity. The geometry of this discharge cavity made consistent alignment of the optical fibre difficult, so it is possible that the dip in the top of the curve is an artifact. The third graph, for V3, shows significant variation in intensity along the discharge although much less than V1. These curves were taken at a pressure of 10 torr. Generally at this pressure the discharge is easy to strike and results in a "reasonable" looking plasma. At higher pressures ($\sim$ 30 torr) significant deterioration is observed.

In an RF discharge which has been inductively terminated in the correct manner, intensity variations in the sidelight emissions can be reduced to the level of $\sim$ 15% [18]. This is significantly less variation than was observed for any of the measurements shown in figure 8.16.

8.11 Other observations

During investigation of the spectra from the V1 and V3 lasers an interesting difference was discovered. In the V1 laser emission bands were present between 382 and 390 nm and between 412 and 423 nm. While these bands were always present in the V1 laser they were significantly stronger when there was no gas flowing through the device. Figure 8.17 shows two spectra taken from the V1 laser with and without gas flow. The strong emission between 382 and 390 nm on the lower plot indicates that some excitation process other than ones normally associated with CO_2 laser excitation is taking place, possibly absorbing significant amounts of energy. When these bands are of low intensity, compared with the other nitrogen bands in the spectrum, lasing is observed. When the bands are of high intensity no laser output is observed.

In contrast to the V1 measurements, these bands are not observed in the V3 laser with the quartz dielectric present. Figure 8.18 shows three spectra from the V3 laser, all at 15 torr. In the first, power input is similar to the first plot in figure 8.17 with a duty cycle of 10%. In the second, the duty cycle has been increased to 50%. Neither of these plots shows any sign of the two bands described above. The third plot in figure 8.18 was taken from the V3 laser after the quartz dielectric had been removed, leaving a gap spacing of 7.5 mm. Under these conditions the discharge is made up of small regions of plasma about 1 cm across which form at the centre

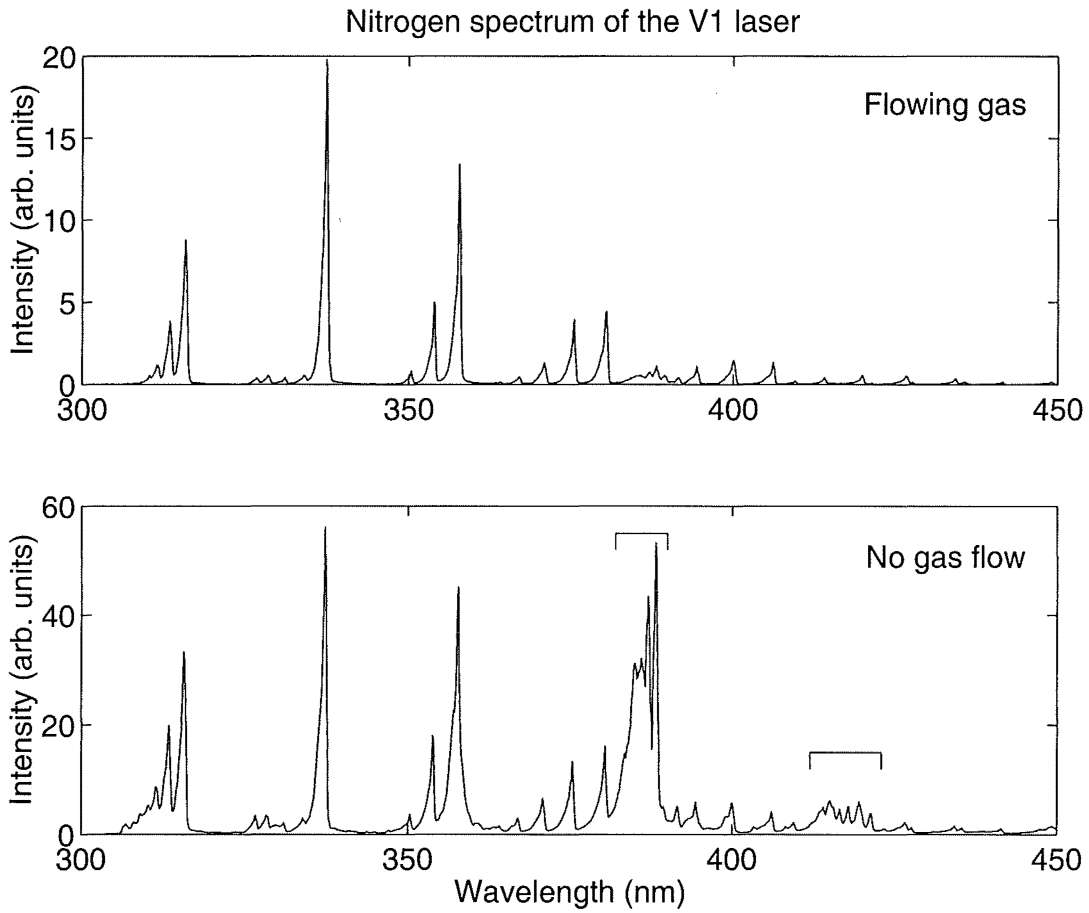

Figure 8.17: Nitrogen spectra from the V1 laser. The top plot shows a typical V1 discharge spectrum at 15 torr. The lower plot shows dramatic changes in two regions when the discharge is excited without gas flow. Pulse width 40 μs. Pulse period 400 μs.

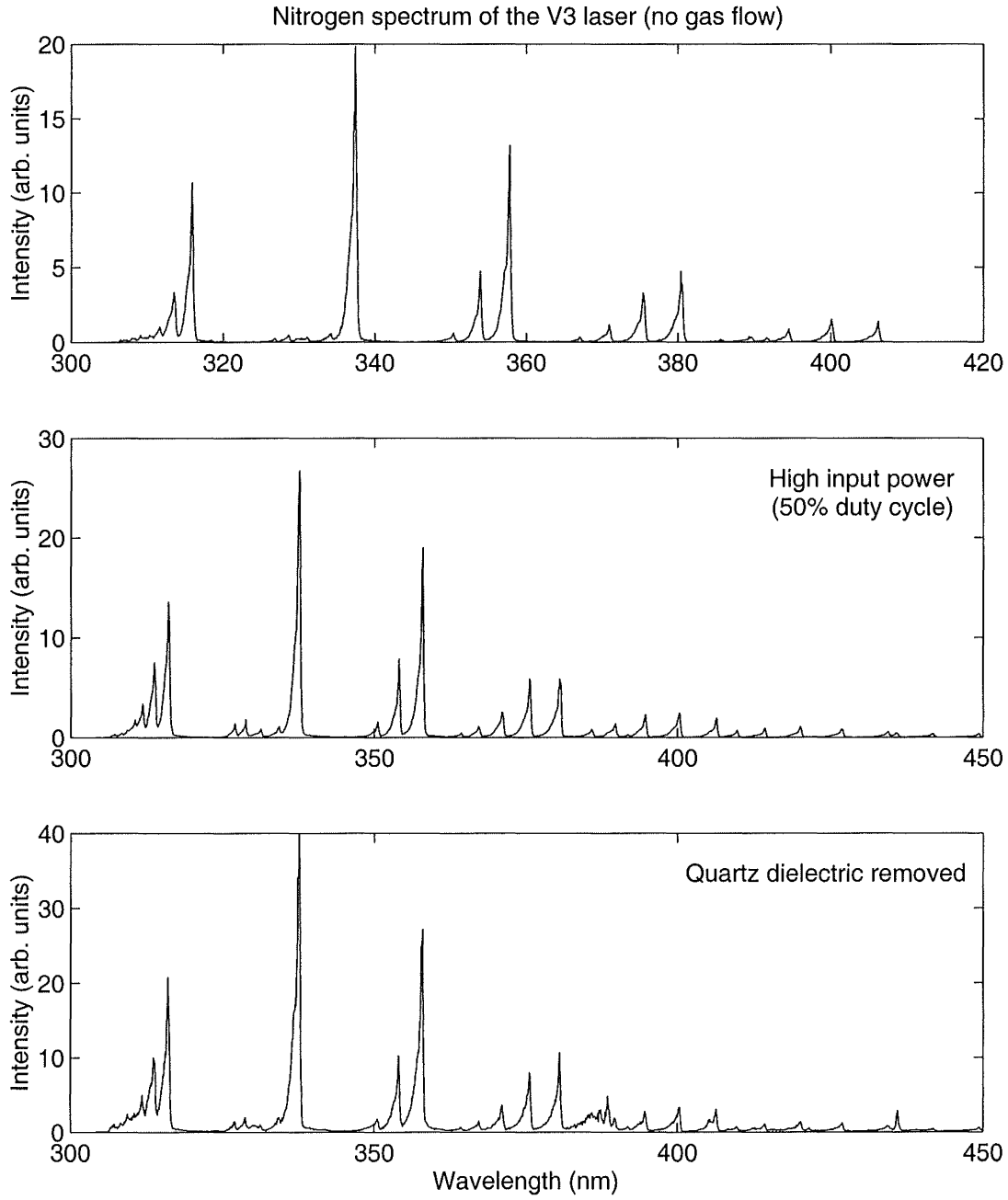

Figure 8.18: Nitrogen spectra from the V3 laser. The top spectrum shows a typical V3 spectrum at 15 torr with a pulse width and period of 40 and 400 μs respectively. Even at high power input (50% duty cycle) there is no obvious increase in the regions marked in figure 8.17. However, when the quartz dielectric is removed from V3 an increase in emission between 382 and 390 nm is observed.

of the cavity and move towards the ends. The spectrum of this discharge clearly shows the presence of the band between 382 and 390 nm, indicating that the presence of the quartz dielectric in the discharge circuit has a pivotal role in the suppression of this emission.

The spectrum arising from these bands is thought to be due to N_2^+ emissions, however the exact cause is not entirely clear. Similar, but not identical, results where found by Vidaud *et al.* [97] for gamma RF-discharges in N_2. In addition to the emission bands shown here, the transition to a gamma discharge was accompanied by strong emission at 391.4, 423.7 and 427.8 nm. These lines were not observed on the V1 or V3 lasers. Furthermore, the likelihood of a transition to a gamma discharge decreases with increasing frequency and decreasing pressure [97].

Regardless of the actual cause, discharges whose spectra contain these bands always perform poorly as a gain medium. Such spectroscopic measurements can be used as simple diagnostic. Further investigation of this phenomenon may help to clarify some of the differences between RF- and microwave-excited discharge behaviour.

Chapter 9

Conclusion

The aims of this research were to investigate how a microwave pumped CO_2 laser might differ from RF-excited devices and to design and build a microwave-excited laser to determine what limitations or advantages it may possess. To that end, three microwave-excited lasers were designed, built and investigated experimentally. A summary of the findings follows.

9.1 Achievements

Three laserheads and a microwave coupling system were examined. Chapter 3 discussed the design details and construction of the three laserheads along with other practical issues such as heat dissipation in the laserhead.

Chapter 4 introduced microwaves as a method of discharge excitation and dealt with coupling radiation from the magnetron to the laserhead. Standard magnetron power supplies were found to lack versatility in an experimental setting and be unsuitable for discharge excitation. A more configurable power supply was designed and built to function in a wide range of operating conditions. While the first laserhead examined, V1, was able sustain a discharge and lase, there were significant problems with discharge uniformity and stability. The addition of a quartz dielectric to the discharge circuit resulted in significant improvements in discharge uniformity in the V2 and V3 lasers. Even with the presence of this dielectric, uniform discharge operation was only possible up to pressures of 30 torr. Other microwave coupling methods were suggested which might allow more uniform power input to the discharge.

The optics of waveguide lasers were discussed in chapter 5 as they relate to the designs investigated in this work. The simple, low-loss, Case I waveguide resonator was used for the V1 and V3 lasers. This configuration has very little mode discrimination and methods to correct this problem were discussed. Special attention was given to a method of adding optics to the V2 cavity which had high mode discrimination.

Microwave discharges differ from RF discharges in a number of respects. Chapter 6 examined these differences in relation to their effect on the performance of a

CO_2 laser. Plasma sheaths were shown to be much less significant at microwave frequencies due to the reduced electron oscillation amplitude. A minimum electron density of $\approx 7 \times 10^{10}\,\mathrm{cm}^{-3}$ was established for stable discharge operation. Thermal instabilities are likely to be more significant at microwave frequencies than at RF. Modelling of the electron density across the discharge gap showed that the electron distribution differed very little from that produced by RF excitation. The stabilising effect of adding the quartz dielectric to the discharge was explained in terms of current limiting. While effective E/N values for optimum excitation were predicted to be slightly higher in a microwave excited discharge it was not obvious that this or any other factor would severely limit the performance of a microwave-excited device.

The performance of the lasers was examined in chapter 7. The highest observed output power from the V1 laser was 1.2 W at an efficiency of 2.5%. The addition of a quartz dielectric to the discharge circuit in the V3 laser saw the output power rise to 3 W with an efficiency of 5%. Although no specific preparations were made to the device, sealed-off operation for many hours was possible. An interesting chemical process in the laser gas was also discovered.

The magnetrons used in these experiments were not very versatile. The output power from such devices can be controlled to a small degree only. Besides the small control available by changing the voltage to the magnetron, the only method of changing the input power to the discharge was by altering the pulse width and rate of the microwave pulse. Discharge uniformity may well have been improved if the magnetron could have been run in CW mode at other power input configurations.

A method for measuring the vibrational temperature of the ground state of N_2 was presented in chapter 8. Vibrational temperature measurements from the three lasers varied between 2000 and 5000 K where reliable measurement was possible and was found to increase with power input. In the V1 laser, which did not have its current moderated by a quartz dielectric, significantly higher vibrational temperatures were observed than in the V2 and V3 lasers. A spectroscopic method of identifying discharges in which lasing was impossible or severely impaired was also found.

While microwave-excited CO_2 lasers have existed for some time, the lasers presented in this work are among only a few [68, 59, 86] which have attempted to take advantage of area-scaling using the slab geometry. In addition, the V3 would appear to be the only report of such lasers being operated in the sealed-off mode. Except for [68] which is ambiguous in many respects, the efficiencies reported for these lasers are similar to those achieved by the V3 laser.

9.2 Future work

Currently it is not clear whether the ability of microwave-excited CO_2 lasers to extract power from a gas discharge is on par with RF-excited devices of the same type. While significant power, at reasonable efficiency, has been extracted from the V3 laser, discharge coupling and plasma uniformity issues meant that higher power operation was not possible. It is regrettable that the effect which changes in gas mixture had on the the laser output were not discovered earlier in the experiments on the V3 laser. A more detailed study of gas mixtures is required.

More diagnostic procedures need to be developed, specifically, the difficulty with measuring plasma parameters such as E/N needs to be resolved. Spectroscopy has proved to be a useful non-invasive method of extracting information about the state of a discharge. A system capable of real-time measurement, perhaps a linear diode array spectrometer, would be an invaluable tool for diagnostic and optimisation purposes. To this end a more comprehensive spectroscopic model needs to be developed.

Operation at high frequency means, in principle, that narrow gap spacings can be used in conjunction with higher input power. A more efficient microwave coupling mechanism needs to be developed in order to take advantage of the increase in output power such narrow gap spacings offer. A magnetron/waveguide system capable of variable frequency and variable output power operation would greatly facilitate the investigation of such coupling systems.

Changes in gas mixture were found have a significant effect on lasing characteristics. An optimum gas mixture for a microwave-excited CO_2 laser needs to be determined perhaps with the use of plasma kinetics codes such BOLTZ [92] which calculate optimum E/N values for specific gas mixes. Such models may have to be altered to take account of the higher excitation frequency under investigation here.

Vibrational temperatures in the laser need to be investigated further. Experiments examining how the vibrational temperature varies with CO_2 partial pressure and dissociation fraction may lead to a better understanding of the unusual excitation processes described in section 7.3.1.

9.3 Design improvements

As the lasers designed and built for this work were constructed for experimental purposes they have a number of disadvantages compared with commercial RF-excited CO_2 lasers on the market today. However, there does not appear to be any reason why microwave-excited devices can not be made as compact and convenient as RF lasers.

The power supply used for these experiments was a large and relatively expensive

device as it was required it to be highly flexible. In a purpose built laser with known operational parameters, a simpler power supply design could used. If, for example, CW operation is not required, a pulse transformer power supply might suffice.

Compact, portable devices are always preferred to larger devices whose transport is restricted for some reason. Of the designs used in this research the most restricting aspect of the laser is the size of the microwave waveguide. Alternatives to this design were discussed in chapter 4. One method which was tentatively investigated, but not used because it was less versatile than the horn arrangement, was to feed the laserhead in a T arrangement where the magnetron is placed adjacent to one of the quartz vacuum seals. This arrangement was very compact and led to a moderately uniform discharge.

Waveguide optics is a topic which has been well studied for CO_2 lasers. Much of this effort has been devoted to extracting good beam quality from waveguide lasers. Methods employing high mode discrimination and unstable optics, for example, can be directly applied to all the designs studied in this work.

9.4 Summary

Microwave-pumped slab-cooled infrared-waveguide CO_2 lasers present many interesting opportunities and challenges. Such lasers have great potential. It has been shown that it is possible to build a microwave-excited CO_2 laser using simple and inexpensive equipment which is capable of 3 W output at efficiencies in excess of 5%.

Appendix A

Physical constants

The following table is a list of useful physical constants.

Speed of light	c	$2.997924580 \times 10^{8}$	ms^{-1}
Planck constant	h	$6.6260755 \times 10^{-34}$	Js
Rationalised Planck constant	$\hbar$	$1.05457266 \times 10^{-34}$	Js
Electronic charge	e	$1.60217733 \times 10^{-19}$	C
Vacuum permeability	μ_0	$4\pi \times 10^{-7}$	NA^{-2}
Vacuum permittivity[1]	ϵ_0	$8.8541878 \times 10^{-12}$	Fm^{-1}
Electron mass	m_e	$9.1093897 \times 10^{-31}$	kg
Proton mass	m_p	$1.6726231 \times 10^{-27}$	kg
Boltzmann constant	k	1.380658×10^{-23}	JK^{-1}

Ideal gas equation,

$$PV = nRT \quad \text{or} \quad PV = NkT \tag{A.1}$$

$$\frac{N}{VP} = \frac{1}{kT} = 3.22 \times 10^{16}\ \mathrm{cm}^{-3}/\mathrm{torr} \quad \text{at } 300\ \mathrm{K} \tag{A.2}$$

In the following E represents the energy in joules (J), T is a temperature in kelvin (K), E_{eV} is the energy in electron-volts (eV), E_k implies the energy in wavenumbers (cm^{-1}) and λ is a wavelength. Some useful relations are,

$$E_k = \frac{10000}{\lambda_{(\mu m)}}\ (\mathrm{cm}^{-1}) \qquad E_k = \frac{E}{100hc}\ (\mathrm{cm}^{-1}) \qquad E = kT\ (J) \qquad E_{eV} = \frac{E}{e}\ (eV) \tag{A.3}$$

$$1\ \mathrm{torr} = 1\ \mathrm{mmHg} = \tfrac{1}{760}\ \mathrm{atm} \qquad 1\ \mathrm{mbar} = 0.76\ \mathrm{torr} = 100\ \mathrm{Pa}$$

[1]Note that this value is exact when obtained via $\epsilon_0 = 1/\mu_0 c^2$ as the values for c, μ_0 and hence ϵ_0 are adopted and therefore exact.

Bibliography

[1] R L Abrams, *Coupling losses in hollow waveguide laser resonators*, *IEEE J. Quantum Electron.*, **8**(11), 838–843, 1972.

[2] R L Abrams and Chester A N, *Resonator theory for hollow waveguide lasers*, *Applied Optics*, **13**(9), 2117–2125, 1974.

[3] K M Abramski, A D Colley, H J Baker and D R Hall, *Power scaling of large-area transverse radio frequency discharge CO_2 lasers*, *Appl. Phys. lett.*, **54**(19), 1833–1835, 1989.

[4] W P Allis, S C Brown and E Everhart, *Electron density distribution in a high frequency discharge in the presence of plasma resonance*, *Phys. Rev.*, **84**(3), 519–522, November 1951.

[5] S Avrillier and J Verdonck, *Coupling losses in laser resonators containing a hollow rectangular dielectric waveguide*, *J. Appl. Phys.*, **48**(12), 4937–4941, 1977.

[6] C J Baker, D R Hall and A R Davies, *Electron energy distributions, transport coefficients and electron excitation rates for RF excited CO_2 lasers*, *J. Phys. D: Appl. Phys.*, **17**, 1597–1606, 1984.

[7] W Benesch and J T Vanderslice, *Frank-Condon factors for observed transitions in N_2 above 6 eV*, *Astrophys. J.*, **143**, 236–252, 1965.

[8] W Benesch and J T Vanderslice, *Potential curves for the observed states of N_2 below 11 eV*, *Astrophys. J.*, **142**(2), 1227–1240, 1965.

[9] W Benesch and J T Vanderslice, *Frank-Condon factors for permitted transitions in N_2*, *Astrophys. J.*, **144**, 408–418, April 1966.

[10] R Bleekrode, *A study of the spontaneous emission from CO_2-N_2-He-H_2 laser discharges $C^3\Pi_u - B^3\Pi_g$ emission bands of N_2*, *IEEE J. Quantum Electron.*, **5**(2), 57–60, February 1969.

[11] S C Brown, *Introduction to electrical discharges in gases*, Wiley and Sons, Inc., New York, 1966.

[12] J J Burke, *Propagation constants of resonant waves on homogeneous, isotropic slab waveguides*, *Appl. Opt.*, **9**(11), 2444–2452, 1970.

[13] A A Cameron, F Villareal, A D Colley, H J Baker and D R Hall, *CW molecular lasers at atmospheric pressure using planar waveguides*, in *XX international quantum electronics conference*, Sydney, 1996.

[14] P P Chenausky, *Paper TUKK4*, in *Conference on lasers and electrooptic systems*, San Diego, 1980.

[15] P O Clark and J Y Wada, *Characteristics of CO_2-Xe-He lasers*, in *13th IEEE International Electron Devices Meeting*, Washington, D.C., October 1967.

[16] P O Clark and J Y Wada, *The influence of xenon on sealed-off CO_2 lasers*, *IEEE J. Quantum Electron.*, **4**(5), 263–266, May 1968.

[17] S B Cohn, *Properties of ridge wave guide*, *Proc. IRE*, 783–788, August 1947.

[18] A D Colley, H J Baker and D R Hall, *Planar waveguide, 1 kW CW, carbon dioxide laser excited by a single transverse RF discharge*, *Appl. Phys. Lett.*, **61**(2), 136–138, July 1992.

[19] T A Cool, *Power and gain characteristics of high speed flow lasers*, *J. Appl. Phys.*, **40**(9), 3563–3573, August 1969.

[20] J J Degnan and D Hall, *Finite-aperture waveguide-laser resonators*, *IEEE J. Quantum Electron.*, **9**(9), 901–910, September 1973.

[21] T F Deutch, F A Horrigan and R I Rudko, *CW operation of high-pressure flowing CO_2 lasers*, *Appl. Phys. Lett.*, **15**(3), 88–91, August 1969.

[22] E Everhart and C B Sanborn, *The admittance of high frequency gas discharges*, *Phys. Rev.*, **76**(6), 839–942, September 1949.

[23] M C Fowler, *Influence of plasma kinetic processes on electrically excited CO_2 laser performance*, *J. Appl. Phys.*, **43**(8), 3480–3487, August 1972.

[24] A G Fox and T Li, *Resonant modes in a maser interferometer*, *Bell. Sys. Tech. J.*, **40**, 453–488, March 1961.

[25] B Freisinger, H Frowein, M Pauls, G Pott and J Schäfer J Uhlenbusch, *Excitation of CO_2 lasers by microwave discharges.*, *SPIE - CO_2 lasers and applications II*, **1276**, 29–40, 1990.

[26] E L Ginzton, *Microwave measurements*, McGraw-Hill, New York, 1957.

[27] G A Griffiths, in *Proceedings of SPIE Meeting*, volume 227, 6–11, Washington, D.C., 1980.

[28] R D Hake and Jr and A V Phelps, *Momentum-transfer and inelastic-collision cross sections for electrons in O_2, CO, and CO_2*, *Phys. Rev.*, **158**(1), 70–84, June 1961.

[29] K G Handy and J E Brandelik, *Laser generation by pulsed 2.45 GHz microwave excitation of CO_2*, *J. Appl. Phys.*, **49**(7), 3753–3756, July 1978.

[30] N S Harris, *Modern vacuum practice*, McGraw Hill, Berkshire, England, 1989.

[31] D He and D R Hall, *A 30-W radio frequency excited waveguide CO_2 laser*, *Appl. Phys. Lett.*, **43**(8), 726–728, 1983.

[32] D He and D R Hall, *Longitudinal voltage distribution in transverse rf discharge waveguide lasers*, *J. Appl. Phys.*, **54**(8), 4367–4373, August 1983.

[33] D He and D R Hall, *Influence of xenon on sealed-off operation of rf-excited CO_2 waveguide lasers*, *J. Appl. Phys.*, **56**(3), 856–857, August 1984.

[34] E Hect, *Optics*, Addison-Wesley, second edition, 1987.

[35] D M Henderson, *Waveguide lasers with intracavity electrooptic modulators: misalignment loss*, *Appl. Opt.*, **15**(4), 1066–1070, 1976.

[36] M A Herlin and S C Brown, *Breakdown of a gas at microwave frequencies.*, *Phys. Rev.*, **74**(3), 291–296, 1948.

[37] M A Herlin and S C Brown, *Electrical breakdown of a gas between coaxial cylinders at microwave frequencies*, *Phys. Rev.*, **74**(8), 910–913, 1948.

[38] A E Hill, *Role of thermal effects and fast flow power scaling techniques in CO_2-N_2-He lasers*, *Appl. Phys. Lett.*, **16**(11), 423–426, June 1970.

[39] J R Howorth, *The excitation mechanism for the $C^3\Pi_u$ state of nitrogen in a glow discharge*, *J. Phys. B: Atom. Molec. Phys.*, **5**, 402–407, February 1972.

[40] T Ikeda and M Danno, *Diagnostics of TM_{010}-mode microwave cavity discharges in CO_2-N_2-He laser gas mixtures I. Measurement of dielectric constant*, *IEEE J. Quantum Electron.*, **31**(8), 1525–1532, August 1995.

[41] T Ikeda and M Danno, *Diagnostics of TM_{010}-mode microwave cavity discharges in CO_2-N_2-He laser gas mixtures II. Measurement of vibration temperature*, *IEEE J. Quantum Electron.*, **31**(8), 1533–1536, August 1995.

[42] T Ikeda, M Danno, H Shimazutsu, T Abe and J Tanaka, *TM_{010}-mode microwave excited high power CO_2 laser using a cylindrical resonant cavity*, *IEEE J. Quantum Electron.*, **30**(11), 2657–2662, November 1994.

[43] D J Jackson, *Classical electrodynamics*, John Wiley & Sons, second edition, 1975.

[44] P E Jackson, H J baker and Hall D R, *CO_2 large-area discharge laser using an unstable-waveguide hybrid resonator*, *Appl. Phys. Lett.*, **54**(20), 1950–1952, 1989.

[45] G W C Kaye and T H Laby, *Tables of physical and chemical constants and some mathematical functions*, Longman, London, 15th edition, 1986.

[46] H Kogelnik and T Li, *Laser beams and resonators*, *Applied Optics*, **5**(10), 1550–1566, October 1966.

[47] A D Kosoruchkina and E S Trekhov, *Method for determining the vibrational temperature of the $X^1\Sigma_g^+$ state of the nitrogen molecule*, *Sov. Phys. Tech. Phys.*, **20**(5), 679–681, 1976.

[48] H Krammer, *Field configurations and propagation constants of modes in hollow rectangular dielectric waveguides*, *IEEE J. Quantum Electron.*, **12**(8), 505–507, August 1976.

[49] Laakmann, in *Proceedings of Lasers '78 Conference*, Orlando, Florida, 1978.

[50] Laakmann, in *Proceedings of Lasers '79 Conference*, 741–743, Orlando, Florida, 1979.

[51] J L Lachambre, J Macfarlane, G Otis and P Lavigne, *A transversely rf-excited CO_2 waveguide laser*, *Appl. Phys. Lett.*, **32**(10), 652–653, 1978.

[52] A Lapucci, F Rossetti, M Ciofini and G Orlando, *On the longitudinal voltage distribution in radio-frequency-discharged CO_2 lasers with large-area electrodes*, *IEEE J. Quantum Electron.*, **31**(8), 1537–1542, August 1995.

[53] T Ledig and B Schröder, *Electron energy distribution functions and power transfer data for radio-frequency discharges in CO_2 laser gas mixtures*, *J. Phys. D: Appl. Phys.*, **23**(12), 1624–1632, 1990.

[54] P Loosen and R Wester, *Parameter limits of thermal instabilities in high-frequency CO_2 laser discharges*, *J. Phys. D: Appl. Phys.*, **28**, 849–855, 1995.

[55] J J Lowke, A V Phelps and B W Irwin, *Predicted electron transport coefficients and operating characteristics of CO_2-N_2-He laser mixtures*, *J. Appl. Phys.*, **44**(10), 4664–4671, October 1973.

[56] E A J Marcatili and R A Schmeltzer, *Hollow metallic and dielectric waveguides for long distance optical transmission and lasers*, *Bell Syst. Tech. J.*, **43**, 1783–1809, July 1964.

[57] D Marcuse, *Hollow dielectric waveguide for distributed feedback lasers*, *IEEE J. Quantum Electron.*, **8**(7), 661–669, 1972.

[58] T L Martin, *Electronic circuits*, Prentice-Hall, 1959.

[59] M März and Oestreicher, *Microwave excitation of a diffusion-cooled CO_2 laser*, *J. Phys. D: Appl. Phys.*, **27**(3), 470–474, March 1994.

[60] M März and W Oestreicher, *A versatile microwave plasma source and its application for a CO_2 laser*, *Rev. Sci. Instrum.*, **65**(9), 2980–2983, September 1994.

[61] J D McMullen, D B Anderson and R L Davis, *Optical-gain measurements in a CW transverse-discharge transverse-gas-flow CO_2:N_2:He planar-waveguide laser*, *J. Appl. Phys.*, **45**(11), 5084–5087, 1974.

[62] R C Metaxas and R J Meredith, *Industrial microwave heating*, Peter Peregrinus Ltd., London, 1983.

[63] A Kh Mnatsakanyan and L I Podlubnyi, *Change of the vibrational distribution function in transitions between electron states in diatomic molecules due to collisions with electrons*, *Sov. Phys. - Tech. Phys.*, **16**(10), 1680–1683, April 1972.

[64] G Moeller and J D Rigden, *High-power laser action in CO_2-He mixtures*, *Appl. Phys. Lett.*, **7**(10), 274–276, November 1965.

[65] C G Montgomery, editor, *Technique of microwave measurements*, volume 11 of *Radiation laboratory series*, McGraw-Hill, New York, 1947.

[66] A J Moses, *Optical materials properties*, volume 1 of *Handbook of electronic materials*, IFI/Plenum, 1971.

[67] H Nishihara, T Inoue and J Koyama, *Low-loss parallel-plate waveguide at 10.6μm*, *Appl. Phys lett.*, **25**(7), 391–393, 1974.

[68] J Nishimae and K Yoshizawa, *Development of CO_2 laser excited by 2.45 GHz microwave discharge*, *SPIE - High power gas lasers*, **1225**, 340–348, 1990.

[69] R Nowack, H Opower, U Shaefer, K Wessel and T Hall, *High power CO_2 waveguide laser of 1 kW category*, *SPIE*, **1276**, 18, 1990.

[70] S Ono and S Teii, *Vibrational temperature in a weakly ionised steady-state nitrogen discharge plasma*, *J. Phys. D: Appl. Phys.*, **16**, 163–170, 1983.

[71] S Ono and S Teii, *Vibrational temperature in a weakly ionised CO_2-N_2-He discharge*, *J. Phys. D: Appl. Phys.*, **18**, 441–450, 1985.

[72] Jamison S P, *2.45 GHz plasma excitation for the production of a diffusively cooled CO_2 laser*, Master's thesis, University of Canterbury, Christchurch, New Zealand, 1993.

[73] R A Paananen, *A CO_2-N_2-He-Xe laser*, *Proc. IEEE (Letters)*, **5**, 2035, November 1967.

[74] M L Passow, M L Brake, P Lopez, W B McColl and T E Repetti, *Microwave resonant-cavity-produced air discharges.*, *IEEE Trans. Plasma Sci.*, **19**(2), 219–228, 1991.

[75] C Patel, W Faust and R McFarlane, *CW laser action on rotational transitions of the $\Sigma_\mu^+ - \Sigma_g^+$ vibrational band of CO_2*, *Bull. Am. Phys. Soc.*, **9**, 500, 1964.

[76] C K N Patel, *Continuous-wave laser action on vibrational-rotational transitions of CO_2*, *Phys. Rev.*, **136**(5A), 1187–1193, November 1964.

[77] C K N Patel, *Interpretation of CO_2 optical maser experiments*, *Phys. Rev. Lett.*, **12**(21), 588–590, May 1964.

[78] C K N Patel, *Selective excitation through vibrational energy transfer and optical maser action in N_2-CO_2*, *Phys. Rev. Lett.*, **13**(21), 617–619, November 1964.

[79] C K N Patel, P K Tien and J H McFee, *CW high-power CO_2-N_2-He laser*, *Appl. Phys. Lett.*, **7**(11), 290–292, December 1965.

[80] Radio corporation of America, Langcaster, Pa. USA, *RCA phototubes and photocells*, 1963.

[81] R S Reynolds and J D Schlafer, *20-watt single frequency CO_2 laser*, in *13th IEEE International Electron Devices Meeting*, Washington, D.C., October 1967.

[82] A Roth, *Vacuum technology*, North-Holland, Amsterdam, third edition, 1990.

[83] G J Schultz, *Measurement of excitation of N_2, CO and He by electron impact*, *Phys. Rev.*, **116**(5), 1141–1146, December 1959.

[84] G J Schultz, *Vibrational excitation of N_2, CO, and H_2 by electron impact*, *Phys. Rev.*, **135**(4A), 988–994, August 1964.

[85] C J Shackleton, K M Abramski, H J Baker and D R Hall, *Lateral and transverse mode properties of CO_2 slab waveguide lasers*, *Optics Comm.*, **89**(5), 423–428, May 1992.

[86] Y Sintov, A Gabay and S Yatsiv, *Self-activated, forced convective cooling in a pulsed slab CO_2 laser*, *J. Phys. D: Appl. Phys.*, **30**, 2530–2535, 1997.

[87] P W Smith, *A waveguide gas laser*, *Appl. Phys. Lett.*, **19**(5), 132–134, September 1971.

[88] G C Southworth, *Principles and applications of waveguide transmission*, D. Van Nostrand Company Inc., Princeton, New Jersey, New York, 1950.

[89] J D Strohschein, W D Bilida, Seguin H J J and C E Capjack, *Computational model of longitudinal discharge uniformity in RF-excited CO_2 slab lasers*, *IEEE J. Quantum Electron.*, **32**(8), 1289–1298, August 1996.

[90] L V Sutter, in *Proceedings of SPIE Meeting*, volume 227, Washington, D.C., 1980.

[91] O Svelto, *Principles of lasers*, Plenum Press, New York, third edition, 1989.

[92] R M Thomson, K Smith and A R Davies, *BOLTZ: A code to solve the transport equation for electron distributions and then calculate transport coefficients and vibrational excitation rates in gases with applied fields*, *Comp. Phys. Comm.*, **11**, 369–383, 1976.

[93] W B Tiffany, R Targ and J D Foster, *Kilowatt CO_2 gas-transport laser*, *Appl. Phys. Lett.*, **15**(3), 91–93, August 1969.

[94] H C Torrey and C A Whitmer, *Crystal rectifiers*, volume 15 of *Radiation laboratory series*, McGraw-Hill, New York, 1948.

[95] Y S Touloukian, editor, *Thermophysical properties of matter*, volume 7 - Thermal radiative properties: metallic elements and alloys, Plenum, New York, 1979.

[96] J T Verdeyen, *Laser electronics*, Prentice-Hall, New Jersey, second edition, 1989.

[97] P Vidaud, S M A Durrani and D R Hall, *Alpha and gamma RF capacitative discharges in N_2 at intermediate pressures*, *J. Phys. D: Appl. Phys.*, **21**, 57–66, 1988.

[98] R Wester and S Seiwert, *Investigation of microwave excited CO_2 laser discharges*, *J. Phys. D: Appl. Phys.*, **24**, 1101–1107, 1991.

[99] W J Witteman, *High-output powers and long lifetimes of sealed-off CO_2 lasers*, *Appl. Phys. Lett.*, **11**(11), 337–338, December 1967.

[100] W J Witteman, *The CO_2 Laser*, volume 53 of *Springer series in optical sciences*, Springer-Verlag, Berlin, 1987.

[101] S Yatsiv, in *Gas flow and chemical laser conference*, edited by Rosenwaks, 252–254, Berlin, 1987, Springer.